PETROGENETIC RELATIONSHIPS BETWEEN RELATIVELY POTASSIC AND RELATIVELY SODIC ALKALINE ROCKS FROM THE SPANISH PEAKS AREA NEAR WALSENBURG, COLORADO

by

HEATH A. MCGREGOR

(Under the Direction of Michael F. Roden)

ABSTRACT

Alkaline lamprophyre rocks crop out as sills and sub parallel dikes near the Spanish Peaks, CO. Lamprophyre dikes and sills north, south, and west of Spanish Peaks are moderately mafic (~7 wt.% MgO), basic (~49 wt.% SiO_2), and range from relatively sodic ($Na_2O>K_2O$) to relatively potassic ($K_2O>Na_2O$). Previous geochronologic and isotopic research on rocks investigated in this study, indicate that sodic and potassic magmatism originated at approximately the same time and from isotopically similar mantle sources. Rock types include minettes and sannaites, which have phlogopite or amphibole ± clinopyroxene ± olivine phenocrysts and groundmass potassium feldspars. Rare diopside grains in potassic rocks have greenish, Fe- and Al-rich cores found worldwide in other potassium-rich, mafic igneous rocks. Major and trace element abundance data from this study indicate that the two magma series formed independently from distinct sources.

INDEX WORDS: Spanish Peaks; alkaline lamprophyre; sodic rocks; potassic rocks; major element abundances; trace element abundances; minettes; sannaites; Rio Grande Rift; mantle metasomatism; phlogopite; amphibole

PETROGENETIC RELATIONSHIPS BETWEEN RELATIVELY POTASSIC AND RELATIVELY SODIC ALKALINE ROCKS FROM THE SPANISH PEAKS AREA NEAR WALSENBURG, COLORADO

by

HEATH A. MCGREGOR

A.A., Georgia Perimeter College, 2005

B.S., University of Georgia, 2007

A Thesis Submitted to the Graduate Faculty of The University of Georgia in Partial Fulfillment of the Requirements for the Degree

MASTERS OF SCIENCE

ATHENS, GEORGIA

2010

PETROGENETIC RELATIONSHIPS BETWEEN RELATIVELY POTASSIC AND RELATIVELY SODIC ALKALINE ROCKS FROM THE SPANISH PEAKS AREA NEAR WALSENBURG, COLORADO

by

HEATH A. MCGREGOR

Major Professor:	Michael F. Roden
Committee:	Douglas Crowe Alberto E. Patiño Douce

Electronic Version Approved:

Maureen Grasso
Dean of the Graduate School
The University of Georgia
May 2010

DEDICATION

This thesis is dedicated to my grandfather Clarence E. Taylor who in his passing encouraged me to pursue an education. This is also dedicated to my wife Jennifer A. McGregor who if not for her my promise to him would not be fulfilled.

ACKNOWLEDGEMENTS

I would like to thank the Geology department of The University of Georgia and all of its faculty and staff. Thank you; Mike Roden for your guidance and understanding, Alberto Patiño Douce for understanding of the universe, Doug Crowe and Jim Wright for your knowledge and humor of geology, Rob Hawman and Steve Holland for ability to teach, Sandra Wyld, Sally Walker, Paul Schroeder, and Sam Swanson for your patience and challenging class work; Jeff Chaumba, Steve Clark and Chris Fleisher for your friendship and endless help in my endeavors, and Linda Davis for your help in securing access to my research area.

TABLE OF CONTENTS

Page

LIST OF TABLES

Page

LIST OF FIGURES

Page

1. INTRODUCTION

An extensive dike system located in the northern part of the Raton Basin, in south-central Colorado, is world renowned for its prominence and relationship to the Spanish Peaks and other igneous stocks in the area. The East and West Spanish Peaks (Figure 1.1) are two prominent features located within the La Veta syncline of the Raton Basin. The Raton Basin is situated to the east of the Rio Grande Rift, a failed intercontinental rift system which initiated between ~30Ma to ~25 Ma (Lipman et al., 1972) (Figure 1.2). Dike and sill emplacement in the northwestern part of the Raton Basin (including East and West Spanish peaks and other stocks in the area) occurred post Laramide orogeny (i.e. < ~46Ma) (Penn et al., 1996). Previous works studying the orientation of the dikes generally attribute the placement to multiple and varying stress fields. These stress fields, regional and local, reflect tectonic events, which occurred between ~37Ma to ~11Ma (Johnson, 1961, Muller, 1986, Odé, 1957, Smith, 1975). Johnson (1968) divided the dikes into three separate groups (radial, subparallel, and independent) based on their structural relationships and orientations with respect to the East and West Spanish Peaks, and Dike Mountain.

1.1. *PREVIOUS STUDIES OF DIKES*

R.C. Hill was the first geologist that extensively mapped the stocks, sills and two thirds of the dikes that crop out in the area (Knopf, 1936). The study was conducted for the United States Geological Survey in the search for possible coal bearing resources. Hill classified dikes, based on field observations, in an ordered sequence: (1) early monzonite porphyry (2) early lamprophyre (3) Late monzonite porphyry (4) late lamprophyre and (5) basalts.

Knopf (1936) was the first geologist to investigate the chemistry and petrology of the Spanish Peaks dikes extensively. He recognized that the classifications of lamprophyres were not sufficient to characterize the extent of bulk variations. Therefore, he named the dike rocks based on the predominant phenocrysts in the rock. He also discovered that unless a lamprophyric dike cut another dike of known

age, you could not distinguish between the “earlier” and “later” stage lamprophyres, petrographically or chemically (Knopf, 1936).

Figure 1.1 The East and West Spanish Peaks (from left to right) located in south-central Colorado. Photograph taken from atop Walsenburg dike looking southwest. Note the Sangre de Cristo Range in the backdrop to the right.

Johnson (1968) created a highly detailed map of the dikes and sills of the area (Figure 1.3). In his study, consisting of fieldwork from 1948-1962, the igneous rocks were categorized into seven groups based on modal mineralogy of petrographic thin sections: granites, granodiorites, syenites, syenodiorites, diorites, syenogabbros, and gabbros. He then included lamprophyres under five of these group names. The lamprophyres were classified as follows: minettes and vogesites as syenites, soda-minettes and soda-vogesites as syenodiorites, spessartites as diorites, odinites and monchiquites as syenogabbros, and fourchites (with some odinites and monchiquites) as gabbros.

Smith (1975) did a two-year study on the dikes and sills located south of the Spanish Peaks. His goal was to investigate the structural features to gain a better understanding of the origin of the spatial pattern of the dikes and to understand the possible connection to the central stocks. Additionally he

collected a range of samples to determine variations in composition and absolute ages. He concluded that even though many geologists prior to his study interpreted stocks, dikes and sills of the area to be associated with the Laramide orogeny, they were in fact post-orogenic and associated with the Rio Grande rift, which initiated in the mid-late Tertiary. The absolute age dating conflicted with prior ordering of intrusive events. He also suggested that the cause of the magmatism was a rising diapir or plume of hot mantle that partially melted and/or mixed with a partially melted, biotite-rich lower crustal source. The variation in chemistry and petrology of the dikes could also indicate varying degrees of melting of the source region or exhaustion of water content in the lower crustal source rock. The lamprophyres in his study were categorized as odinites, and spessartites.

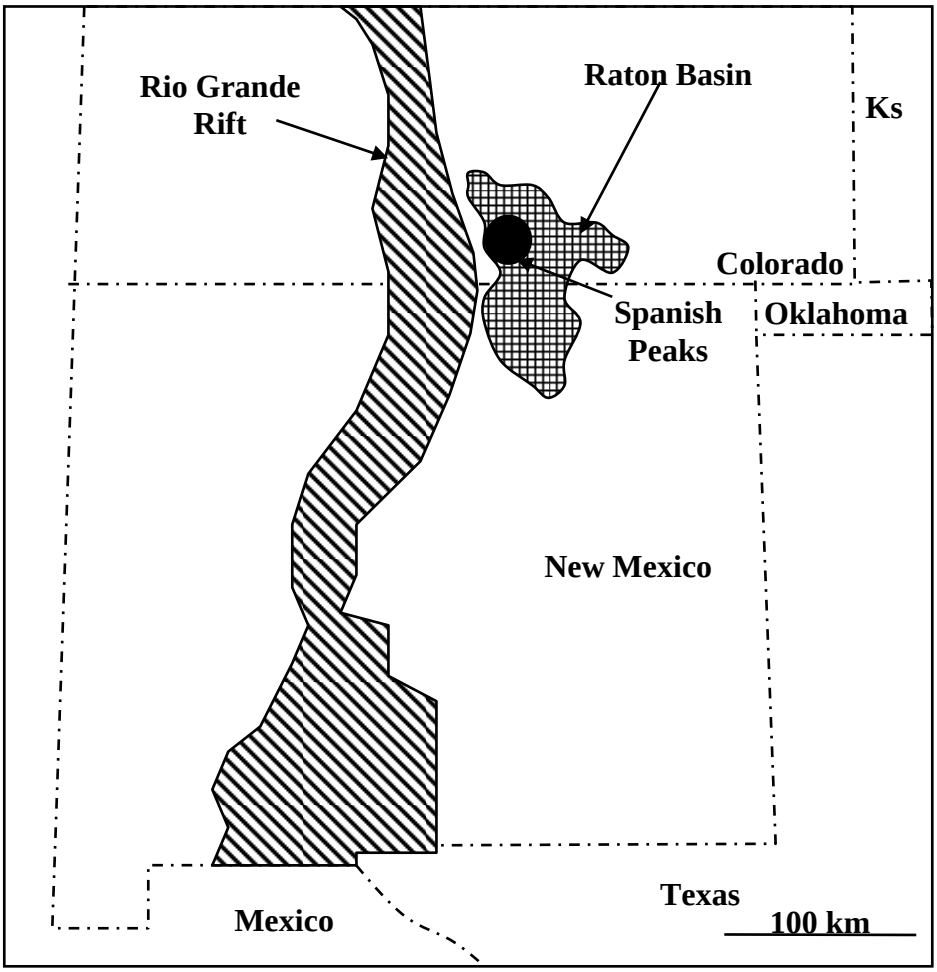

Figure 1.2. Spanish Peaks location with respect to Rio Grande Rift and Raton Basin.

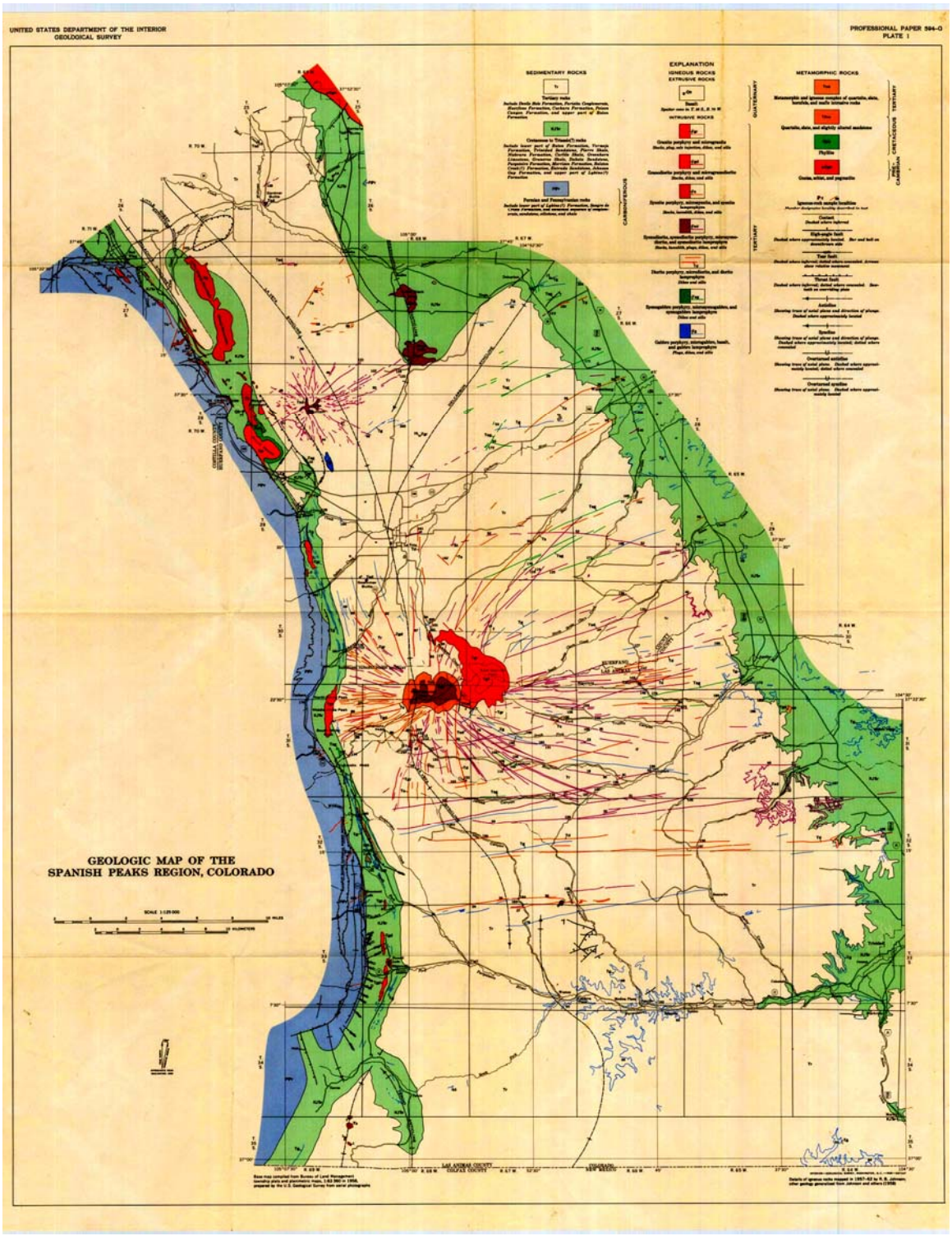

Figure 1.3. Quadrangle of Spanish Peaks region, Colorado from Johnson (1968)

Jahn (1979) did a study of the various rock suites that included the lamprophyres of the subparallel dikes. He performed trace and rare earth element analyses to better define the possible source of variation in the different suite of rocks in the surrounding area. He concluded that although differentiation and magma mixing could have played a role in the variation of the rocks, it was a small role and that the controlling factor was different parent sources. He also concluded that partial melting of an upper mantle (garnet peridotite) generated the lamprophyres (minettes and camptonites).

Penn (1994, 1996) did high precision $^{40}Ar/^{39}Ar$ dating in the area to resolve the inconsistencies in the ordering of intrusive history. His study included the lamprophyre dikes of the area. He placed the lamprophyres into two broad groups ("camptonite" variety and "minette" variety). He concluded that the camptonite variety of lamprophyre which forms N80E dikes to the south of the Spanish Peaks, was the "earlier" stage of intrusion preceding the emplacement of the East and West Spanish Peaks. The minette varieties which form N60E dikes to the north of the Spanish Peaks, were a "later" phase of lamprophyres intruded after the emplacement of the stocks and radial dikes.

Most recent Miggins (2002) included additional high-precision $^{40}Ar/^{39}Ar$ dating, petrographic and chemical analysis of dikes and sills of the area. His data analyses and age dating revealed that both "camptonite" variety (which he labeled as "hornblende" lamprophyres) and "minette" variety (named "biotite" lamprophyres) intruded after stock emplacement. Some of the hornblende lamprophyres based on petrographic field observations had biotite lamprophyre chemistry and vice versa. Furthermore, some of these hornblende lamprophyres and biotite lamprophyres were in very close proximity and were not restricted to just the south N80E or north N60E trends, but were also identified in sills.

1.2. *PURPOSE OF THIS STUDY*

$^{40}Ar/^{39}Ar$ isotope dating of the stocks, sills and dikes of the area constrain the age of magmatism from middle to late Eocene (~ 46 million years ago) to the late Miocene (~ 11million years ago). Radiometric dating vs. field relationship work conducted on the sub-parallel dike group has yielded contradictory evidence concerning the relationship between composition and time of emplacement of these lamprophyric dikes and associated sills.

The subparallel dikes, based on orientation, fall into two sub-groups. To the north of the Spanish Peaks, the subparallel dikes trend ~N60E and to the south they trend ~N80E. All the subparallel dikes are ultramafic to mafic in composition and are similar in composition to nearby sills. Many of these subparallel dikes and sills are considered lamprophyric in nature. These lamprophyres have been further divided into two general groups, camptonites (alkaline) and minettes (calc-alkaline). Camptonites are silica under-saturated, have $Na_2O>K_2O$, and are characterized by the presence of Na-amphiboles. Minettes are silica saturated, have $K_2O>Na_2O$ and are characterized by phenocrysts of biotite. These two lamprophyre groups originated from a parental magma generated by melting of the upper mantle based on REE patterns (Jahn, 1979), the relatively high MgO contents and the common presence of Fo-rich olivine. The relationship between the two types of lamprophyres in this area has never been fully explained. The objective of my thesis project is to determine the petrogenetic relationships between the two general types of lamprophyres and determine what, if any, liquid line of descent or evidence of crystal fractionation processes can be observed. Additionally, if possible, a further objective is to provide insight to the possible parental source or sources of the lamprophyres. Determining petrogenetic relationships is made possible due to age constraints which show that both types of lamprophyres were emplaced at the same time. Age-compositional relationships guided me in my sample selection for this study.

2. EXPERIMENTAL METHODS

The following contains detailed descriptions of field and laboratory methods.

2.1. *FIELD SAMPLING METHODS*

2.1.1. Determining field samples

In order to investigate petrogenetic relationships between the relatively potassic and relatively sodic lamprophyres in the Spanish Peaks area, the age of the rocks was a key variable. Sample selection was guided by a review of previous studies done in the area using the Ar^{40}/Ar^{39}dating method (Miggins, 2002, Penn, 1994) with the aim of sampling dike rocks with approximately the same age. Thus relatively sodic and relatively potassic samples were selected based upon K_2O/Na_2O wt %, Mg#, and various REE ratios. Map coordinates from Miggins (2002) and Penn (1994) were entered into Google Earth™ and detailed map views were printed to ensure accurate sampling correlation (Figures **2.1, 2.2, 2.3**).

2.1.2. Collection of field samples

Due to the composition of alkaline mafic rocks, surface weathering and alteration become problematic when trying to collect fresh, unaltered samples. In addition, hypabyssal intrusives can experience meteoric water alteration and country rock contamination during emplacement. Careful consideration of these problems influenced where samples were taken within outcrops. With each dike or sill, samples were gathered away from chill margins, and surface rock was removed to expose the freshest sample for collection. Approximately 9 kg of material was collected from each sample site. Brief descriptions, GPS coordinates, sketches, and pictures were taken at each site (results section).

2.2. *LIGHT MICROSCOPY METHODS*

2.2.1. Determining samples for thin sections

Thirty-two samples were collected from 15 different dikes and sills from the Spanish Peaks area. Three samples were collected from a volcanic neck (Goemmer Butte trachyandesite) located just west of the Spanish Peaks (Figure 2.2). Of those 32 samples, 27 were selected for thin section analysis. Nine samples were collected from the Walsenburg dike. Three of the Walsenburg samples and two of the Northlake sill complex samples were eliminated from thin section analysis based on sample duplication and alteration.

2.2.2. Preparation of hand samples for thin section blanks

A ~ 6mm thick slice was cut from large pieces of hand sample using a carbide tipped 20cm wet saw. From each slice a ~ 25mm x 75mm x 6mm rectangular block was cut from the center, labeled with sample number, and placed in individual bags with sample number for redundancy. All samples were then mounted to glass, ground to a thickness of ~ 30um, and polished by Quality Thin Sections, Inc. (Tucson, Arizona).

2.2.3. Light Microscopy analysis of thin sections

Microscopic analyses of thin sections were carried out using a Leica™ DM EP Polarized light microscope. Description of texture, groundmass, phenocrysts (including size, habit, color, zoning, modal %), and pictures, (using a Cannon Power Shot S50™ camera), were done for each thin section (refer to thin section notes in results section). Modal % of phenocrysts was based solely on occurrence of phenocrysts excluding the groundmass and ocelli. Using the lowest power magnification, a count of phenocrysts (view ~78mm^2) was performed. Individual totals for each type of phenocryst were divided by the total counted to determine modal percent (equation 2.1). This calculation was performed in four different locations on the thin section. The four separate totals were then averaged to give the modal % of each phenocryst. 200 grains were counted per thin section analysis.

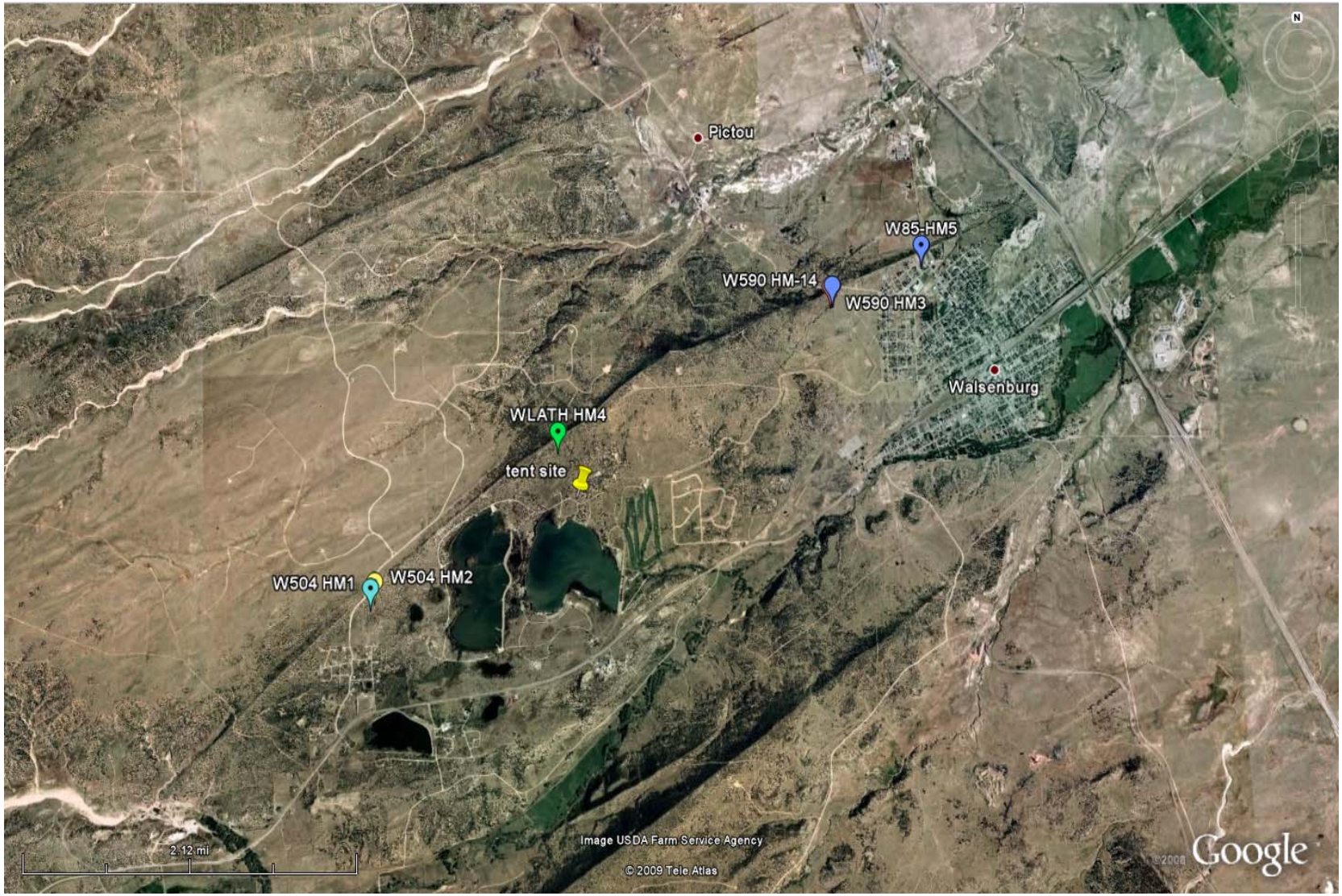

Figure 2.1 Map view of the town of Walsenburg, Colorado and Lathrop State Park. North side of town and park are bordered by Walsenburg dike. Colored balloons indicate where samples were collected along the dike, (refer to field note section for sample description). The dike is ~ 10km long. Image is from Google Earth™.

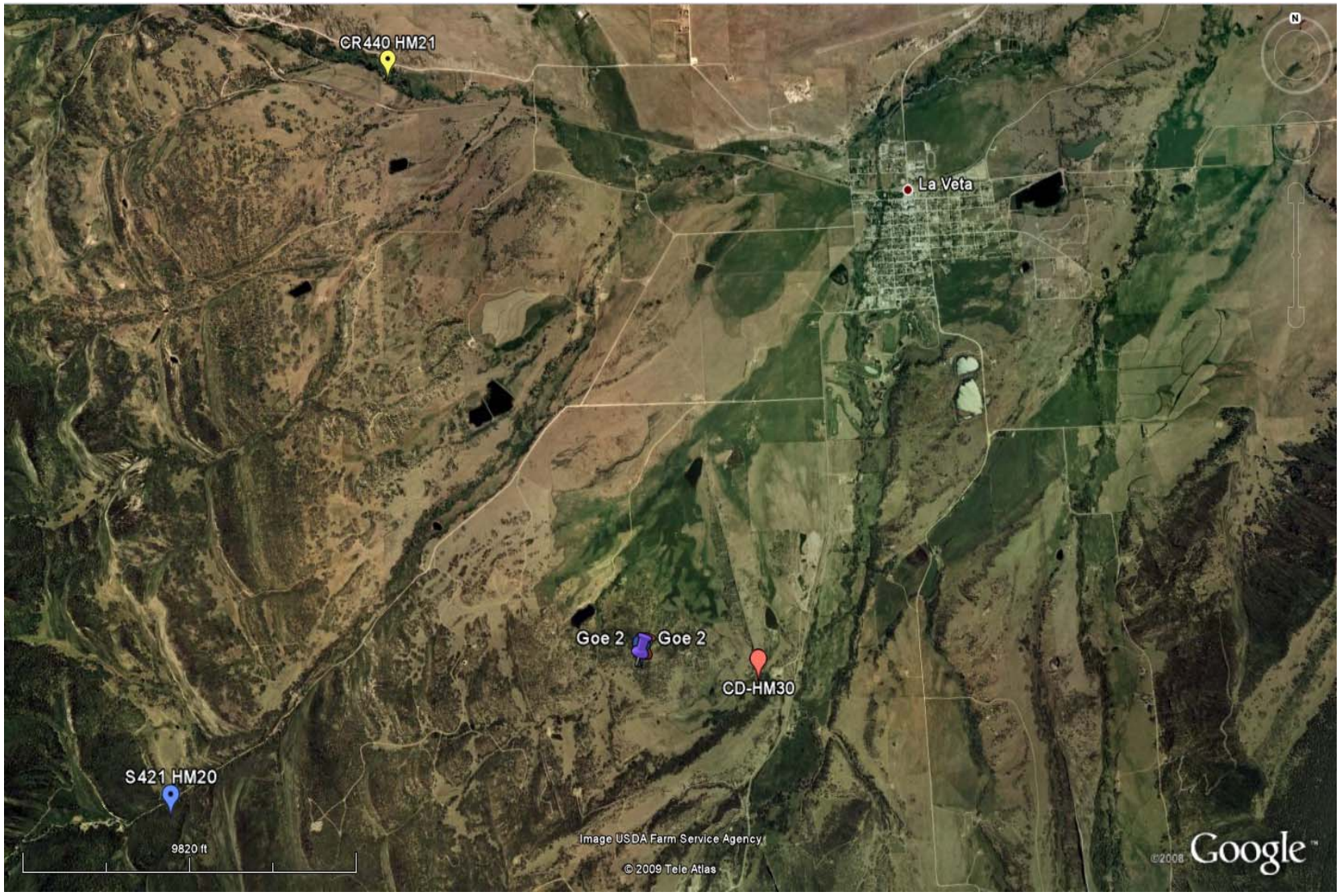

Figure 2.2 Map view of LaVeta, Colorado. To the southwest and northwest of town balloons and tack pins indicate where samples were collected from Goemmer Butte trachyandesite, two dikes, and one sill, (refer to field note section for sample description). Image is from Google Earth™.

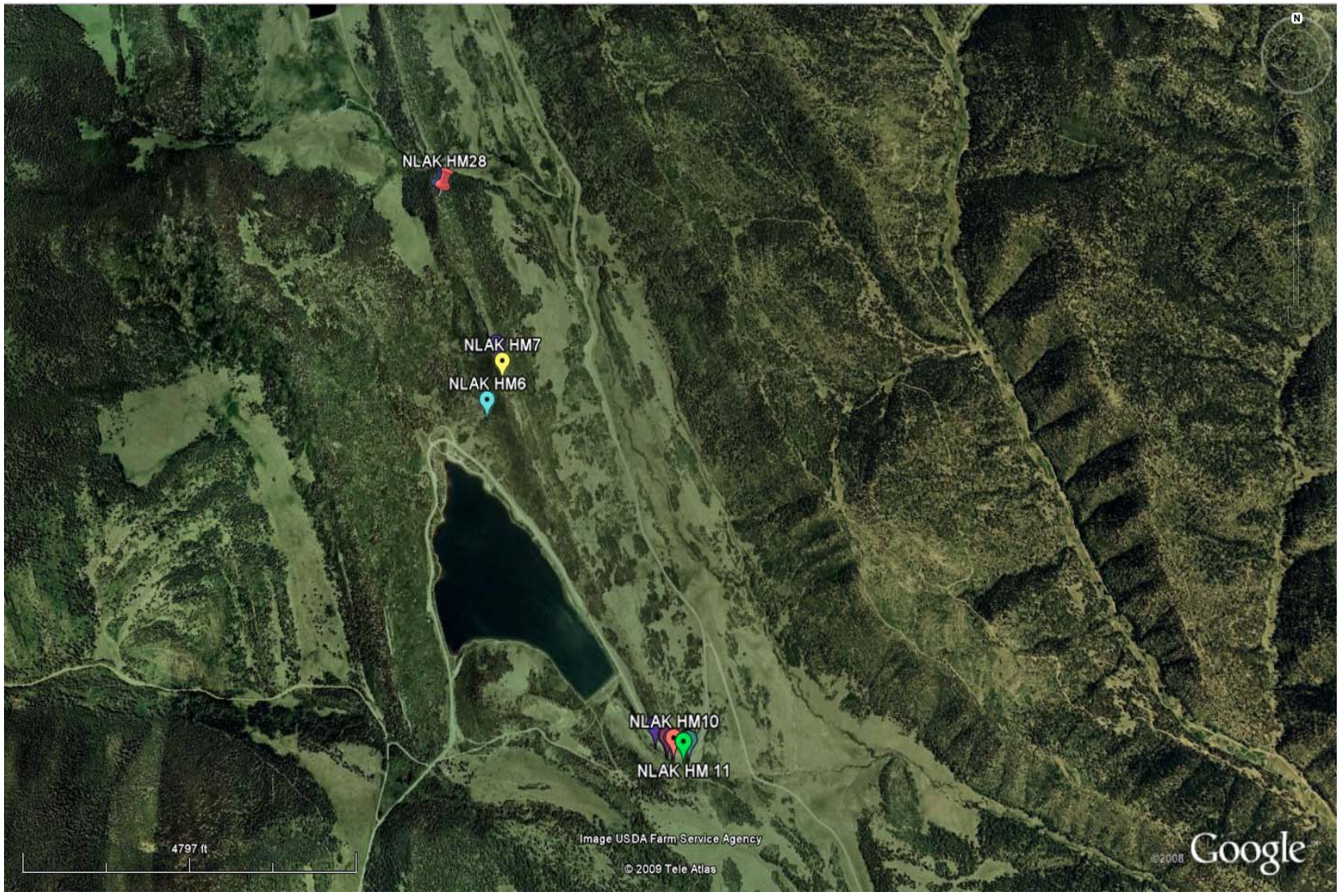

Figure 2.3 Map view of North Lake reservoir near Stonewall, Colorado. Adjacent to the north and east of the lake is a large continuous outcrop consisting of many sills. Balloons and tack pins indicate where samples were collected, (refer to field note section for sample description). Image is from Google Earth™.

$$\frac{Xi}{\sum(Xi, Yi, Zi, \ldots)} * 100$$

Equation 2.1 Equation used to calculate modal % of phenocrysts. X, Y, Z represent different types of phenocrysts.

2.3. *ELECTRON MICROPROBE ANALYTICAL METHODS*

2.3.1. Determining samples for electron microprobe analysis

Twenty-seven thin sections were made from the original 32 samples collected for this research. Only 15 of the 27 thin sections were selected for electron microprobe analysis. Each sample was chosen based on the presence and condition of; olivine, clinopyroxene, amphibole, and biotite. Further elimination of samples was determined by sample duplication, K_2O/Na_2O ratio of sample, field relations, and age constraints.

2.3.2. Electron microprobe analysis of thin sections

All electron microprobe analyses were performed using a JEOL JXA-8600 Superprobe located at the University of Georgia Athens, Georgia. Thin section polish was checked for smoothness, and then each section was carbon coated. Sketches were made of thin section positions on the mounting stage to ensure sample identification. X-ray analysis was performed with WDS (wavelength dispersive spectrometers) using 10s counting times. The diameter of the beam used was 1um; accelerating voltage was set at 15Kv and beam current at 15nA.

When analyzing the ocelli structures found in some of the samples, the beam current was adjusted to 5nA and the focus of the beam was changed to 5-10um to prevent damage to sample. Analyses were processed using dQANT32 stage and spectrometer automation created by Geller Microanalytical Laboratory. (GML) analyses were corrected using a phi-rho-z matrix correction procedure. Imaging software dPICT32 created by (GML) was used to produce backscatter images and mapping of samples. Microprobe analyses followed those of Roden and Shimizu (1993).

2.4. *X-RAY FLUORESCENCE METHODS*

2.4.1. Preparation of samples for analysis

Before grinding samples for x-ray fluorescence all weathered rind and exposed surfaces were removed. Approximately 700cm^3 of sample was broken into small pebble sized chips using a Braun Chipmunk Crusher (Bico, Inc., Burbank, California). These chips were then laid out on a clean surface layered with copy paper and divided into four separate piles taking special care to divide various sized chip pieces equally amongst the piles. One of the four chip piles was then milled to ~ 10um by cycling through an enclosed ring and puck shatter box milling machine (Spex Industries, Inc., Metuchen, New Jersey) for 2.5 minutes. Powdered samples were then transferred to individually marked containers for the fusion disc and pellet making process. All equipment was cleaned between samples using a wire brush, sterile chemical wipes, and acetone. For additional prevention of cross contamination, a small amount of pure silica was processed through the milling machine between each sample.

2.4.2. Preparation of fusion discs for major elemental analysis

Using a mass balance (Mettler AT201) each fusion disc was prepared by weighing 10,000 ± 0.5mg of lithium-borate flux (Lithium Borates/Lithium Bromide Fusion Flux, Spex Certiprep, Metuchen, New Jersey) then adding 2500 ± 0.5mg of sample powder (prepared using steps described in previous paragraph) to a combined weight of 12,500 ± 0.5mg. All weighed fusion disc samples were labeled and stored in a drying oven (~120^{o}F) to prevent moisture contamination.

Next, each sample was transferred to a 50mL 95/5 Pt/Au crucible and thoroughly mixed with a Vortex brand electric shaker. An oxidizing agent (6 drops of $LiNO_3$) and a wetting agent (6 drops of NH_4I) were then added to the sample before placing into a ~1085^{o}C oven (Thermolyne 46100 High Temperature Furnace). After 7.5 minutes the sample was removed and swirled for 30 seconds over an acetylene/compressed air Bunsen flame, then reinserted into the oven for an additional 7.5 minutes. Samples were removed once more, swirled for 30 seconds over the Bunsen flame, and then poured into a platinum casting dish (Premier Lab Supply, Inc.). After cooling, discs were removed, inspected for consistency in color, labeled, and placed into a 47mm Millipore clear microbial covered dish and labeled

for redundancy. To ensure no cross contamination occurred between samples, the crucible was cleaned in a solution of 1 part 20%HCl and 3 parts deionized water and wiped with a chemical wipe and acetone before reuse.

2.4.3. Preparation of pellets for trace element analysis

Using a mass balance (Denver Instrument Company Model A-250), 10000 ± 1mg of sample was weighed and then thoroughly mixed with 2.0mL of elvacite/acetone (resin). The mixture was then added to an aluminum cup (a Spex Certiprep 9 x 38 mm SPEC20 CAP), inserted into a stainless steel dye press (Loomis Engineering & Manufacturing Company Model 341-20, Caldwell, New Jersey), and subjected to ~23,000psi for 5 minutes. Each sample was inspected for consistency in texture, labeled, and stored in a desiccator to prevent moisture and cross contamination. Between each sample preparation all surfaces were cleaned with chemical wipes and acetone.

2.4.4. X-ray fluorescence of prepared samples

XRF analyses were performed on a Philips Panalytical Wavelength-Dispersive Sequential Spectrometer at the CAIS, Athens, GA. To monitor accuracy of the spectrometer, USGS Columbia River basalt was analyzed and compared to published values for major and trace elements of the standard (Table 2.1). Three individually prepared fusion discs and pellets from sample HM29 were analyzed to check reproducibility and quality of sample preparation, (Table 2.2).

2.4.5. Preparation of samples for LOI (loss on ignition)

Using a mass balance (Denver Instrument Company Model A-250), 850 ± 1mg of sample was added to a 30mL crucible with ceramic cover. Each sample was baked using the furnace mentioned in paragraph 2.4.2., for 45 minutes at ~ 925^{o}C. Each sample was removed and cooled in a desiccator for 45 minutes and reweighed using the same mass balance. The difference in weight before heating and after was divided by 850mg and multiplied by 100 to obtain loss on ignition total (Equation 2.2). Each crucible was cleaned with chemical wipe and acetone before using to prevent cross contamination.

Table 2.1 XRF analysis of standard and accepted values of standard

Label ox %	HM-BCR-2	USGS report values with 1σ			difference in HM-BCR-2 and USGS values	MDL**
SiO_2	54.05	54.10	±	0.80	0.05	<0.01
TiO_2	2.26	2.26	±	0.05	0.00	<0.01
Al_2O_3	13.48	13.50	±	0.20	0.02	<0.01
Fe_2O_3	13.88	13.80	±	0.20	0.08	<0.01
MnO	0.20	0.20	±	0.01	0.00	<0.01
MgO	3.56	3.59	±	0.05	0.03	<0.01
CaO	7.08	7.12	±	0.11	0.04	<0.01
Na_2O	3.17	3.16	±	0.11	0.01	<0.01
K_2O	1.79	1.79	±	0.05	0.00	<0.01
P_2O_5	0.37	0.35	±	0.05	0.02	<0.01
Total	99.84	99.87				
Trace (ppm):						
V	409	416	±	14	7	3
Cr	14	18	±	2	4	5
Ni	9	n.l.*				5
Cu	15	<u>19</u>	±	<u>2</u>	4	3
Zn	121	127	±	9	6	3
Rb	50	48	±	2	2	5
Sr	334	346	±	14	12	3
Y	36	37	±	2	1	1
Zr	179	188	±	16	9	3
Nb	11	n.l.*				1
Ba	661	683	±	28	22	15
Th	4.4	6.2	±	0.7	1.8	3
Ce	48	53	±	2	5	3
La	28	25	±	1	2.5	3
Pb	10	<u>11</u>	±	<u>2</u>	1	3

* n.l. not listed, ** MDL minimum detection limit, all values are recommended values except where <u>underlined</u>, which are listed by USGS as information values (Wilson, 1997)

$$\frac{Mi - Ma}{Ms} * 100$$

Equation 2.2 Equation used to calculate LOI (loss on ignition) totals of Spanish Peaks samples. Mi = mass of sample + crucible before heating, Ma = mass of sample + crucible after heating, Ms = mass of sample.

Table 2.2 XRF analyses of HM-29

Label ox%	HM29A	HM29B	HM29C	MDL*
SiO_2	4.21	4.19	4.20	<0.01
TiO_2	1.62	1.63	1.63	<0.01
Al_2O_3	16.40	16.42	16.59	<0.01
Fe_2O_3	60.26	59.92	61.18	<0.01
MnO	0.52	0.52	0.52	<0.01
MgO	3.42	3.42	3.42	<0.01
CaO	5.16	5.17	5.17	<0.01
Na_2O	0.78	0.78	0.78	<0.01
K_2O	0.11	0.11	0.11	<0.01
P_2O_5	6.51	6.52	6.53	<0.01
Total	98.99	98.68	100.14	
Trace (ppm):				
V	77	81	80	3
Cr	11	5	5	5
Ni	1	2	1	5
Cu	10	7	9	3
Zn	96	96	97	3
Rb	67	67	67	5
Sr	756	754	755	3
Y	21	20	20	1
Zr	184	184	186	3
Nb	20	20	20	1
Ba	1308	1325	1338	15
Th	7	7	7	3
La	45	45	43	3
Pb	12	11	11	3

* minimum detection limit, all samples prepared separately

2.5. *CALCULATIONG Fe^{2+} AND Fe^{3+} METHODS*

A problem with EMPA (electron microprobe analysis) and XRF (x-ray fluorescence) analysis of rock samples and minerals is that the element iron is reported as either FeO or Fe_2O_3. Recalculation of iron into both FeO and Fe_2O_3 is necessary in order to accurately report Mg# (Mg/ (Mg + Fe^{2+}) of bulk rock and mineral analyses, normative calculations, proper nomenclature of common volcanic rocks and nomenclature of many Fe, Mg silicates. Therefore, various methods were used to estimate the FeO/Fe_2O_3 ratio in bulk sample analyses and mineral analyses in this study.

2.5.1. Estimating the oxidation state of iron in XRF bulk sample analysis

In this study, oxide weight % totals of bulk samples were obtained using XRF analysis. With this type of analysis, iron is reported as Fe_2O_3 only. Irvine and Baragar (1971) describe a method for estimating FeO and Fe_2O_3 where Fe_2O_3 wt% is set to be equal to TiO_2 wt% + 1.5 (a modification of Coombs,1963). This method works for most common volcanic rocks, but in the case of the alkaline rocks of this study, TiO_2 weight % exceeds 2.0 in most samples. Therefore, to prevent possible over reporting of Fe^{3+}, a Fe_2O_3/FeO weight % ratio of 0.15 based on an average of fresh basaltic glasses (Brooks, 1976), was used to recalculate Fe_2O_3. The remaining Fe_2O_3 wt% was then converted to FeO wt% following Winter (2001).

2.5.2. Calculating iron in EMPA mineral analyses

In this study atomic proportion of elements in clinopyroxenes, phlogopites, and amphiboles were obtained using EMPA. With this type of analysis, iron is reported as FeO only. Various methods were employed to estimate FeO from Fe_2O_3 in the mineral structure.

2.5.2.1. *Calculating iron in clinopyroxene*

When calculating the mineral structural formula for clinopyroxene using EMPA, normalizing to four cations is the most accurate method Vieten and Hamm (1978). Limited coupled substitutions in the pyroxene structure allow estimation of FeO and Fe_2O_3 by charge balance constraints; filling the deficiency left in the tetrahedral site by Si with Al^{IV} and Fe^{3+} first, then filling the *M2* octahedral site with Al^{VI}, Ti, Mg, Mn, Fe^{2+}, and excess Fe^{3+}, all while maintaining overall charge balance with the *M1* site

(Morimoto, 1989). The Fe^{3+} is then recast by using the conversion method referenced in 2.5.1. Cation totals are then recalculated using the new totals obtained from the method described above.

2.5.2.2. *Calculation iron in amphibole*

In the case of the of the amphibole structure, complexity prevents the use of the method applied to the pyroxenes. Leake (1978) describes an effective way to determine the FeO/Fe_2O_3 ratio when using microprobe analyses, by calculating amphibole formulas on the basis of 23 oxygens and then readjust the total cations, (excluding Ca, Na, and K), to 5 + 8 = 13. This adjustment is achieved by changing some of the FeO weight% reported by the EMPA to Fe_2O_3 wt%. Additionally the general equation for calculating Fe^{3+} in Fe, Mg silicates (modification iii) from Droop (1987) was used to reinforce results obtained using the Leake (1978) method.

2.5.2.3. *Calculation of iron in phlogopite*

Calculation of Fe^{3+} and Fe^{2+} in the mica structure is problematic when using EMPA. All Fe^{3+}, Fe^{2+} proportions from phlogopite analyses were calculated using equations from the program "fe23" developed by Nenova (1996, see Equation 2.3). This method is based on the rule that all natural occurring chemical compounds must have a balanced charge between anions and ions. The sum of each valances in the atoms of the molecule is equivalent to the number of atoms multiplied by its valences.
With this in mind two equations can be set up to solve for Fe^{2+} and Fe^{3+} in mineral structure. This method can be applied to all minerals having bi and tri valence iron in their structure. This derivation is necessary for calculating the Mg# accurately. The difference between results for biotite obtained following Nenova compared to results using Mössbauer spectroscopy (Dyar and Burns, 1986) are less than 1%.

$$X = 3\lambda - (A - B)$$

$$Y = (A - B) - 2\lambda$$

Equation 2.3 Equations used to calculate Fe^{3+} and Fe^{2+} in phlogopites. X= Fe^{2+}, Y= Fe^{3+}, A= anions in mineral formula, B= cations in mineral formula, and $\lambda = \sum Fe$ (Nenova, 1996).

3. RESULTS

The following sections contain field descriptions, locations, petrographic descriptions, and results from XRF analyses and electron microprobe analyses of samples collected for this study. Full petrographic thin section descriptions are available in the appendix.

3.1. *FIELD AND THIN SECTION DESCRIPTIONS*

The purpose of this study is to investigate the possible petrogenetic relationship between the relatively potassic and relatively sodic samples of the Spanish Peaks area. In order to compare rocks of approximately the same age, previous studies using the Ar^{40}/Ar^{39}dating method Miggins, (2002), Penn, (1994, Figure 3.1). Thirty-two samples were collected from north, south, and around the Spanish Peaks. Sample locations are shown in Figures 2.1- 2.3. Sample labeling and location coordinates of each collection point are listed in table 3.1, and a summary of major phenocrysts and groundmass minerals are listed in table 3.2.

3.1.1. Walsenburg dike near Walsenburg, Colorado

The Walsenburg dike is one of many independent dikes surrounding the East and West Spanish Peak stocks (Figure 2.1). Two county roads and one major highway (county road 590, county road 504, and Highway 85) crosscut the dike. Samples were collected from each of the road intersections and at an outcrop of the dike behind Lathrop State Park. The overall length of the dike is ~10 km, its width is ~16m (at the Walsen Crag) to ~3m (at its most southern point), and is composed of at least 2 separate intrusives noted by Knopf (1936) and Johnson (1968).

3.1.1.1. *Samples from county road 504*

Samples HM1 and HM2 were collected from an outcrop on county road 504 (Figure 3.2, 3.3). At this location the dike is ~5 to 7 meters wide with the road cutting into the dike ~2m vertically. The exposed dike, heavily weathered in places, exhibits spectacular spheroidal weathering at its chill margins.

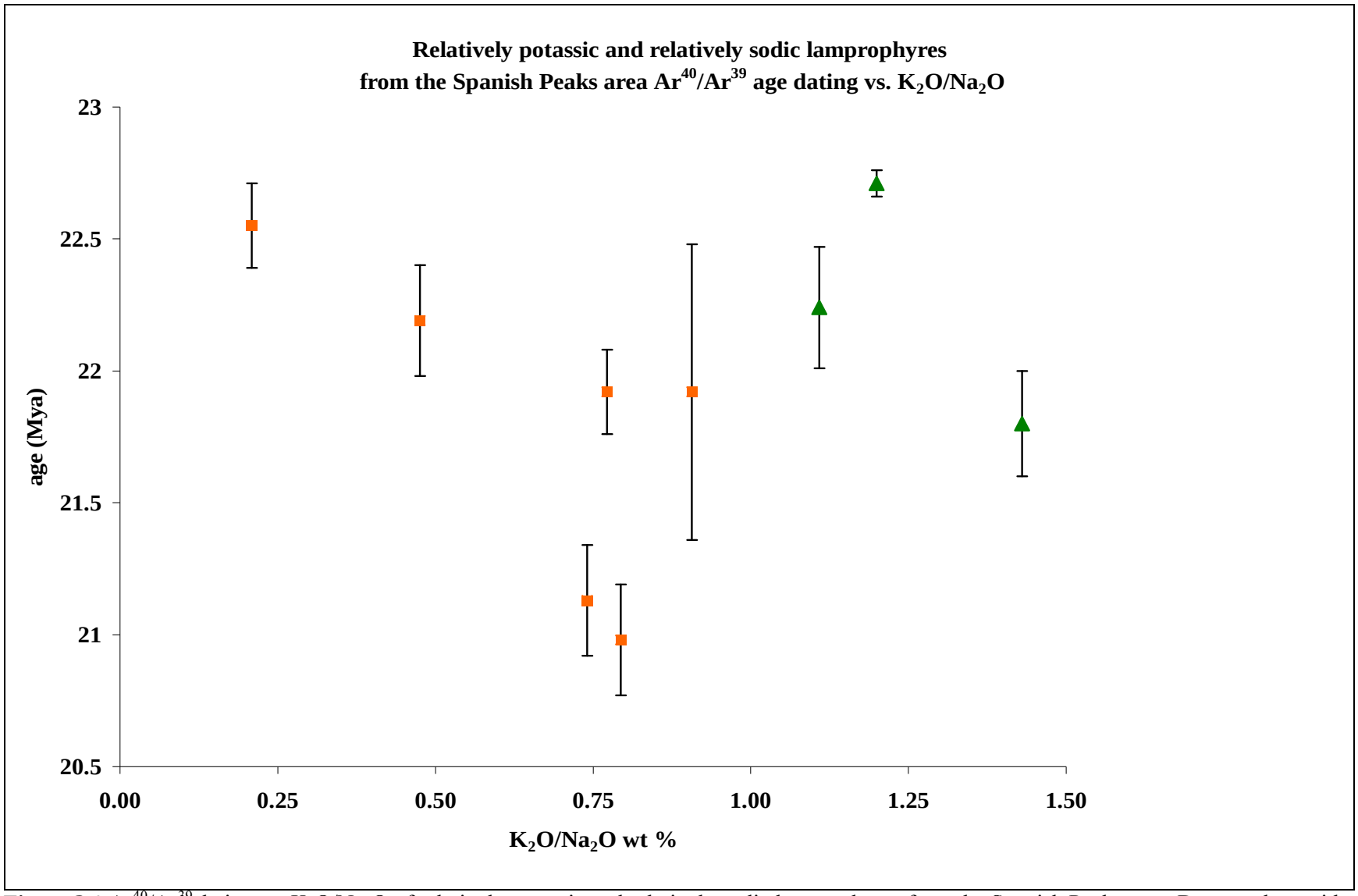

Figure 3.1 Ar^{40}/Ar^{39} dating vs. K_2O/Na_2O of relatively potassic and relatively sodic lamprophyres from the Spanish Peaks area. Data used to guide selection of samples for this study from Miggins (2002) and Penn (1994).

Table 3.1 Location coordinates and grouping of samples from Spanish Peaks area

Type	**relatively potassic**			**relatively sodic**			
Location	Walsenburg dike			**Location**	dike, sill complex Northlake reservoir		
ID #	**Latitude***	**Longitude***	**Elevation**	**ID#**	**Latitude***	**Longitude***	**Elevation**
W504-HM1	37.6080	-104.8590	6602ft	NLAK-HM7	37.2535	-105.0418	9030ft
W504-HM2	37.6082	-104.8583	6615ft	NLAK-HM8	37.2536	-105.0418	9030ft
W590-HM3	37.6327	-104.8003	6371ft	NLAK-HM10	37.2372	-105.0311	8531ft
WLATH-HM4	37.6209	-104.8345	6619ft	NLAK-HM17	37.2372	-105.0311	8531ft
W85-HM5	37.6358	-104.7890	6290ft	NLAK-HM23	37.2372	-105.0311	8531ft
W85-HM12	37.6358	-104.7890	6290ft	NLAK-HM25	37.2372	-105.0311	8531ft
W590-HM13	37.6327	-104.8003	6371ft	NLAK-HM26	37.2372	-105.0311	8531ft
W590-HM14	37.6327	-104.8003	6371ft	**Location**	C.R.421 dike near Sulfur Springs		
W590-HM15	37.6327	-104.8003	6371ft	S421-HM20	37.4670	-105.0885	6510ft
Location	dike, sill complex Northlake reservoir			**Location**	sill off C.R.440		
NLAK-HM9	37.2372	-105.0311	8531ft	CR440-HM21	37.5227	-105.0686	7316ft
NLAK-HM11	37.2372	-105.0311	8531ft	**Location**	dike near Goemmer Butte		
NLAK-HM16	37.2372	-105.0311	8531ft	CD-HM30	37.4705	-105.0297	7357ft
NLAK-HM18	37.2372	-105.0311	8531ft				
NLAK-HM19	37.2372	-105.0311	8531ft				
NLAK-HM22	37.2372	-105.0311	8531ft				
NLAK-HM24	37.2372	-105.0311	8531ft				
NLAK-HM27	37.2609	-105.0460	8836ft				
NLAK-HM28	37.2609	-105.0460	8836ft				
Location	Goemmer Butte trachyandestite						
GB-HM29	37.4731	-105.0420	7817ft	Goe 1	37.4731	-105.0420	7817ft
Goe 2	37.4731	-105.0420	7817ft				

**Longitude Latitude reported in Degree Decimal*

Table 3.2 Phenocryst/groundmass mineralogy of samples from Spanish Peaks area

Type	**relatively potassic**		**relatively sodic**		
Location	Walsenburg dike		**Location**	dike, sill complex Northlake reservoir	
ID #	**major phenocryst**	**groundmass**	**ID#**	**major phenocryst**	**groundmass**
W504-HM1*	ma		NLAK-HM7*	ma,fp,amp	
W504-HM2	cpx>ma>oliv	cpx,ma,Ksp,ox,ap	NLAK-HM8	amp,fp,cpx,ox,ma	amp,fp,cpx,ox,ma,sp,ap
W590-HM3	oliv>ma>cpx>Ksp	cpx,ma,Ksp,ox,ap	NLAK-HM10*	ma,fp,cpx	
WLATH-HM4	ma>cpx	cpx,ma,Ksp,ox,ap	NLAK-HM17*	ma,fp,cpx	
W85-HM5	ma>cpx>oliv	cpx,ma,oliv,sp,ap,Ksp	NLAK-HM23*	ma,cpx,fp	
W85-HM12*	ma,cpx,oliv		NLAK-HM25	fp,cpx,ox,ma,ap,amp	phy,ox,ma,ap
W590-HM13*	ma		NLAK-HM26	amp,ox,Ksp,cpx	amp,calc,phy,ox,ap,ma
W590-HM14	ma>oliv>cpx>Ksp	cpx,ma,Ksp,ox,ap	**Location**	C.R.421 dike near Sulfur Springs	
W590-HM15*	ma		S421-HM20	fp,amp,cpx,ox	
Location	dike, sill complex Northlake reservoir		**Location**	sill off C.R.440	
NLAK-HM9*	ma,fp		CR440-HM21	fp,cpx,ox	
NLAK-HM11*	cpx,fp		**Location**	dike near Goemmer Butte	
NLAK-HM16*	ma,fp,cpx		CD-HM30	Kspar,amp,ox,cpx	cpx,amp,ox,sp,ap
NLAK-HM18*	ma,cpx,amp				
NLAK-HM19	ma,cpx,fp,ox,amp	ma,cpx,fp,ox,amp,ap,calc,phy			
NLAK-HM22	ma,cpx,fp,ox,amp	ma,cpx,fp,ox,amp,ap,calc,phy			
NLAK-HM24	ma,cpx,fp,ox,amp	ma,cpx,fp,ox,amp,ap,calc,phy			
NLAK-HM27*	amp,fp,cpx				
NLAK-HM28	cpx>ma>Ksp	cpx,ma,Ksp,sp,calc,ox			
Location	Goemmer Butte trachyandestite				
GB-HM29	amp>ox	amp,ox,Ksp			

* mineralogy based on hand sample only. Abbreviations are as follows: fp=feldspar, Ksp=potassium feldspar, sp=sphene,

Figure 3.2 View looking east at Walsenburg dike, which is crosscut by county road 504.

Figure 3.3 View of Walsenburg dike at county road 504 (note band of spheroidal weathering at edge of dike).

Sample HM1 is a light-grey rock with a fine-grained porphyritic texture that has numerous biotite phenocrysts up to ~3mm in length. Sample HM2 was collected further east of HM1 where the dike is less altered. The color of the rock here is dark-grey with a very fine-grained porphyritic texture. White segregation veins ~1 to 2mm wide are associated with spherical inclusions (termed "ocelli" in this report) ~ 2-3cm in diameter filled with a translucent clear mineral. Petrographic analysis of HM2 reveals that clinopyroxene, biotite, and olivine (~ 48%, 42%, and 10% respectively) form the phenocrysts that range up to ~ 1.5mm in length and diameter. The clinopyroxenes are clear to pale-yellow-green, subhedral to euhedral in shape, most have normal concentric zoning, some have polysynthetic twinning, and a few have xenocrystic green cores or inclusions of iron oxide and biotite. The biotites are brown to reddish-brown, strongly pleochroic, subhedral to euhedral, with some having inclusions of iron oxide. The olivines are colorless, anhedral to subhedral, and some have been altered to a greenish-brown mineral and are rimmed with iron oxide. The surrounding groundmass consists of the above-mentioned phenocrysts, abundant iron oxides, sparse apatite and slightly altered anhedral feldspar. Additionally there are rare ocelli (up to ~ 5mm in diameter) bound by prisms of clinopyroxene that are filled with an altered colorless mineral (Figure 3.4).

3.1.1.2. *Sample behind Lathrop State Park*

Sample HM4 was collected southwest of the Walsen Crag, behind Lathrop State Park (Figure 2.1). The dike at this location rises ~30m above the park grounds and is ~5 to 7m wide (Figure 3.5). The rock is light-grey green and has a medium-grained porphyritic texture with a fine-grained groundmass. There are numerous phenocrysts of biotite up to 3mm in length. The visible groundmass consists of anhedral feldspar. Petrographic analysis of HM4 reveals that biotite and clinopyroxene (~80%, 20% respectively) comprise the majority of the large phenocrysts that range in size up to 3mm in length. The biotites are brown to reddish-brown, strongly pleochroic, subhedral to euhedral, with many inclusions of apatite, clinopyroxene, and iron oxide. The clinopyroxenes are pale yellow-green, subhedral to euhedral, a few form clusters, and many occur as inclusions in the surrounding biotite. The groundmass consists of

smaller grains of biotite, clinopyroxene, apatite, and iron oxides all of which are enclosed in anhedral potassium feldspar (Figure 3.6).

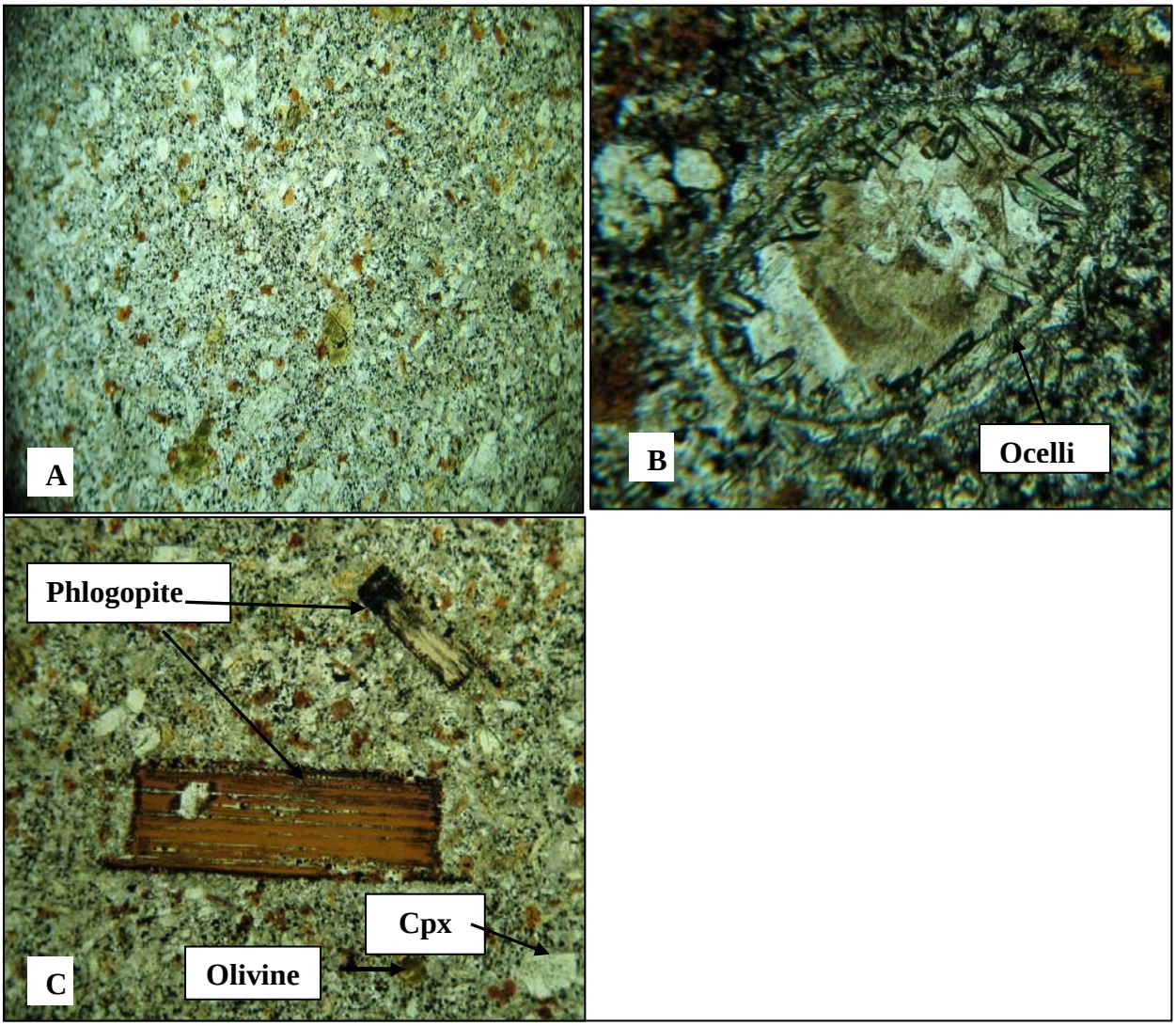

Figure 3.4 HM2 Multiple views displaying typical micro-porphyritic texture and ocelli of sample HM2 from the Walsenburg dike, (for locations refer to table 3.1), **A;**(~ 4mm across) of HM2**; B;** (~2mm wide) of ocelli**; C;** (~3mm across) of phlogopite rimmed with iron oxide, altered olivine, and clinopyroxene (for locations refer to table 3.1).

Figure 3.5 View looking east atop Walsenburg dike behind Lathrop State Park. Red dot denote sample collection point.

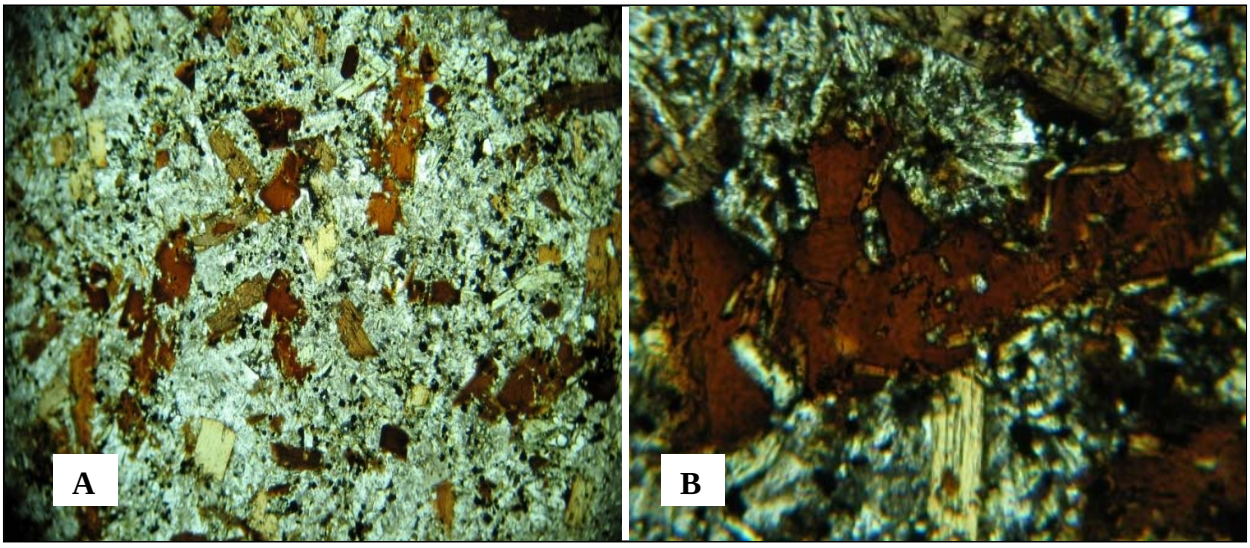

Figure 3.6 HM4 Multiple views displaying porphyritic texture and mineral inclusions of sample HM4 from Walsenburg dike, **A;**(~3mm across) of dark brown phlogopite with iron oxide and apatite inclusions, **B;**(~1mm across) of close-up of phlogopite with apatite inclusions (for locations refer to table 3.1).

3.1.1.3. *Samples from county road 590*

Samples HM3, HM13, HM14, and HM15 were collected where county road 590 intersects the dike (Figure 3.7). The width of the dike at this location is ~8 to 10m with the county road cutting across the dike obliquely. The height of the outcrop is ~ 2.5 to 3m. Metamorphosed shale extends ~70cm from the edge of the dike, which also has spheroidal weathering at its flanks similar to that of the outcrop near county road 504, only more pronounced (Figure 3.8, 3.9). The outcrop is composed of two separate intrusions, (noted by Johnson, 1968). The dike transitions from dark-grey color at the center to light grayish-green at the edge. Textures vary from medium to fine-grained porphyritic with visible biotite up to 2mm in length at the center, to coarse-grained porphyritic (heavily weathered) with biotite up to ~4mm in length at the edge (Figure 3.10).Additionally, towards the edge there are ~1cm diameter clots filled with a white chalky mineral. Most of the dike at this location is dark-grey, has a medium to fine-grained porphyritic texture, with discernable biotite up to ~2mm in length, altered olivine up to ~2mm in diameter, and anhedral potassium feldspar in the groundmass.

Figure 3.7 View looking west towards Walsenburg dike, which is crosscut by county road 590. Red dots denote sample collection points.

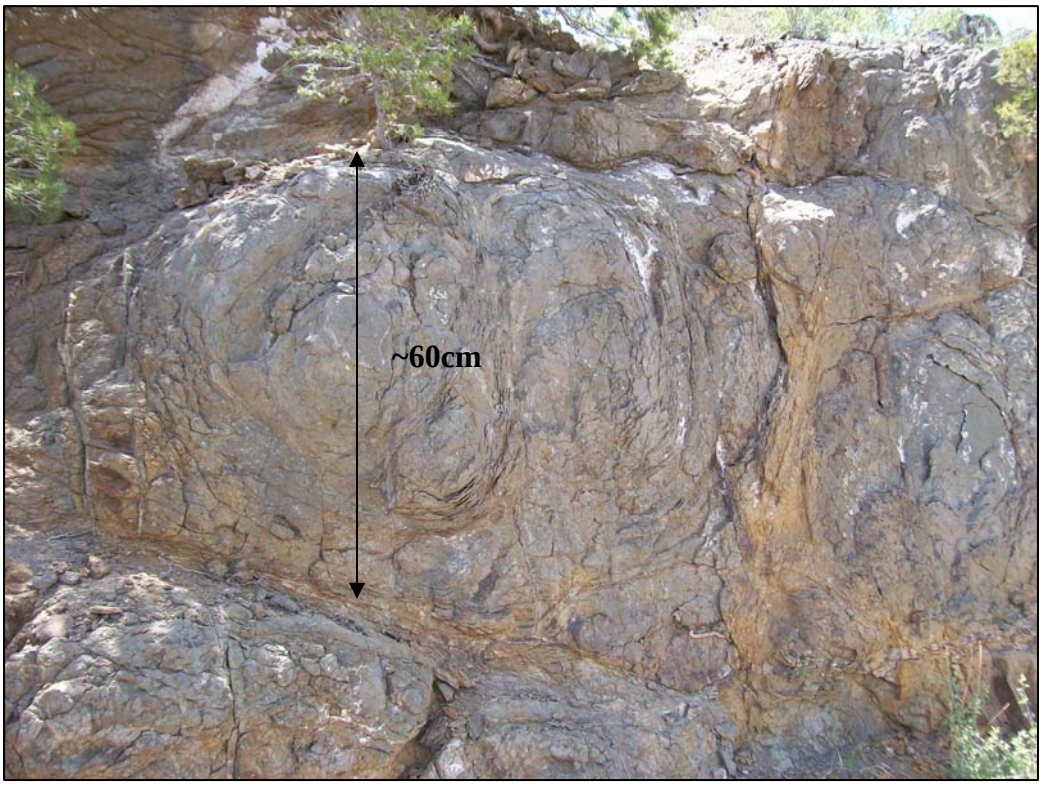

Figure 3.8 View of spheroidal weathering at the edge of Walsenburg dike at county road 590.

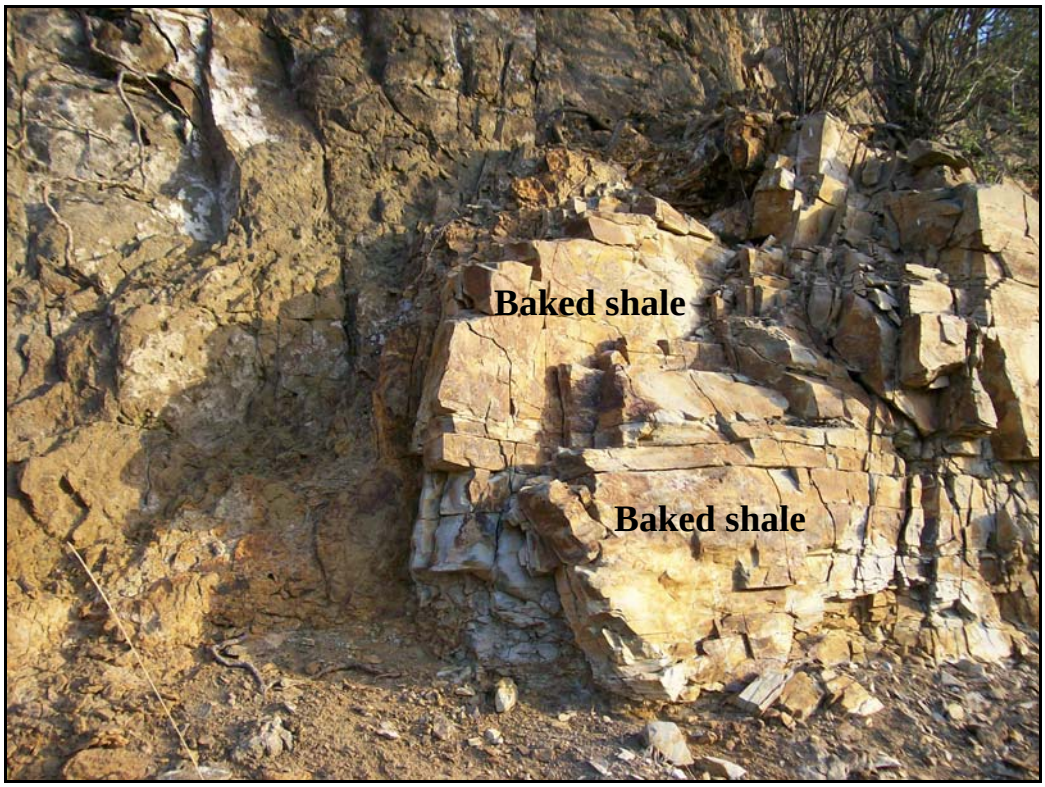

Figure 3.9 View of baked shale metamorphosed during emplacement of the dike.

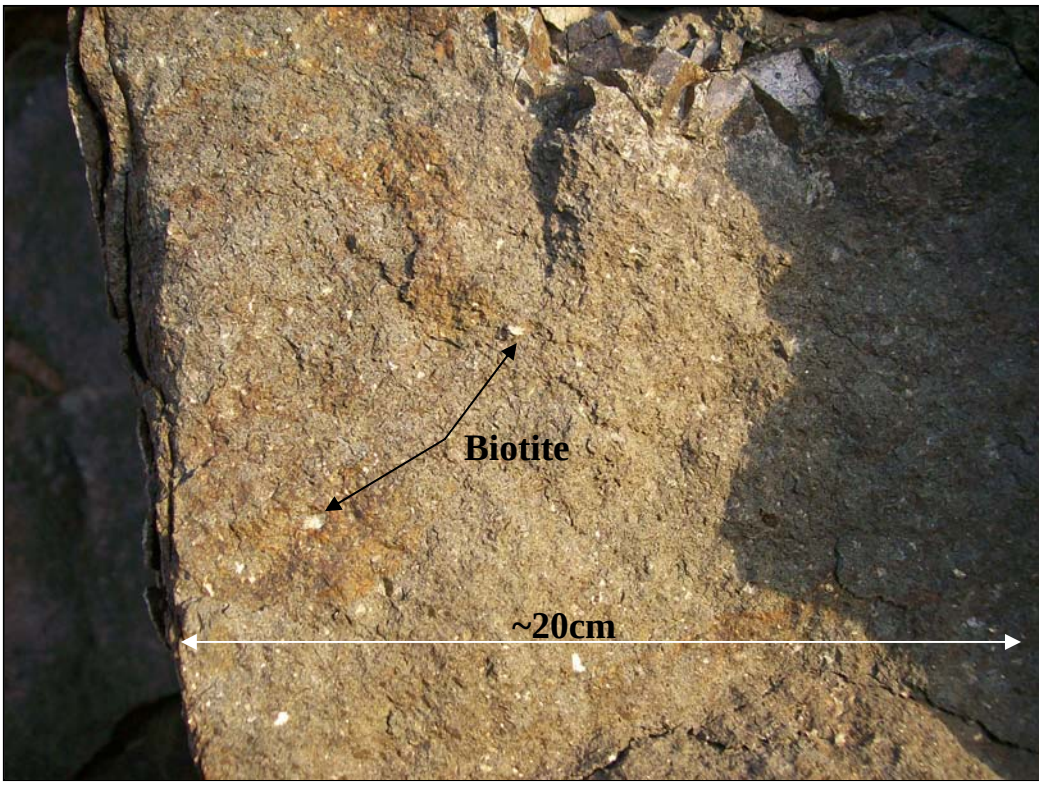

Figure 3.10 View of weathered edge of Walsenburg dike. Note large plates of mica reflecting in sunlight.

Additionally there are ocelli structures filled with prisms of clinopyroxene, quartz, and feldspar (based on thin section analysis done on HM-5). Petrographic analysis of HM-3 (collected at the center of the dike) reveals that large fresh olivine, biotite, clinopyroxene, and potassium feldspar (~30%, 30%, 25%, and 15% respectively) comprise the phenocryst assemblage and range in size up to 4.5mm in length. The olivines are colorless, anhedral to subhedral, with some relict grains that have been altered to a greenish-brown mineral rimmed with iron oxide. The biotites are brown to reddish-brown, strongly pleochroic, subhedral to euhedral, with inclusions of cpx, and iron oxide. The clinopyroxenes are pale yellow-green, euhedral to subhedral, elongate and blocky, normally zoned, with some altered to chlorite around the edges. A few of the grains have green cores and some have inclusions of biotite, apatite and iron oxide. The feldspars are mainly restricted to the groundmass, but a few of these grains are anhedral and quite large, (up to ~4.5mm in width). The groundmass consists of smaller grains of biotite, cpx, olivine, apatite, and iron oxide all of which are enclosed in anhedral potassium feldspar (Figure 3.11). Petrographic

analysis of sample HM14 collected right of the dike center (Figure 3.7), reveals a slightly different modal percentage with biotite, olivine, clinopyroxene, and potassium feldspar (~35%, 35%, 20%, and 10% respectively) as phenocrysts that range in size up to 3mm in length and diameter.

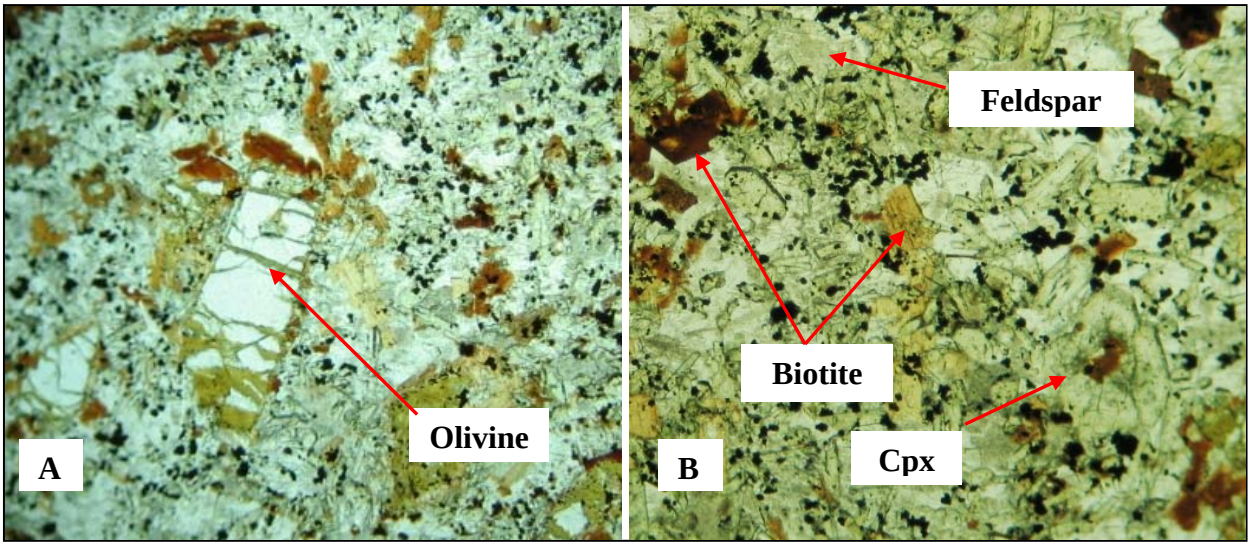

Figure 3.11 Multiple views displaying porphyritic texture of sample HM3 from the Walsenburg dike, **A;** (~2.5mm across) of large fresh olivine with greenish-brown alteration mineral along cracks, **B;** (~2.5mm across) of clinopyroxene with inclusions, biotite, and feldspar (for locations refer to table 3.1).

The biotites are brown to reddish-brown, strongly pleochroic, subhedral to euhedral, with inclusions of cpx, iron oxide and some apatite. The olivines are colorless, anhedral to subhedral, blocky to elongate in shape, and range from fresh to complete alteration to some type of greenish-brown mineral. The clinopyroxenes are pale yellow-green, euhedral to subhedral, elongate and blocky in shape, normally zoned, and some have altered to chlorite around the edges. Similar to HM3, a few of the grains have green cores and some inclusions of biotite, apatite and iron oxide. The feldspars in this sample are the same as in HM3, with a few of these grains anhedral up to ~3mm in width. The groundmass consists of smaller grains of biotite, cpx, olivine, apatite, and iron oxides all of which are enclosed in anhedral potassium feldspar (Figure 3.12).

3.1.1.4. *Samples from Highway 85*

Samples HM5 and HM12 were collected where Highway 85 intersects the dike, just north of the town of Walsenburg. At this location, the dike is ~ 10m wide and the road cut is ~ 30m high. Extending ~ 1m from both sides of the chill margins is slightly altered shale (Figure 3.13). The samples collected at this location are slightly altered, medium grey in color, have fine-grained porphyritic texture with numerous visible biotite phenocrysts ~2mm in length, along with altered olivine.

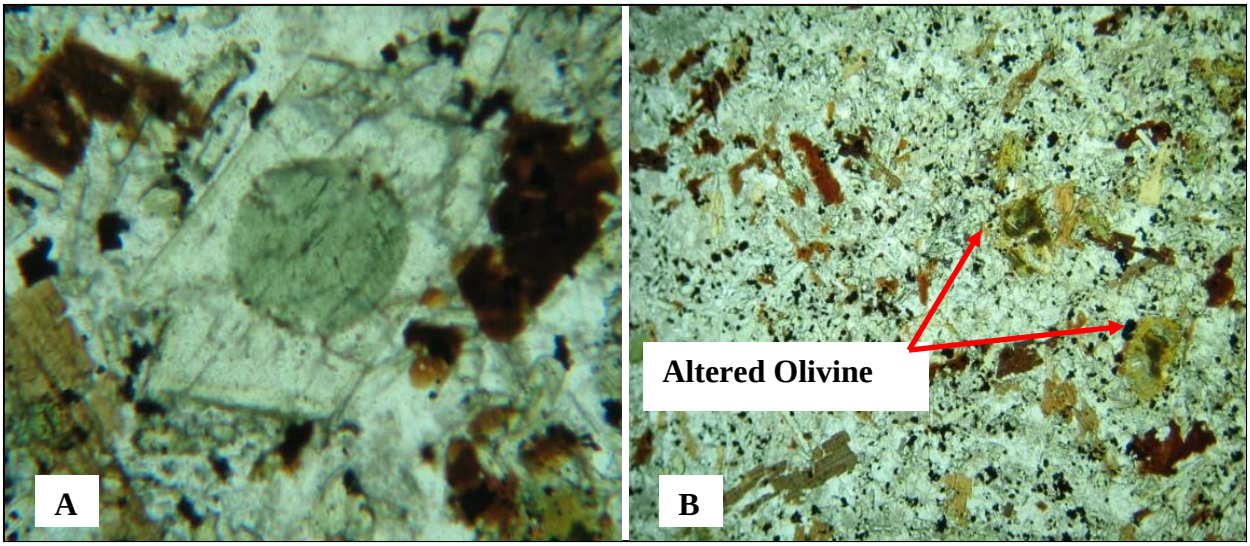

Figure 3.12 Multiple views displaying porphyritic texture and a green cored pyroxene of sample HM14 from Walsenburg dike, **A;**(~2mm across) of cpx with circular green core**, B;** (~4.5mm across) of altered olivine (for locations refer to table 3.1).

There are some ocelli filled with quartz, pyroxene, and possibly feldspar (based on textural similarity to the ocelli of HM3, which were analyzed by the electron microprobe). Petrographic analysis of HM5 revealed that abundant biotite, clinopyroxene and olivine (~48%, 42%, and 10% respectively) comprise the phenocrysts that range in size up to 2.5mm in length and diameter. The biotites are brown to reddish-brown in color, strongly pleochroic, subhedral to euhedral, with inclusions of cpx and iron oxide. The clinopyroxenes are clear to pale yellow-green, euhedral to subhedral, a few exhibit hourglass zoning, and a few have inclusions of biotite, iron oxide, and needle-like apatite. The olivine is mostly anhedral to subhedral, colorless when fresh or slightly altered or completely altered to a greenish-brown mineral.

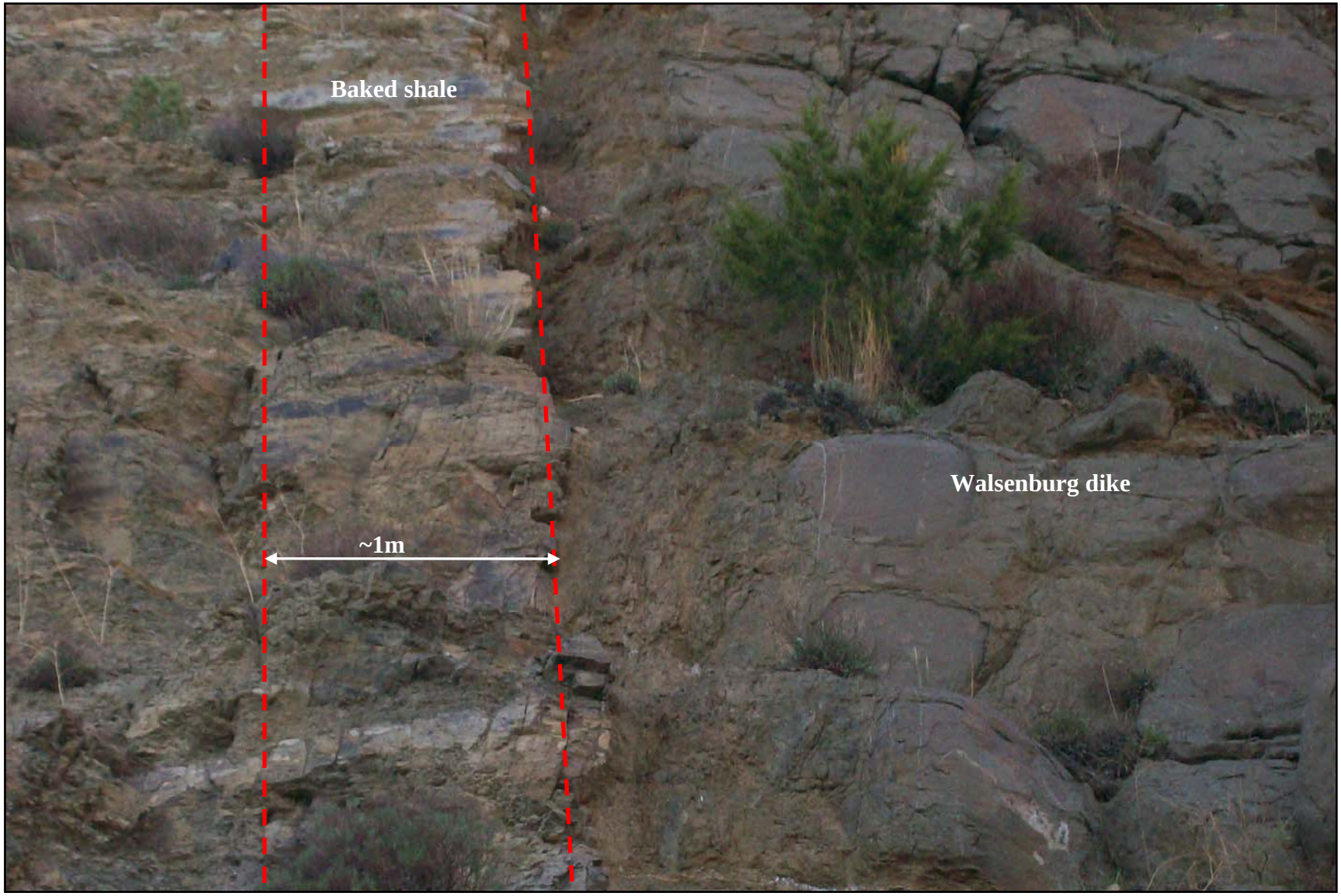

Figure 3.13 View of Walsenburg dike exposure cross cut by Main Street/ Highway 85. Sample HM12 and HM5 were collected at this location near the center of the dike and ~ 7 meters up from the road. Dashed lines outline shale heated during dike emplacement.

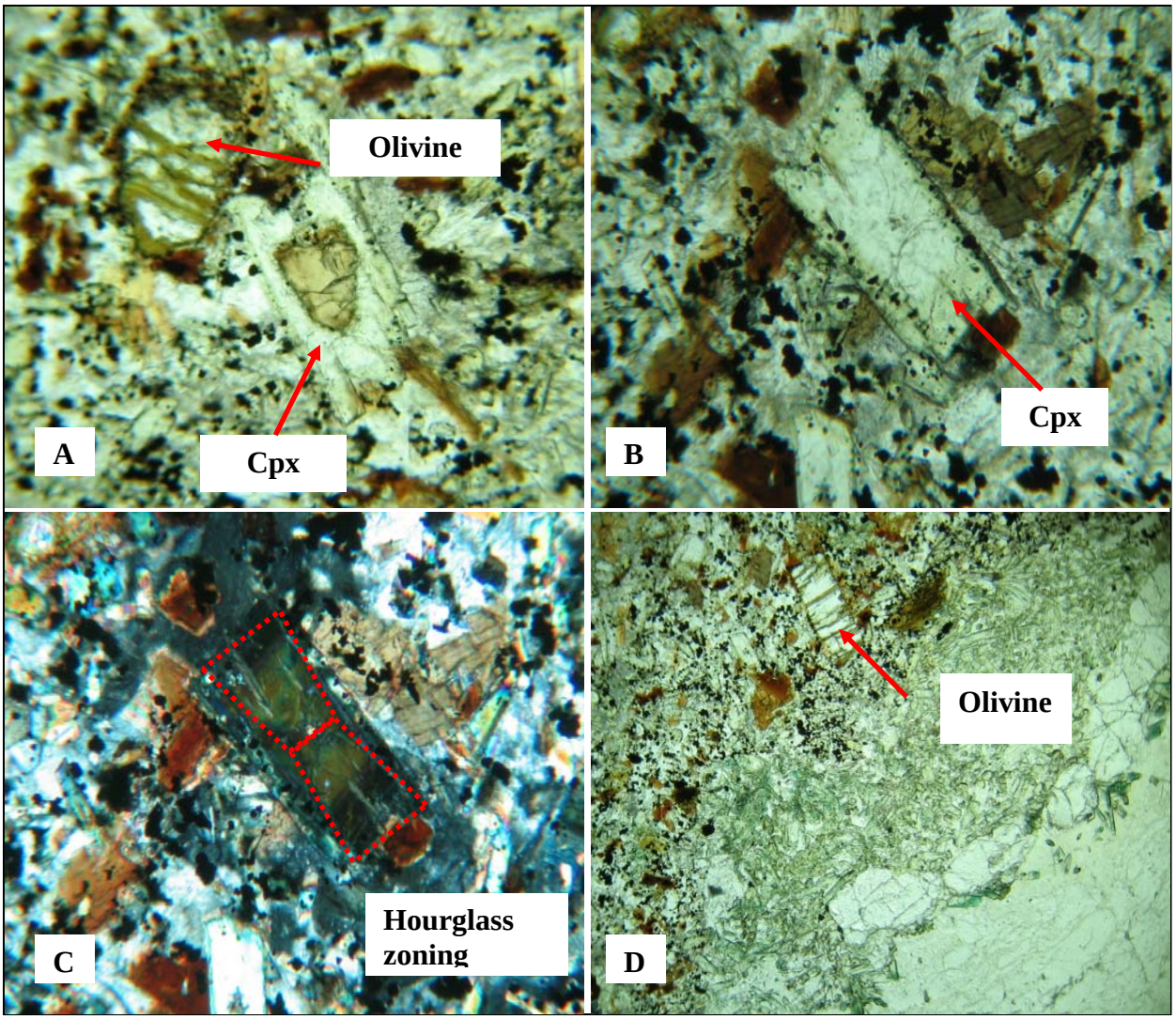

Figure 3.14 Multiple views displaying porphyritic texture, zoning of minerals and ocelli of sample HM5 from the Walsenburg dike (for locations refer to table 3.1), **A;**(~2mm across) of clinopyroxene with brownish core juxtaposed with slightly altered olivine, **B;**(~2mm across) of clinopyroxene with hourglass zonation, **C; (**~1.25mm) same as B viewed under cross polars, **D**;(~ 3mm across) of fresh olivine with alteration in fractures juxtaposed by large ocelli filled with clinopyroxene and feldspar (for locations refer to table 3.1).

The groundmass consists of smaller grains of biotite, cpx, altered olivine, apatite, sphene and iron oxides all of which are enclosed in anhedral potassium feldspar. Additionally there are ocelli (up to ~ 6mm in diameter) bound by prisms of clinopyroxene embedded in feldspar and quartz (Figure 3.14).

3.1.2. Goemmer Butte trachyandesite, surrounding dikes, and sill near LaVeta, Colorado

3.1.2.1. *Goemmer Butte trachyandesite*

The Goemmer Butte trachyandesite is a volcanic neck that is located just north and west of the Spanish Peaks and south of the town of LaVeta, Colorado (Figure 3.15). Goemmer Butte, along with four other buttes in the area, provide evidence for extrusive volcanism (Knopf, 1936). Three samples (HM29, Goe1, and Goe2) were collected ~ 152m up from the base of Goemmer Butte. Goe1 and Goe2 are samples of an amphibole megacryst from the Goemmer Butte and a xenolith found in the Goemmer Butte trachyandesite. The intrusive rock of the butte is dark-grey in color, has a fine-grained groundmass, with large phenocrysts of amphibole averaging ~ 4mm to ~8mm in diameter. There are a few megacrysts up to ~75mm in diameter. Thin section analysis of HM29, which consists of no large phenocrysts of amphibole, revealed that most if not all the ground mass is composed of trachytic bladed potassium feldspar, blocky amphibole, and euhedral iron oxide. Less than 2% of the groundmass in the sample consists of micro-xenocrysts, angular to rounded fragments from the surrounding sediments, incorporated during emplacement. A few of the larger amphiboles in the groundmass show signs of alteration to iron oxides along grain edges. The xenocrysts obviously derived from the country rock consist of; feldspar, quartz, clinopyroxene, sphene, and apatite (Figure 3.16).

3.1.2.2. *Dike near Goemmer Butte trachyandesite*

Located approximately 1km east of Goemmer Butte trachyandesite is a radial dike that is ~ 2km long and up to ~ 10m wide (Figure 3.17). This dike has a light grey color, medium-grained porphyritic texture, and visible euhedral dark-brown amphibole phenocrysts that are blocky to acicular and seriate from ~7mm in length down to a size typical of the groundmass. The fine-grained groundmass contains potassium feldspar, pyroxene, amphibole and amygdules up to ~4mm in diameter that are filled with calcite or feldspar and quartz. Petrographic analysis of HM30 reveals phenocrysts of potassium feldspar, amphibole, iron oxide, and clinopyroxene, (~ 40%, 24%, 19%, and 16% respectively) that range in size up to ~ 2.5mm in length and diameter.

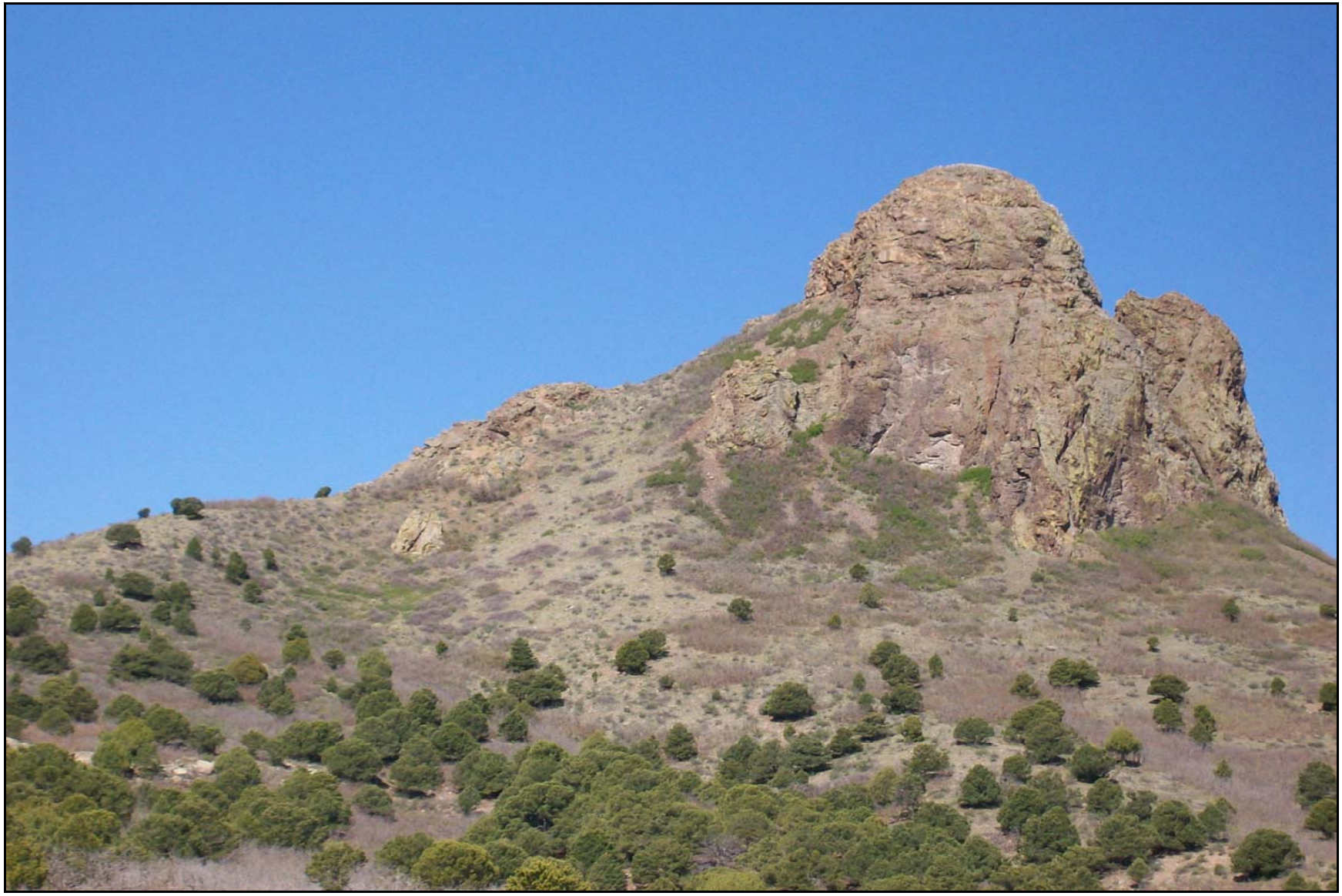

Figure 3.15 View looking west at Goemmer Butte trachyandesite (volcanic neck near La Veta, Colorado).

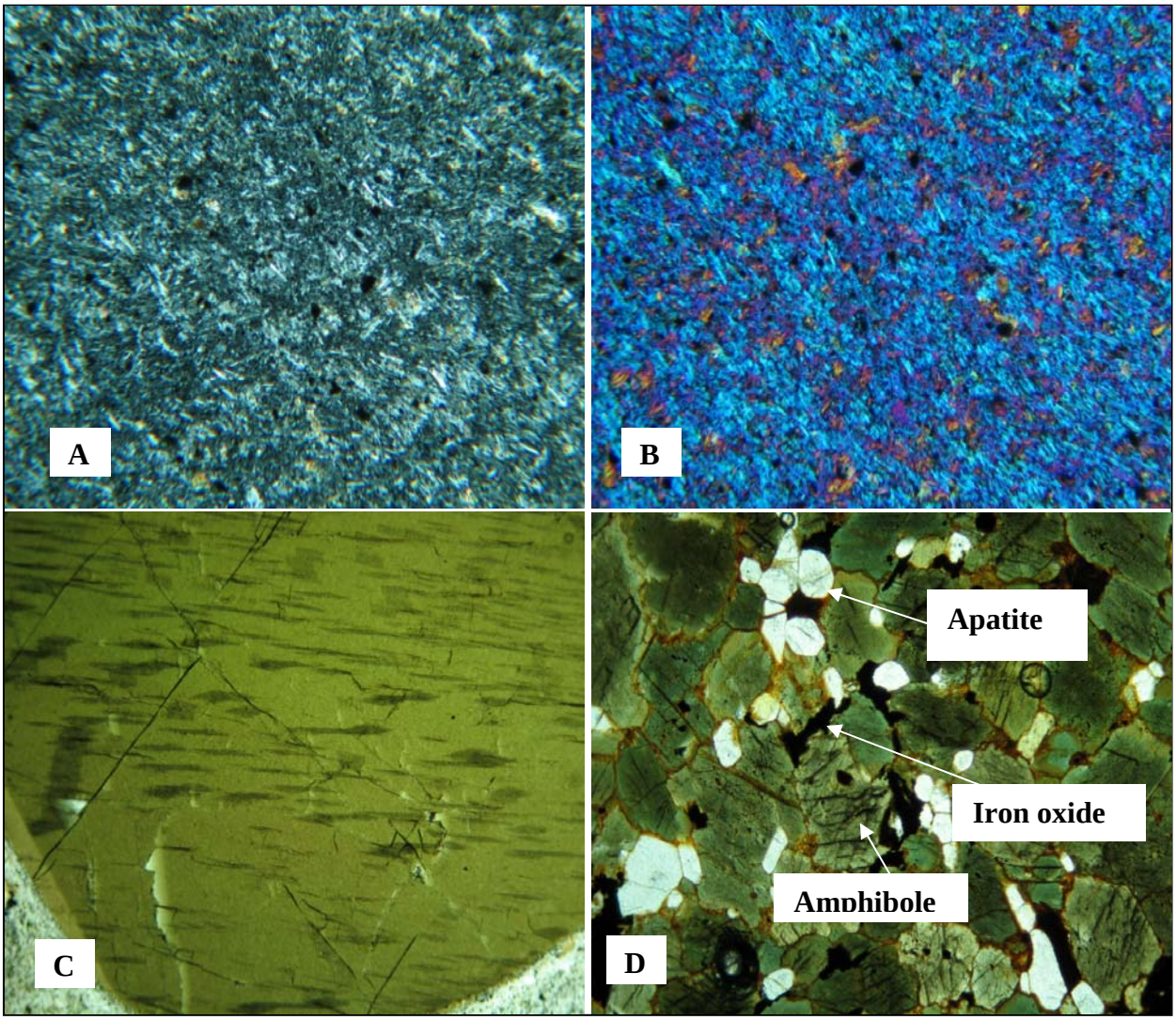

Figure 3.16 Multiple views of trachytic texture of HM29 from Goemmer Butte trachyandesite, **A;** (~4mm across) of HM29, **B;** (~4mm across) of HM29 under crossed polars with gypsum plate inserted. Note how the feldspars exhibit trachytic texture**, C;** (~4mm across) large amphibole megacryst, **D;** (~4mm across) xenolith comprised of amphibole, apatite, and iron oxide (for locations refer to table 3.1).

The potassium feldspar is euhedral, elongate, exhibits rim alteration and surrounds many of the larger phenocrysts of amphibole. The amphiboles are brown to colorless, strongly pleochroic, euhedral to subhedral, elongate to acicular with a few that are blocky. Some grains are twinned and have inclusions of apatite and sphene. The iron oxide is blocky, subhedral to euhedral in shape (magnetite) and is associated with the amphibole phenocrysts in thin section. The clinopyroxenes are clear to pale yellow-green, euhedral to subhedral, elongate to blocky, and some ~ 1mm euhedral grains clustered together.

Figure 3.17 View looking east at the dike outcrop adjacent to Goemmer Butte trachyandesite.

Lesser amounts of sphene and apatite are present ranging in size up to ~ 0.15mm in length. The groundmass consists of altered potassium feldspar, clinopyroxene, amphibole, iron oxide, sphene and apatite. There is one large amygdule present (~3mm in diameter) that is filled with quartz and feldspar (Figure 3.18).

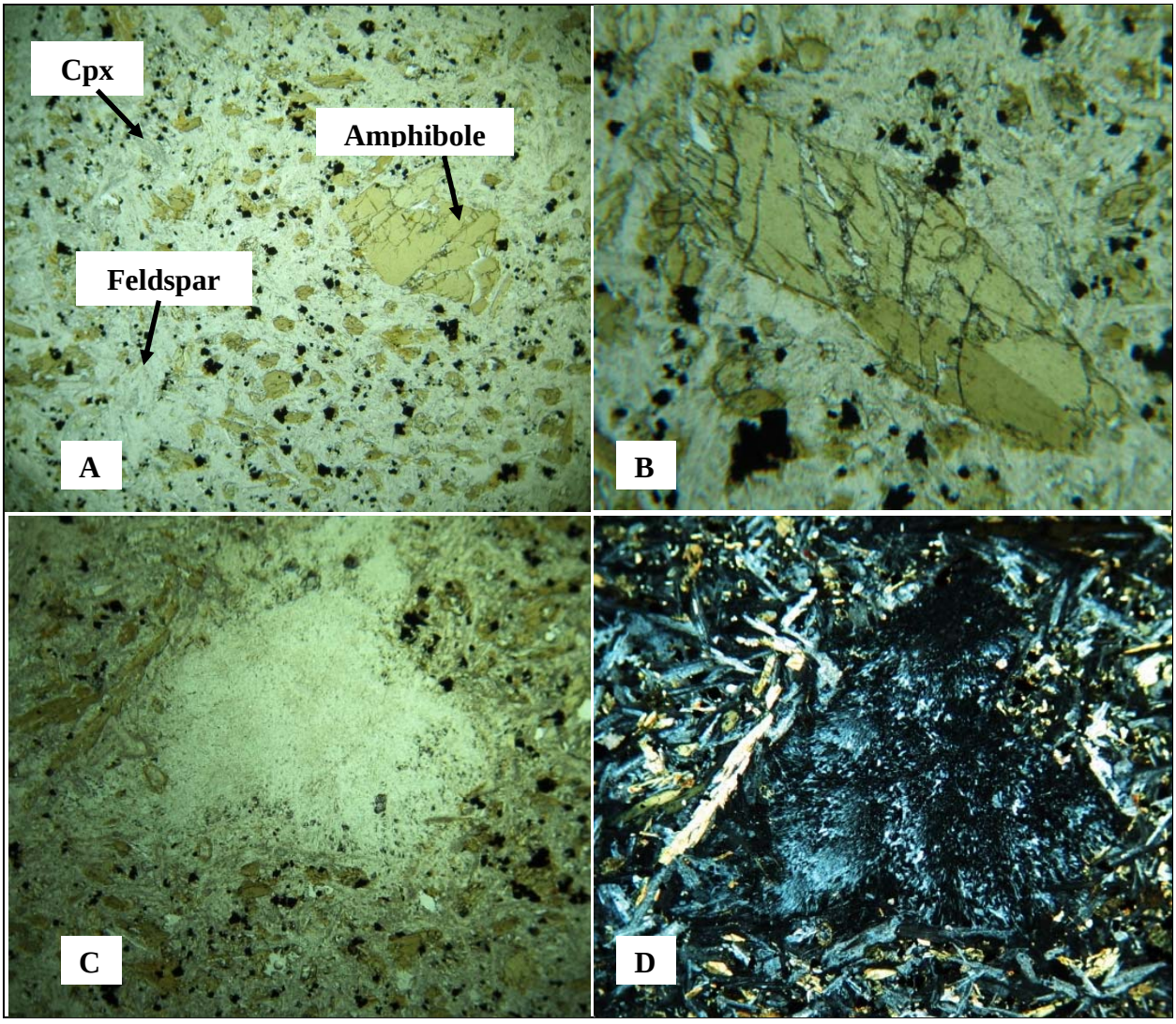

Figure 3.18 Multiple views displaying porphyritic texture, mineral twinning, and amygdule of sample HM30, **A;**~ 4mm **B;** view (~2mm across) is of close-up amphibole phenocryst. **C;**(~ 4mm across) of amygdule filled with a colorless mineral. **D;** same view as C with crossed polars (for locations refer to table 3.1).

3.1.2.3. *Sill off county road 440 northwest of LaVeta*

This outcrop is the first of a series of sills outcropping sporadically along county road 440 west of the town of La Veta. The sill is approximately ~2 meters thick, striking 160^{o}, and dipping eastwardly 27^{o} towards the Spanish Peaks. The rock has a light grayish-green color with a fine to medium-grained phaneritic texture (Figure 3.19). Petrographic analysis of HM21 reveals a mineral assemblage consisting of feldspar, clinopyroxene, and iron oxide (~45%, ~45%, and ~10% respectively) ranging up to ~ 1mm in length. The feldspars are euhedral, elongate, and altered to calcite or some type of phyllosilicate. Some oscillatory zoning is observed as well. The clinopyroxenes have light-pink rims surrounding colorless centers, are euhedral to subhedral, blocky, and some grains show alteration to a dark colored mineral (biotite and amphibole?) and iron oxide. Most of the clinopyroxenes are normally zoned, but a few exhibit hourglass zoning (Figure 3.20).

3.1.2.4. *Dike off county road 420 near Sulfur Springs*

This dike outcrop is located west of the Goemmer Butte trachyandesite on county road 420 near Sulfur springs campground. The outcrop at this location is ~ 8m thick and ~ 13m high (Figure 3.21). This rock has a medium grey-green color and a medium to coarse-grained phaneritic texture. Petrographic analysis of HM20 reveals a phenocryst assemblage consisting of feldspar, amphibole, clinopyroxene and iron oxide (~40%, ~35%, and ~15%, and ~10% respectively) ranging in size up to ~4.5mm in length and diameter. The feldspars are cloudy to clear, euhedral to subhedral, elongate to slightly blocky and include clinopyroxene and amphibole. Most show some signs of alteration to phyllosilicate minerals and some have Carlsbad twinning. The amphiboles are reddish-brown to brown, strongly pleochroic, euhedral to subhedral, blocky, and elongate to acicular. Some grains are twinned and have inclusions of apatite, iron oxide, and biotite. Some of the larger amphiboles exhibit compositional zoning, with darker brown cores to light brown rims. The clinopyroxenes are clear to pale yellow, euhedral to subhedral, and blocky. The iron oxide is blocky, subhedral to euhedral , and associated with the amphibole in the sample (Figure 3.22).

Figure 3.19 View looking west on county road 440 at ~ 2m thick sill outcrop.

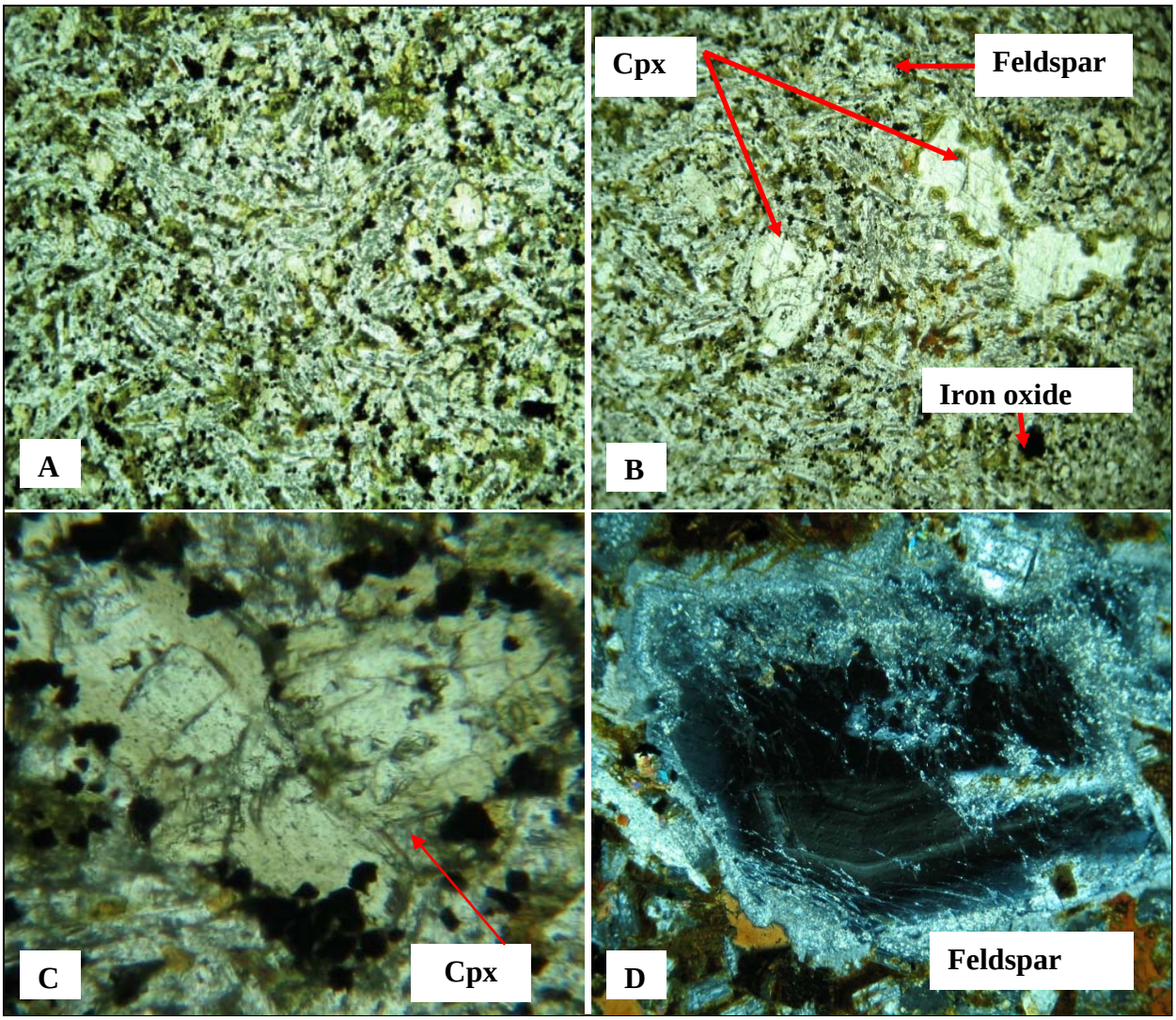

Figure 3.20 Multiple views displaying phaneritic texture, mineral alteration, and chemical zoning of clinopyroxenes and feldspars of sample HM21 (for locations refer to table 3.1), **A;**(~ 4mm across) of HM21 **B;** (~4mm across) of clinopyroxene with altered rims of iron oxide and amphibole or biotite. Most feldspar has been altered to clay or calcite, **C;** (~1mm across) noting compositional zoning in clinopyroxene and iron oxide around rims, **D;** crossed polars (~1mm across) oscillatory zoning in feldspar (for locations refer to table 3.1).

3.1.3. North Lake sill complex

North Lake is a manmade reservoir located west of the Spanish Peaks along Highway 12 a few miles south of Cordova Pass (Figure 2.3). Adjacent to the reservoir, Highway 12 cuts into a high ridge that is comprised of multiple sills intruded into the Pierre Shale. These sills are striking ~360^{o} and dipping ~39^{o} towards the east in the direction of the Spanish Peaks (Figure 3.23).

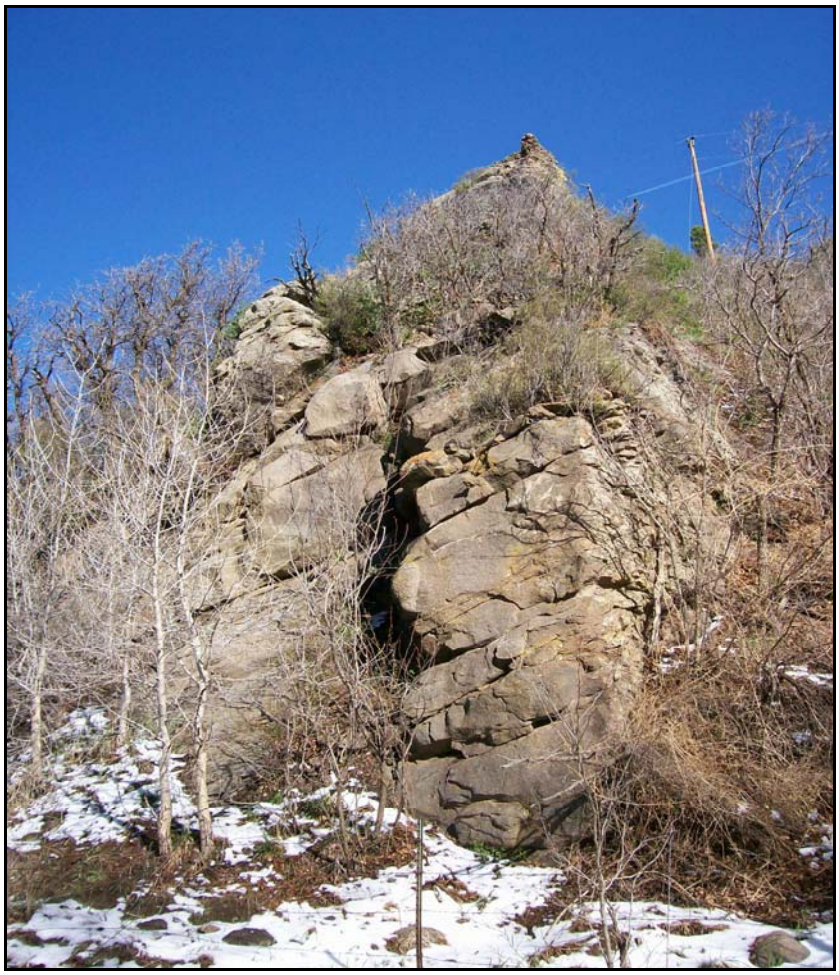

Figure 3.21 View looking west at ~ 8 meter thick dike outcrop on county road 420.

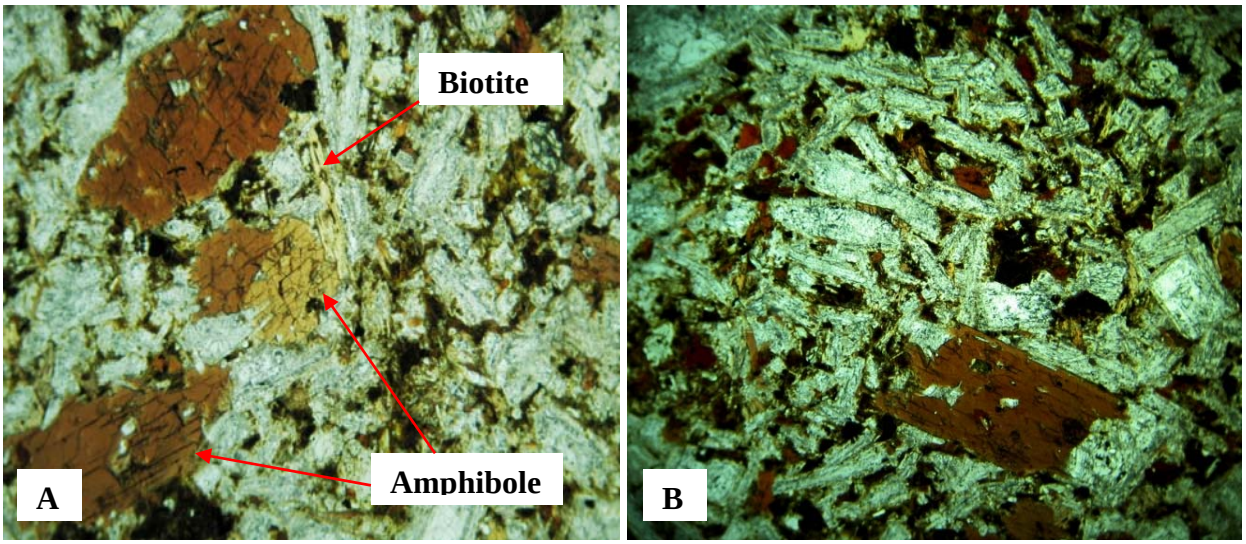

Figure 3.22 Multiple views displaying texture of sample HM20, **A;** (~2.5mm across) note simple twinning in amphibole. Note biotite size compared to amphibole. **B;** (~3mm across) of HM20, (for locations refer to table 3.1).

Figure 3.23 Multiple views of sill complex near North Lake reservoir from the exposed north end (looking east), to the south end (looking north). Red dots denote location of samples from lamprophyre facies sills.

3.1.3.1. *Large sill of North Lake complex*

A large sill ~ 3.5m thick located near the northern end where highway 12 cuts into the sill complex (Figure 3.24) has a wide variation in color and appearance. This sill ranges from dark grey to grey-green, and has a fine-grained porphyritic texture (HM22) to a coarse-grained porphyritic texture (HM18, 19, and 24). Petrographic analysis reveals a phenocryst assemblage consisting of biotite, clinopyroxene, feldspar, iron oxide and amphibole (~39%, ~24%, ~20%, ~17% and >1% respectively) that are seriate from grain sizes typical of the groundmass up to 9mm in length and diameter. The biotites are brown to dark-brown, pleochroic, euhedral to subhedral, equant to elongate in shape, and some have inclusions of iron oxide and apatite. The clinopyroxenes are pale yellow and pinkish, euhedral to subhedral, and blocky. Some grains are clustered, exhibiting polysynthetic twinning, inclusions (iron oxide, biotite and apatite), normal zoning, and some show alteration to phyllosilicates. The feldspars are euhedral, elongate, sericitized, and altered to calcite or phyllosilicates. The iron oxides are blocky, euhedral to subhedral in shape and appear as inclusions in other phenocrysts in the sample. The amphiboles are brown to dark brown, euhedral to subhedral, and predominately seen in the samples from the base of the sill as large phenocrysts. The groundmass consists of the aforementioned minerals in addition to apatite, calcite, and phyllosilicates (Figure 3.25). In one thin section there is a calcite-filled segregation vein ~0.5mm in width that spans the length of the thin section. The large amphibole phenocrysts (up to ~2cm in diameter) appear to have accumulated in the lower ~ 1m of the sill and white segregation veins (spaced ~ 20cm apart) run parallel to the bedding plane (Figure 3.26).

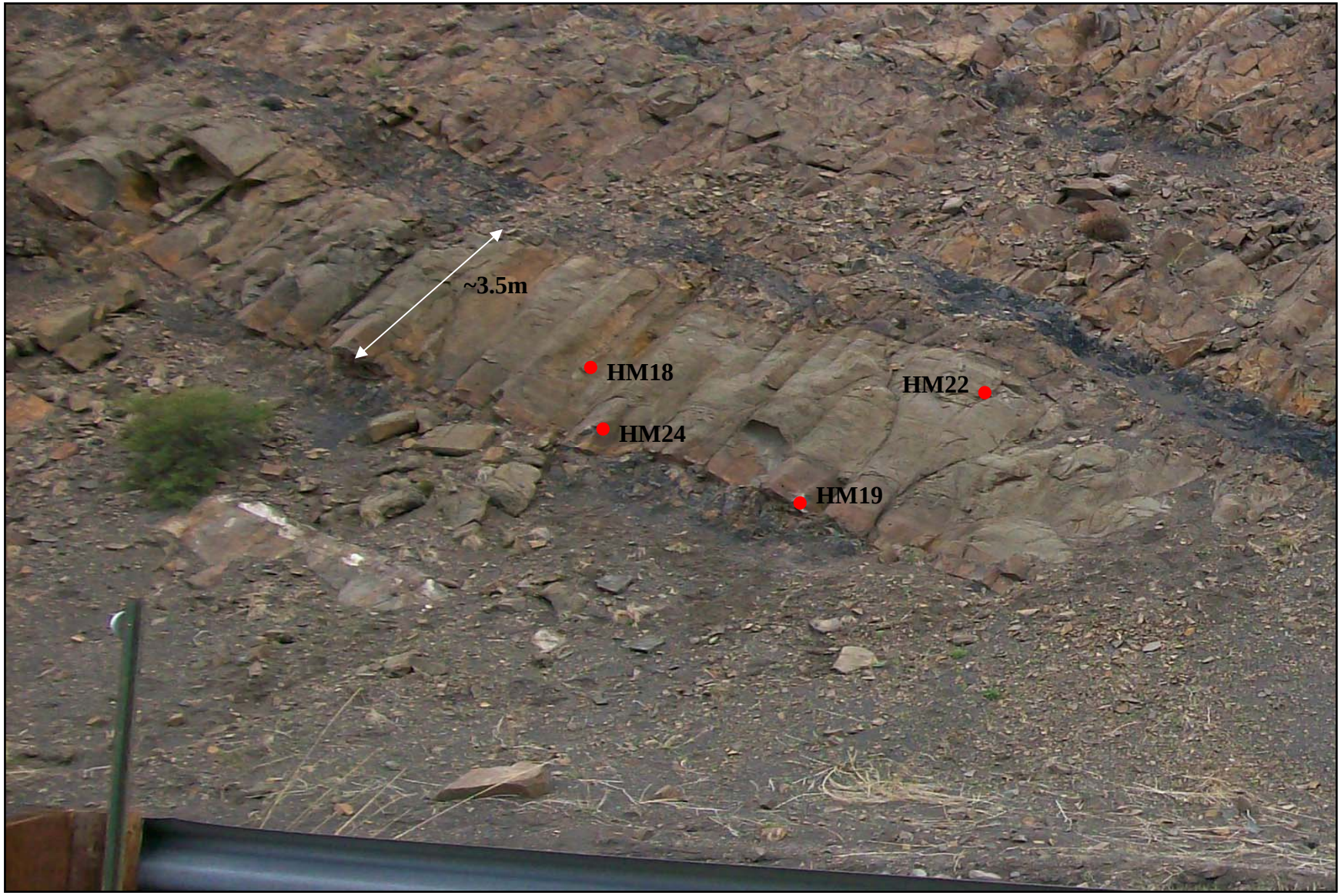

Figure 3.24 View of large sill off Highway 12 near North Lake reservoir. Red dotes denote sample sites.

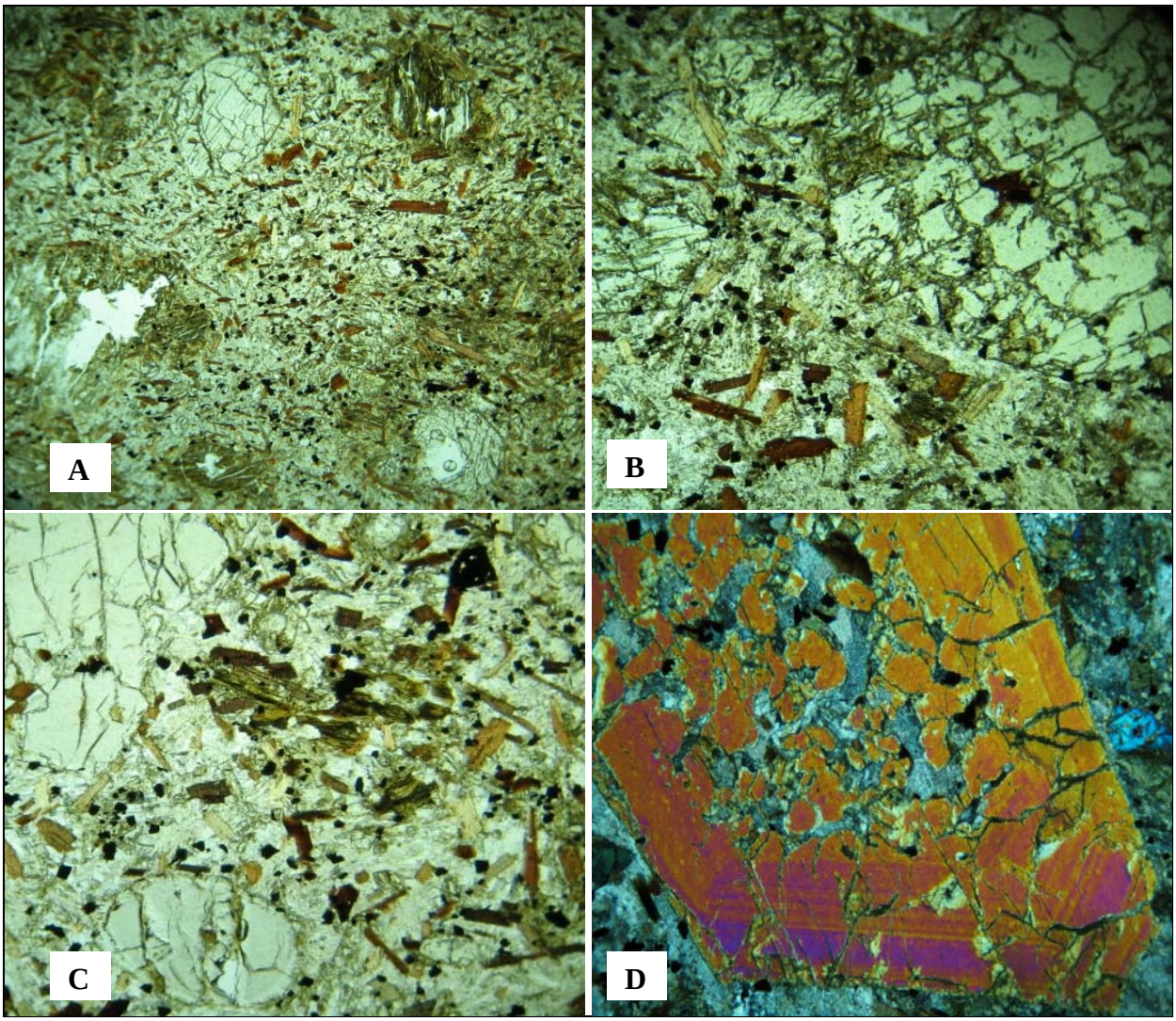

Figure 3.25 Multiple views displaying porphyritic texture, mineral clustering, and cpx oscillatory zoning of cpx in samples HM19, HM22, and HM24, **A;**(~4mm across) note relict amphibole that is altered to calcite and clay, **B;**(~4mm across) of large clinopyroxene with alteration in fractures of the grain, **C;** (~4mm across) of HM24**, D;** (~4mm across) of large clinopyroxene under crossed polars (for locations refer to table 3.1).

3.1.3.1. *Adjoining sannaite and minette lamprophyre sills*

Two adjoined sills at the north end of the visible part of the sill complex appear to be contemporaneously emplaced (Figure 3.27). One is a minette sill that is ~ 3m thick, grey-green in color, and has a medium- to coarse-grained porphyritic texture. Numerous biotite phenocrysts in this sill range from visible groundmass up to 8mm in length.

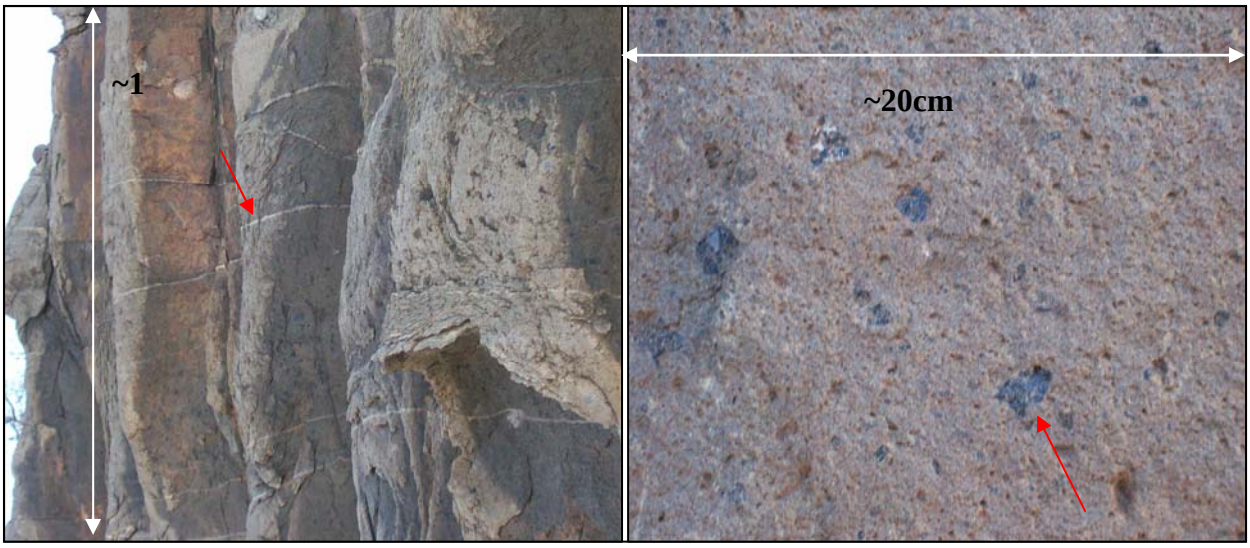

Figure 3.26 Multiple views of large sill at Northlake outcrop, A; view of basal portion of the large sill (note red arrow pointing at white veinlet), B; view of basal portion of large sill (note large amphibole [red arrow]).

The visible groundmass consists of dark-green cpx, biotite, and anhedral feldspar. Petrographic analysis of HM25 reveals a phenocryst assemblage consisting of feldspar, altered clinopyroxene, iron oxide, biotite, apatite and amphibole (~30%, ~20%, ~20%, ~19%, ~8%, and ~3% respectively) ranging in size up to 4mm in length and diameter. The feldspars are euhedral, elongate, and altered to some type of phyllosilicate. Some Carlsbad twinning is visible. The clinopyroxenes are pale-yellow, euhedral to subhedral, blocky, and show alteration to some type of phyllosilicate. The iron oxides are blocky, subhedral to euhedral, and are associated with the altered clinopyroxene and biotite phenocrysts. The biotites are dark brown to light tan, pleochroic, anhedral to subhedral, and blocky. The apatites are sporadic with a few large grains that are blocky or elongate, but most are needle-like and restricted to the groundmass. The amphiboles are dark-brown to brown, pleochroic, euhedral to subhedral, and are associated with the rims of the clinopyroxenes in the sample. The groundmass consists of phyllosilicates, iron oxide, biotite and sparse amounts of apatite. In thin section there is one large ocellus present (~3mm in diameter) that is filled with quartz, altered clinopyroxene, and iron oxide (Figure 3.28).

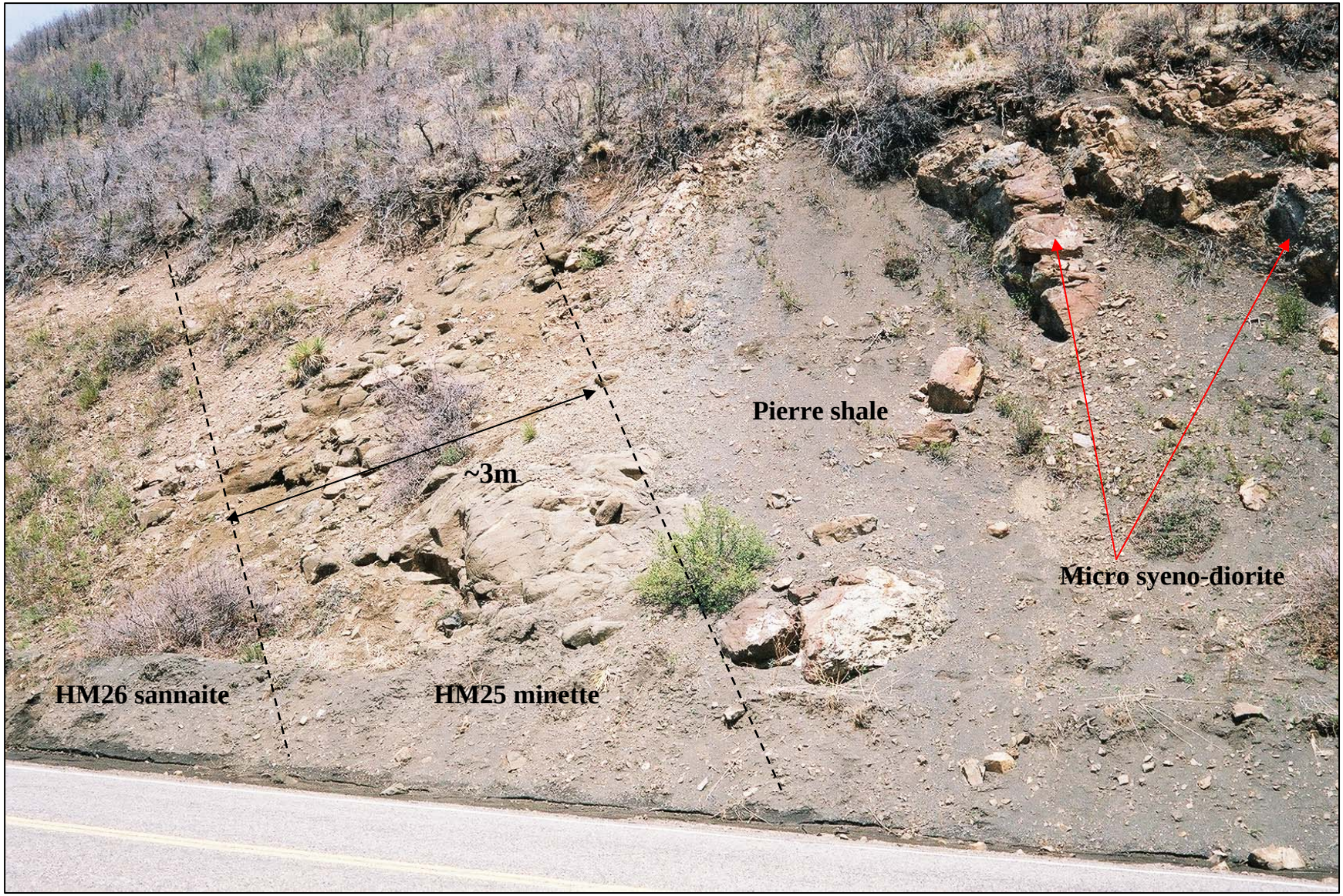

Figure 3.27 View looking east at the northernmost exposure Northlake sill complex. Dashed lines mark approximate margins of sills. Red arrows point at sills that are compositionally similar to the west Spanish Peak intrusion.

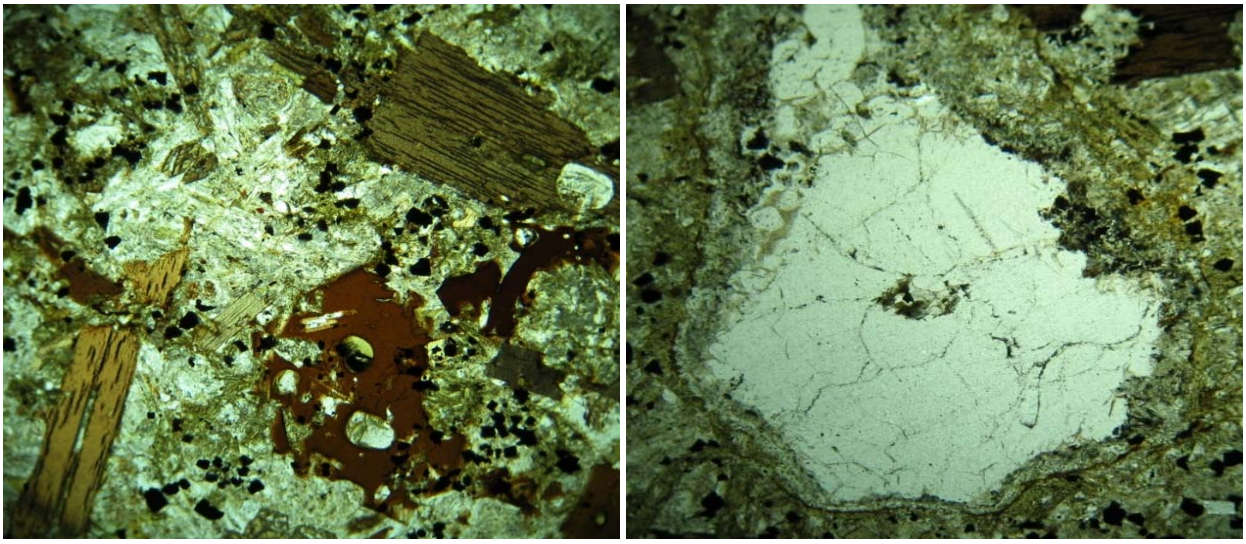

Figure 3.28 Multiple views displaying porphyritic texture, skeletal biotite, and ocellus of sample HM25, **A;**(~ 3mm across) of HM25, **B;**(~3mm across) of ocellus filled with quartz, iron oxide and altered clinopyroxene (for locations refer to table 3.1).

The second sill is a sannaite. A sample was taken from a ~ 1m exposure of the sill where the color of the rock is light grey-green with a medium to coarse-grained porphyritic texture. Abundant amphibole phenocrysts form star-like composite acicular crystals ~1cm in diameter. The visible groundmass is heavily altered and consists of altered clinopyroxene, feldspar, relict olivine, and amphibole. Petrographic analysis of HM26 reveals a phenocryst assemblage consisting of amphibole, iron oxide, feldspar, and altered clinopyroxene, (~42%, ~22, and ~21%, and ~15% respectively) that range in size up to 4.5mm in length and diameter. The amphiboles are brown to light brown in color, pleochroic, euhedral to subhedral, blocky, and elongate to needle-like. Some amphiboles exhibit twinning and have inclusions of apatite and iron oxide. The iron oxides are blocky, subhedral to euhedral, and are associated with the amphibole phenocrysts. The feldspars are euhedral, elongate, and altered to calcite or some type of phyllosilicate mineral. Some albite twinning is evidenced. The clinopyroxenes are pale-yellow in color, euhedral to subhedral, blocky, and altered to a phyllosilicate mineral. Some of the grains are clustered, and exhibit polysynthetic twinning. The groundmass consists of amphibole, calcite, phyllosilicates, iron oxide, and sparse amounts of apatite (Figure 3.29).

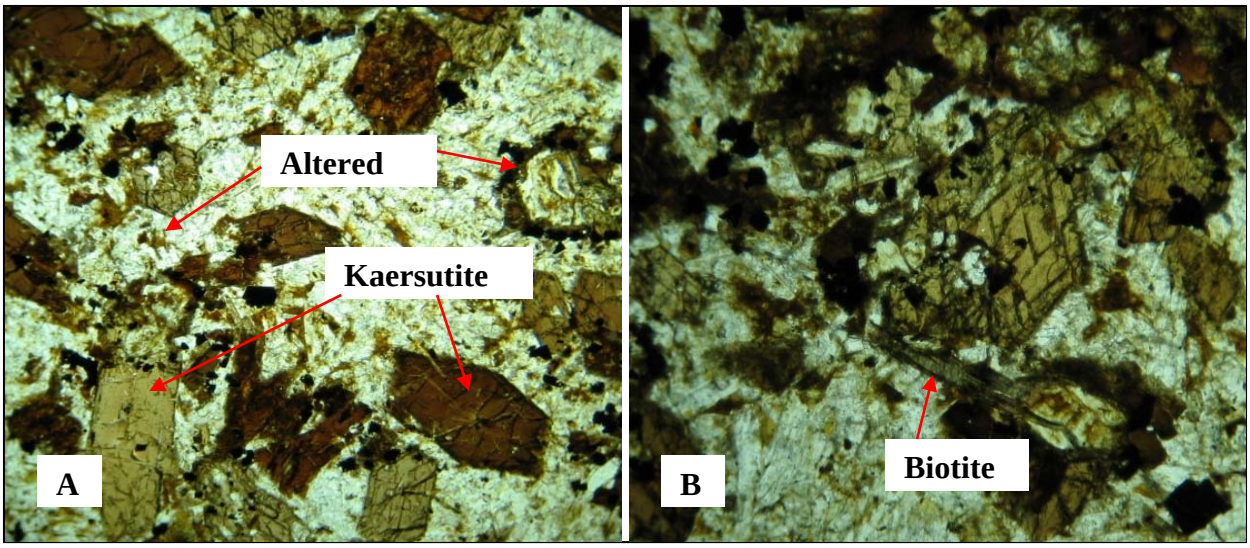

Figure 3.29 Multiple views displaying porphyritic texture and alterations of sample HM26 (for locations refer to table 3.1), **A;** (~ 3mm across) of HM26. **B;** (~1.8mm across) note small biotite phenocryst (for locations refer to table 3.1).

3.1.3.2. *Sample from dike exposure north end of North Lake sill complex*

Continuing northward sills become obscured by grass and small scrub oak. Samples HM7 and HM8 were collected at the top of the ridge where a dike outcrops (Figure 3.30). Sample HM7 was collected at the top of the ridge at the southern end of the exposed dike. The width of the dike here is ~ 5m. It has a light grey color, medium-grained porphyritic texture, phenocrysts of euhedral amphibole ~ 2mm in diameter, and composite acicular amphibole clusters up to 1cm in diameter. The visible groundmass consists of potassium feldspar and a dark mineral (iron oxide). Sample HM8 was collected ~ 8m north from HM7. The exposure widens to ~ 7m here and has a small vertical break in the ridgeline. The rock here is medium grey in color, has a medium-grained porphyritic texture with a fine-grained groundmass consisting of plagioclase and iron oxides. The phenocrysts consist of clinpyroxene (greenish in color) up to 2mm in length, and the same acicular amphibole phenocrysts, but no visible clusters. Petrographic analysis of HM8 reveals the main phenocryst assemblage to consist of amphibole, potassium feldspar, clinopyroxene, iron oxide, and biotite (~31%, ~25%, ~24%, 15% and ~5% respectively) that range up to ~ 4.5mm in length and diameter.

Figure 3.30 View of ~ 7m wide dike at the north end of Northlake sill complex.

The amphiboles are brown to light brown, pleochroic, euhedral to subhedral, elongate to needle-like with a few that are blocky. Some of the grains exhibit twinning, core to rim color change from dark brown to light brown, and have inclusions of apatite, clinopyroxene, sphene and iron oxide. The potassium feldspar is euhedral, elongate, and some alteration to phyllosilicates. The clinopyroxenes are pale-yellow, euhedral to subhedral, and blocky. Some of the cpx grains are clustered, exhibit polysynthetic twinning, and are rimmed with amphibole. The iron oxides are blocky, subhedral to euhedral in shape, and are associated with the amphibole phenocrysts in sample. The biotites are brown to light brown, pleochroic, anhedral to

subhedral, elongate to blocky, and are associated with amphibole in the sample. The groundmass consists of feldspar, cpx, amphibole, iron oxide, sphene, and apatite (Figure 3.31).

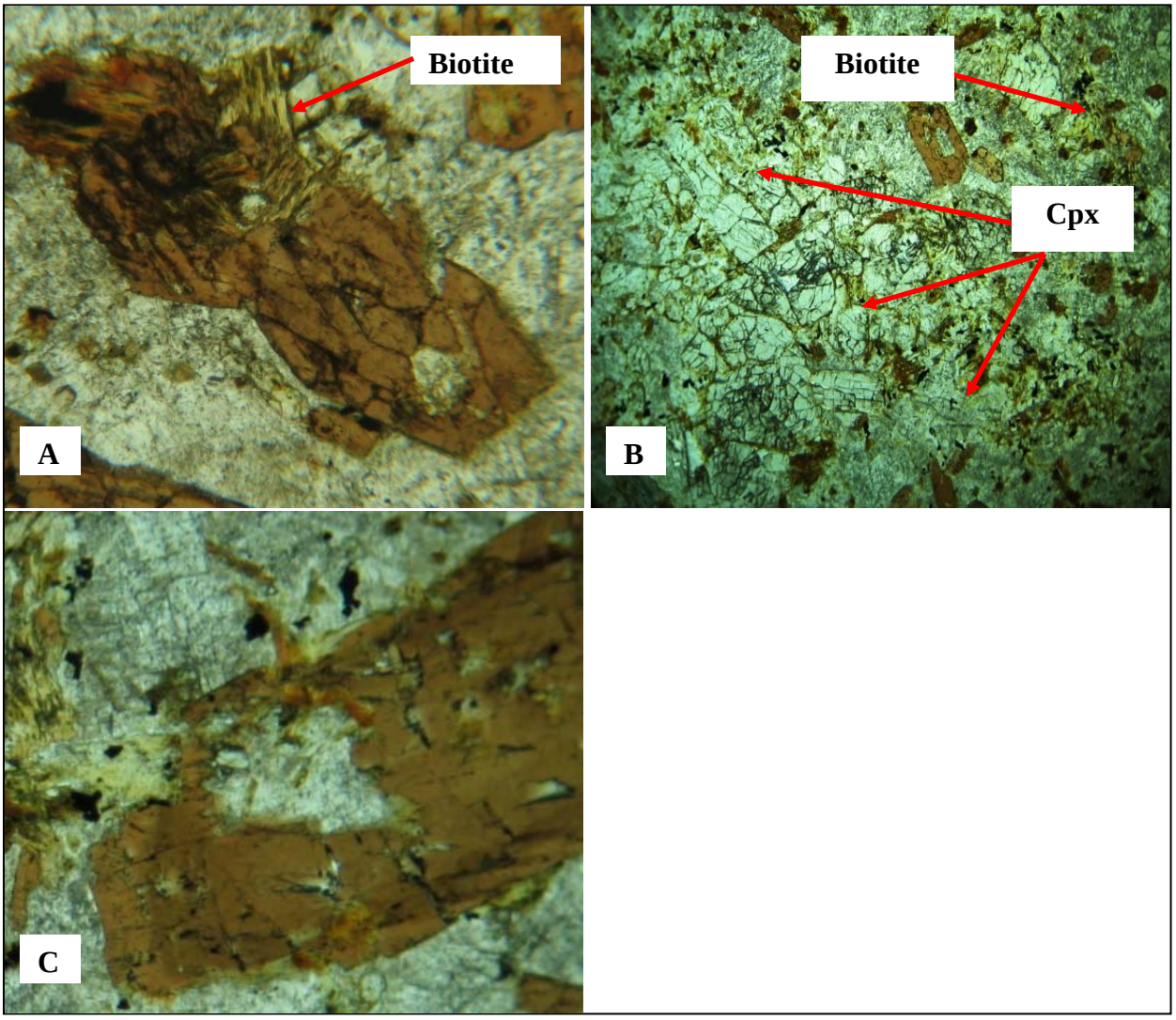

Figure 3.31 Multiple views of porphyritic texture, amphibole chemical zoning, and biotite-amphibole associations in sample HM8, **A;** (~1.5mm across) of biotite association with amphibole, **B;**(~3.5mm across) of large cluster of clinopyroxenes bottom left and biotite upper left associated with amphibole, **C;** (~2mm across) of biotite in association with amphibole which exhibits color zoning (light brown to dark brown, then back to light brown), inclusions of small apatite and iron oxide(for locations refer to table 3.1).

3.1.3.3. *Sample of dike exposure north of the North Lake sill complex*

The ridgeline from North Lake is crosscut again by an unmarked county road near Coal creek along Highway 12 towards Cordova pass (Figure 3.32). At this exposure, the outcrop is composed of two or more vertical dikes. Sample HM27 and HM28 were collected here and are representative samples of the two dikes. HM27 is a light grey rock that has a medium to coarse-grained porphyritic texture with notable phenocrysts of amphibole, (acicular clusters up to ~5mm in diameter), feldspar, and pyroxene up to ~1 to 2mm in length. The visible groundmass consists of the same minerals as the phenocryst assembledge. HM28 is a dark grey-green rock that has a medium to coarse-grained porphyritic texture with phenocrysts of biotite, amphibole, and pyroxene up to ~1 to 2mm in length and diameter. The visible groundmass consists is similar to the phenocryst assemblage, in addition to altered olivine. Also present are amygdules ~ 3mm in diameter, which are filled with calcite and feldspar. Petrographic analysis of HM28 reveals a phenocryst assemblage comprised of clinopyroxene, biotite, and potassium feldspar (~40%, 40%, and 20% respectively) ranging up to ~3mm in length and diameter. The clinopyroxenes are clear to pale yellow-green, euhedral to subhedral, and elongate to blocky. Some clinopyroxene have biotite, amphibole, and iron oxide in and around fractures and the edges of the grains. A few of the cpx have polysynthetic twinning and relict cores altered to some phyllosilicate mineral. The biotites are brown to reddish-brown, pleochroic, subhedral, elongate, and blocky. Some of the biotites have inclusions of cpx, iron oxide and apatite. The feldspars are anhedral in shape mainly restricted to the groundmass but a few are present as phenocrysts up to ~2.5mm in width. Most of the feldspar grains show signs of alteration to fine grained carbonate. The groundmass consists of smaller grains of clinopyroxene, biotite, potassium feldspar, calcite, iron oxides, apatite and sphene. Additionally there are ocelli-type structures filled with calcite and potassium feldspar, (Figure 3.33).

Figure 3.32 View looking west at exposure north of the North Lake complex on unmarked county road near Coal creek.

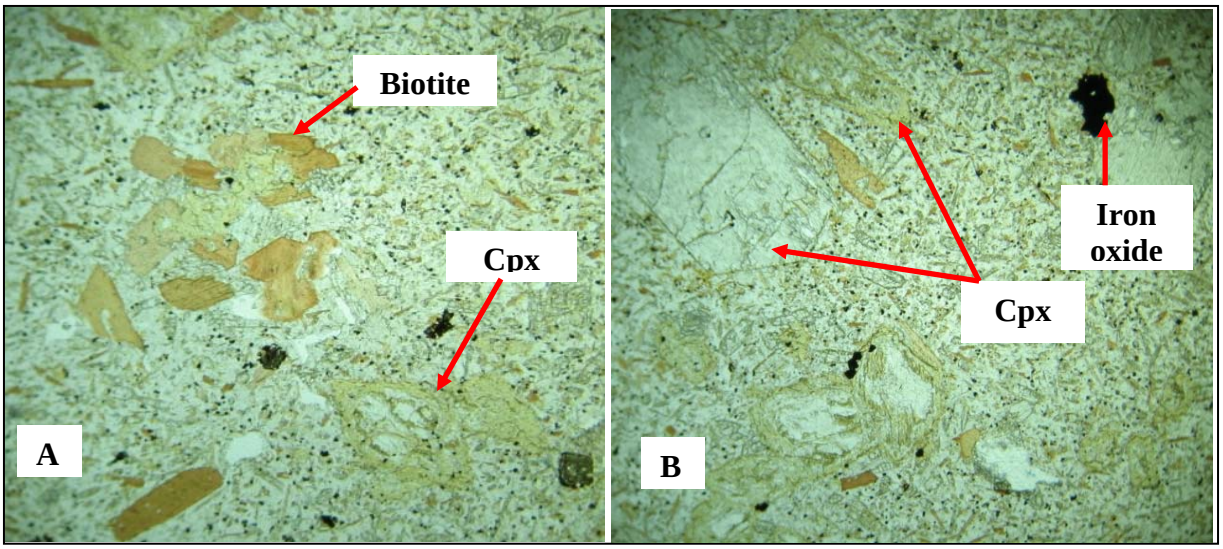

Figure 3.33 Multiple views showing porphyritic texture of sample HM28 dike, **A;**(~3.5mm across) of cluster of biotite **B;**(~4mm across) of HM28 (for locations refer to table 3.1).

3.2. *MAJOR AND TRACE ELEMENT ANALYSIS RESULTS*

Major and trace element analyses were performed on 30 samples from this study using XRF methods described in section 2.4. Table 3.3 is a list of these results along with normative calculations obtained using KWare Magma software version 2.48.0116 created by Ken Wohletz. LOI (loss on ignition) values were obtained by methods described in section 2.4.5., and added to the total weight percent yielded by XRF analysis. XRF analyses were normalized to 100% without LOI values for plotting purposes. All samples (excluding the Goemmer Butte trachyandesite) were assigned one of two labels based upon their K_2O/Na_2O weight percent ratio. If the $K_2O/Na_2O > 1$, the sample is referred to as "relatively potassic". If the $K_2O/Na_2O < 1$, the sample is referred to as "relatively sodic" (Figure 3.34). A similar method of classifying lamprophyric rocks (with K_2O/Na_2O ratios) was used by Rock (1977, 1987). Other studies done in the Spanish Peaks area classified lamprophyric rocks based on petrography and modal mineralogy, Knopf (1936), Johnson (1968), Smith (1975), Jahn (1979), Penn (1994), and Miggins (2002).

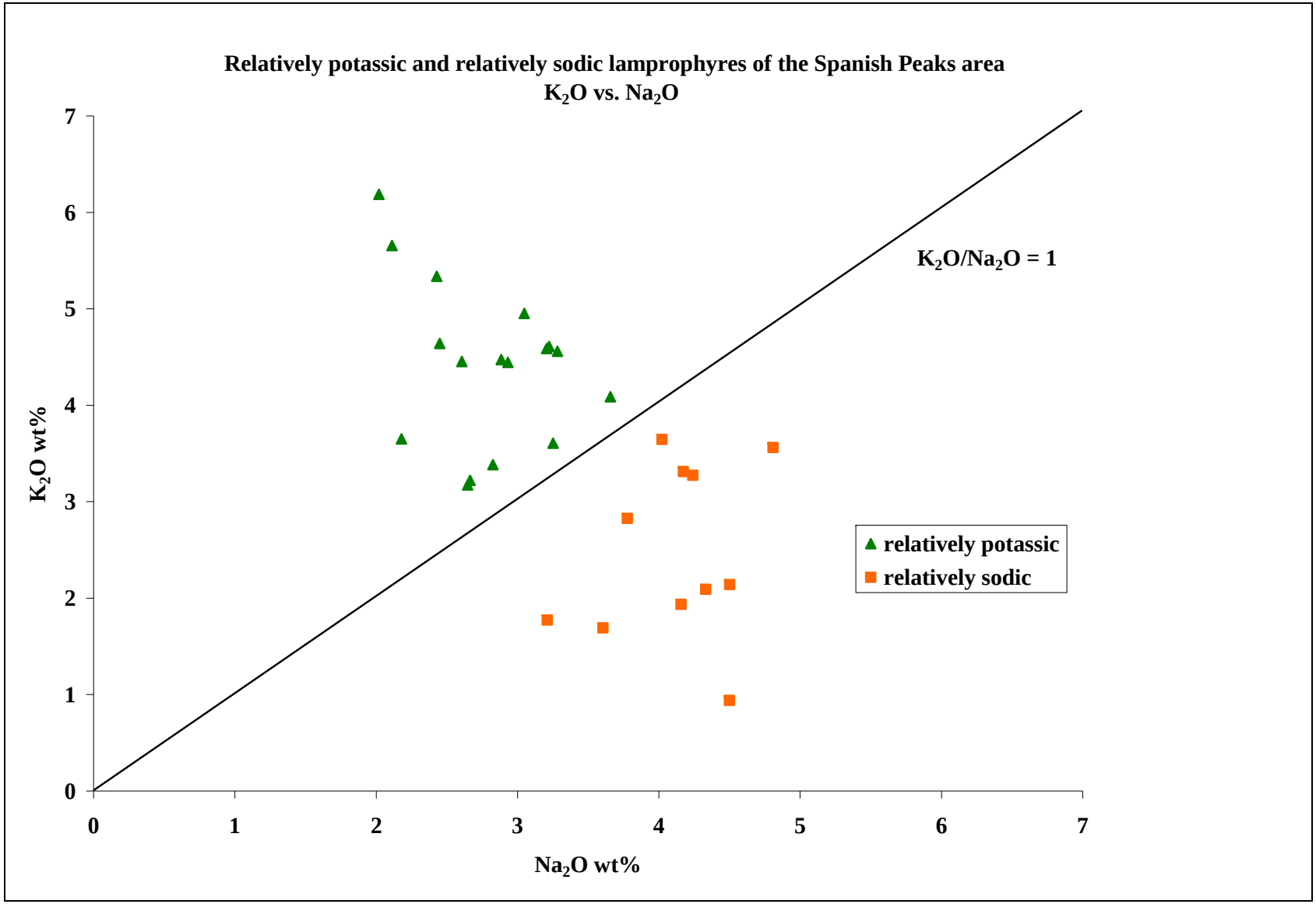

Figure 3.34 K_2O wt% vs. Na_2O wt% from XRF analyses of lamprophyric dikes and sills from the Spanish Peaks area. Samples plotting above $K_2O/Na_2O = 1$ line are defined as "relatively potassic". Samples plotting below this line are defined as "relatively sodic".

Table 3.3 XRF analyses of Spanish Peaks samples

Location	Walsenburg dike								
	Cr504		Lathrop	Hwy85		Cr590			
Label	HM1	HM2	HM4	HM5	HM12	HM3	HM13	HM14	HM15
ox.wt%:									
SiO_2	46.37	45.50	45.42	45.78	45.62	46.43	45.03	45.99	45.41
TiO_2	2.34	2.28	2.99	2.29	2.36	2.33	3.00	2.31	2.85
Al_2O_3	11.64	11.80	11.52	11.49	10.91	11.41	11.09	11.39	11.64
Fe_2O_3*	1.27	1.24	1.34	1.24	1.28	1.26	1.36	1.27	1.28
FeO*	8.45	8.23	8.93	8.27	8.53	8.42	9.06	8.44	8.50
MnO	0.29	0.15	0.16	0.15	0.16	0.15	0.15	0.16	0.14
MgO	7.86	7.51	7.01	7.91	8.29	8.02	7.54	8.15	6.93
CaO	9.99	10.32	9.21	9.33	9.80	9.30	8.29	9.23	8.23
Na_2O	2.37	2.81	2.03	3.06	2.76	3.16	2.31	3.09	2.88
K_2O	4.49	4.26	5.44	4.38	4.28	4.39	5.08	4.42	4.68
P_2O_5	1.69	1.74	2.13	1.56	1.69	1.42	2.26	1.43	1.96
LOI	2.35	2.35	2.35	2.35	2.35	2.35	3.53	3.53	3.53
Total	99.11	98.19	98.52	97.81	98.02	98.64	98.69	99.40	98.02
Mg# **	62	62	58	63	63	63	60	63	59
Trace (ppm):									
V	232	219	250	230	237	230	252	230	236
Cr	250	216	174	265	287	260	194	263	157
Ni	146	130	121	152	168	164	128	167	119
Cu	66	60	62	66	52	67	64	73	67
Zn	117	116	134	114	117	105	145	116	129
Rb	89	76	94	91	87	98	87	101	87
Sr	1732	3300	1495	2620	2150	2610	1570	2460	1890
Y	21	21	21	19	20	18	22	20	21
Zr	278	278	333	261	253	262	334	258	332
Nb	67	69	82	65	62	64	80	63	78
Ba	3060	3230	3360	2860	5970	3290	3190	3000	3840
Th	9	8	10	9	9	10	9	11	9
La	103	110	100	97	99	87	101	93	88
Pb	9	11	10	9	9	8	10	8	10
CIPW Norms:***									
qz									
co									
or	26.50	25.15	32.11	25.85	25.26	25.91	29.99	26.09	27.63
ab	6.23	4.50	4.42	5.58	5.45	5.84	8.58	4.93	10.48
an	7.86	7.00	6.46	4.68	4.74	3.99	4.89	4.16	5.01
ne	7.48	10.43	6.90	11.00	9.69	11.31	5.93	11.48	7.52
di	25.00	26.79	20.92	25.60	26.78	26.78	17.59	26.30	18.86
hy									
ol	13.52	11.86	13.07	13.05	13.57	12.97	15.33	13.43	13.26
mt	1.84	1.80	1.95	1.80	1.86	1.83	1.98	1.84	1.86
il	4.45	4.34	5.69	4.35	4.48	4.43	5.71	4.39	5.42
ap	3.69	3.80	4.65	3.41	3.68	3.10	4.94	3.12	4.27

*iron recalculated following Brooks (1976), ** Mg# =100 Mg/ ($Mg+Fe^{2+}$), *** calculated using KWare Magma software version 2.48.0116 by Ken Wohletz

Table 3.3 XRF analyses of Spanish Peaks samples continued

Location	North Lake sill complex									
	dike outcrop near Coal Creek		dike outcrop at north end		sills from south end of complex					
Label	HM28	HM27	HM7	HM8	HM10	HM17	HM23	HM9	HM11	HM16
ox wt%:										
SiO_2	46.56	52.49	53.37	52.72	47.93	48.09	50.63	42.76	50.48	45.42
TiO_2	2.16	1.68	1.70	1.72	1.73	1.71	1.61	2.46	1.70	2.17
Al_2O_3	12.24	14.40	14.67	14.79	14.85	14.62	14.90	12.51	14.95	10.87
Fe_2O_3*	1.14	1.01	0.99	0.99	1.15	1.16	1.05	1.19	1.00	1.26
FeO*	7.61	6.73	6.57	6.62	7.64	7.70	6.98	7.90	6.65	8.39
MnO	0.14	0.13	0.14	0.13	0.14	0.16	0.11	0.15	0.14	0.17
MgO	5.62	5.56	5.13	4.97	6.21	5.81	5.16	5.36	5.14	6.83
CaO	10.14	7.55	7.42	7.21	7.16	8.25	8.03	10.26	6.72	10.72
Na_2O	3.03	4.07	3.95	4.12	4.06	3.91	3.39	1.85	3.47	2.01
K_2O	3.36	3.23	3.58	3.18	1.96	1.82	1.59	5.67	3.88	3.37
P_2O_5	1.19	0.66	0.69	0.70	0.87	0.83	0.60	1.53	0.77	1.06
LOI	4.71	1.18	2.35	2.35	5.88	5.88	5.88	8.24	4.70	7.06
Total	97.90	98.70	100.55	99.50	99.58	99.93	99.93	99.88	99.59	99.33
Mg# **	57	59	58	57	59	57	57	55	58	59
Trace (ppm):										
V	223	201	205	216	260	232	177	263	210	233
Cr	264	166	118	92	167	159	115	142	108	393
Ni	138	50	40	37	52	58	89	77	47	241
Cu	62	65	35	55	53	54	37	76	54	76
Zn	118	77	94	105	92	99	85	118	94	99
Rb	60	69	72	71	43	37	34	101	77	63
Sr	1260	1270	786	1150	995	1150	891	654	927	1100
Y	25	20	22	21	26	26	20	23	21	22
Zr	316	212	210	244	261	252	223	328	288	288
Nb	63	52	52	57	41	40	38	86	58	58
Ba	3080	1280	1380	1530	2170	2140	938	2860	1290	3250
Th	6	7	7	7	4	3	3	11	8	6
La	63	59	64	69	65	61	50	86	67	54
Pb	10	12	12	13	11	12	9	9	9	8
CIPW Norms: ***										
qz							0.59			
co										
or	19.83	19.07	21.13	18.77	11.57	10.74	9.39	19.67	22.90	19.89
ab	14.35	30.71	30.92	33.64	30.75	29.36	28.66		27.07	10.62
an	9.87	11.48	11.18	12.47	16.50	16.96	20.74	9.08	13.76	10.68
ne	6.11	2.00	1.34	0.64	1.93	2.00		10.82	1.22	3.45
di	26.79	17.72	17.31	15.36	10.94	15.24	12.47	26.16	11.94	29.11
hy							16.21			
ol	7.77	10.37	9.52	9.95	15.06	12.93		7.53	11.55	10.16
mt	1.66	1.47	1.44	1.44	1.67	1.69	1.53	1.73	1.45	1.83
il	4.11	3.20	3.23	3.27	3.29	3.25	3.06	4.68	3.23	4.13
ap	2.60	1.44	1.51	1.53	1.90	1.81	1.31	3.34	1.68	2.31

*iron recalculated following Brooks (1976), ** Mg# = 100 Mg/ ($Mg+Fe^{2+}$), *** calculated using KWare Magma software version 2.48.0116 by Ken Wohletz

Table 3.3 XRF analyses of Spanish Peaks samples continued

Location	North Lake sill complex					
	minette	camptonite	large sill near south end			
Label	HM25	HM26	HM18	HM19	HM22	HM24
oxide wt%:						
SiO_2	40.57	41.87	44.12	46.39	46.81	46.23
TiO_2	2.37	2.18	2.13	2.09	2.20	2.10
Al_2O_3	11.41	12.95	10.83	11.03	11.81	11.35
Fe_2O_3*	1.36	1.27	1.14	1.21	1.16	1.24
FeO*	9.08	8.47	7.60	8.08	7.74	8.28
MnO	0.15	0.16	0.15	0.14	0.12	0.15
MgO	8.71	6.46	7.29	8.67	8.11	7.89
CaO	10.54	10.34	11.85	8.91	6.85	9.32
Na_2O	2.90	3.45	2.44	2.46	2.41	2.64
K_2O	1.60	2.58	2.95	2.95	4.12	3.16
P_2O_5	1.64	1.60	1.08	1.05	1.14	1.04
LOI	9.41	8.24	7.06	7.06	5.88	5.88
Total	99.75	99.56	98.64	100.04	98.36	99.29
Mg# **	63	58	63	66	65	63
Trace (ppm):						
V	262	240	237	233	229	221
Cr	312	250	423	408	365	384
Ni	216	160	217	259	207	247
Cu	63	67	70	66	60	66
Zn	116	121	126	97	105	98
Rb	37	48	59	56	74	61
Sr	1100	2420	896	1040	927	994
Y	19	21	23	22	24	23
Zr	221	249	293	275	308	284
Nb	76	87	58	54	62	57
Ba	1970	3280	3200	3100	5860	2740
Th	3	4	6	5	7	6
La	80	95	60	45	57	55
Pb	11	13	8	8	6	8
CIPW Norms:***						
qz						
co						
or	9.44	15.23	17.41	17.41	24.32	18.65
ab	10.24	7.37	5.71	18.00	18.52	14.85
an	13.39	12.23	9.89	10.30	9.24	9.79
ne	7.74	11.81	8.09	1.47	1.00	4.05
di	22.99	23.50	34.05	21.97	14.07	24.15
hy						
ol	16.33	11.55	8.30	15.67	16.85	13.77
mt	1.98	1.84	1.66	1.76	1.69	1.80
il	4.51	4.15	4.05	3.98	4.19	3.99
ap	3.58	3.49	2.36	2.27	2.49	2.28

*iron recalculated following Brooks (1976), ** Mg# = 100 Mg/ ($Mg+Fe^{2+}$), *** calculated using KWare Magma software version 2.48.0116 by Ken Wohletz

Table 3.3 XRF analyses of Spanish Peaks samples continued

Location	Cr420	Cr440	Goemmer Butte	dike by Goemmer Butte
Label	HM20	HM21	HM29	HM30
oxide wt%:				
SiO_2	53.37	48.99	61.18	48.28
TiO_2	1.65	1.95	0.78	1.44
Al_2O_3	15.67	16.40	16.59	16.75
Fe_2O_3*	0.94	1.30	0.78	1.20
FeO*	6.28	8.64	5.18	8.01
MnO	0.12	0.22	0.11	0.17
MgO	4.45	5.32	1.63	4.16
CaO	5.06	7.10	5.17	8.33
Na_2O	4.63	4.31	4.20	4.31
K_2O	3.43	0.90	3.42	2.05
P_2O_5	0.69	0.64	0.52	1.03
LOI	2.35	4.77	0.00	3.53
Total	98.64	100.54	99.56	99.27
Mg# **	56	52	36	48
Trace (ppm):				
V	157	232	80	202
Cr	102	25	5	2
Ni	92	38	1	13
Cu	26	45	9	48
Zn	110	92	97	87
Rb	80	19	67	35
Sr	977	619	755	953
Y	21	24	20	27
Zr	263	186	186	226
Nb	56	37	20	47
Ba	1180	922	1340	1440
Th	8	n.d.[1]	6.5	3
La	52	38	43	86
Pb	10	7	11	11
CIPW Norms:***				
qz			8.57	
co				
or	20.25	5.31	20.19	12.10
ab	39.14	36.43	35.59	28.19
an	11.85	22.74	15.75	20.30
ne				4.47
di	7.21	6.87	5.48	11.93
hy	0.69	2.81	9.01	
ol	11.06	14.00		11.91
mt	1.37	1.89	1.12	1.74
il	3.14	3.71	1.48	2.74
ap	1.51	1.40		2.25

*iron recalculated following Brooks (1976), ** Mg# = 100 Mg/ ($Mg+Fe^{2+}$), *** Calculated using KWare Magma software version 2.48.0116 by Ken Wohletz,
[1] not detected

3.2.1. Major elements

All rocks in this study are hypabyssal and mostly porphyritic with a fine-grained groundmass. Rather than using the QAPF (quartz, alkali feldspar, plagioclase, and feldspathoid) based on modal mineralogy, I used the IUGS TAS (total alkali silica) nomenclature for extrusive rocks following Le Bas et al, (1986) (Figure 3.35). The lamprophyric rocks in this study plot in the tephrite basanite, trachybasaltic, basaltic trachyandesitic, and trachyandesite fields. All samples plot above the alkaline/sub-alkaline dividing line except for one relatively sodic sample, which plots on the dividing line, and the Goemmer Butte sample, which plots just below the dividing line.

Various oxide weight percent values were plotted against Mg# values (molar ratio Mg/ Mg+Fe^{2+}, Figure 3.36). Most of the relatively potassic samples have higher Mg# values, CaO wt%, K_2O wt%, P_2O_5 wt%, and TiO_2 wt%, than the relatively sodic samples. Most relatively sodic rocks contain higher Na_2O wt% and Al_2O_3 wt% values than the relatively potassic rocks.

In addition, various ratios of major oxide analyses from each sample were plotted against Mg# values (Figure 3.37). Several ratios appear to discriminate between the two groups. For example, relatively potassic samples have K_2O/Na_2O ratios greater than one, and relatively sodic samples have K_2O/Na_2O ratios less than one. Relatively sodic samples have higher Al_2O_3/K_2O (>4), Na_2O/TiO_2 ratios (>2), Na_2O/P_2O_5 (>4), and Al_2O_3/TiO_2 ratios (>6) compared to relatively potassic samples Al_2O_3/K_2O (<4), Na_2O/TiO_2 ratios (<2), Na_2O/P_2O_5 (<4), and Al_2O_3/TiO_2 ratios (<6). Relatively sodic samples have approximately constant K_2O/Na_2O, Na_2O/TiO_2, Al_2O_3/TiO_2, and Al_2O_3/Na_2O ratios whereas; relatively potassic samples have nearly constant in Al_2O_3/K_2O, Na_2O/TiO_2, Al_2O_3/TiO_2, and Na_2O/P_2O_5 ratios.

3.2.2. Trace elements

Various trace elements were also plotted against Mg# values (Figure 3.38). Most of the relatively potassic samples have higher abundances of some incompatible trace elements (barium, rubidium, thorium, and strontium) compared to most of the relatively sodic samples. Most of the relatively potassic samples have higher abundances of chromium and nickel comparative to most of relatively sodic samples (Figure 3.39).Various trace elements normalized to CI Chondrite values from Anders & Grevesse (1989)

were also plotted (Figures 3.40). Average relatively potassic and relatively sodic samples have similar trace element patterns. The average potassic sample is higher in normalized values compared to that of the average relatively sodic sample except for yttrium (Figure 3.41).

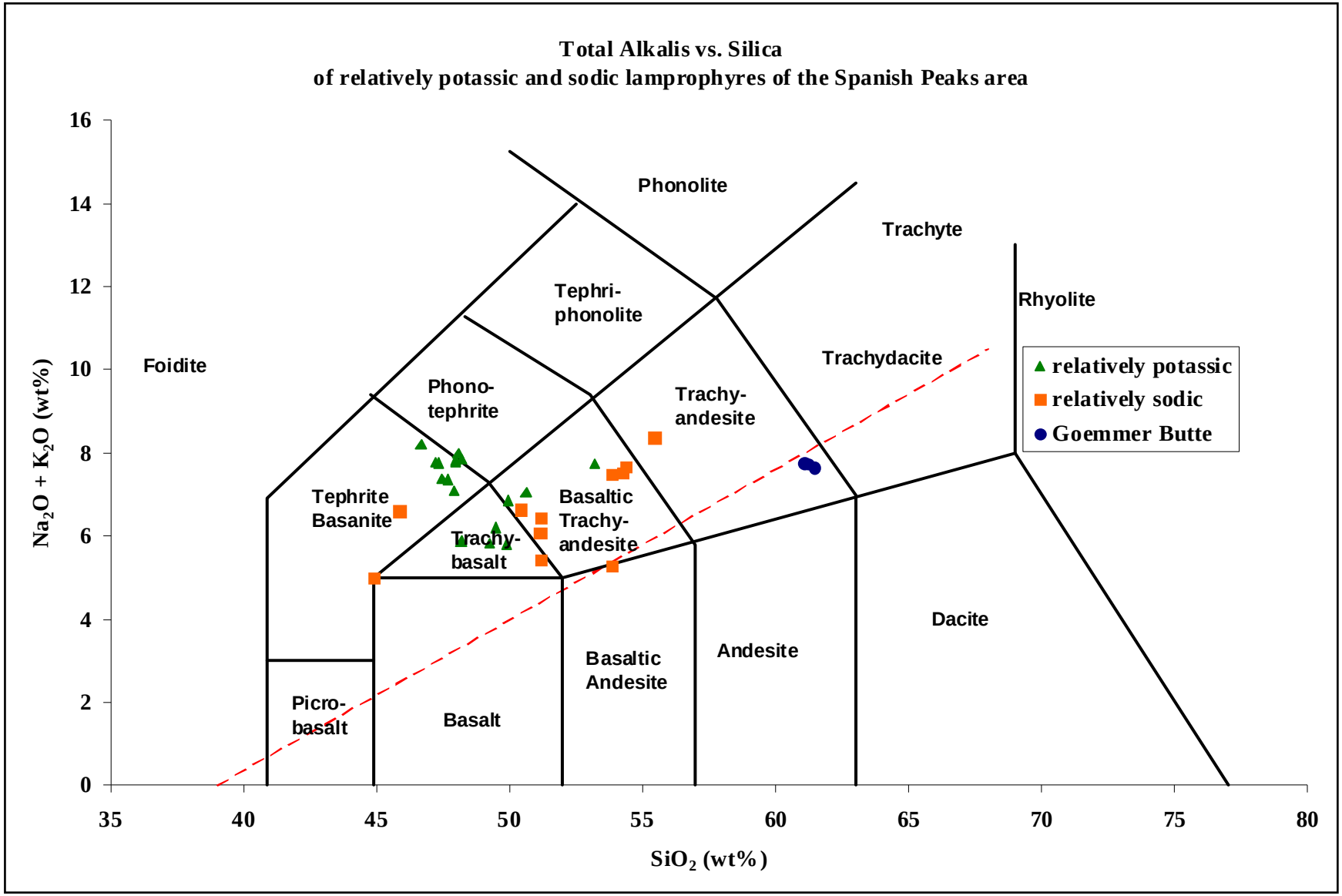

Figure 3.35 IUGS classification diagram after LeBas et al, (1986) with normalized anhydrous XRF analyses of relatively potassic and relatively sodic dikes and sills from the Spanish Peaks area. Above the redline is the alkaline field; below the red line is sub-alkaline field.

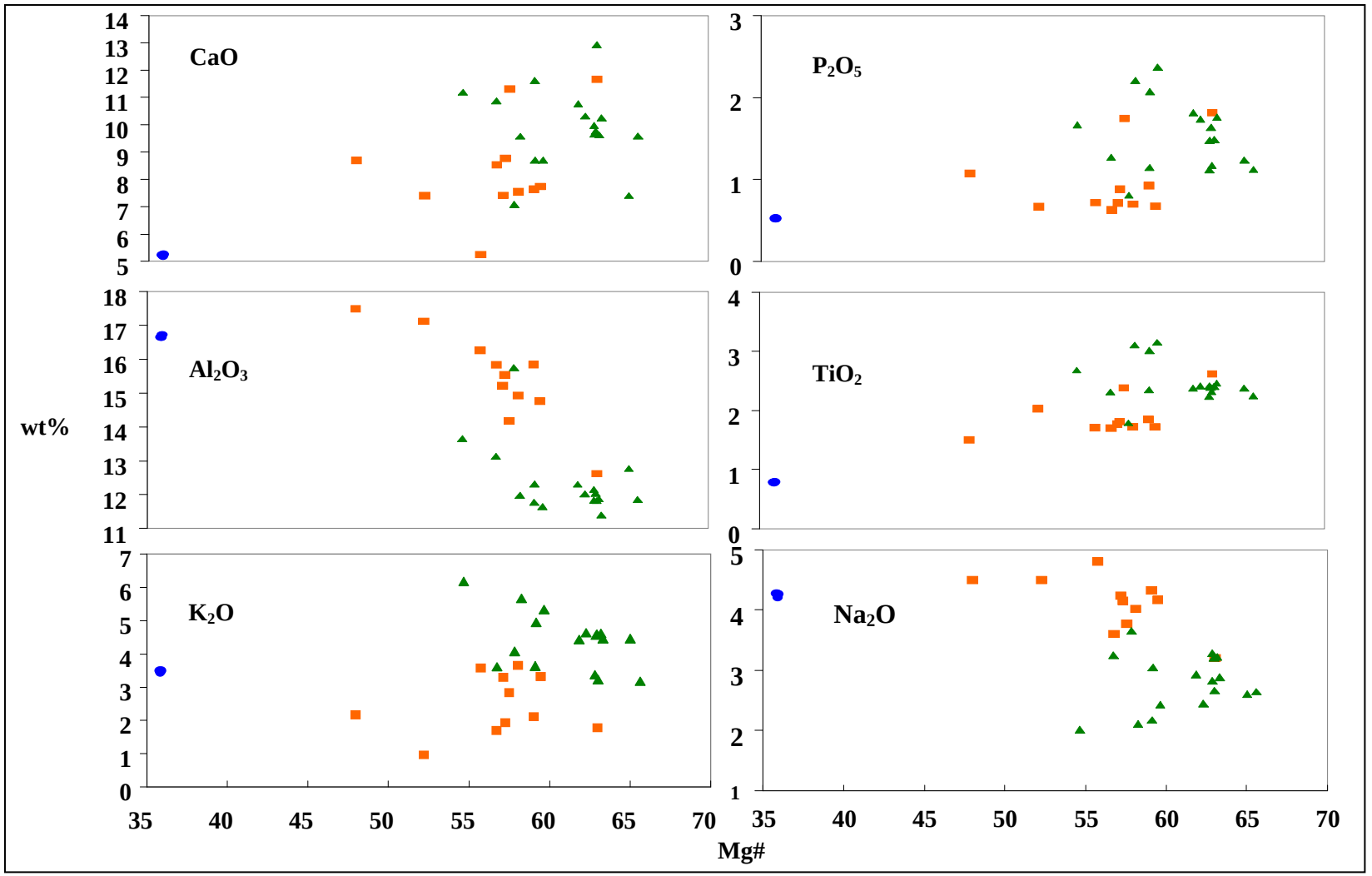

Figure 3.36 Major oxide variation diagrams showing relationships between relatively potassic and relatively sodic lamprophyres of the Spanish Peaks area. Green triangles = relatively potassic samples, orange squares = relatively sodic samples, blue circles = Goemmer Butte trachyandesite sample. Mg# = 100Mg/ (Mg + Fe^{2+}).

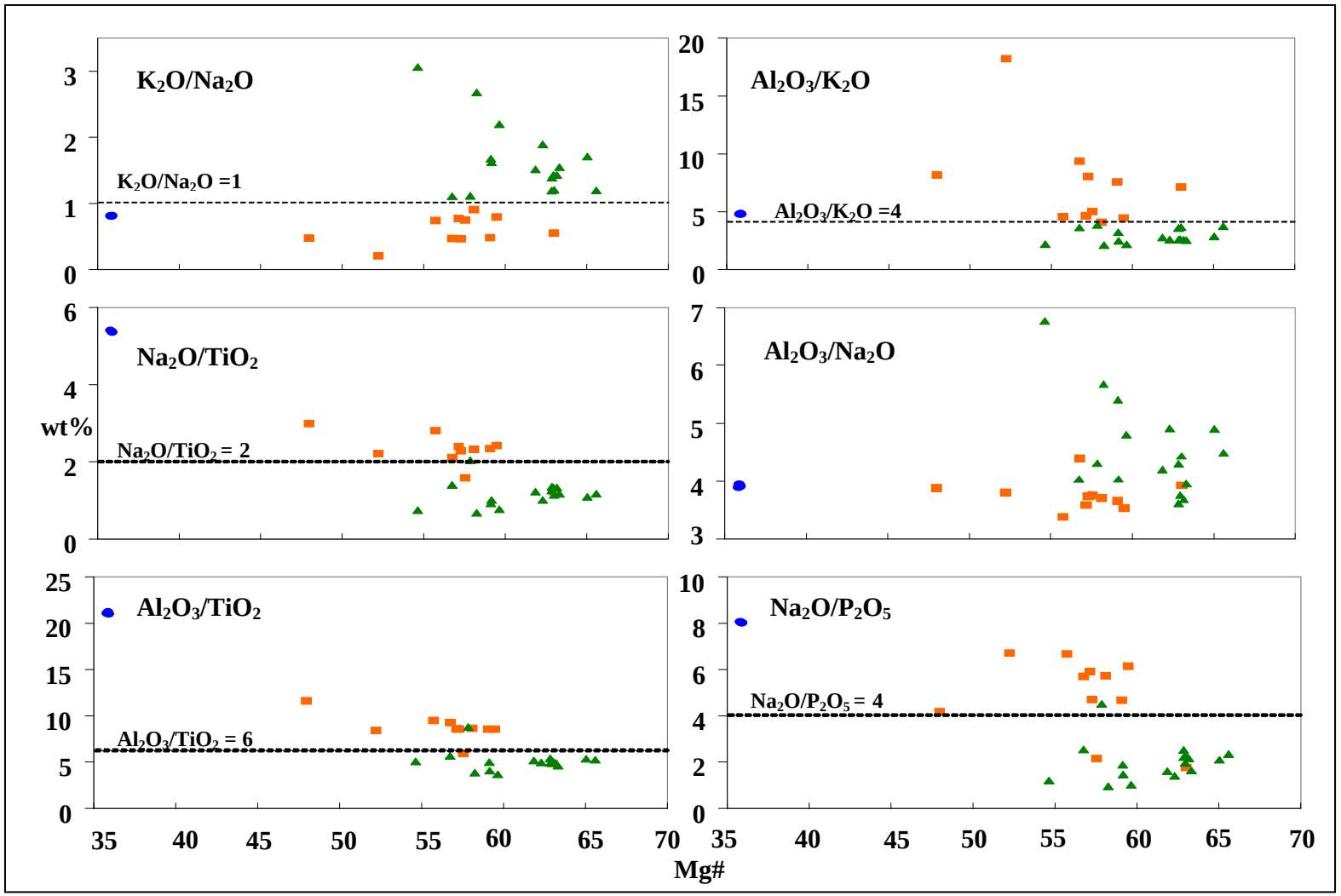

Figure 3.37 Major oxide ratios of relatively potassic and relatively sodic samples from Spanish Peaks area. Dashed lines are for reference. Green triangles = relatively potassic samples, orange squares = relatively sodic samples, blue circles = Goemmer Butte trachyandesite sample. Mg# = 100Mg/ (Mg + Fe^{2+}).

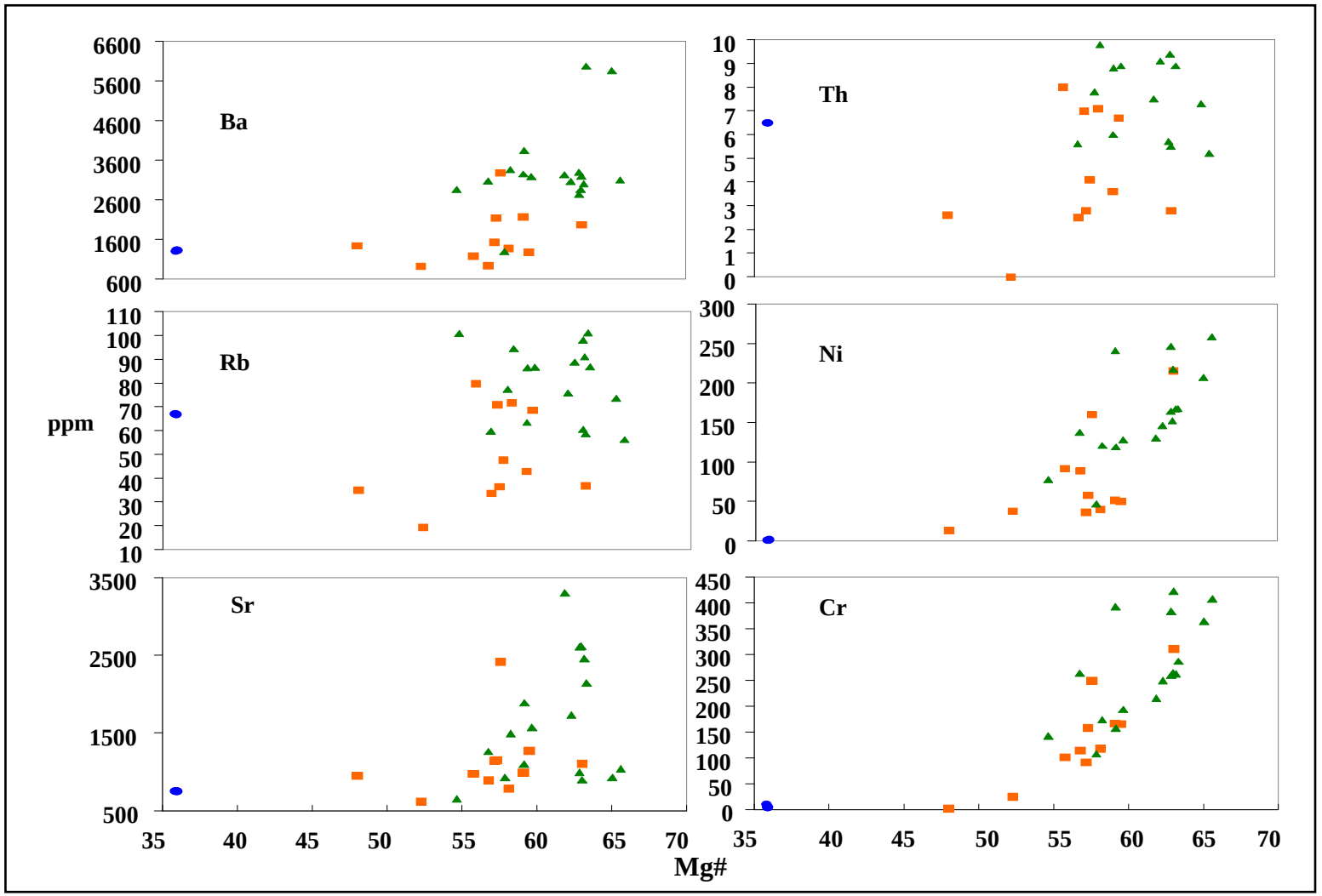

Figure 3.38 Trace element variation diagrams showing relationships between relatively potassic and relatively sodic lamprophyres of the Spanish Peaks area. Green triangles = relatively potassic samples, orange squares =relatively sodic samples, blue circles = Goemmer Butte trachyandesite sample. Mg# = 100Mg/ (Mg + Fe^{2+}).

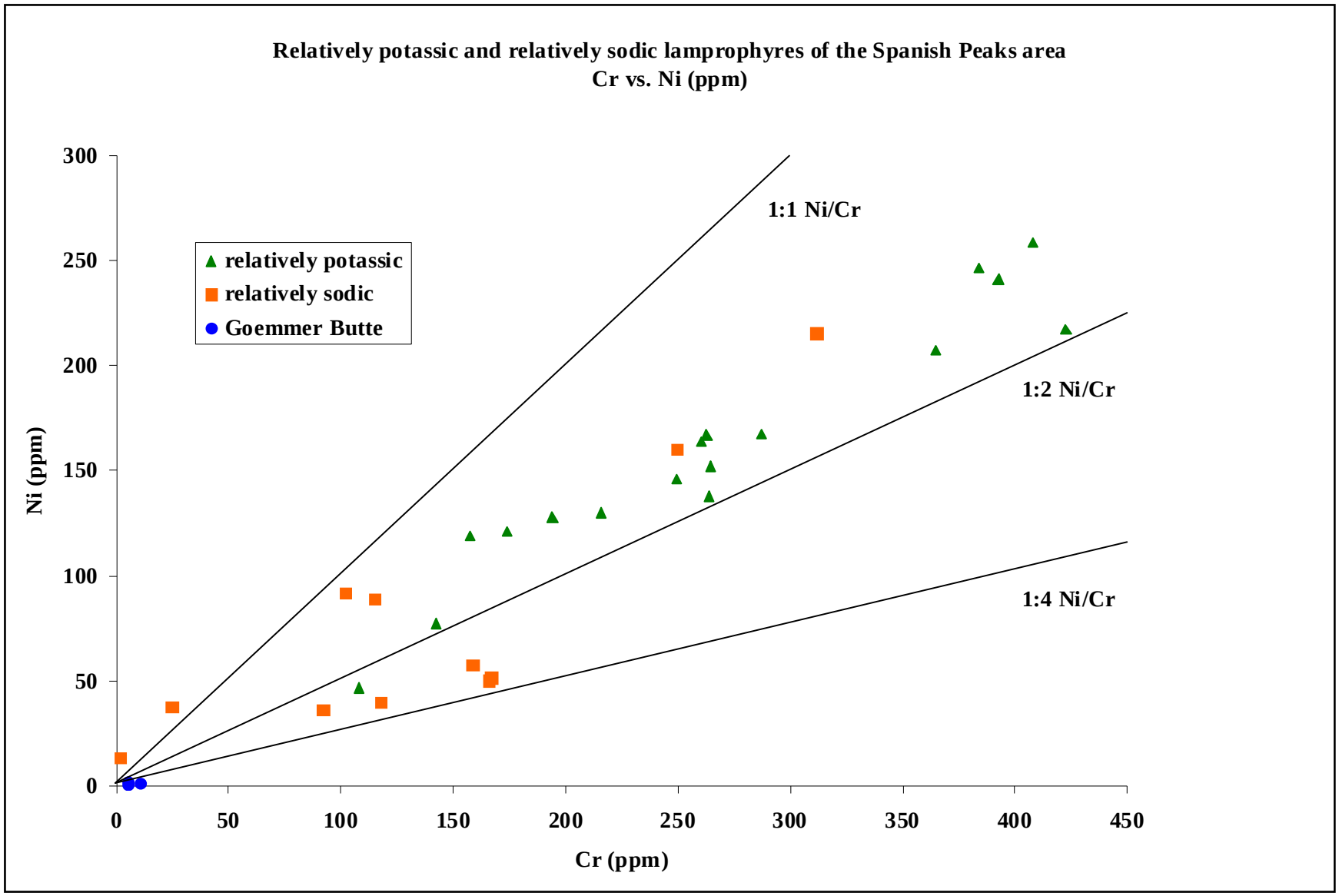

Figure 3.39 Compatible trace elements (chromium and nickel) of relatively potassic and relatively sodic lamprophyres of the Spanish Peaks area.

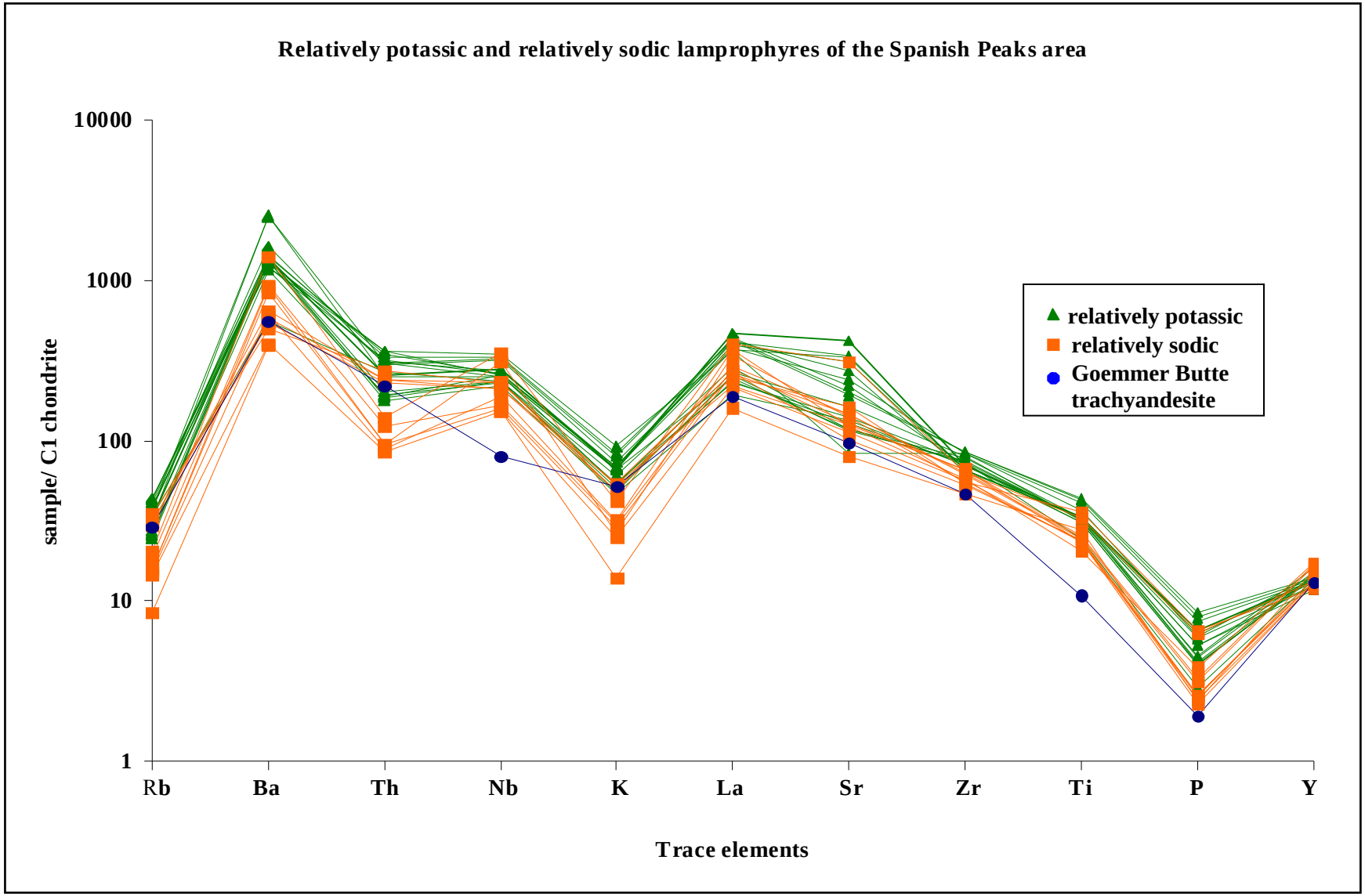

Figure 3.40 Chondrite-normalized trace element abundance diagram modeled after McDonough & Sun, (1995).

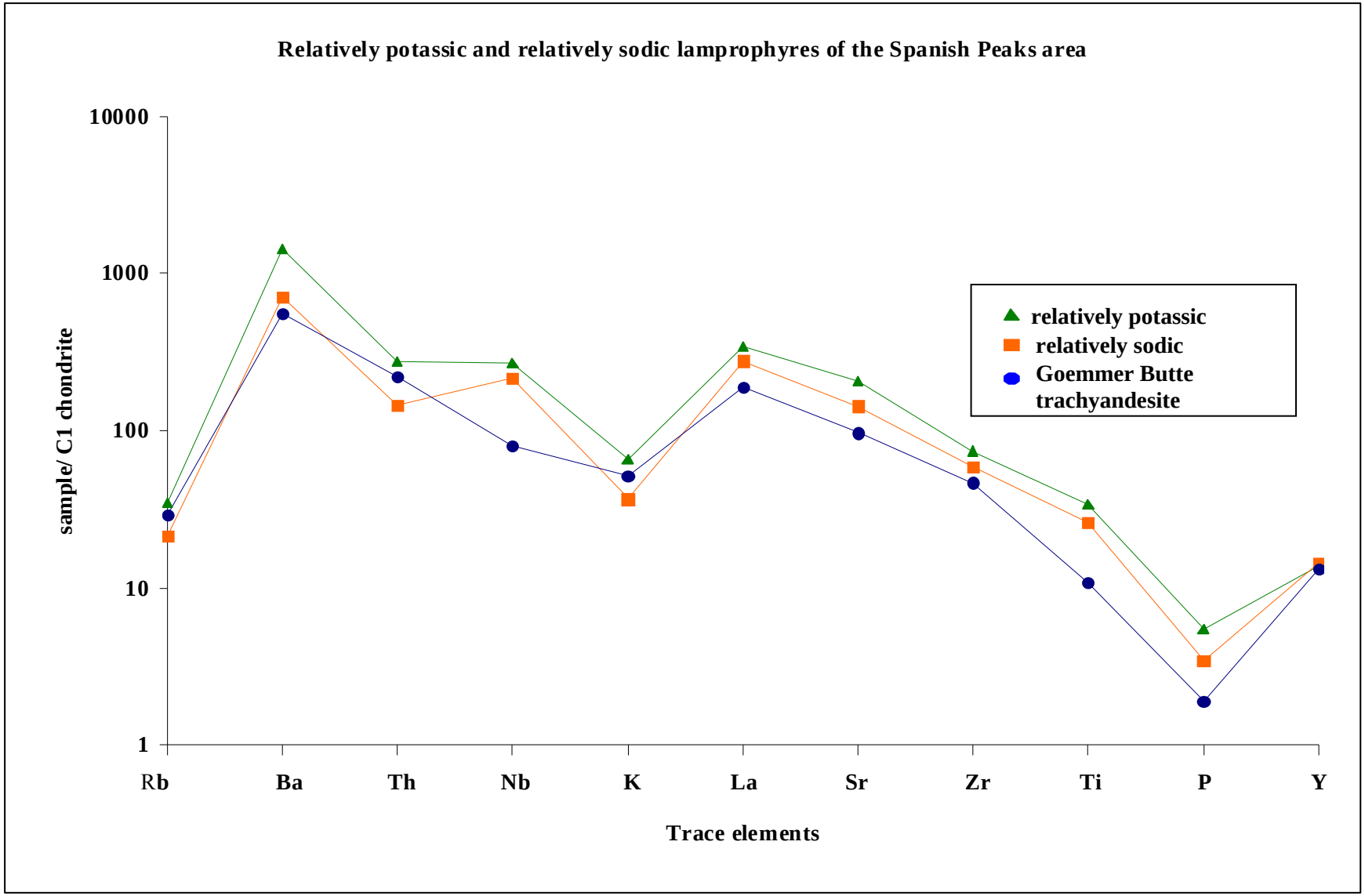

Figure 3.41 Chondrite-normalized spider diagram, McDonough & Sun, (1995) displaying averaged relatively potassic and relatively sodic lamprophyres.

3.3. *ELECTRON MICROPROBE ANALYSIS RESULTS*

Electron microprobe analyses were performed on minerals in both relatively potassic and relatively sodic samples of the Spanish Peaks area to determine specific mineralogy, compositional zoning, and possible petrogenetic relationships between the two types of rocks. Focus was on the Fe-Mg silicates (pyroxenes, amphiboles, and biotite) present in both types of samples. Some additional exploratory work was done to determine mineralogy of some of the ocelli and amygdule structures found in the samples.

3.3.1. Pyroxene analyses results

Table 3.4 is a representative record of over 200 point analyses on pyroxenes from both relatively potassic and relatively sodic samples. Analyzed pyroxenes plot in the diopside or augite field of the pyroxene quadrilateral (Morimoto, 1989). The pyroxenes from the relatively potassic samples are more magnesium-rich than the pyroxenes of the relatively sodic samples (Figure 3.42).

Two-point analyses (one from the center of grain and one close to the edge of the grain) were performed on pyroxenes from both types of rocks in this study. Results show that some of the pyroxenes have higher Mg# values at the edge of the grain comparative to the center of the grains. This was seen in some pyroxenes from relatively sodic samples (the dike near Goemmer Butte trachyandesite and the dike at north end of the North Lake sill complex) and from one relatively potassic sample (large sill at the south end of the North Lake sill complex). Center to rim compositional mapping for pyroxenes of both relatively sodic and relatively potassic samples, show distinct oscillations in Mg#, titanium, and aluminum (Figure 3.43-3.45). Oscillatory zoning in the pyroxenes can be seen readily in the cross-polarized photomicrograph in Figure 3.25 and back-scattered electron images seen in Figure 3.46.

Table 3.4 electron microprobe analyses of representative pyroxenes

Location	Walsenburg dike								
	Cr504		Hwy 85		Cr590		Lathrop Park		
Label oxide wt%	cc6 hm2	cc8 hm2	cc5 hm5	ce5 hm5	ce3 hm14	ce4 hm14	cc1a hm4	cc6 hm4	MDL oxide wt%**
SiO_2	51.63	52.11	50.72	53.49	53.51	53.39	52.23	51.88	0.03
TiO_2	0.94	0.57	0.30	0.58	0.64	0.63	1.19	1.10	0.04
Al_2O_3	1.74	2.60	3.23	1.26	1.13	1.23	1.49	1.84	0.03
MgO	16.86	16.58	10.93	16.90	17.13	16.98	16.20	16.17	0.04
FeO***	4.61	4.56	11.32	4.76	3.50	3.98	3.65	3.41	0.16
Fe_2O_3***	1.97	0.88	1.21	0.58	1.32	1.28	1.83	1.84	
CaO	21.01	20.12	21.55	22.13	22.98	22.56	23.48	23.30	0.03
MnO	0.11	0.18	0.46	0.10	0.10	0.05	0.20	0.05	0.14
K_2O	n.d.*	n.d.*	n.d.*	n.d.*	n.d.*	n.d.*	n.d.*	n.d.*	0.03
Na_2O	0.38	0.68	0.56	0.30	0.34	0.39	0.33	0.37	0.06
Cr_2O_3	0.18	0.74	n.d.*	n.d.*	n.d.*	0.23	n.d.*	0.18	0.15
Total	99.44	99.03	100.28	100.10	100.66	100.71	100.61	100.14	
			cations normalized to 6 oxygen						
Si	1.910	1.925	1.917	1.957	1.946	1.943	1.913	1.906	
Ti	0.026	0.016	0.009	0.016	0.018	0.017	0.033	0.030	
Al^{IV}***	0.076	0.071	0.077	0.040	0.048	0.051	0.064	0.080	
Al^{VI}***	0.000	0.042	0.067	0.014	0.001	0.002	0.000	0.000	
Mg	0.930	0.913	0.616	0.922	0.929	0.921	0.885	0.886	
Fe^{2+}***	0.143	0.141	0.358	0.146	0.107	0.121	0.112	0.105	
Fe^{3+}***	0.055	0.024	0.034	0.016	0.036	0.035	0.050	0.051	
Ca	0.833	0.796	0.873	0.867	0.895	0.880	0.921	0.917	
Mn	0.003	0.006	0.015	0.003	0.003	0.001	0.006	0.001	
K	n.d.*	n.d.*	n.d.*	n.d.*	n.d.*	n.d.*	n.d.*	n.d.*	
Na	0.027	0.049	0.041	0.022	0.024	0.027	0.023	0.027	
Cr	0.005	0.022	n.d.*	n.d.*	n.d.*	0.007	n.d.*	0.005	
Total	4.009	4.004	4.006	4.003	4.006	4.006	4.008	4.008	
Mg#	87	87	63	86	90	88	89	89	
Wo	0.42	0.42	0.46	0.44	0.46	0.45	0.47	0.47	
En	0.47	0.49	0.33	0.47	0.47	0.47	0.45	0.45	
Fs	0.10	0.09	0.21	0.08	0.07	0.08	0.08	0.08	
sum	1.00	1.00	1.00	1.00	1.00	1.00	1.00	1.00	

*not detected, **minimum detection limit, ***iron and aluminum totals recalculated, cc; center, ce; edge Mg# = 100Mg / (Mg + Fe^{2+})

Table 3.4 electron microprobe analyses of representative pyroxenes continued

Location	North Lake sill complex								
	Minette	Camptonite	Large sill near south end						
Label									MDL
oxide wt%	ce5 hm25	ce1 hm26	ce6 hm22	ce7 hm22	cc1a hm19	ce5 hm19	cc2 hm24	cc5 hm24	oxide wt%**
SiO_2	51.28	50.45	51.97	51.13	52.64	52.58	51.93	52.14	0.03
TiO_2	1.34	1.47	0.85	1.15	0.54	0.98	1.02	0.76	0.04
Al_2O_3	2.79	3.88	1.90	2.47	1.30	1.62	1.73	2.69	0.03
MgO	15.71	14.72	16.04	16.04	15.40	16.68	16.54	16.25	0.04
FeO***	3.99	4.52	5.02	3.68	7.05	4.69	5.19	3.82	0.16
Fe_2O_3***	1.88	1.80	1.56	1.65	1.61	1.39	1.21	1.30	
CaO	23.27	23.23	21.62	22.30	20.49	21.87	21.22	22.79	0.03
MnO	n.d.*	0.15	n.d.*	n.d.*	0.47	0.15	0.17	n.d.*	0.14
K_2O	n.d.*	n.d.*	n.d.*	n.d.*	n.d.*	n.d.*	n.d.*	n.d.*	0.03
Na_2O	0.34	0.38	0.48	0.43	0.63	0.39	0.33	0.35	0.06
Cr_2O_3	n.d.*	n.d.*	n.d.*	0.58	n.d.*	0.25	0.21	n.d.*	0.15
Total	100.60	100.61	99.50	99.50	100.13	100.59	99.54	100.12	
	cations normalized to 6 oxygens								
Si	1.707	1.679	1.730	1.702	1.752	1.750	1.729	1.736	
Ti	0.033	0.037	0.021	0.029	0.014	0.024	0.025	0.019	
Al^{IV}***	0.111	0.136	0.069	0.102	0.043	0.070	0.074	0.085	
Al^{VI}***	0.009	0.032	0.013	0.006	0.014	0.000	0.001	0.032	
Mg	0.859	0.807	0.885	0.884	0.850	0.909	0.912	0.887	
Fe^{2+}***	0.122	0.139	0.155	0.114	0.218	0.143	0.161	0.117	
Fe^{3+}***	0.052	0.050	0.043	0.046	0.045	0.038	0.034	0.036	
Ca	0.914	0.915	0.857	0.883	0.813	0.857	0.841	0.894	
Mn	n.d.*	0.005	n.d.*	n.d.*	0.015	0.005	0.005	n.d.*	
K	n.d.*	n.d.*	n.d.*	n.d.*	n.d.*	n.d.*	n.d.*	n.d.*	
Na	0.024	0.027	0.034	0.031	0.045	0.027	0.024	0.025	
Cr	n.d.*	n.d.*	n.d.*	0.017	n.d.*	0.007	0.006	n.d.*	
Total	4.009	4.008	4.007	4.008	4.007	4.006	4.006	4.006	
Mg#	88	85	85	89	80	86	85	88	
Wo	0.469	0.479	0.442	0.458	0.422	0.440	0.432	0.462	
En	0.441	0.422	0.456	0.459	0.441	0.467	0.468	0.459	
Fs	0.089	0.099	0.102	0.083	0.137	0.093	0.100	0.079	
sum	1.00	1.00	1.00	1.00	1.00	1.00	1.00	1.00	

*not detected, **minimum detection limit, ***iron and aluminum totals recalculated, cc; center, ce; edge Mg# = 100Mg / ($Mg + Fe^{2+}$)

Table 3.4 electron microprobe analyses of representative pyroxenes continued

Location	Cr440	dike by Goemmer Butte trachy-andesite		North Lake sill complex dike at north end		dike near Coal Creek		
Label oxide wt%	cc1d hm21	cc5 hm30	ce5a hm30	cc2 hm8	ce2 hm8	cc1 hm28	ce5 hm28	MDL oxide wt%**
SiO_2	50.97	51.67	53.77	52.65	52.12	52.78	52.38	0.03
TiO_2	1.07	0.73	0.40	0.22	0.70	0.98	0.49	0.04
Al_2O_3	2.92	3.13	0.80	0.97	2.66	1.91	1.54	0.03
MgO	15.29	15.41	15.19	13.34	16.62	16.43	15.37	0.04
FeO***	6.22	5.53	5.75	8.40	3.46	5.42	6.68	0.16
Fe_2O_3***	1.92	1.42	1.35	1.28	0.92	0.86	1.14	
CaO	21.56	22.06	21.45	21.53	22.18	21.81	20.57	0.03
MnO	n.d.*	0.20	0.93	0.92	n.d.*	0.16	0.37	0.14
K_2O	n.d.*	n.d.*	0.04	n.d.*	n.d.*	n.d.*	n.d.*	0.03
Na_2O	0.33	0.35	0.86	0.66	0.40	0.34	0.60	0.06
Cr_2O_3	n.d.*	n.d.*	n.d.*	n.d.*	0.72	0.18	n.d.*	0.15
Total	100.41	100.49	100.53	99.97	99.78	100.87	99.14	
			cations normalized to 6 oxygens					
Si	1.697	1.898	1.977	1.972	1.910	1.926	1.953	
Ti	0.027	0.020	0.011	0.006	0.019	0.027	0.014	
Al^{IV}***	0.108	0.095	0.016	0.022	0.086	0.070	0.042	
Al^{VI}***	0.019	0.040	0.018	0.021	0.029	0.012	0.026	
Mg	0.842	0.844	0.833	0.745	0.908	0.894	0.854	
Fe^{2+}***	0.192	0.170	0.177	0.263	0.106	0.165	0.208	
Fe^{3+}***	0.053	0.039	0.037	0.036	0.025	0.024	0.032	
Ca	0.853	0.868	0.845	0.864	0.871	0.852	0.822	
Mn	n.d.*	0.006	0.029	0.029	n.d.*	0.005	0.012	
K	n.d.*	n.d.*	0.002	n.d.*	n.d.*	0.000	0.000	
Na	0.024	0.025	0.061	0.048	0.029	0.024	0.043	
Cr	n.d.*	n.d.*	n.d.*	n.d.*	0.021	0.005	0.000	
Total	4.009	4.007	4.007	4.006	4.004	4.004	4.005	
Mg#	81	83	82	74	90	84	80	
Wo	0.440	0.45	0.45	0.45	0.46	0.44	0.43	
En	0.434	0.44	0.44	0.39	0.48	0.46	0.45	
Fs	0.127	0.11	0.11	0.16	0.07	0.10	0.13	
sum	1.00	1.00	1.00	1.00	1.00	1.00	1.00	

*not detected, **minimum detection limit, ***iron and aluminum totals recalculated, cc; center, ce; edge Mg# = 100Mg / (Mg + Fe^{2+})

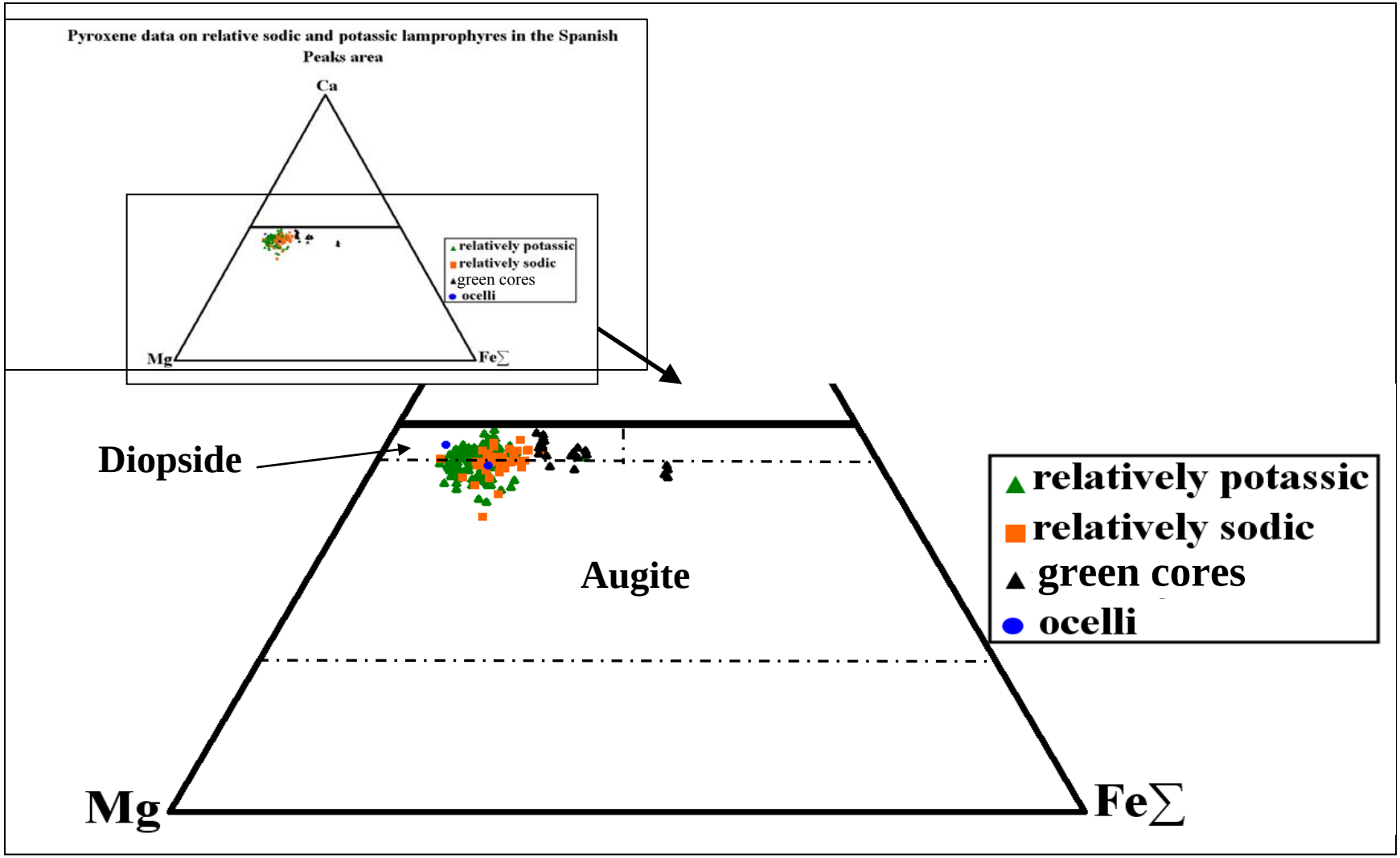

Figure 3.42 Pyroxene analyses obtained for samples in the Spanish Peaks area are plotted in the pyroxene quadrilateral (modified after Morimoto, 1989) displaying relative atomic proportions of total iron, magnesium, and calcium in pyroxene structure. Orange squares represent pyroxenes from relatively sodic samples, green triangles represent pyroxenes from relatively potassic samples, black triangles represent green cores found in pyroxenes from Walsenburg dike, and blue circles represent pyroxenes from ocelli in the Walsenburg dike. Ternary Mg and Fe∑ represent enstatite and ferrosilite respectively.

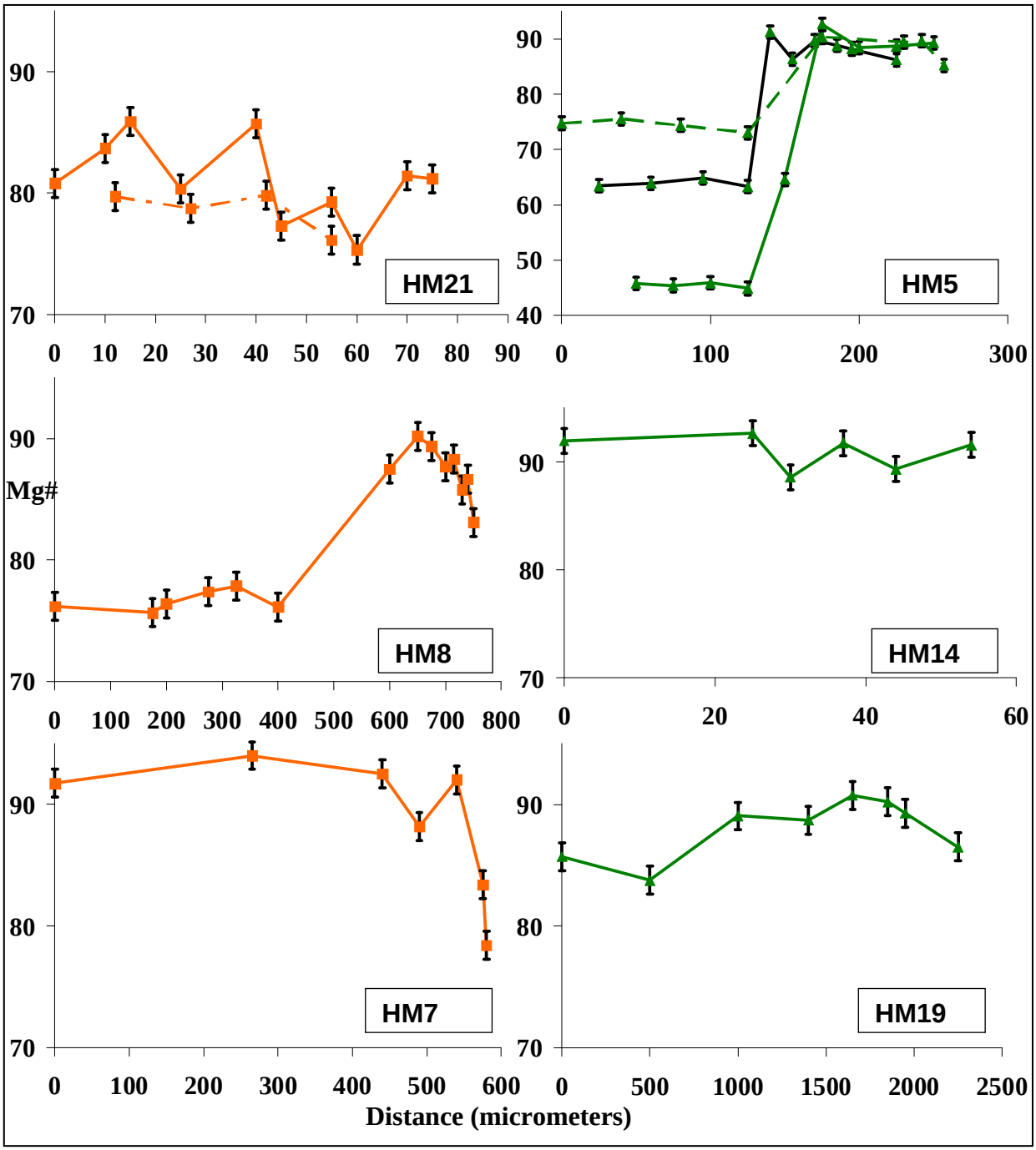

Figure 3.43 Center of grain (left) to rim (right) mapping of Mg# in clinopyroxenes from the Spanish Peaks area. Green triangles represent pyroxenes from relatively potassic rocks and orange squares represent pyroxenes from relatively sodic rocks. Error bars represent 2σ, X-axis represents distance from center to rim in micrometers, and Y-axis represents Mg# 100 (Mg/ (Mg + Fe^{2+}).

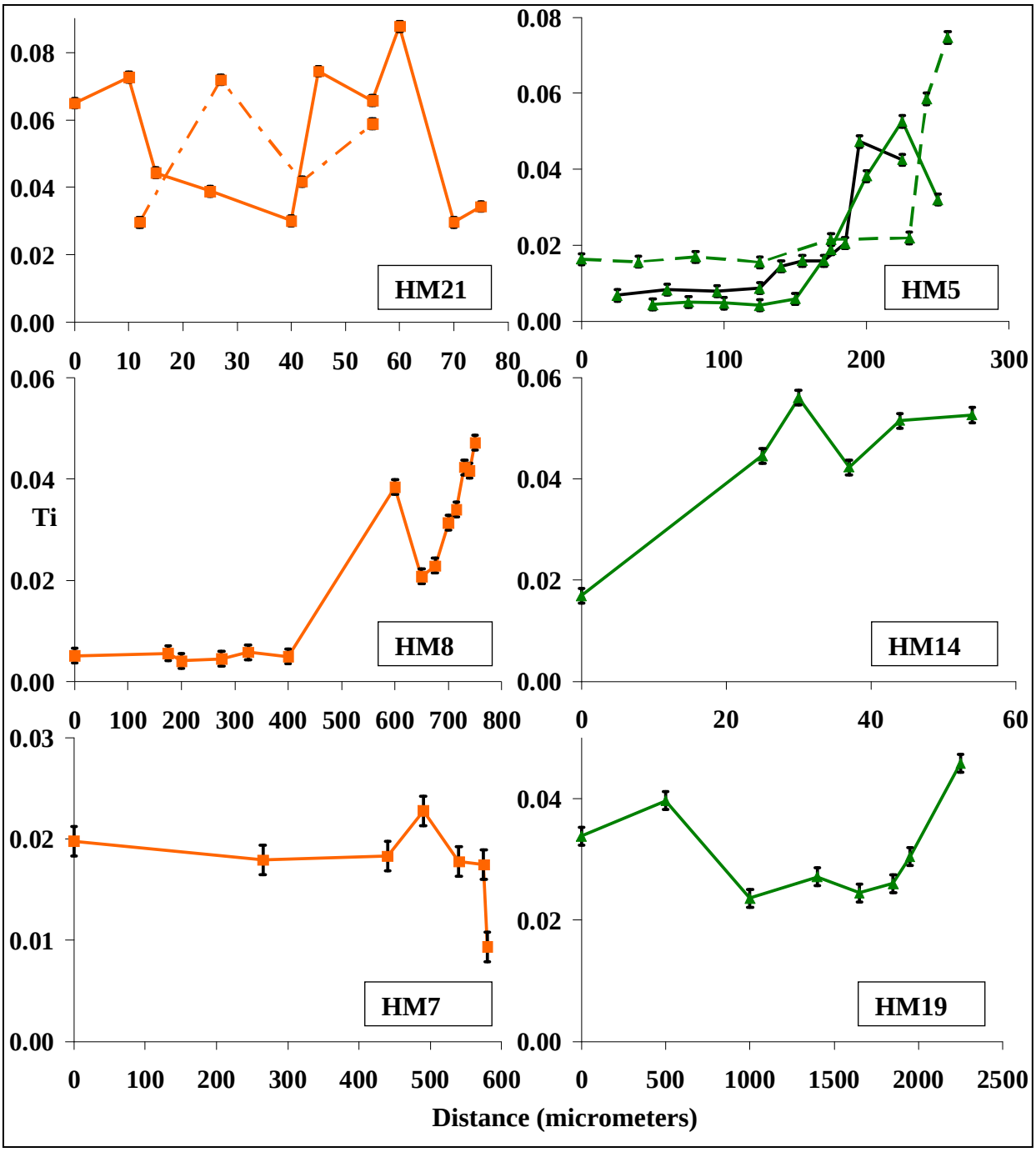

Figure 3.44. Center of the grain (left) to rim (right) mapping of titanium in clinopyroxenes from the Spanish Peaks area. Green triangles represent pyroxenes from relatively potassic rocks and orange squares represent pyroxenes from relatively sodic rocks. Error bars represent 2σ, X-axis represents distance from center to rim in micrometers, and Y-axis represents atomic proportions of titanium in pyroxene structure.

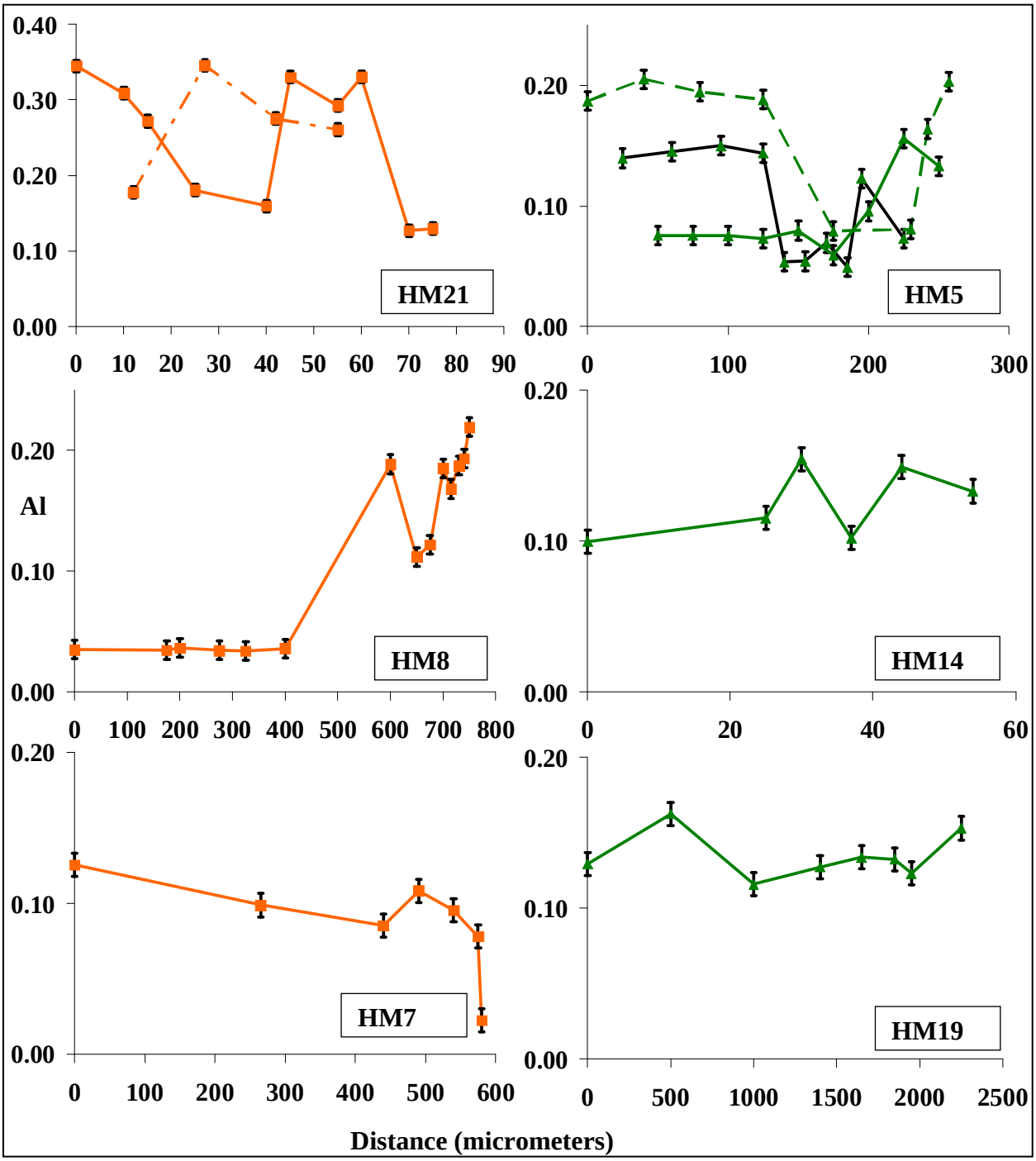

Figure 3.45 Center of grain (left) to rim (right) mapping of aluminum in clinopyroxenes from the Spanish Peaks area. Green triangles represent pyroxenes from relatively potassic rocks and orange squares represent pyroxenes from relatively sodic rocks. Error bars represent 2σ, X-axis represents distance in micrometers, and Y-axis represents atomic proportions of aluminum in pyroxene structure.

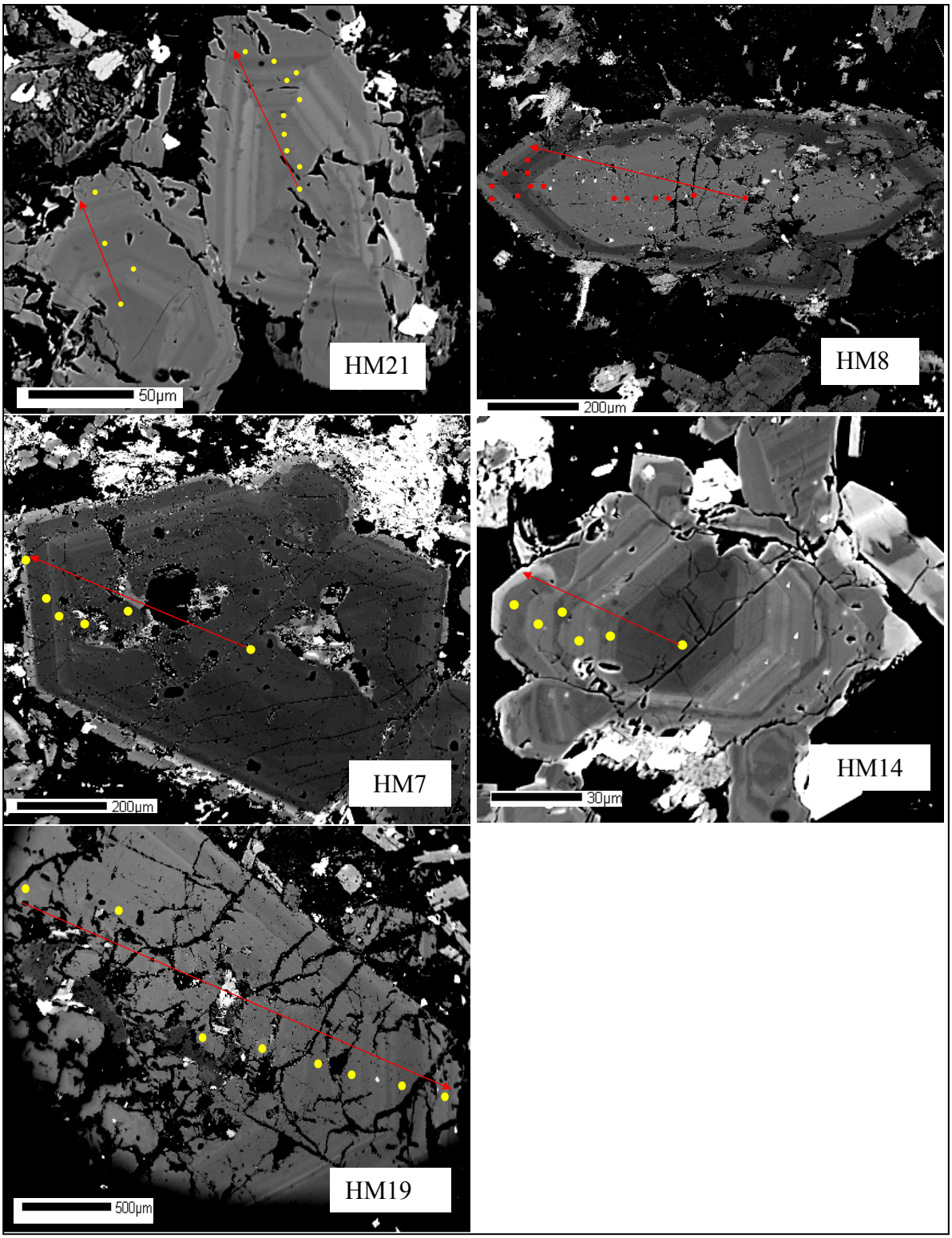

Figure 3.46 Multiple back-scattered electron images of concentric and oscillatory zoning of clinopyroxenes from the Spanish Peaks samples. Contrast and brightness adjusted to enhance changes in composition. Yellow circles indicate where point analyses were taken and correspond to core to rim mapping in Figures 3.43-3.45. Red arrow indicates beginning and direction of run.

Four analyzed pyroxenes from the Walsenburg dike have distinct green cores relative to the whole grain (Figure 3.12). As shown in Figure 3.43, an abrupt increase in Mg# occurs in analyses from green-cored pyroxenes as one leaves the core (relative to other non-green-cored pyroxenes). This abrupt compositional change can also be seen in back-scattered electron imagery (Figure 3.47).

Some of the pyroxenes observed in the ocelli from the Walsenburg dike exhibit a dark-green color in plane-polarized light (Figure 3.48). These are different from the clear to pale yellow pyroxenes and green-cored pyroxenes observed as phenocrysts (Figure 3.4 and Figure 3.12). Electron microprobe analysis reveals that the dark-green portions of the pyroxenes in the ocelli are higher in ferric iron and sodium relative to the clear to pale yellow part of the pyroxenes (found in and outside the ocelli). These compositional differences can also be seen in back-scattered electron imagery (Figure 3.49). The dark-green portion of the pyroxenes from the ocelli plot outside the pyroxene quadrilateral in Figure 3.42., therefore a sodium-pyroxene quadrilateral was used to plot these points (Figure 3.50). One pyroxene analysis plots in the aegirine-augite field and one plots in the aegirine field following Morimoto (1989).

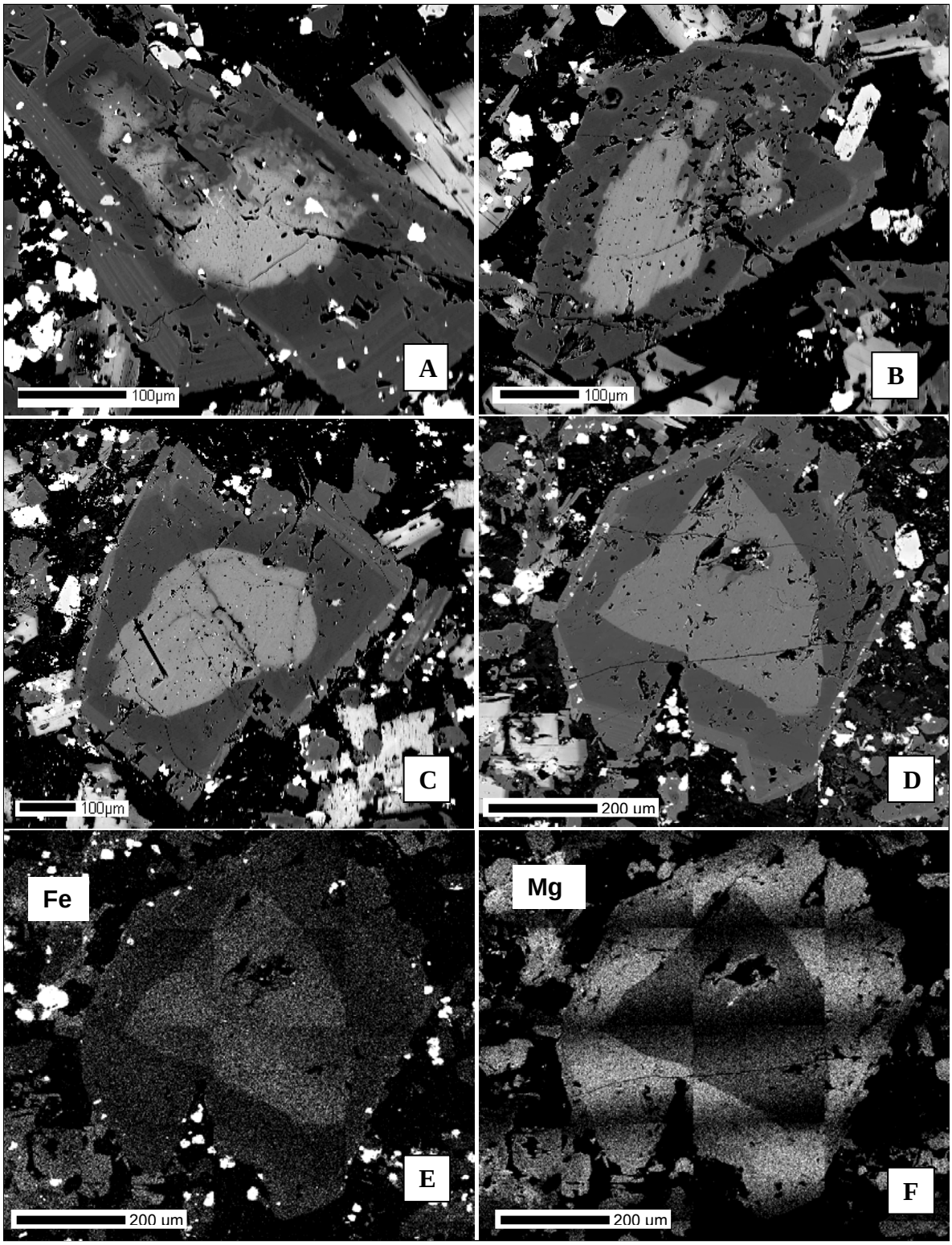

Figure 3.47 Multiple back-scattered electron images of xenocryst-cored pyroxenes from the Walsenburg dike samples HM5. Note embayment of cores in panel A and B. Panel E and F are single element scans of pyroxene from panel D (relatively light areas denote higher concentration of scanned element). Contrast and brightness adjusted to enhance image.

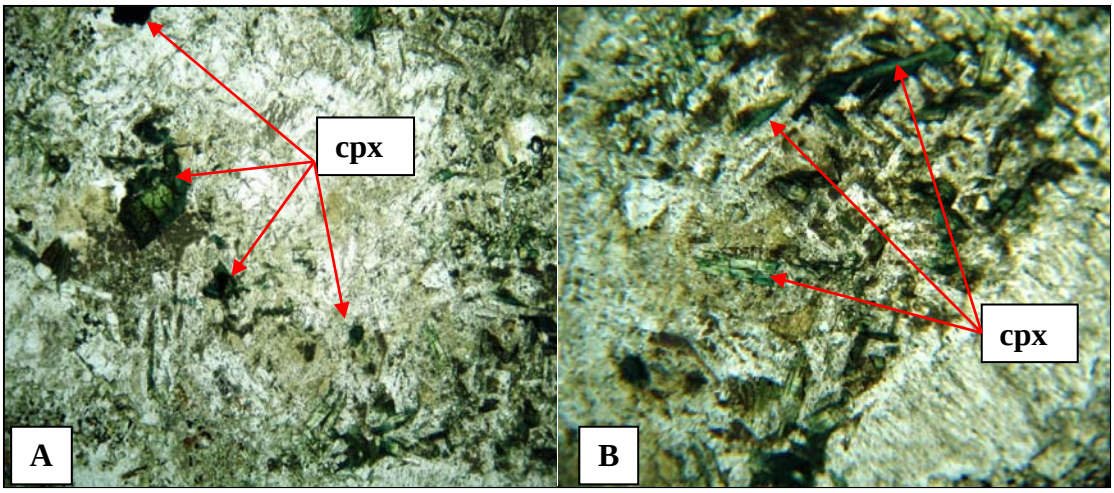

Figure 3.48 Multiple views displaying dark-green clinopyroxenes in ocellus. A; (~4.5mm across) ocellus, B; (~2mm across) ocellus. Red arrows are pointing to dark-green pyroxenes.

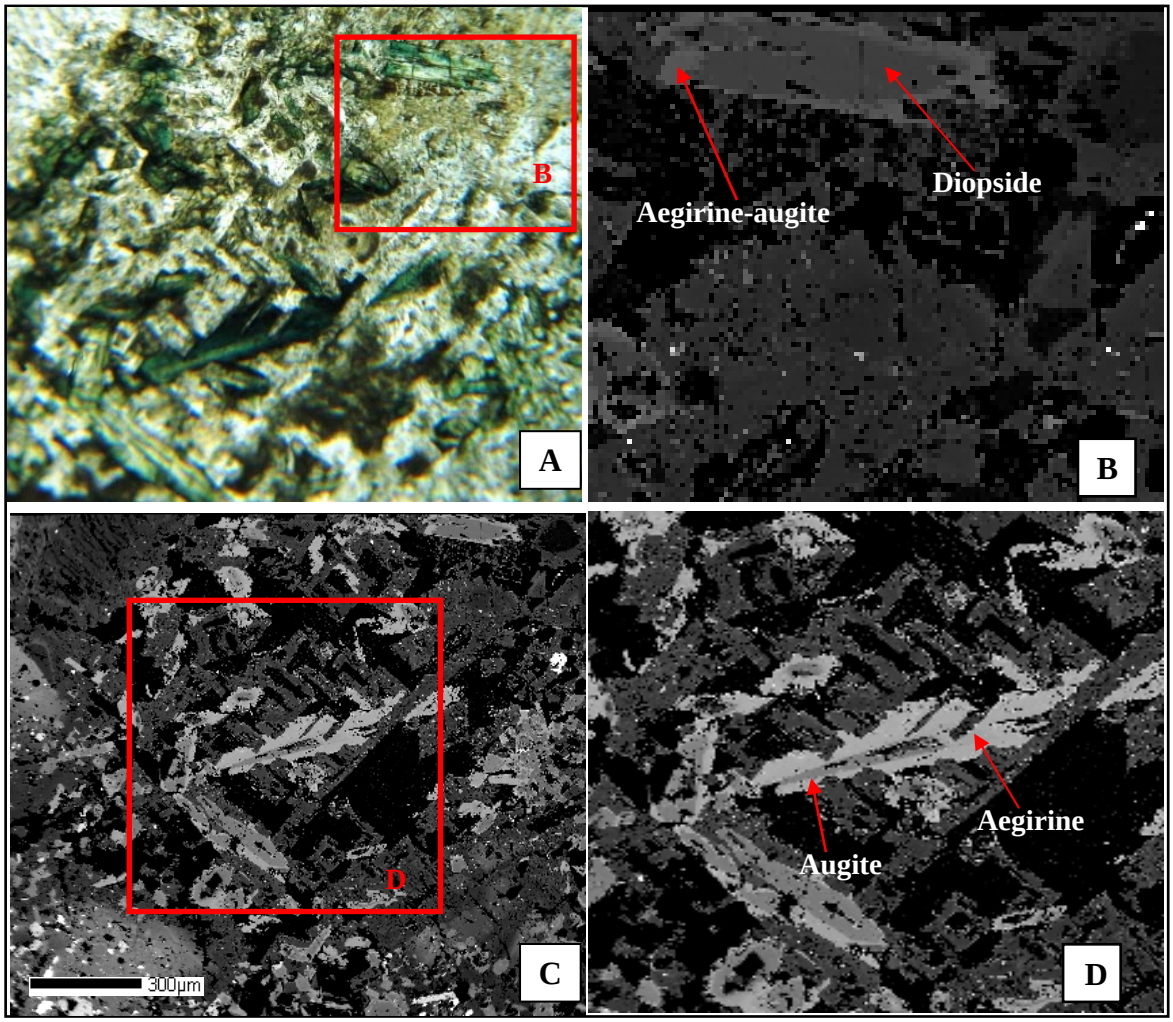

Figure 3.49 Panel A; plane polarized view (~1.6mm across) of ocellus structure with compositionally zoned pyroxene, panel B; close-up of inset B, panel C; back-scattered electron image of panel A, panel D; close-up of inset D.

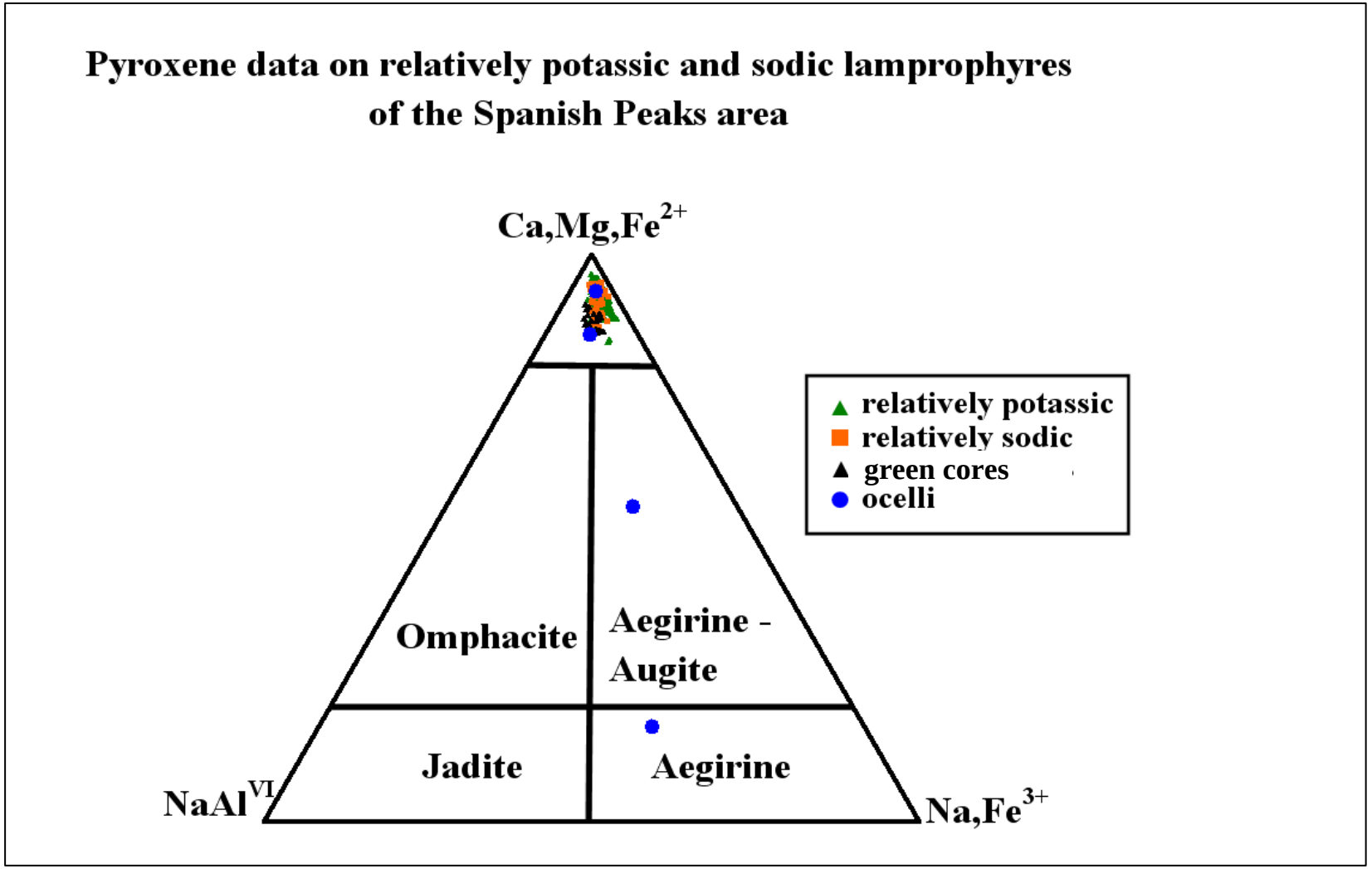

Figure 3.50 Pyroxene analyses obtained with electron microprobe from samples in the Spanish Peaks area. The top 20% portion of the sodium pyroxene quadrilateral is the Ca, Mg, Fe^{2+} pyroxene quadrilateral (modified after Morimoto, 1989). Orange squares represent pyroxenes from relatively sodic samples, green triangles represent pyroxenes from relatively potassic samples, black triangles represent green cores found in pyroxenes from Walsenburg dike, and blue circles represent pyroxenes from ocelli in the Walsenburg dike Ternary $NaAl^{VI}$, $NaFe^{3+}$, $CaMgFe^{2+}$ represent jadite , aegirine, and pyroxene quadrilateral

3.3.2. Amphibole analyses results

Over fifty point analyses were performed on amphiboles from relatively potassic, relatively sodic, and Goemmer Butte trachyandesite samples. Representative results are listed in Table 3.5. Most of the amphiboles analyzed from both relatively potassic and relatively sodic samples are not compositionally zoned. As noted in the previous section on pyroxenes, Mg# values are higher at the center of some amphibole grains comparative to the edge of the grains. This was seen in the amphiboles from the relatively sodic dike near Goemmer Butte (HM30), the relatively sodic dikes near the north end of the North Lake sill complex, (HM7 and HM8)(Figure 3.30), and one relatively potassic sill near the south end of the North Lake sill complex.

Based on methods developed by Leake (1978), amphiboles from both relatively potassic and relatively sodic samples are classified as calcic-amphiboles (calcium exceeds 67% in the A-site). Most analyses reveal that the amphiboles are relatively silica poor, with atomic proportions of sodium and potassium approaching 25% in the A-site of the amphibole structure. All amphiboles analyzed have enough titanium in their structure to be considered titanian. Figure 3.51 is an x-y plot assigning specific nomenclature within the calcic-amphibole group, including kaersutite. Ten amphibole analyses from the relatively sodic samples HM26, HM25, and HM8 (camptonite, minette and dike at north end of North Lake sill complex) have atomic proportions of titanium in excess of 0.50 in their structure and are considered kaersutite. All of the analyzed amphiboles from the relatively potassic sample HM19 (large sill near south end of North Lake sill complex) are kaersutite as well. The rest of the analyses from the relatively sodic samples, the megacryst from Goemmer Butte, and the amphiboles from the xenolith found in the Goemmer Butte (except for one analysis), plot in the edenite, hastingsite, and pargasite field in diagram 3.51. These analyses are further broken into hastingsite or pargasite based on the amount of silicon plotted against the ferric iron to octahedral aluminum ratio in the amphibole structure (Figure 3.52).

Table 3.5 electron microprobe analyses of representative amphiboles

Location	North Lake sill complex								
	large sill near south end		dike near north end		camptonite		minette		
Label oxide wt%	ac2 hm19	ac1 hm19	ac4 hm8	ae4 hm8	ac1 hm26	ae1 hm26	ac hm25	ae hm25	MDL oxide wt%**
SiO_2	40.87	40.27	39.16	40.13	38.56	38.30	39.98	41.67	0.05
TiO_2	5.73	5.95	5.23	4.54	5.24	4.91	4.21	3.94	0.07
Al_2O_3	13.36	13.36	13.13	12.33	13.40	13.70	13.09	11.81	0.05
MgO	13.55	13.70	12.48	13.74	14.07	13.23	14.31	14.74	0.05
FeO***	9.65	9.49	9.93	7.32	5.97	7.75	8.34	7.40	0.15
Fe_2O_3***	0.54	0.91	1.75	4.27	4.99	3.78	1.83	3.69	
CaO	11.70	11.70	11.56	11.69	11.83	11.83	12.56	11.69	0.04
MnO	n.d*	n.d*	n.d*	0.19	0.20	n.d*	0.32	n.d*	0.17
K_20	1.23	1.21	1.01	0.96	1.30	1.16	0.77	0.85	0.03
Na_2O	2.43	2.70	2.38	2.25	2.12	2.29	2.68	2.87	0.08
Ba	n.d*	n.d*	0.18	n.d*	n.d*	0.18	n.d*	n.d*	0.12
Cl	n.d*	n.d*	n.d*	n.d*	n.d*	n.d*	0.04	n.d*	0.02
	99.05	99.29	96.81	97.43	97.69	97.12	98.10	98.66	
-O=F,Cl	n.d*	n.d*	n.d*	n.d*	n.d*	n.d*	0.01	n.d*	
Total	99.05	99.29	96.81	97.43	97.69	97.12	98.09	98.66	
	cations normalized to 23 oxygens								
Si	5.930	5.847	5.860	5.924	5.684	5.705	5.871	6.054	
Ti	0.625	0.650	0.589	0.504	0.581	0.550	0.465	0.431	
Al	2.284	2.286	2.316	2.145	2.328	2.405	2.265	2.022	
Mg	2.931	2.965	2.784	3.024	3.092	2.938	3.133	3.192	
Fe^{2+}***	1.171	1.153	1.242	0.903	0.736	0.965	1.024	0.898	
Fe^{3+}***	0.058	0.099	0.198	0.475	0.554	0.423	0.203	0.403	
Ca	1.819	1.820	1.853	1.849	1.868	1.888	1.976	1.819	
Mn	n.d*	n.d*	n.d*	0.024	0.025	n.d*	0.040	n.d*	
K	0.227	0.224	0.193	0.181	0.245	0.220	0.144	0.158	
Na	0.683	0.759	0.690	0.644	0.606	0.662	0.763	0.809	
Ba	n.d*	n.d*	0.012	n.d*	n.d*	0.012	n.d*	n.d*	
Total	15.728	15.803	15.736	15.674	15.720	15.769	15.884	15.787	
Mg#	71	72	69	77	81	75	76	78	

*not detected, ** minimum detection limit, ***iron recalculated according to Leake (1978) ac; center, ae; edge Mg# = 100Mg / (Mg + Fe^{2+})

Table 3.5 electron microprobe analyses of representative amphiboles continued

Location	xenocryst from Goemmer Butte		megacryst from Goemmer Butte		dike near Goemmer Butte		
Label oxide wt%	goe5	goe1	amph1 goe1	amph2 goe1	ac3a hm30	ae3a hm30	MDL oxide wt%**
SiO_2	43.43	39.06	39.81	40.68	41.93	41.95	0.05
TiO_2	2.35	2.73	1.99	2.02	3.86	3.83	0.07
Al_2O_3	14.75	15.01	14.48	14.24	12.27	12.34	0.05
MgO	9.90	10.30	10.89	11.04	14.35	14.48	0.05
FeO***	12.19	10.30	10.99	11.74	9.47	7.52	0.15
Fe_2O_3***	3.10	6.24	5.00	4.13	1.13	4.03	
CaO	10.37	11.25	12.12	12.29	12.02	11.67	0.04
MnO	n.d.*	n.d.*	0.25	0.28	n.d.*	0.27	0.17
K_20	1.52	1.50	1.19	1.31	0.78	0.76	0.03
Na_2O	2.04	2.09	2.13	2.07	3.09	3.11	0.08
Ba	n.d.*	0.18	n.d.*	n.d.*	0.15	n.d.*	0.12
Cl	0.03	0.05	0.06	0.04	0.03	n.d.*	0.02
	99.65	98.66	98.54	99.47	99.05	99.96	
-O=F,Cl	0.01	0.01	0.01	0.01	0.01	n.d.*	
Total	99.64	98.65	98.53	99.46	99.04	99.96	
	cations normalized to 23 oxygens						
Si	6.283	5.800	5.896	5.969	6.089	6.026	
Ti	0.256	0.305	0.222	0.223	0.422	0.414	
Al	2.515	2.627	2.527	2.462	2.100	2.089	
Mg	2.135	2.280	2.404	2.415	3.107	3.101	
Fe^{2+}***	1.474	1.279	1.360	1.440	1.149	0.903	
Fe^{3+}***	0.337	0.697	0.557	0.456	0.123	0.435	
Ca	1.607	1.790	1.923	1.932	1.870	1.796	
Mn	n.d.*	n.d.*	0.032	0.035	n.d.*	0.033	
K	0.281	0.285	0.225	0.245	0.145	0.139	
Na	0.571	0.601	0.611	0.590	0.870	0.866	
Ba	n.d.*	0.012	n.d.*	n.d.*	0.010	n.d.*	
Total	15.461	15.676	15.758	15.766	15.885	15.801	
Mg#	59	64	64	63	73	77	

*not detected, ** minimum detection limit, ***iron recalculated according to Leake (1978) ac; center, ae; edge Mg# = 100Mg / (Mg + Fe^{2+})

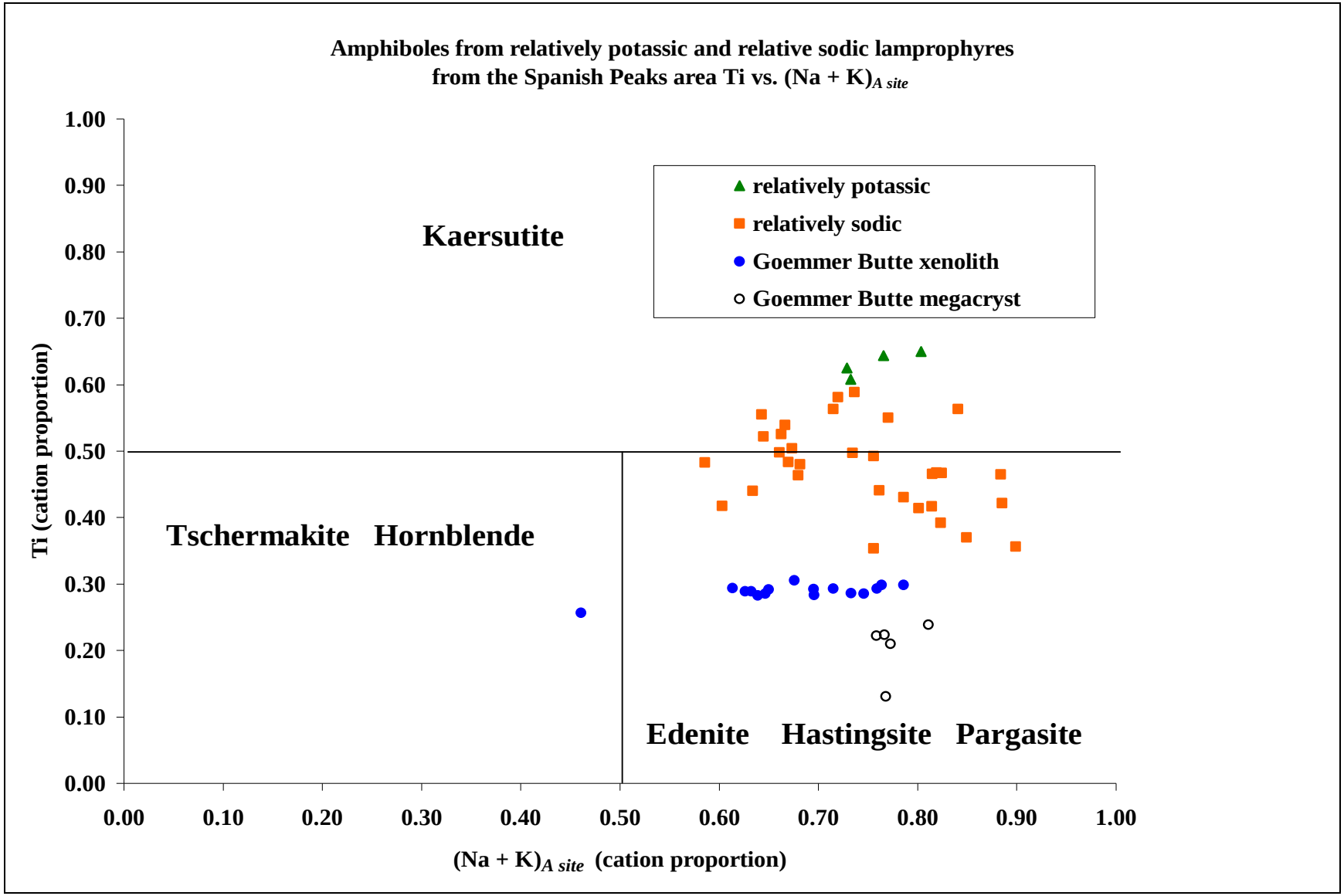

Figure 3.51 Amphibole analyses obtained with electron microprobe showing atomic proportions of titanium and sodium + calcium from the A-site in the amphibole structure. Nomenclature assigned according to Leake, (1978).

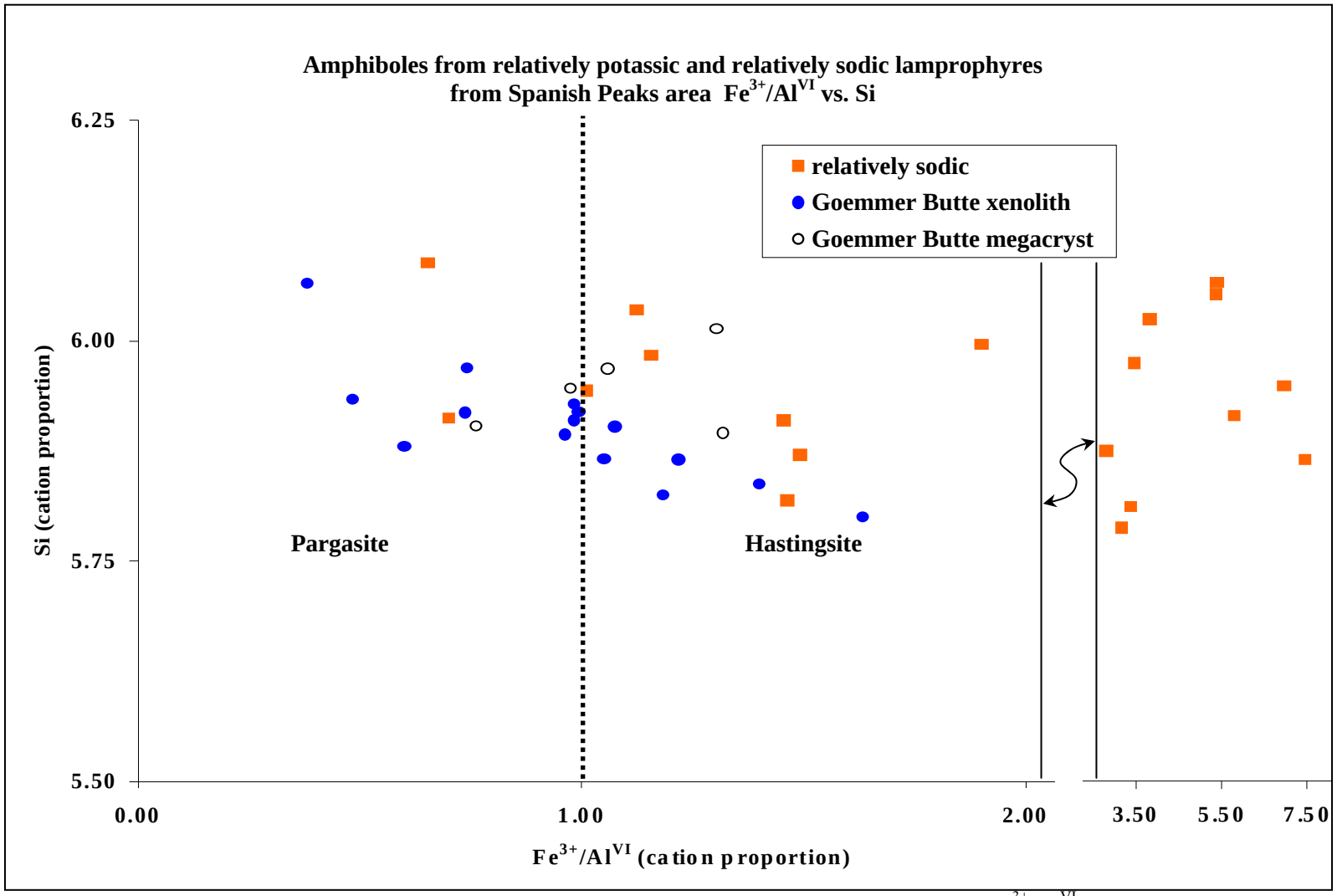

Figure 3.52 Amphibole analyses obtained with electron microprobe showing atomic proportions of Fe^{3+}/Al^{VI} and silicon in the amphibole structure. Nomenclature assigned according to Leake (1978).

3.3.3. Olivine analyses results

Olivine phenocrysts were only observed in the Walsenburg dike. Representative results are listed in Table 3.6. Back-scattered electron imagery of some of the olivine shows no significant compositional zoning (Figure 3.53). The analyzed olivines have an average Mg# of 85. Chromium was analyzed for but not detected in olivines from HM14 and is omitted from table 3.6.

Table 3.6 electron microprobe analyses of olivine from Walsenburg dike

Location	Walsenburg dike								
	collected center of dike outcrop at Cr 590								
Label oxide wt%	oe2 hm3	oc4 hm3	oe4 hm3	oe5 hm3	oe1 hm3	oc2 hm3	oe3a hm3	oc6 hm3	MDL oxide wt%**
SiO_2	39.53	39.78	39.55	39.51	38.87	38.99	39.51	39.15	0.05
TiO_2	n.d.*	n.d.*	n.d.*	n.d.*	0.07	n.d.*	n.d.*	n.d.*	0.07
MgO	44.68	45.38	45.00	44.62	43.70	45.33	45.33	45.41	0.05
FeO	14.40	14.08	15.50	14.88	16.18	14.05	14.98	14.07	0.15
CaO	0.23	0.15	0.22	0.26	0.22	0.21	0.18	0.18	0.04
MnO	n.d.*	n.d.*	0.23	0.44	0.48	0.23	0.30	0.28	0.17
NiO	n.d.*	0.42	n.d.*	n.d.*	0.24	0.31	0.32	0.36	0.22
Cr_2O_3	n.d.*	n.d.*	n.d.*	n.d.*	n.d.*	n.d.*	0.16	n.d.*	0.16
Total	98.84	99.81	100.51	99.71	99.77	99.12	100.78	99.46	
	cations normalized to 4 oxygens								
Si	1.001	0.998	0.991	0.996	0.988	0.987	0.988	0.988	
Ti	n.d.*	n.d.*	n.d.*	n.d.*	0.001	n.d.*	n.d.*	n.d.*	
Al	n.d.*	n.d.*	n.d.*	n.d.*	n.d.*	n.d.*	n.d.*	n.d.*	
Mg	1.687	1.697	1.681	1.677	1.656	1.711	1.689	1.708	
Fe	0.305	0.295	0.325	0.314	0.344	0.298	0.313	0.297	
Ca	0.006	0.004	0.006	0.007	0.006	0.006	0.005	0.005	
Mn	n.d.*	n.d.*	0.005	0.009	0.010	0.005	0.006	0.006	
Ni	0.000	0.008	n.d.*	n.d.*	0.005	0.006	0.007	0.007	
Cr	n.d.*	n.d.*	n.d.*	n.d.*	n.d.*	n.d.*	0.003	n.d.*	
Total	2.999	2.994	3.009	3.004	3.006	3.006	3.001	3.004	
$Mg\#_{Olivine}$	85	85	84	84	83	85	84	85	

*not detected, **minimum detection limit, oc; olivine center, oe; olivine edge
Mg# =100 Mg / (Mg + Fe)

Table 3.6 electron microprobe analyses of olivine from Walsenburg dike continued

Location	Walsenburg				
	collected off center of dike at Cr590				
Label oxide wt%	oc1a hm14	oc3 hm14	oc4b hm14	oc4c hm14	MDL oxide wt%%
SiO_2	40.24	40.35	40.08	40.24	0.05
TiO_2	n.d.*	n.d.*	n.d.*	0.07	0.07
MgO	45.35	45.53	45.42	45.41	0.05
FeO	14.70	13.60	14.04	14.31	0.15
CaO	0.23	0.15	0.20	0.18	0.04
MnO	0.34	0.33	0.26	0.21	0.17
NiO	0.27	0.37	0.32	0.25	0.22
Total	101.12	100.33	100.32	100.66	
	cations	normalized	to 4	oxygens	
Si	0.999	1.005	1.000	1.001	
Ti	n.d.*	n.d.*	n.d.*	0.001	
Al	n.d.*	n.d.*	n.d.*	n.d.*	
Mg	1.678	1.689	1.689	1.684	
Fe	0.305	0.283	0.293	0.298	
Ca	0.006	0.004	0.005	0.005	
Mn	0.007	0.007	0.005	0.004	
Ni	0.005	0.007	0.007	0.005	
Cr	n.d.*	n.d.*	n.d.*	n.d.*	
Total	2.996	2.988	2.993	2.993	
$Mg\#_{Olivine}$	85	86	85	85	

*not detected, **minimum detection limit, oc; olivine center, oe; olivine edge
Mg# =100 Mg / (Mg + Fe)

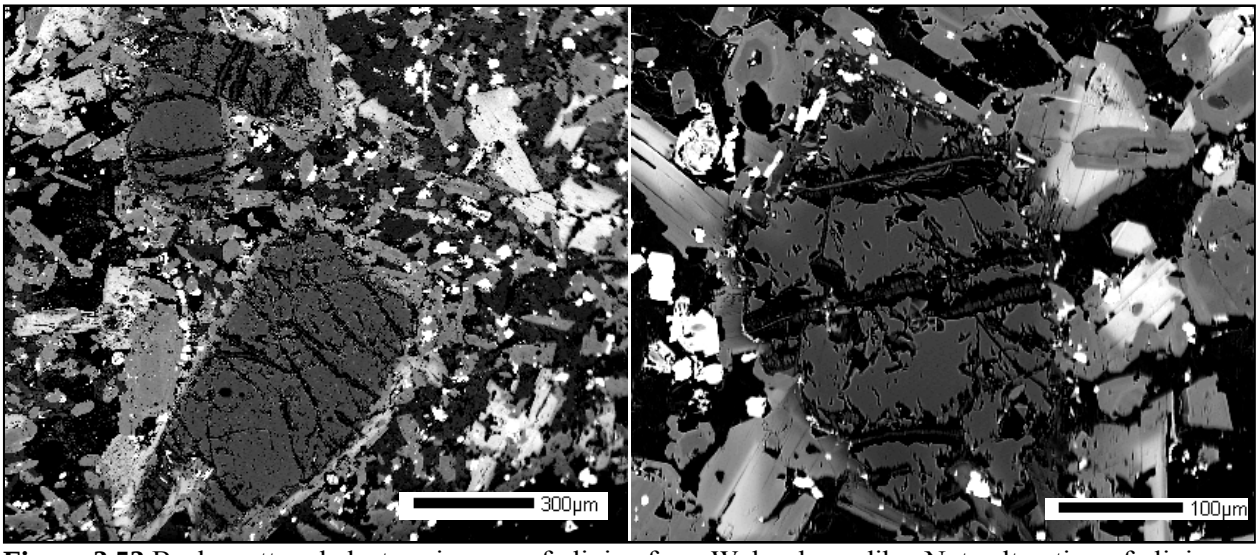

Figure 3.53 Back-scattered electron images of olivine from Walsenburg dike. Note alteration of olivine along fractures within the grains. Contrast and brightness adjusted to enhance image.

3.3.4. Mica analyses results

Over forty point analyses were performed on micas from both relatively potassic and relatively sodic samples. Representative results are listed in table 3.7. Chlorine and chromium were not detected in any analyzed mica and are omitted from table 3.7. All sampled micas are relatively rich in barium (exceeding 0.10 in atomic proportion) and titanium (exceeding 6.0 wt %). Most of the micas from the relatively potassic samples have high fluorine (exceeding 0.10 in atomic proportion) and relatively higher titanium values compared to that of the micas from the relatively sodic samples which have no fluorine and relatively lower titanium values (Figure 3.54). Most of the micas from the relatively sodic samples are higher in Mg# and sodium compared to that of the micas from the relatively potassic samples (Figure 3.55). Most of the analyzed micas from the relatively potassic samples are phlogopite and all micas sampled from relatively sodic samples are phlogopite (Figure 3.56). Most of the micas from both relatively potassic and relatively sodic rocks show normal zoning (higher Mg# in the center of the grain progressing to lower Mg# towards the edge of the grain). Back-scattered electron imagery of the probed micas, show types of zoning (Figure 3.57).

Table3.7 electron microprobe analyses of representative micas

Location	Walsenburg dike									
	Lathrop Park							Cr590		
Label oxide wt%	bc3 hm4	be3 hm4	b5a hm4	b5b hm4	b5c hm4	b5d hm4	b5e hm4	bc1a hm14	be1b hm14	MDL oxide wt%**
SiO_2	34.96	36.28	36.67	37.09	37.23	36.76	35.44	36.23	36.74	0.05
TiO_2	7.81	7.30	7.44	7.96	7.79	7.48	7.33	7.41	8.58	0.07
Al_2O_3	13.59	13.56	13.72	13.93	13.96	13.59	13.34	13.59	12.98	0.05
MgO	16.92	13.63	14.22	16.89	16.57	14.38	13.27	17.76	14.66	0.05
FeO***	8.96	14.11	13.62	9.14	10.63	12.88	16.57	9.27	12.76	0.18
Fe_2O_3***	1.07	0.78	0.80	0.94	0.84	0.67	0.67	1.44	0.36	
CaO	n.d.*	n.d.*	n.d.*	0.06	0.10	0.11	0.16	0.16	n.d.*	0.04
MnO	n.d.*	0.22	0.26	0.19	0.19	0.25	0.19	0.16	0.21	0.16
K_20	8.75	8.42	8.19	8.18	7.95	7.90	7.94	6.68	8.84	0.03
Na_2O	0.48	0.58	0.58	0.31	0.52	0.29	0.61	0.56	0.47	0.07
BaO	1.86	1.36	1.39	1.64	1.46	1.17	1.16	2.50	0.63	0.14
F	0.49	0.32	0.36	0.33	0.28	0.50	0.26	0.22	0.34	0.15
	94.30	96.17	96.83	96.25	97.15	95.43	96.61	95.63	96.19	
-O=F,Cl	0.21	0.13	0.15	0.14	0.12	0.21	0.11	0.09	0.14	
Total	94.09	96.04	96.68	96.11	97.04	95.21	96.50	95.54	96.05	
	cations normalized to 22 oxygens									
SiO_2	5.251	5.421	5.418	5.399	5.393	5.467	5.327	5.325	5.432	
TiO_2	0.882	0.820	0.827	0.871	0.849	0.837	0.829	0.819	0.954	
Al_2O_3	2.406	2.388	2.389	2.390	2.383	2.382	2.363	2.354	2.262	
MgO	3.789	3.036	3.132	3.665	3.579	3.188	2.973	3.891	3.231	
FeO***	1.125	1.763	1.683	1.113	1.287	1.601	2.083	1.139	1.578	
Fe_2O_3***	0.121	0.088	0.089	0.103	0.092	0.075	0.075	0.159	0.040	
CaO	n.d.*	n.d.*	n.d.*	0.010	0.015	0.017	0.025	0.025	n.d.*	
MnO	n.d.*	0.027	0.033	0.023	0.023	0.032	0.024	0.020	0.026	
K_20	1.676	1.605	1.544	1.519	1.469	1.499	1.522	1.252	1.667	
Na_2O	0.140	0.169	0.167	0.089	0.145	0.085	0.178	0.160	0.134	
BaO	0.122	0.089	0.090	0.104	0.093	0.076	0.076	0.161	0.041	
Total	15.512	15.407	15.371	15.287	15.327	15.259	15.476	15.306	15.364	
Mg#	77	63	65	77	74	67	59	77	67	

*not detected, ** minimum detection limits, *** iron recalculated according to Nenova (1996) bc; center, be; edge Mg# = 100Mg / (Mg = Fe^{2+})

Table 3.7 electron microprobe analyses of representative micas continued

Location	Northlake sill complex								
	large sill near south end of Northlake sill complex						minette		
Label oxide wt%	bc1 hm19	be1a hm19	bc1 hm22	be1 hm22	bc1 hm24	be1 hm24	bc3 hm25	be3 hm25	MDL oxide wt%**
SiO_2	36.26	34.69	36.09	34.04	36.75	35.33	36.99	35.95	0.05
TiO_2	7.33	7.73	7.37	7.99	7.41	7.44	6.27	5.87	0.07
Al_2O_3	14.65	14.99	14.40	14.12	14.93	14.82	15.57	15.50	0.05
MgO	17.01	13.16	16.29	12.14	16.45	13.38	18.21	18.39	0.05
FeO***	9.36	13.66	9.76	14.87	10.22	13.52	7.92	9.00	0.18
Fe_2O_3***	1.34	1.00	1.21	1.53	1.16	1.12	1.08	0.78	
CaO	n.d.*	0.05	n.d.*	0.12	0.05	0.04	0.07	0.10	0.04
MnO	n.d.*	0.26	n.d.*	0.24	n.d.*	0.26	n.d.*	n.d.*	0.16
K_20	8.21	8.14	8.36	8.16	8.46	8.26	7.61	7.46	0.03
Na_2O	0.63	0.80	0.44	0.67	0.45	0.82	0.87	0.79	0.07
BaO	2.33	1.74	2.10	2.65	2.01	1.95	1.87	1.36	0.14
F	0.23	0.17	0.61	0.33	0.25	0.33	0.00	0.00	0.15
	97.00	96.12	95.92	96.39	97.78	96.84	96.37	95.14	
-O=F,Cl	0.10	0.07	0.26	0.14	0.10	0.14	0.00	0.00	
Total	96.90	96.05	95.66	96.25	97.68	96.70	96.37	95.14	
			cations	normalized	to 22	oxygens			
SiO_2	5.283	5.203	5.321	5.177	5.313	5.261	5.335	5.266	
TiO_2	0.803	0.872	0.817	0.914	0.806	0.833	0.680	0.647	
Al_2O_3	2.515	2.650	2.502	2.531	2.544	2.601	2.647	2.676	
MgO	3.694	2.943	3.581	2.752	3.545	2.970	3.916	4.016	
FeO***	1.140	1.714	1.203	1.891	1.235	1.683	0.955	1.102	
Fe_2O_3***	0.147	0.113	0.134	0.175	0.126	0.126	0.117	0.086	
CaO	n.d.*	0.008	n.d.*	0.019	0.008	0.006	0.011	0.016	
MnO	n.d.*	0.033	n.d.*	0.031	n.d.*	0.033	n.d.*	n.d.*	
K_20	1.526	1.557	1.572	1.583	1.560	1.569	1.400	1.394	
Na_2O	0.177	0.231	0.127	0.198	0.126	0.236	0.244	0.225	
BaO	0.149	0.114	0.136	0.177	0.127	0.127	0.118	0.087	
Total	15.435	15.438	15.393	15.447	15.390	15.445	15.425	15.516	
Mg#	76	63	75	59	74	64	80	78	

*not detected, ** minimum detection limits, *** iron recalculated according to Nenova (1996) bc; center, be; edge Mg# = 100Mg/ (Mg + Fe^{2+}).

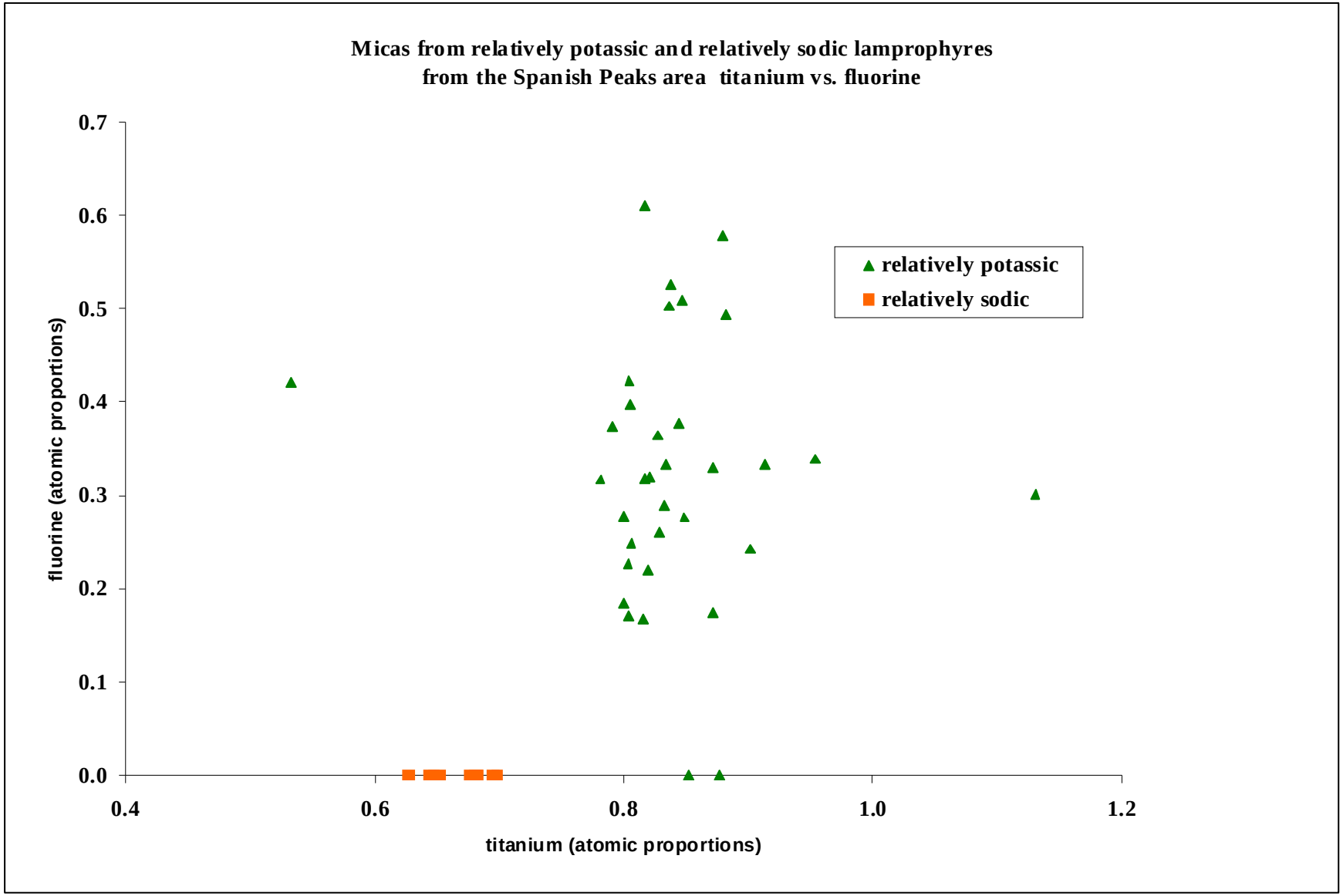

Figure 3.54 Mica analyses obtained with electron microprobe showing atomic proportions of titanium and fluorine in mica.

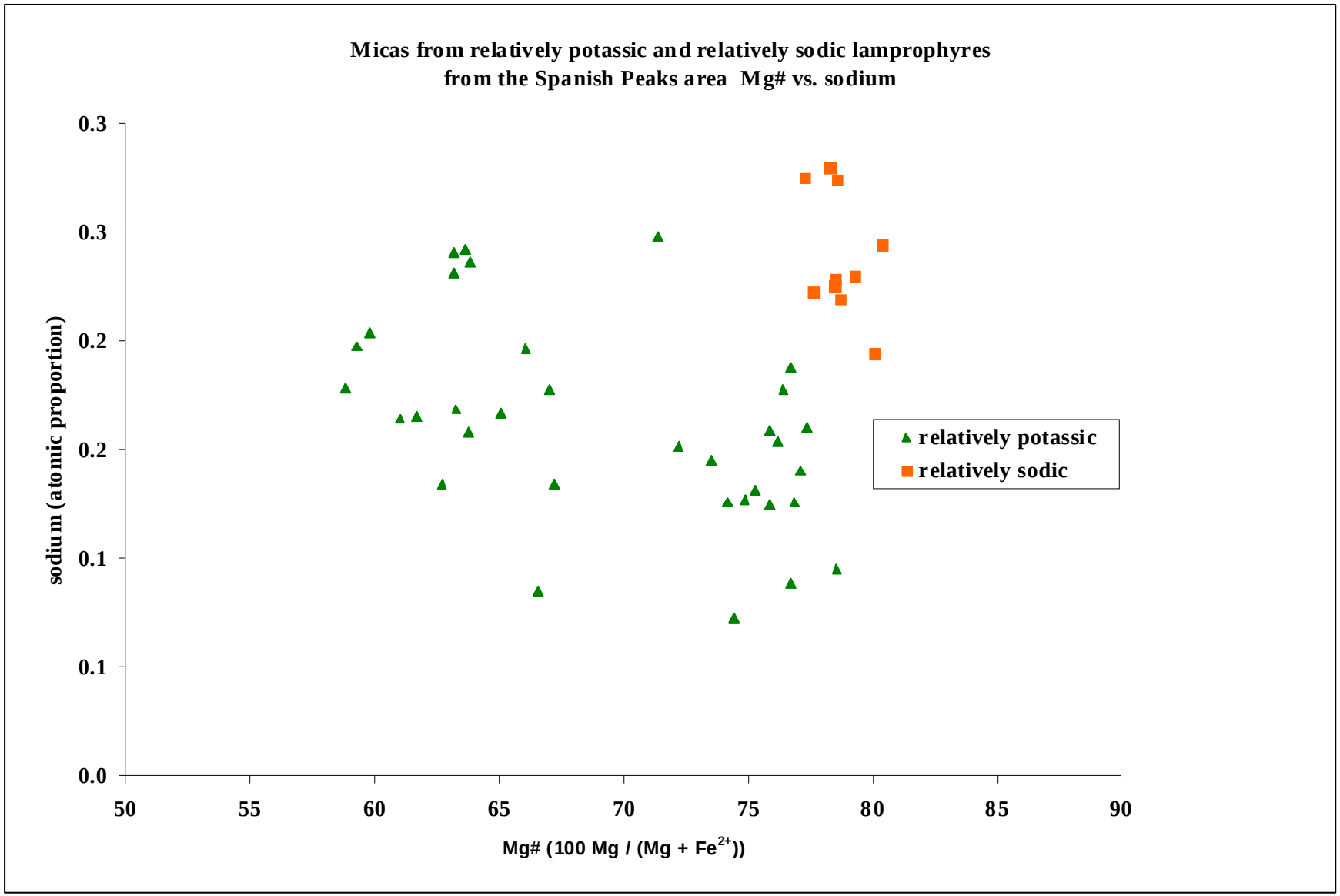

Figure 3.55 Mica analyses obtained with electron microprobe showing Mg# verses atomic proportions of sodium in the mica structure.

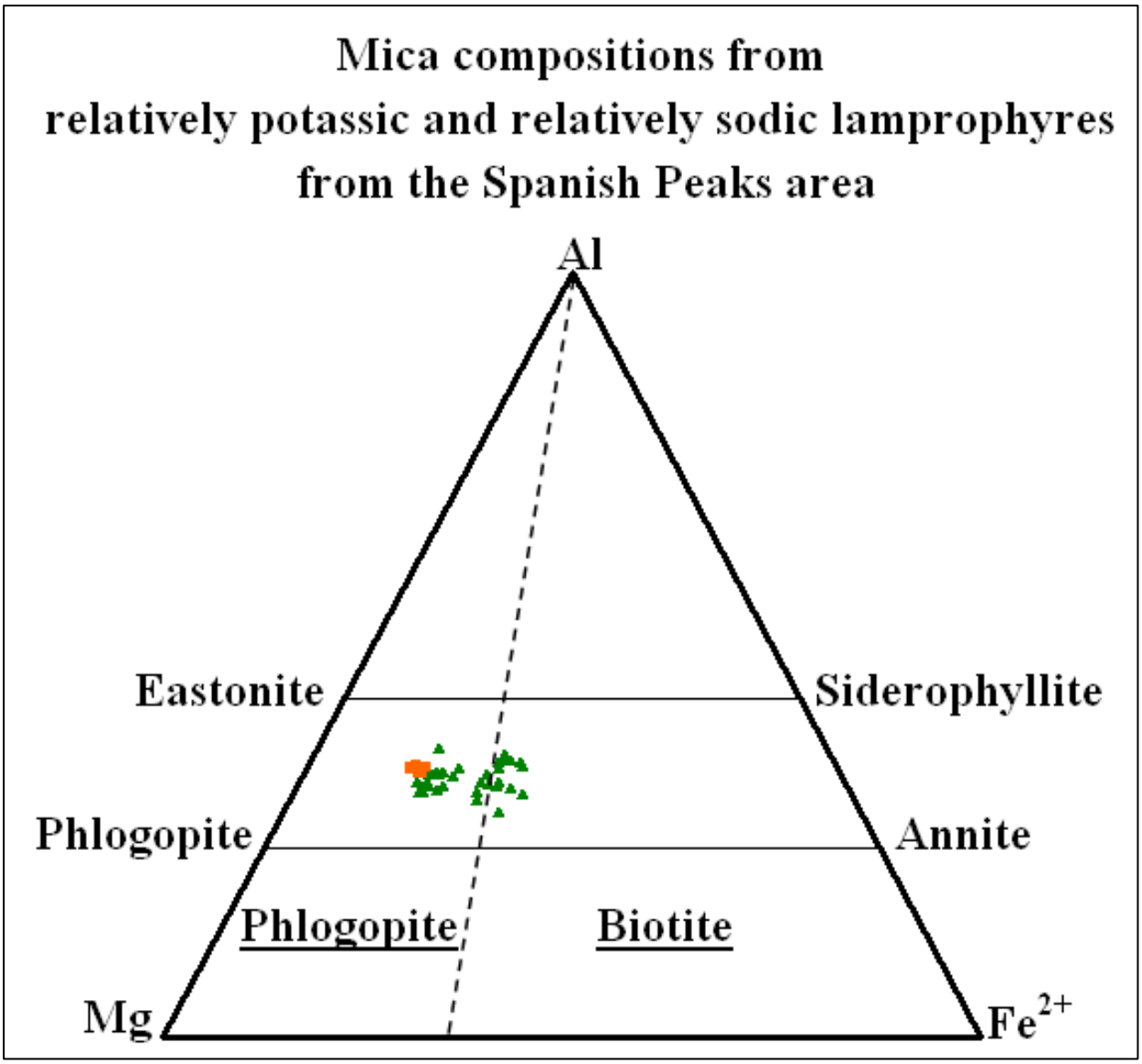

Figure 3.56 Mica analyses from relatively potassic (green triangles) and relatively sodic (orange squares) samples from the Spanish Peaks area. Diagram modeled after Shaw et al., (1996).

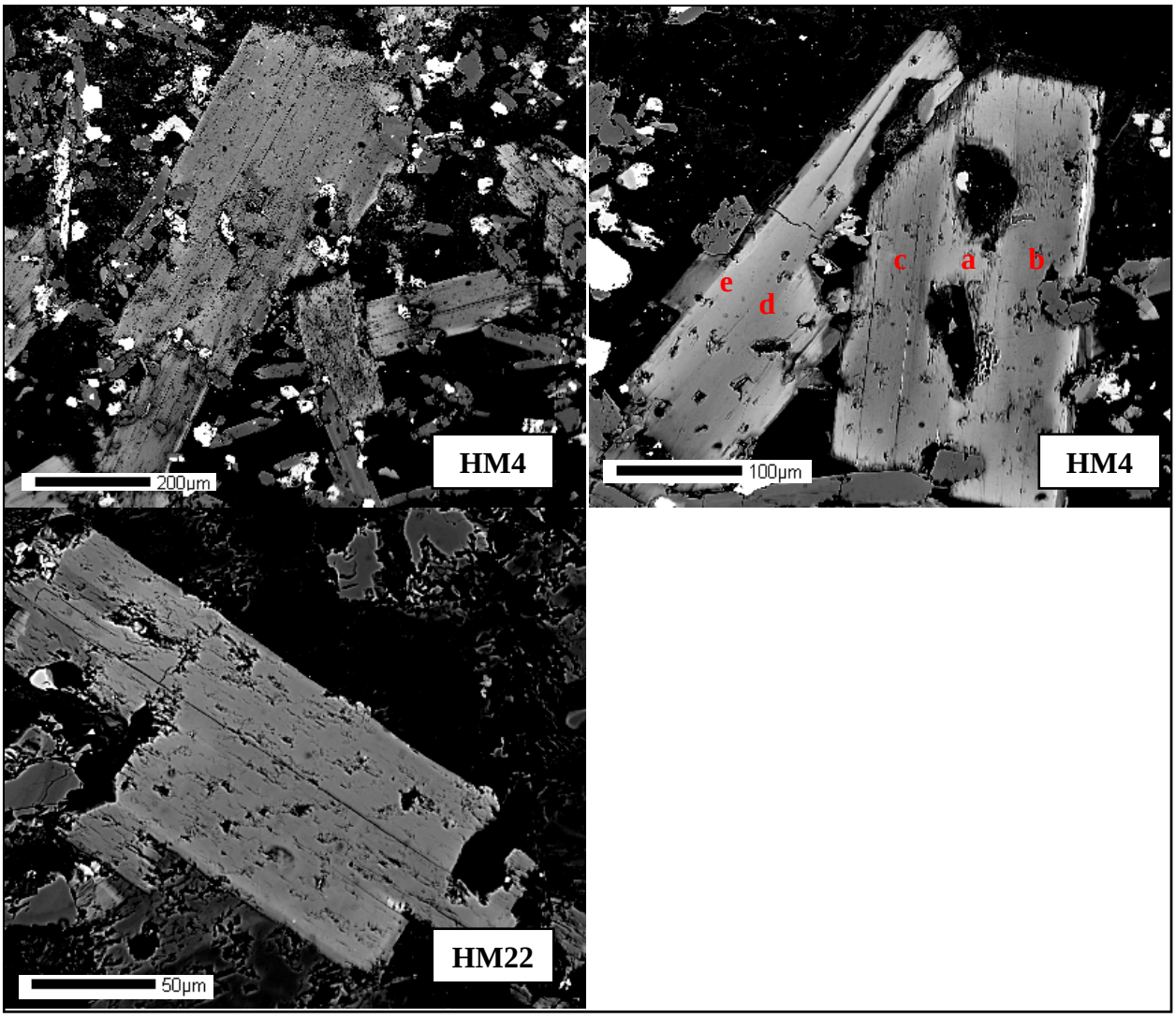

Figure 3.57 Back-scattered electron images of typical micas from Spanish Peaks area. Note the biotite upper right has lower Mg# in the center of grain (lighter area) compared to the rest of the grain (darker area). Lowercase letters represent analysis points for b5a thru b5e HM4 (Table 3.6).

3.3.5. Feldspar analyses results

Over sixty-five analyses were performed on feldspars from both relatively potassic and relatively sodic samples. Table 3.8 shows representative results from both types of lamprophyres. Most of the feldspars exhibit no visible zoning and show signs of alteration at the rims (back-scattered electron imagery Figure 3.58). Feldspars, in which core and rim analyses were obtained, show that the K/Na ratios of the cores were comparatively higher than the K/Na ratios of the rims. As a result, most of the feldspars from core to rim range in composition from orthoclase to anorthoclase. A few of the potassium poor analyses range in composition from oligolclase to andesine (Figure 3.59).

Table 3.8 electron microprobe analyses of representative feldspars

Location	Walsenburg		Northlake sill complex						
	Hwy85	Lathrop park	Large sill near south end		Camp-tonite	North end	dike near Goemmer Butte		MDL
Label	hm5	hm4	hm19	hm19	hm26	hm7	hm30	hm30	ox
ox wt%	fc5	fc3	fc4	fc1	fc3a	fc9	fc6	fc7	wt%**
SiO_2	63.89	64.82	65.36	59.66	63.50	64.77	65.09	64.86	0.06
TiO_2	0.21	n.d.*	n.d.*	n.d.*	n.d.*	n.d.*	n.d.*	n.d.*	0.08
Al_2O_3	19.35	19.18	18.58	23.91	22.78	18.59	18.75	18.82	0.05
MgO	0.25	0.02	n.d.*	n.d.*	n.d.*	n.d.*	n.d.*	n.d.*	0.06
FeO	0.20	0.34	n.d.*	0.40	0.09	n.d.*	n.d.*	n.d.*	0.20
CaO	0.19	0.11	0.09	6.37	2.85	n.d.*	0.08	n.d.*	0.04
K_2O	10.77	14.02	15.03	1.27	0.56	15.87	16.54	15.98	0.04
Na_2O	3.70	1.59	0.95	6.67	9.28	0.63	0.19	0.18	0.09
BaO	0.53	0.60	0.31	n.d.	0.18	0.26	0.42	0.22	0.16
Total	99.10	100.68	100.31	98.28	99.24	100.12	101.07	100.06	
cations normalized to 8 oxygen									
Si	2.942	2.968	3.000	2.712	2.825	2.991	2.987	2.992	
Ti	0.007	n.d.*	n.d.*	n.d.*	n.d.*	n.d.*	n.d.*	n.d.*	
Al	1.050	1.035	1.005	1.281	1.194	1.012	1.014	1.023	
Mg	0.017	0.002	n.d.*	n.d.*	n.d.*	n.d.*	n.d.*	n.d.*	
Fe	0.008	0.013	n.d.*	0.015	0.003	n.d.*	n.d.*	n.d.*	
Ca	0.009	0.005	0.004	0.310	0.136	n.d.	0.004	n.d.*	
K	0.633	0.819	0.880	0.073	0.032	0.935	0.968	0.940	
Na	0.330	0.141	0.084	0.588	0.800	0.057	0.016	0.016	
Ba	0.010	0.011	0.006	n.d.	0.003	0.005	0.008	0.004	
Total	5.007	4.994	4.979	4.979	4.994	4.999	4.998	4.975	
an	0.009	0.006	0.004	0.319	0.140	0.000	0.004	0.000	
ab	0.340	0.146	0.087	0.605	0.827	0.057	0.017	0.016	
or	0.651	0.849	0.908	0.076	0.033	0.943	0.979	0.984	

n.d.* not detected, MDL** minimum detection limit, fc; feldspar center

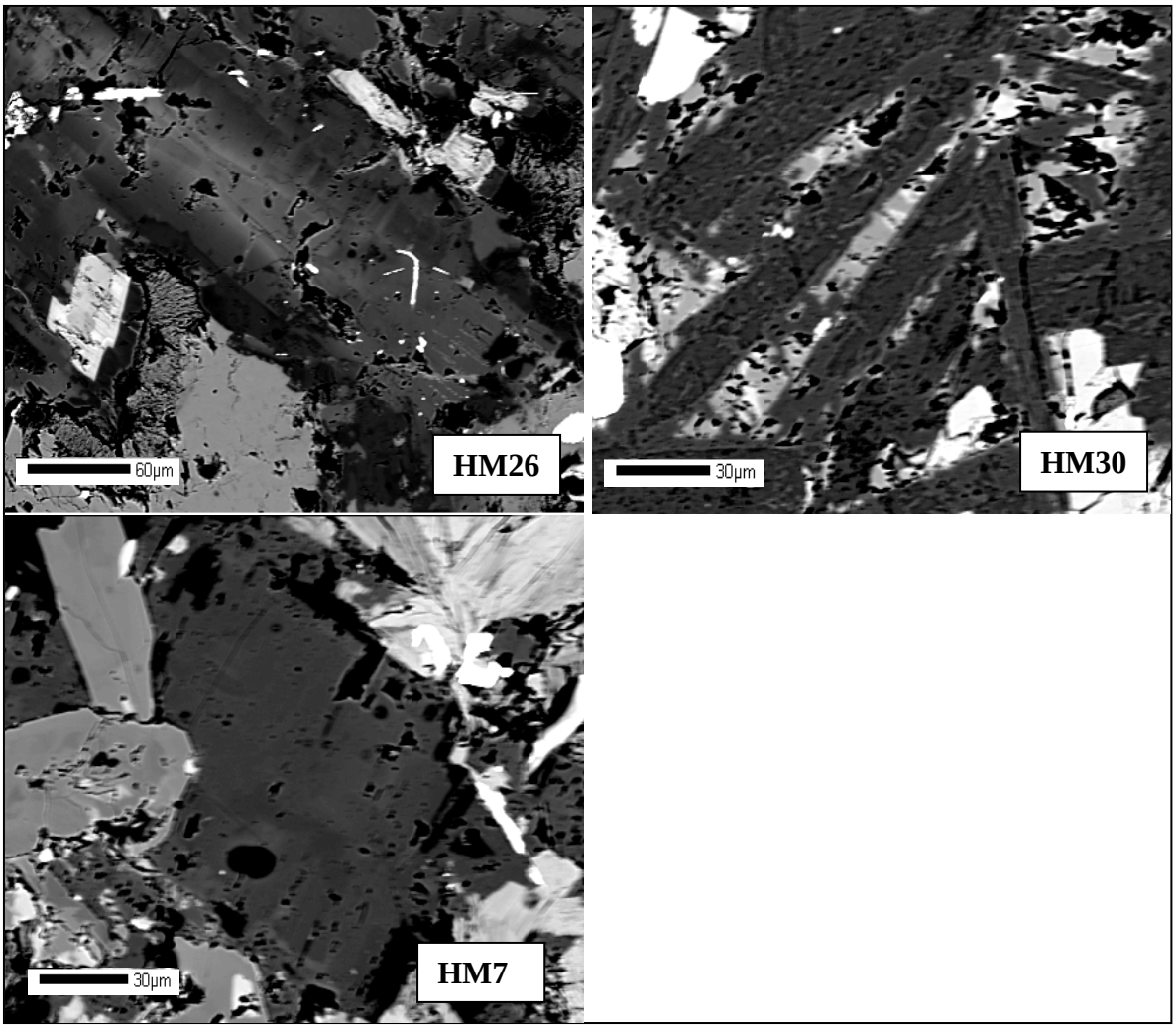

Figure 3.58. Back-scattered electron images of typical feldspars in lamprophyres from the Spanish Peaks area. Note that most feldspars have altered rims and no visible zoning.

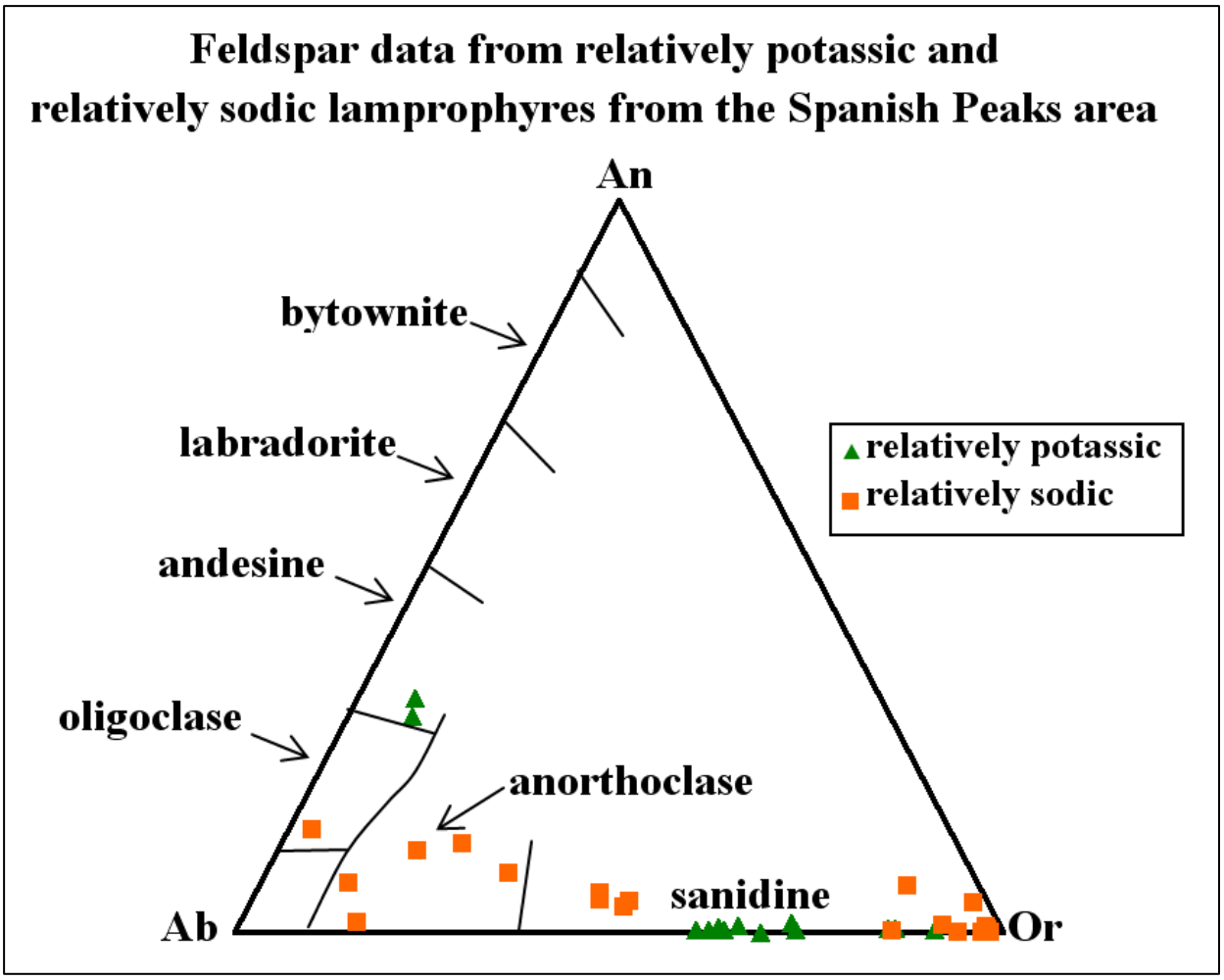

Figure 3.59 Feldspar analyses from relatively potassic and relatively sodic samples of the Spanish Peaks area. Abbreviations An; anorthite, Ab; Albite, Or; orthoclase. Dashed lines represent limits of solid solution. Nomenclatures are from Deer et al (1992).

3.3.6. Oxide analyses results

Over fifty analyses were performed on oxides from both relatively potassic and relatively sodic samples. Table 3.9 shows representative results from both types of lamprophyres. Some of the relatively potassic lamprophyres as well as the Goemmer Butte trachyandesite oxides plot on the ulvöspinel-magnetite solid solution line. Some of the relatively sodic lamprophyre oxides plot on the ilmenite-hematite solid solution line. All other analyses plot in various fields above and below boundary lines (Figure 3.60). Some oxides have both magnetite and ilmenite with components of rutile, pseudo-brookite, and wüstite (Figure 3.61).

Table 3.9 electron microprobe analyses of representative oxides

Location	Walsenburg		Northlake sill complex						
	Lathrop Park	Hwy 85	Large Sill near southend			Northend			
Label	hm4	hm5	hm19	hm19	hm19	hm7	hm7	hm7	MDL
ox wt%	oc	oc4	oc1	oe1	oc4	oc2	oc3	oc3c	ox wt%**
SiO_2	1.02	0.07	1.23	0.85	0.16	0.91	0.87	0.07	0.05
TiO_2	14.61	9.63	11.99	11.98	48.82	42.68	44.31	50.97	0.07
Al_2O_3	0.14	0.23	0.34	0.31	n.d.*	n.d.*	n.d.*	n.d.*	0.05
MgO	n.d.*	0.05	n.d.*	n.d.*	0.07	0.09	0.08	n.d.*	0.06
FeO***	46.27	42.83	45.95	46.46	41.06	38.40	40.24	42.71	0.18
Fe_2O_3**	28.43	38.44	31.90	33.22	n.d.*	13.00	10.47	n.d.*	
CaO	0.43	0.10	0.10	0.18	n.d.*	0.46	0.59	0.39	0.04
MnO	0.33	3.37	0.48	0.16	0.75	0.72	0.68	3.01	0.15
Cr_2O_3	n.d.*	0.50	n.d.*	n.d.*	n.d.*	0.21	n.d.*	n.d.*	0.21
NiO	0.23	n.d.*	n.d.*	n.d.*	n.d.*	0.22	n.d.*	n.d.*	0.22
Total	91.46	95.22	91.99	93.16	90.86	96.69	97.25	97.15	
	normalized to 4 oxygens				normalized to 3 oxygens				
Si	0.043	0.003	0.051	0.035	0.004	0.024	0.023	0.002	
Ti	0.458	0.296	0.376	0.372	1.012	0.841	0.868	0.996	
Al	0.007	0.011	0.016	0.015	n.d.*	n.d.*	n.d.*	n.d.*	
Mg	n.d.*	0.003	n.d.*	n.d.*	0.003	0.003	0.003	n.d.*	
Fe^{2+***}	1.612	1.464	1.600	1.603	0.946	0.842	0.876	0.928	
Fe^{3+***}	0.892	1.182	1.000	1.031	n.d.*	0.256	0.205	n.d.*	
Ca	0.019	0.004	0.004	0.008	n.d.*	0.013	0.017	0.011	
Mn	0.012	0.117	0.017	0.005	0.017	0.016	0.015	0.066	
Cr	n.d.*	0.016	n.d.*	n.d.*	n.d.*	0.004	n.d.*	n.d.*	
Ni	0.008	n.d.*	n.d.*	n.d.*	n.d.*	0.005	n.d.*	n.d.*	
Total	3.050	3.096	3.065	3.070	1.983	2.004	2.007	2.002	

n.d.*; not detected, MDL**; minimum detection limits, ***; iron recalculated using Droop (1987)

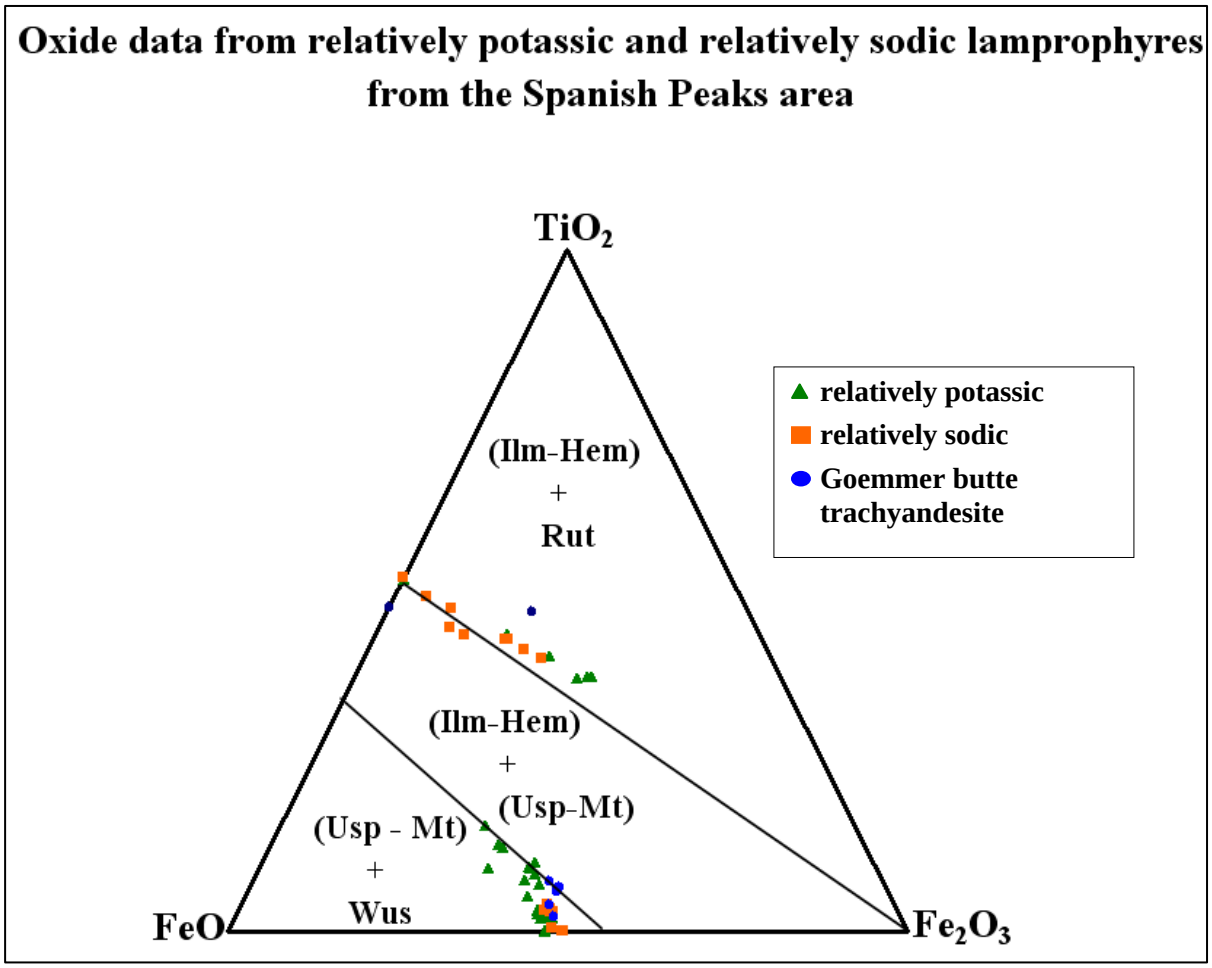

Figure 3.60 Oxide analyses from relatively potassic and relatively sodic samples from the Spanish Peaks area. Abbreviations Wus; wüstite, Usp; ulvöspinel, Mt; magnetite, Ilm; ilmenite, Hem; hematite, Rut; rutile. Ternary components FeO, TiO_2, and Fe_2O_3 represent wüstite, rutile, and hematite, respectively. Modeled after Haggerty (1976).

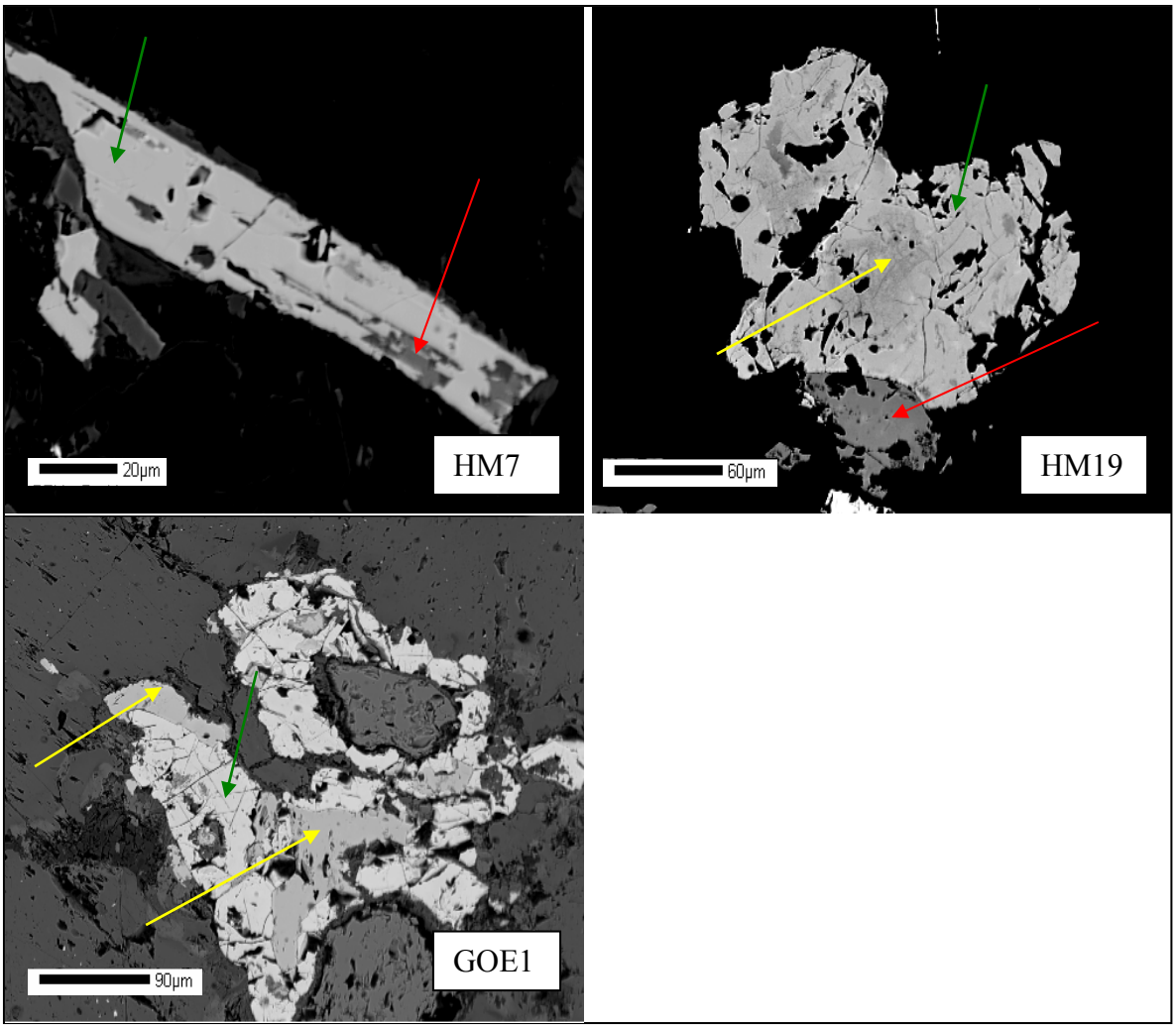

Figure 3.61 Back-scattered electron images of typical oxides in lamprophyres and Goemmer Butte trachyandesite from the Spanish Peaks area. Note that most oxides have been altered. Relatively light areas (green arrows) are magnetite compositions and relatively darker areas (yellow arrows) are ilmenite compositions. Red arrows indicate where oxides have been altered to rutile or pseudo-brookite.

4. DISCUSSION

As stated earlier, the hypothesis being tested is that the relatively potassic and relatively sodic lamprophyres are derived from the same parental source and/or follow a liquid line of descent (one begot the other). A possible mechanism to explain the differences in chemistry and mineralogy of the two types of lamprophyres could be crystal fractionation and/or degrees of partial melting of the original parental source. Collectively this mechanism can be termed crystal-liquid fractionation, (Cox et al., 1979).

4.1. *CRYSTAL FRACTIONATION AND EVOLVING MAGMAS*

One of the observable differences in the two varieties of rocks investigated in this study is the mineralogy. How can both rocks come from the same parental source and/or have a liquid line of descent with such distinct mineralogical differences? Crystal fractionation is a possible explanation.

4.1.1. Major element trends in lamprophyres from this study

In this study, variation diagrams were used to compare the trace and major element abundances of the two types of lamprophyres. Mg# was used as the variable on the x-axis, instead of using silica. Mg# is the molar-based ratio of Mg/ (Mg + Fe^{2+}). This strategy is used because the fractionation of olivine and pyroxene are not readily discerned when using silica as the x-axis variable (Blatt et al., 2006). As iron-magnesium silicates (e.g. olivine, pyroxene) separate from the magma the residual liquid is initially enriched in iron and depleted in magnesium. Therefore, samples that have the highest Mg# are considered the most primitive and the samples with the lowest Mg# are considered the most evolved samples. Linear or curved trends between the most primitive sample and the most evolved sample should define a liquid line of descent, if the most evolved sample is a derivative of the most primitive sample. The relatively potassic lamprophyres have the most primitive signature and the relatively sodic lamprophyres have the most evolved signature (Figure 3.36). Therefore, if a liquid line of descent exists between the two types of lamprophyres, a linear or curved trend should be evident in plots of various oxides against the Mg#. Referring to Figure 3.36, such trends are not evident. Even within the

groups of relatively potassic and relatively sodic lamprophyres, there are no trends connecting the most primitive sample with the most evolved sample, implying complex crystallization paths. These diagrams are inconsistent with, and do not support crystal fractionation as a mechanism that relates the relatively potassic lamprophyres with the relatively sodic lamprophyres in this study. Major element ratios also provide supplementary evidence of the inconsistencies in the two lamprophyres being related by crystal fractionation.

4.1.2. Major element ratios in lamprophyres from this study

Ratios that behave incompatibly or approximately incompatibly "see through" the effects of crystal fractionation imposed upon an evolving magma. These ratios can also be used to evaluate a liquid line of descent between the two types of lamprophyres. Individual oxide abundances increase or decrease as minerals separate from the magma, but the ratio of two oxides that behave incompatibly remain constant or nearly so. If the relatively potassic and relatively sodic sample are cogenetic, they should have the same values in such ratios. Some of the oxide ratios shown in Figure 3.37 show little or no change in value from the most primitive samples to the most evolved samples. Relatively sodic samples show a consistent linear trend in K_2O/Na_2O and Al_2O_3/Na_2O ratios, whereas the relatively potassic samples show a consistent linear trend in Al_2O_3/K_2O and Na_2O/P_2O_5 ratios. Al_2O_3/TiO_2 and Na_2O/TiO_2 ratios in both types of samples show linear and more or less distinct values. These trends imply two separate sources for the lamprophyres.

4.1.3. Trace elements and evolving magmas

Trace elements by definition are elements that are low in concentration (less than 0.1 weight %) and do not give rise to characteristic or accessory mineral phases (Shaw et al., 2006). As with major elements, crystal fractionation processes that occur as magma evolves have an effect on trace element abundances. Because mineral phases can include or exclude certain trace elements, they can be quite sensitive to crystal fractionation and to fractionation by residual phases during melting (Neuman et al., 1954). With this in mind, trace element abundances can also be used to infer or exclude a lineage (liquid line of descent) existing between the relatively potassic and relatively sodic lamprophyres in this study.

Some trace elements (e.g. nickel and chromium) are compatible in the sense that they are readily incorporated in mineral phases (e.g. olivine and spinel) that typically form early in the crystallization history of basaltic magmas. As olivine and spinel crystallize from the magma, the residual liquid is depleted in nickel and chromium, relative to the primary liquid. Therefore, samples with relatively high amounts of nickel and chromium are the most primitive within a given rock suite and have had the least amount of crystal fractionation. Figure 3.38 shows that the relatively potassic lamprophyres with the higher Mg# also have the highest abundances of chromium and nickel, and the relatively sodic lamprophyres which have relatively lower Mg# also have relatively low abundances of chromium and nickel.

Some trace elements (e.g. barium, rubidium, strontium, and thorium) are typically incompatible in the sense that they do not readily incorporate into most mineral structures and thus preferentially remain in the liquid phase (Shaw, 1970). Therefore, in a rock suite that is related by a liquid line of descent, the most evolved samples should have relatively higher abundances of these incompatible trace elements relative to the most primitive samples. In Figure 3.38 the relatively potassic lamprophyres having the highest Mg# (implying the most primitive) also have the highest abundances of incompatible elements. The relatively sodic lamprophyres with the lowest Mg# (implying the most evolved) also have the lowest abundances of incompatible elements. This observation is inconsistent with a fractional crystallization model in which the relatively potassic lamprophyres evolved to the relatively sodic lamprophyres.

Rocks related through a liquid line of descent will have certain consistencies in their chemical compositions that will reflect the common liquid line of descent. When comparing major elements of rocks within a suite, there should be a linear or curved path connecting the most primitive rocks to the most evolved rocks. This linear or curved relationship should also be reflected when comparing certain incompatible and compatible trace elements. In both cases, this relationship is not evident between the relatively potassic and relatively sodic lamprophyres in this study. In fact, most major and trace element plots indicate different crystallization paths within the two separate groups.

4.2. *MINERAL COMPOSITIONS*

In order to explore the possibility of the relatively sodic and relatively potassic lamprophyre groups originating from the same parental source but following different crystallization paths, I looked at the chemical evolution of minerals that are present in both types of lamprophyres.

4.2.1. Pyroxene analyses

As stated earlier in the results section 3.3.1, over 200 point analyses were performed on pyroxenes from both relatively potassic and relatively sodic samples. Averaged cores and rims of pyroxenes from both relatively potassic and relatively sodic lamprophyres (along with green cores) are displayed on a pyroxene quadrilateral in Figure 4.1. Zoned pyroxene crystals can record magma evolution as well as discrete events such as magma mixing that occurred as the magma evolved. Normally, as a pyroxene grows it follows a trend that is characterized by a path parallel to the $Mg_{(Di)}$ (diopside) - $Fe_{(Hd)}$ (hedenbergite). Pyroxenes from each type of lamprophyre show relatively small variation in the core to rim $Mg_{(Di)}$ - $Fe_{(Hd)}$, but a relative enrichment or increasing trend in $Ca_{(Wo)}$.

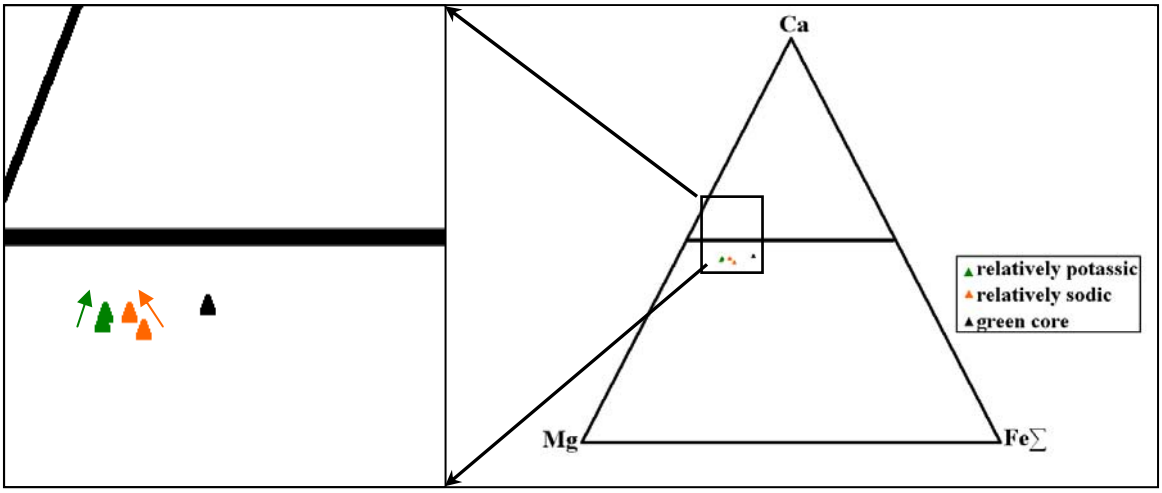

Figure 4.1 Average pyroxene core and rims from relatively potassic (green triangles), relatively sodic (orange squares), and green cores (black triangle). Arrows indicate direction of core to rim compositional change of pyroxenes. Note that there is relatively little change in the Mg# but there is an increase in Ca content. Figure after Morimoto, 1989.

Oscillatory zoning in the pyroxenes of both types of lamprophyres can be readily seen in back-scattered electron and plane cross-polarized light imagery (Figure 3.25, 3.46, and 3.47). With back-scattered electron imagery, crystal zones with compositions characterized by relatively high average

atomic numbers appear brighter than crystal zones characterized by compositions with relatively low average atomic number. Figures 3.43-3.45 show the oscillations/changes in titanium, iron (both relatively high atomic numbers), and magnesium (relatively low atomic number). Relative increases in titanium and iron correspond to a relative decreases in magnesium. Incompatible major and trace elements are incorporated into the pyroxene structure at an increased rate when the magma experiences periods of relatively rapid cooling (Lofgren et al., 2006). Therefore, the relatively light bands which have greater amounts of incompatible Ti and Fe in the pyroxene, could reflect periods where the magma experienced moderately increased rates of cooling. The relatively darker bands (which have lower amounts of Ti and Fe) represent periods of moderately decreased rates of cooling. These compositional oscillations in the pyroxene phenocrysts do not indicate radical disequilibrium between the melt and the pyroxene. In contrast, the distinct compositional changes between the green cores and their mantling rims, along with embayed textures (HM5 and HM8 in Figures 3.43-3.47), indicate significant disequilibrium (i.e. the cores are accidental inclusions that did not crystallize from the melt).

Aluminum content in the pyroxenes also oscillates/changes from core to rim. These changes in aluminum are coupled with the changes in titanium. Figure 4.2 is a plot of aluminum and titanium point analyses from pyroxenes in Figures 3.46 and 3.47. Ti/Al ratios can be used to infer relative pressure of formation for pyroxene (Dobosi et al., 1992, Nekvasil et al., 2004, Wass, 1979). Three distinct positive trends are separated into fields of different pressures in Figure 4.2. The circled pyroxene analyses represent the green cores from both relatively potassic and relatively sodic samples. The green cores found in the relatively potassic rocks have the lowest Ti/Al ratios and plot in the 14.3 kbar field. Ti/Al ratios in the green cores from the relatively potassic samples indicate that they formed at relatively higher pressures compared to that of their mantling rims, green cores from relatively sodic samples, and other pyroxene phenocrysts. This observation reinforces the xenocrystic nature of the green cores, but does not prove that the relatively potassic lamprophyres come from sources deeper in the mantle.

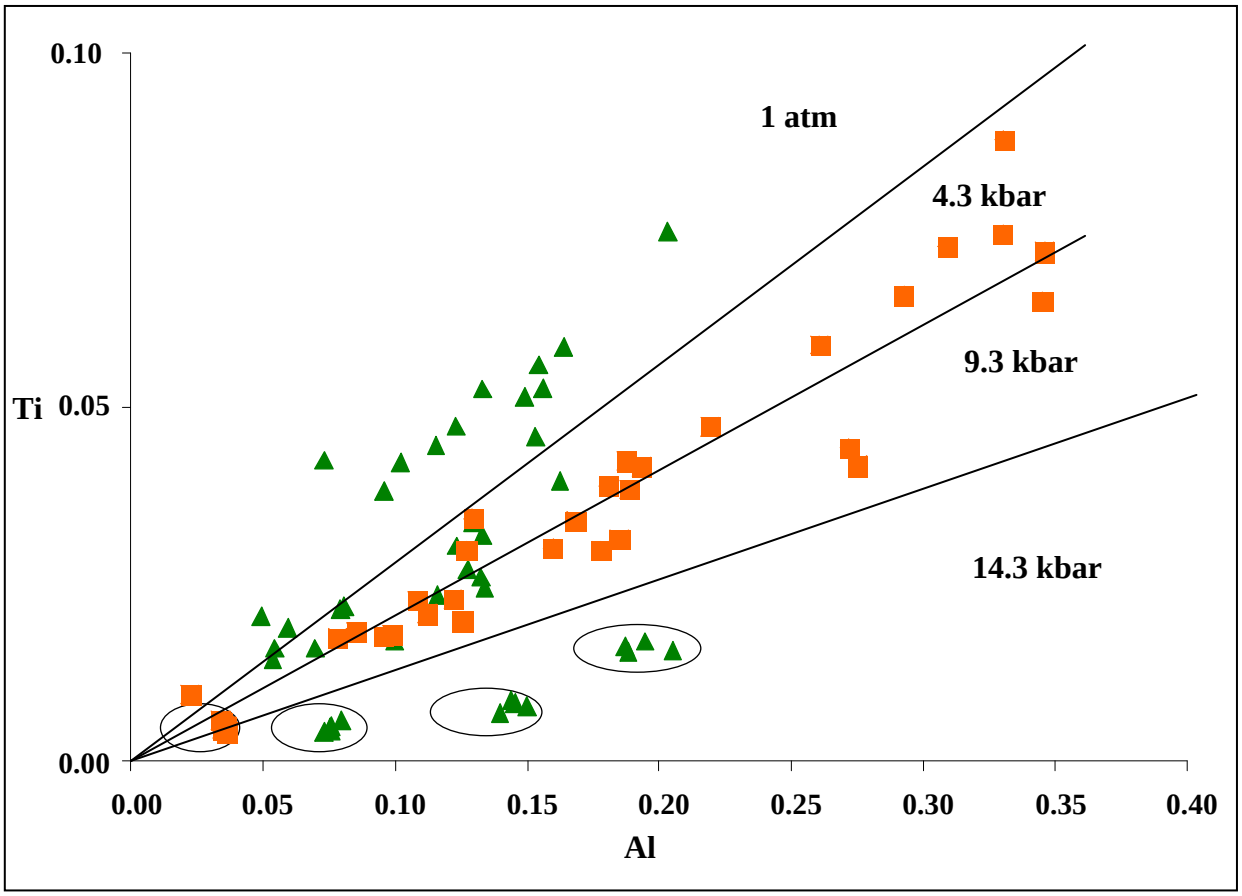

Figure 4.2 Atomic proportions of aluminum and titanium (plotted on x and y-axis respectively). Point analyses are from pyroxenes in Figures 3.46 and 3.47. Green triangles represent samples from relatively potassic, and orange squares represent samples from relatively sodic samples. Circled analyses represent analyses taken from green cores. Pressure field estimates are based on compositions of synthetic cpx created from experiments done on Nandewar hawaiites (Nekvasil et al., 2004).

A positive correlation exists between Ti and Al in the analyzed pyroxenes seen in Figure 4.2. This could reflect a coupled substitution of Ti and Al in pyroxene structure. Pyroxenes can be characterized by the general formula: $(R^{2+}, Ca, Na)_1$ $(R^{2+}, Al, Cr, Ti, Fe^{3+})_1(Si, Al, Fe^{3+})_2O_6$. R^{2+} represents the elements with 2^+ charges (Ca, Mg, Fe, and Mn). As titanium and aluminum are incorporated into the pyroxene structure, the proportions of silicon and magnesium decrease. Figure 4.3 shows that there is a correlation between ½ Ti + Al^{IV} versus Mg and ½ Ti + Al^{IV} versus Si in the pyroxene structure. The trends in Figure 4.3 suggest the following coupled substitution: Ti^{4+}_1, $Al^{3+}_2 \leftrightarrow Mg^{+2}_{-1}$, Si^{+4}_{-2}. This substitution, inferred by the negative trends, is occurring in pyroxenes from both relatively potassic and relatively sodic samples at lower pressures.

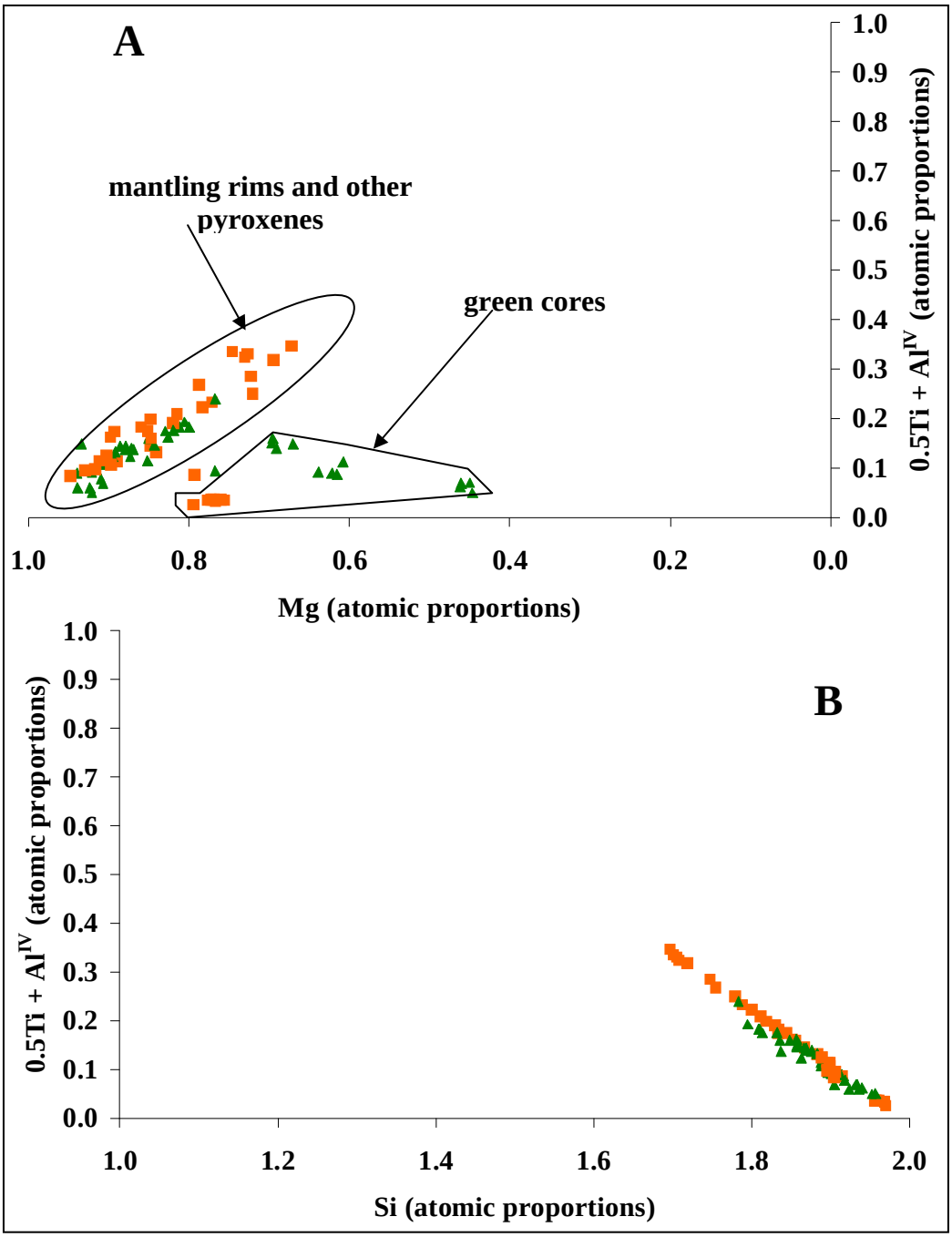

Figure 4.3 A: atomic proportions of magnesium plotted against 0.5 titanium + aluminum of pyroxenes from Figures 3.46 and 3.47. B: atomic proportions of silicon plotted against 0.5 titanium + aluminum of pyroxenes from Figures 3.46 and 3.47.

4.2.2. Amphibole and mica analyses

As stated earlier in sections 3.3.2 and 3.3.4, over 90 point analyses were performed on amphiboles and mica (50 and 40 respectively) from relatively potassic lamprophyres, relatively sodic lamprophyres, and Goemmer Butte trachyandesite. As with pyroxenes, multiple analyses of micas and amphiboles indicate that the ratio of Ti/Al is related to the pressure at which the amphibole and mica form (Patiño Douce, 1993, Konzett, 1997, Tronnes et al., 1985). The Ti/Al ratio decreases in the amphibole and mica structure with increasing pressure. Figure 4.4 shows that the analyzed amphibole and mica from the relatively sodic lamprophyres have lower Ti/Al ratios compared to amphibole and mica from the relatively potassic lamprophyres. These results indicate that the relatively sodic lamprophyres crystallized amphibole at greater pressures (i.e. depth) compared to the relatively potassic lamprophyres. Additionally the amphibole megacrysts and amphiboles from xenocrysts found in the Goemmer Butte trachyandesite have even lower Ti/Al ratios indicating crystallization of amphibole at even greater pressures than in the relatively sodic lamprophyres. Thus, the amphibole Ti/Al ratio reinforce the idea derived from the pyroxene compositions, which is that the relatively sodic lamprophyres underwent some crystallization at relatively high pressures compared to the relatively potassic lamprophyres. However, pressure is not the only intrinsic variable affecting the Ti/Al ratio in the mica structure.

The Ti/Al ratio in the mica is affected by both temperature and pressure (Tronnes et al, 1985). As temperature decreases, the Ti/Al ratio also decreases within the mica structure. An argument could be made that the lower Ti/Al ratio in micas from the relatively sodic magmas could be due to crystallization of the mica at lower temperatures compared to the temperature conditions that the micas from the relatively potassic magmas crystallized. The titanium content in the oxides from the relatively sodic samples reinforces the idea of temperature controlling the Ti/Al in the mica structure. As temperature decreases in magma, oxides crystallizing from the magma will increase the substitution of titanium for iron in the oxide structure (O'Reilly, 1984). Figure 3.60 show that many of the oxides from relatively sodic samples have higher abundances of titanium than the oxides from relatively potassic samples.

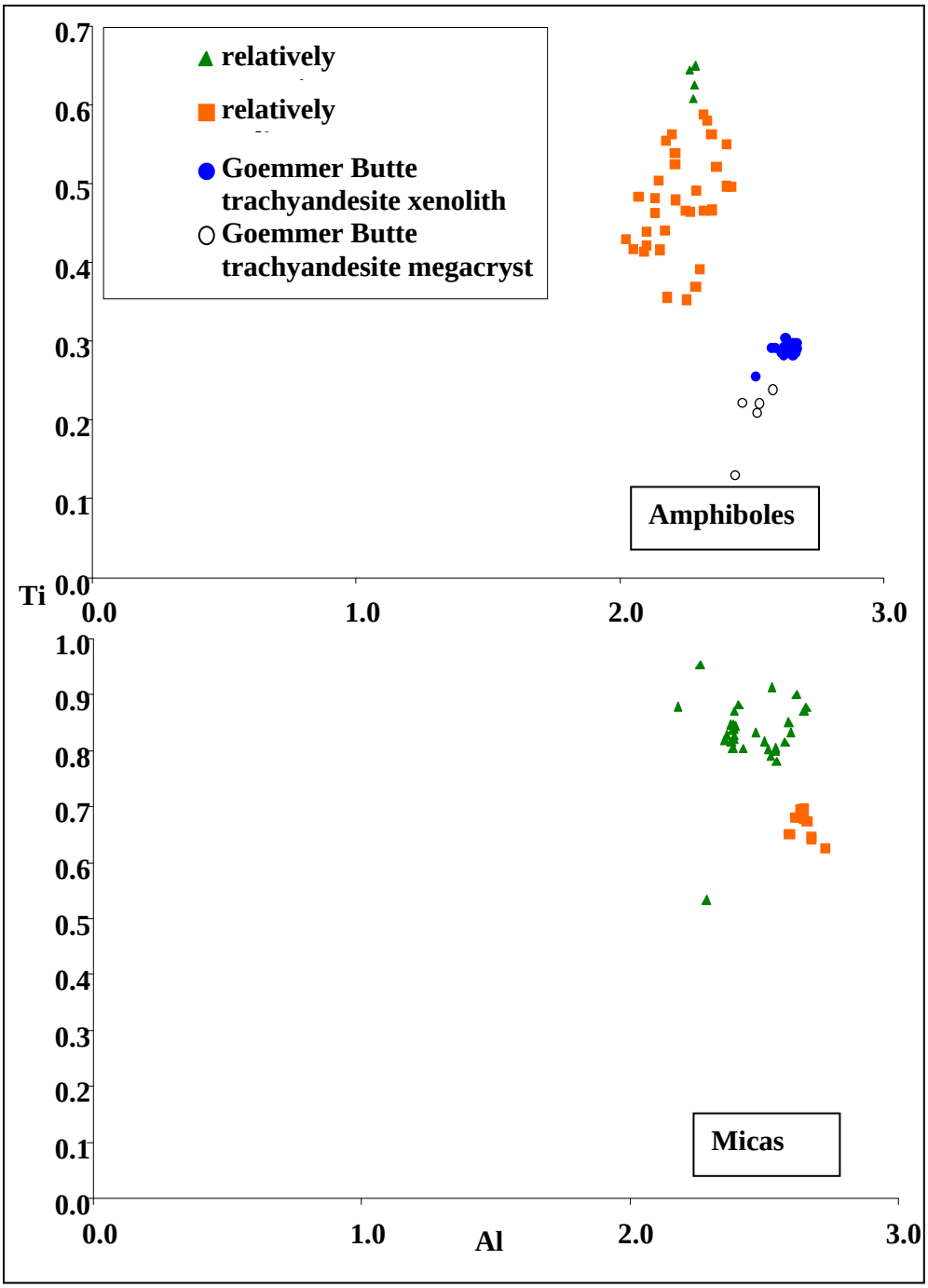

Figure 4.4 Ti and Al cation contents of amphiboles and micas from relatively potassic lamprophyres, relatively sodic lamprophyres, and Goemmer Butte trachyandesite. Note relatively potassic amphiboles and micas have the highest Ti/Al ratios which could indicate formation at relatively shallow depths compared to the amphiboles and micas from the relatively sodic lamprophyres and Goemmer Butte trachyandesite.

In samples where oxides have relatively high Ti/Fe ratios and micas have relatively low Ti/Al ratios, temperature plays a larger role over pressure in the Ti/Al ratio in the mica structure. Additionally, micas

forming at lower temperatures are evidenced texturally in samples that have mica as groundmass mineral only, mica with many inclusions, and mica forming around rims of larger phenocrysts.

4.3. *OCCURRENCE OF BIOTITE/PHLOGOPITE AND AMPHIBOLE IN SPANISH PEAKS LAMPROPHYRES*

Amphibole and mica are the two dominant hydrous phases present in the Spanish Peaks lamprophyres. The lamprophyres with K_2O>4 wt% have phlogopite as the only hydrous phenocryst. "Phlogopite/biotite only" lamprophyres (Figure 4.5) belong to the High K-series, determined by Middlemost (1975). The lamprophyres with $K_2O \leq 4$ wt% can either have phlogopite/biotite, amphibole, or phlogopite/biotite ± amphibole as hydrous phenocryst/groundmass phases. Therefore, a key question is what other factors govern the appearance of mica and amphibole besides the absolute abundance of potassium.

Based on K_2O/Na_2O, the Spanish Peaks lamprophyres were divided into relatively potassic and sodic groups. K_2O/Na_2O works as a discriminant between mica and amphibole dominant assemblages, but as the ratio approaches one, either amphibole or mica can be the dominant hydrous phenocryst. K_2O/Na_2O ratios can be affected by late stage crystal fractionation. This is the case for the relatively potassic sample (HM11) that is dominated by amphibole, and the relative sodic sample (HM25) that is dominated by phlogopite. In both cases, a second hydrous mineral appears only in the groundmass and the dominant hydrous mineral only appears as phenocrysts. This suggests that the K_2O/Na_2O wt% changed during the late stages of the magma evolution (possibly by fractionation of the dominant hydrous phenocryst), which in turn changed the composition of the magma in a way that promoted the growth of a new hydrous phenocryst.

The K_2O/Na_2O ratio compared with TiO_2 wt% is a better discriminant between amphibole and mica dominated assemblages (Figure 4.6). In fact, titanium has been shown to stabilize biotite in magmatic systems (Patiño Douce, 1993). Consequently a plot of TiO_2 wt% versus K_2O/Na_2O wt% is a better discriminant between phlogopite-dominated and amphibole-dominated lamprophyres than just K_2O/Na_2O wt%. An even better discriminant is Na_2O wt% verses Al_2O_3 wt% in Figure 4.7. Any rock

samples with a Na_2O above 3.5 wt % and Al_2O_3 above 14 wt%, are dominated by amphibole. Rocks containing less than these weight percent values are dominated by phlogopite. This could indicate that relatively high Na_2O and Al_2O_3 wt% in magmas with K_2O/Na_2O ratios close to or less than one promote and stabilize the growth of amphibole over phlogopite regardless of TiO_2 wt%.

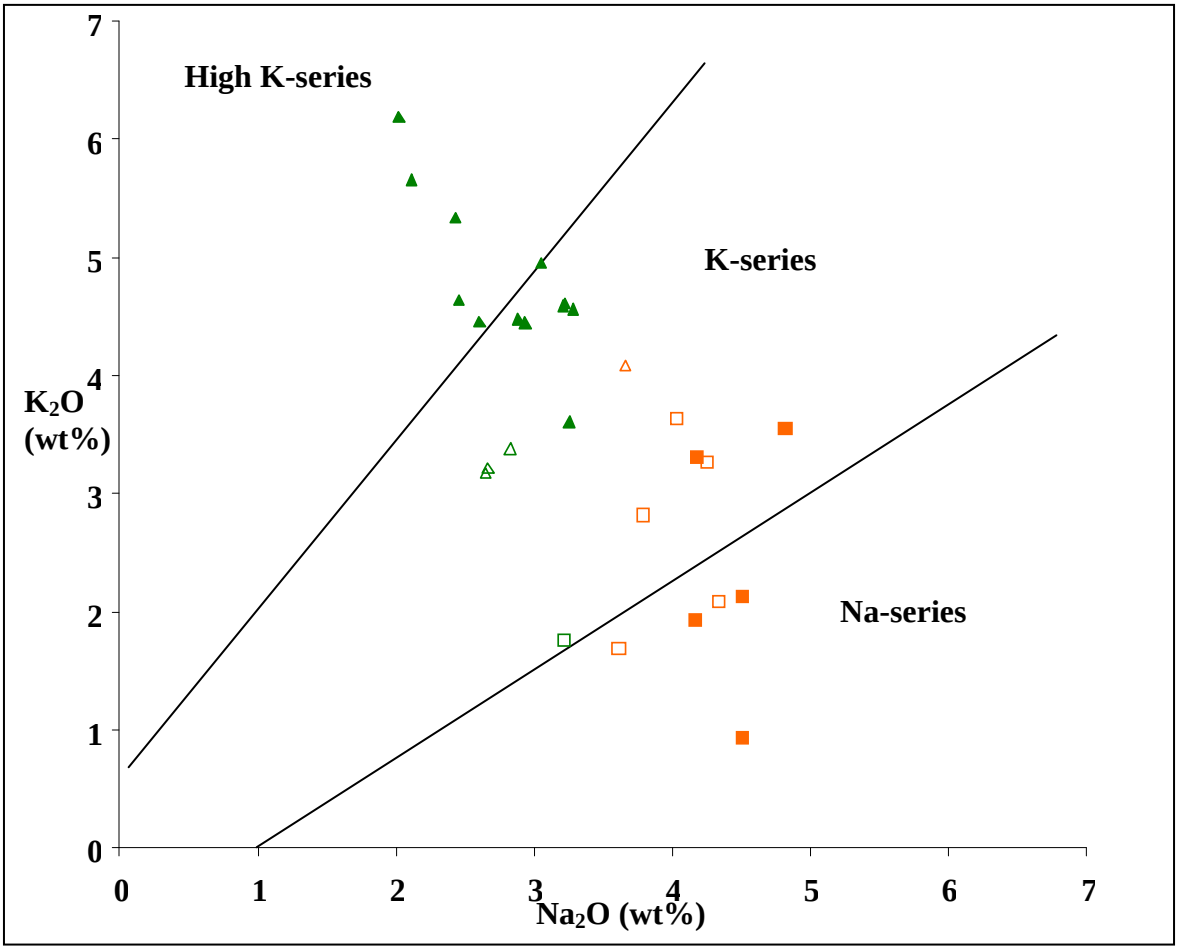

Figure 4.5 K_2O and Na_2O wt% of relatively potassic (green triangles) and relatively sodic (orange squares) lamprophyres of the Spanish Peaks area. Solid symbols represent lamprophyres with phlogopite or amphibole only (solid green triangles, and solid orange squares respectively). Open symbols represent lamprophyres with both mineral phases present and phlogopite or amphibole dominant (open green triangles/squares and open orange squares/triangles respectively). Note that all lamprophyres with more than 4% K_2O have phlogopite only.

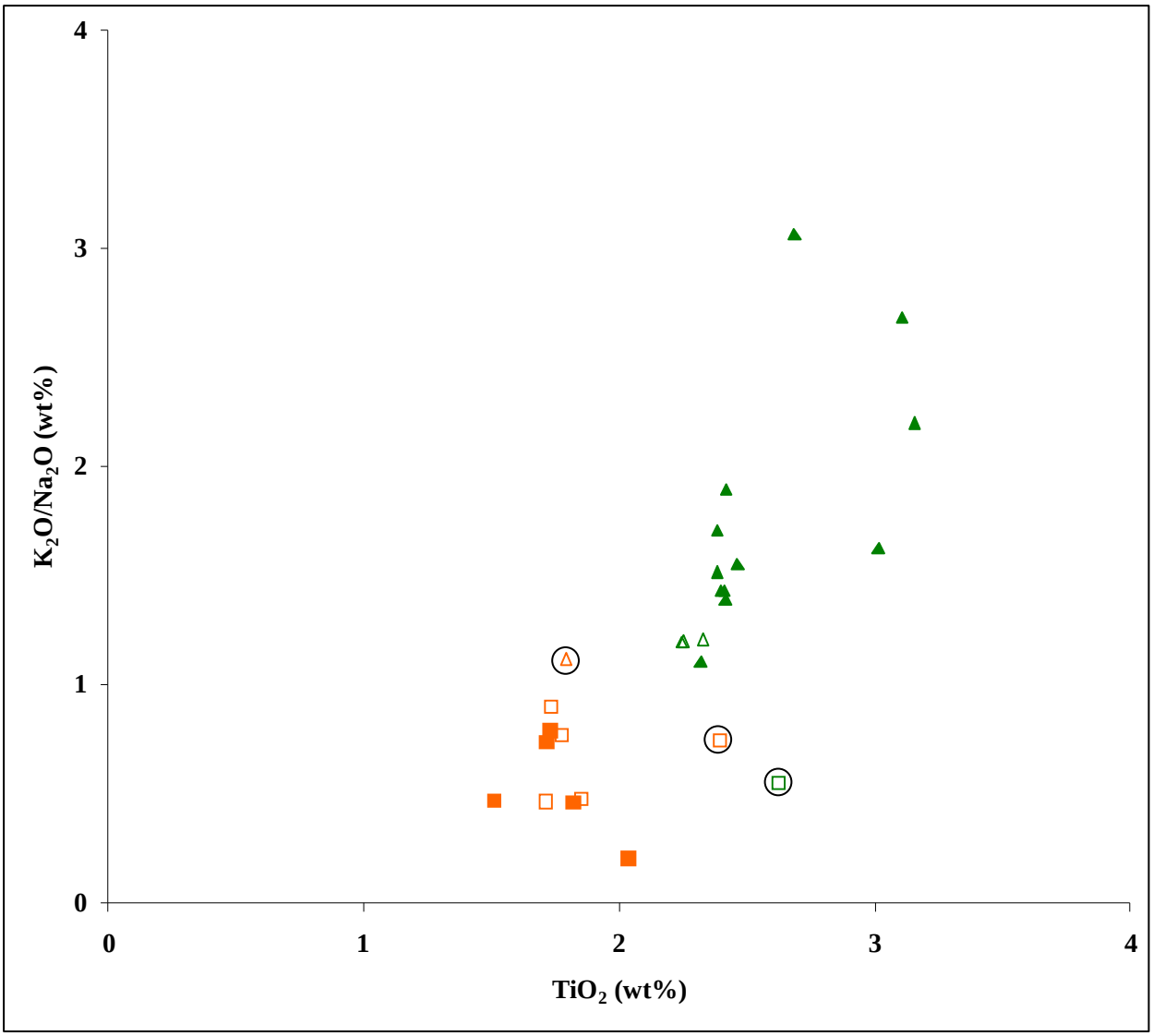

Figure 4.6 Diagram of K_2O/Na_2O wt% ratio vs. TiO_2 wt% of relatively sodic and relatively potassic lamprophyres. Labels are the same as in Figure 4.5. Note how these two variables separate lamprophyres where phlogopite/biotite is the dominant hydrous phenocryst from those which amphibole is the dominant hydrous phenocryst. Circled samples are the exceptions.

In summary, K_2O/Na_2O wt% ratio in the lamprophyres of the Spanish Peaks can be used as a rough guide to discriminate between mica dominant or amphibole dominant assemblages. When using K_2O/Na_2O wt% versus TiO_2 wt%, the separation of rocks in which phlogopite is the dominant phenocryst from those in which amphibole is the dominant phenocryst improves. By using Na_2O wt% versus Al_2O_3 wt% the lamprophyres are completely split into two separate fields consistent with the nature of the dominant hydrous phenocryst. The relatively higher wt% of TiO_2 and K_2O in phlogopite dominated

samples, and relatively higher wt% of Na_2O and Al_2O_3 in amphibole dominated samples, could be indicative of differences in modal mineralogy of the parent source of the two types of rocks in this study.

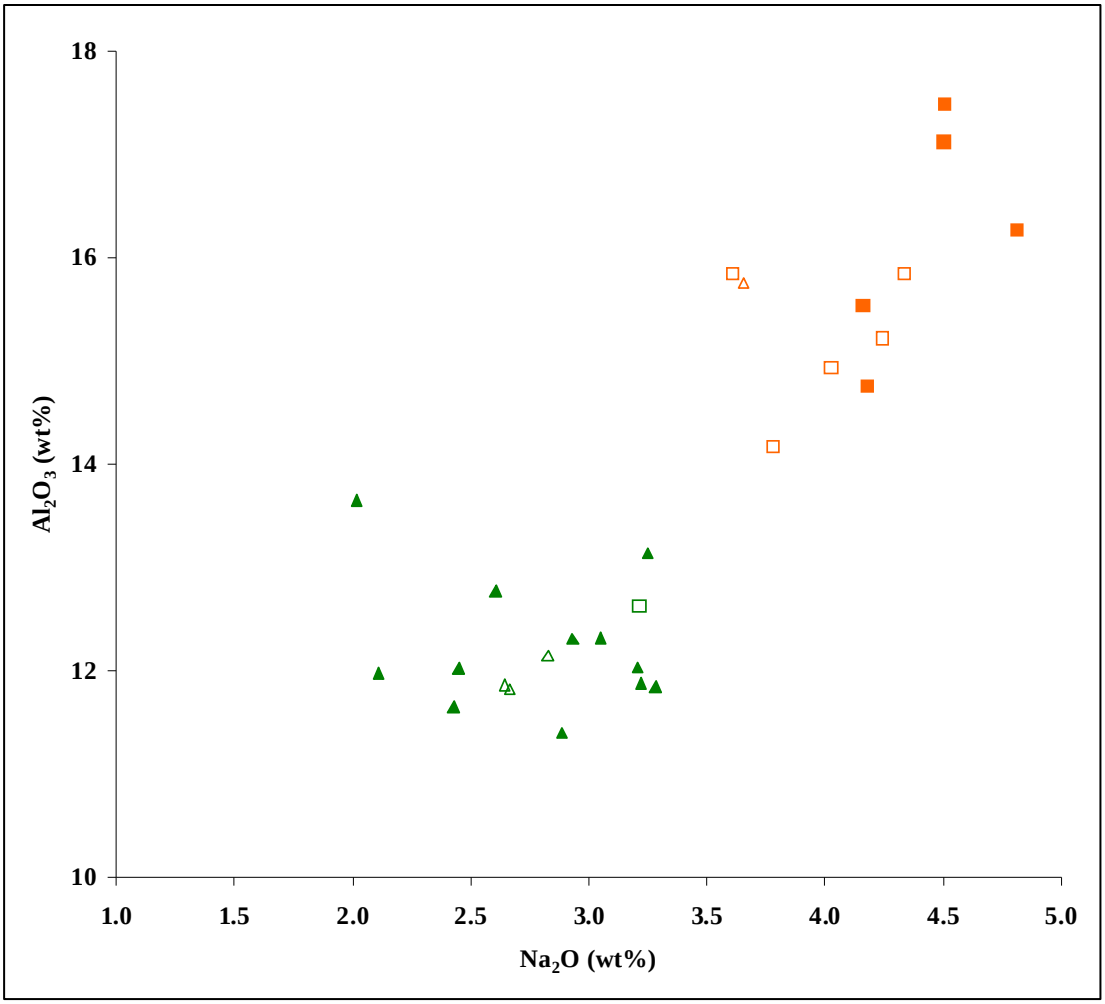

Figure 4.7.Plot of Al_2O_3 wt% vs. Na_2O wt% of relatively sodic and relatively potassic lamprophyres. Labels are the same as in Figure 4.5. Note how these two variables separate the samples by dominant hydrous phase.

4.4. *PARTIAL MELTING OF THE MANTLE AND GENERATION OF LAMPROPHYRES*

Many previous investigations and studies involving lamprophyres have attributed their "parental source" to be located in the mantle (Bachinski et al., 1979, Bachinski et al., 1984, Jahn, 1979, Roden, 1981, Rock, 1990, Miggins, 2002). When the asthenosphere upwells, decompression melting can occur in finite amounts. As a result, subcontinental lithosphere in turn can also melt due to heat transfer from the upwelling asthenosphere.

4.4.1. Upper mantle

The upper mantle is referred to as a "depleted" portion of the mantle because of low abundances of incompatible elements such as LILEs and LREEs (relative to HREEs). This is due to large-scale melting events (up to ~20%) such as those that generate mid-ocean ridge and continental flood basalts. Over time, repeated melting of the residual mantle changes the chemical composition and mineralogy (White, 1985, Litasov, 2000). Melting of the "depleted" upper mantle as a source for the lamprophyres is problematic since lamprophyres are enriched in LREEs and LILEs (relative to HREEs).

Some authors have suggested lamprophyres are generated by relatively small amounts (<<1%)of melting of garnet peridotite (Jahn et al., 1979). In this deeper part of the mantle (i.e. the asthenosphere) large scale melting does not occur (Winter, 2001). Finite melting of a garnet-bearing source could in part explain the high La/Yb ratio and positive slope from HREEs to LREEs (i.e. residual garnet preferentially retains the HREEs). This process alone though, cannot explain the relative high abundances of barium, potassium, and other LILEs.

Various K-silica rich fluids (with varied amounts of H_2O and CO_2) however can "enrich" or recharge portions of the depleted upper mantle with LREEs and LILEs. These metasomatic events can be "cryptic" (such that the existing mineral phases are enriched in LREEs and LILEs without modal changes in mineralogy) (Dawson, 1980). Some metasomatic events also change the modal mineralogy of the mantle. New hydrous phases such as amphibole, phlogopite, apatite, and rutile replace existing phases.

4.4.2. Xenoliths and parental sources of lamprophyric magmatism

Lamprophyres have been identified throughout the world in various tectonic settings (Bussien et al, 2008, Carlier et al, 2005, Dacheng et al, 2004, Fareeduddin et al, 2001, Orejana, 2008). Many rocks associated with and including the lamprophyres are alkalic and range from ultrapotassic to highly sodic in nature. Lithologically variable mantle and crustal xenoliths have been reported in numerous studies involving lamprophyric type rocks (Lloyd, 1981, Kil et al., 2007, Menzies, 1987, Menzies et al., 1987, Roden, 1981, Wilkinson et al, 1987, Vinx et al, 1977). These mafic to ultramafic xenoliths range from harzburgite to lherzolite to clinopyroxenite in composition. Common mineral phases are olivine,

orthopyroxene, clinopyroxene, spinel, ilmenite, and titanomagnetite. In addition, these xenoliths may contain hydrous phases such as pargasite, kaersutite, phlogopite, and/or apatite. In some instances, amphibole and/or mica contribute up to 80% of the modal mineralogy (Frey et al, 1978). The North Lake sill complex contains a clinopyroxenite xenolith in the large sill (results section), and a possible cumulate xenolith was found in the Goemmer Butte trachyandesite (results section). The Goemmer Butte trachyandesite xenolith was comprised of titanian-potassian amphibole, apatite, and magnetite. Other studies of rocks associated in and around the Spanish Peaks area have yielded similar xenolithic material containing kaersutite, titan-augite, oxides and plagioclase (Penn et al, 2009).

Many authors have espoused metasomatized upper mantle as the source of alkaline magmatism (for review Boettcher et al, 1980, Edgar et al., 1992, Waas et al., 1980,). Remelting of this metasomatized mantle generates magmas rich in LILEs (e.g. potassium, rubidium, barium) and LREEs relative to HREEs (high La/Yb ratios). These melts may represent primary magmas that evolved to compositions similar to the lamprophyres of this study.

Ocean island basalts are thought to be a mixture produced by melting of metasomatized mantle and subducted crustal material (Allégre, 1982, Prytulak, 2007, Weaver, 1987, White, 1985). As seen in Figure 4.8, alkaline lamprophyres of this study show affinity to that of ocean island alkaline basalts (OIA). Figure 4.9 is a plot of Al_2O_3 versus MgO and shows data from the Hawaiian Island and other ocean island basalts, along with the lamprophyres from the Spanish Peaks area, and lamprophyric rocks found on the Colorado Plateau and the eastern edge of the Great Plains. The data form two relatively distinct arrays that can be attributed to fractional crystallization and olivine accumulation. Parental magmas for these two trends would have MgO contents of approximately 10-15 wt% and distinct Al_2O_3 content. The relatively sodic lamprophyres would have parental magmas with relatively high Al_2O_3 contents whereas the parental magmas for the relatively potassic lamprophyres would have relatively low Al_2O_3 contents (Figure 4.9). This observation is consistent with and reinforces the generalized view that these two types of lamprophyres have different petrogenesis (Rock, 1990, Jahn, 1979, Williams et al, 1982). However, the two types of lamprophyres from the Spanish Peaks plot in the alkaline field on the

TAS diagram in Figure 3.35. Because of this, there may be some similarity in the parental sources for the two types of lamprophyres.

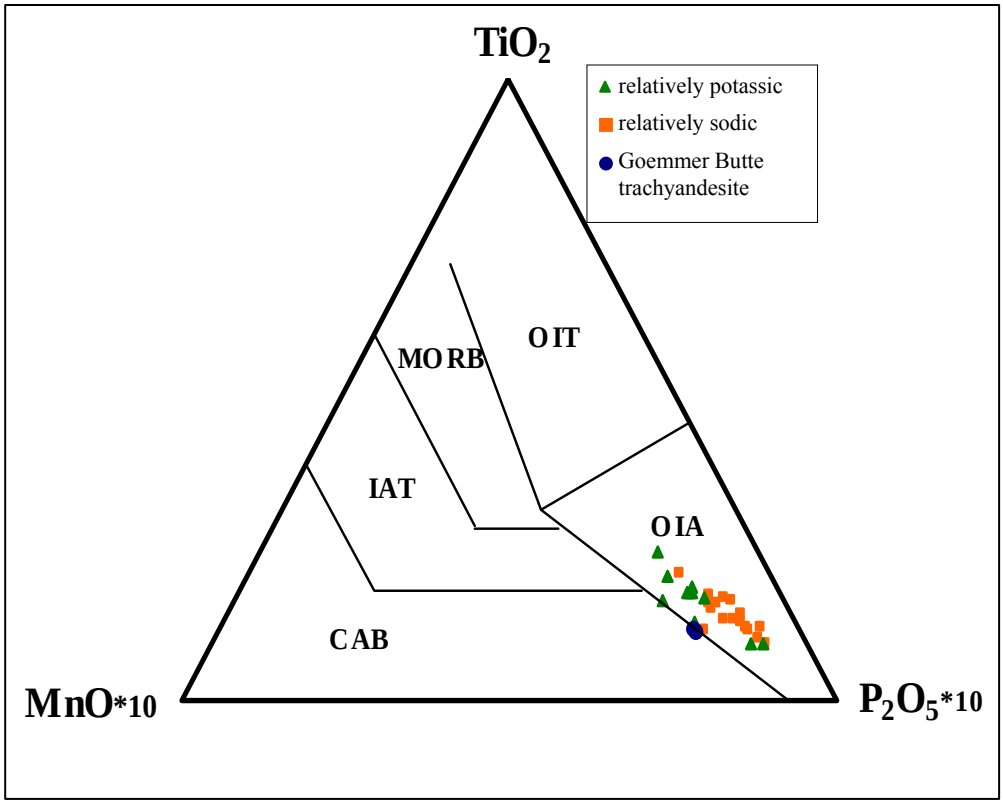

Figure 4.8 Discriminant diagram (Mullen, 1983) illustrating the similarity between ocean island alkaline basalts and the alkaline rocks of this study. OIT= ocean island tholeiite, MORB= mid-ocean ridge basalt, IAT= island arc tholeiite, CAB= calc-alkaline basalt, OIA= ocean island alkaline.

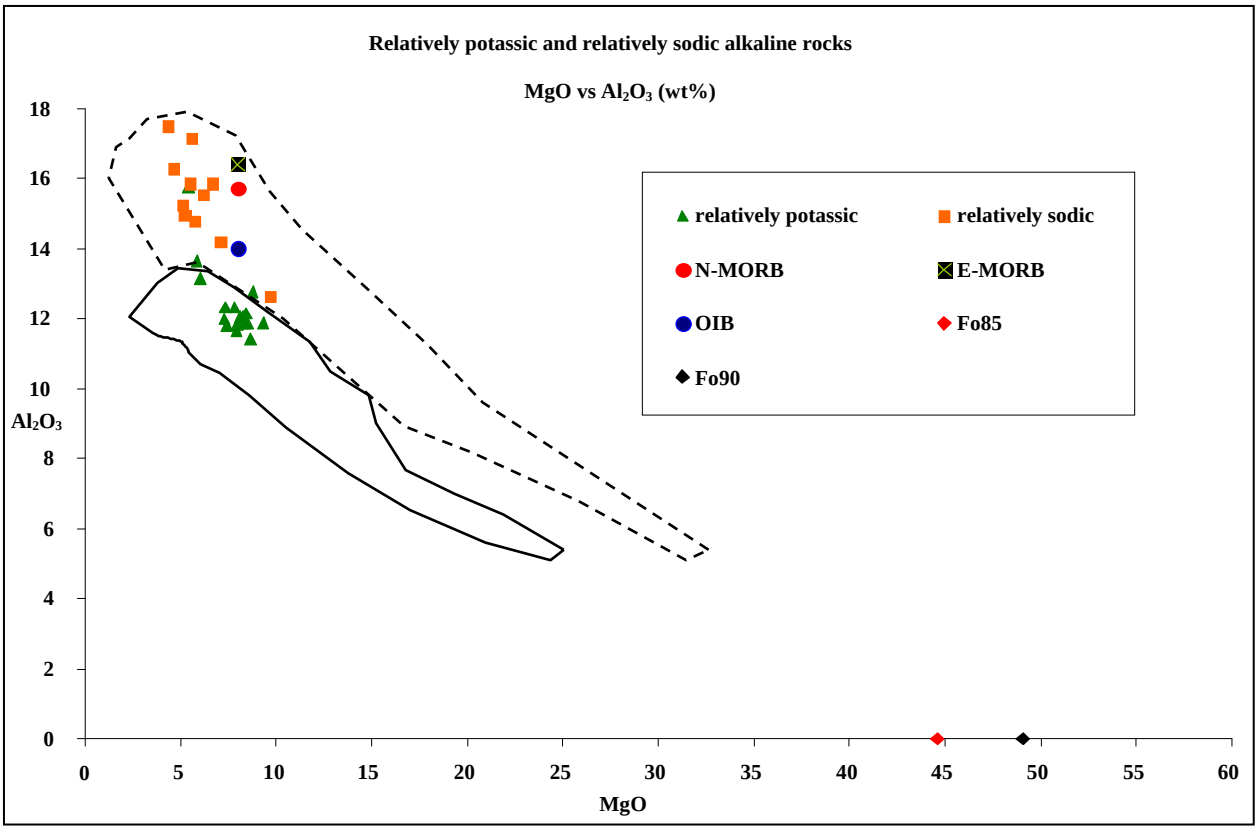

Figure 4.9 Al_2O_3 vs. MgO for lamprophyres from this study compared to averaged N-MORB, E-MORB, and OIB (from Anderson, 2007) Olivine with compositions of Fo_{85} and Fo_{90} are also plotted (Frey et al, 1978). Dashed polygon represents data from ocean islands, alkaline lavas of the San Francisco volcanic field, Hoover dam camptonite, and Two Buttes ultra potassic rocks. Solid polygon represents data from minettes of the Navajo volcanic field, monchiquites of Hopi Buttes, and some ocean island basalts (published and unpublished data from Hawai'i Volcano Geochemical data set and data compiled by D. Smith, written communication, 2009).

4.4.3. Experimental studies on alkaline mafic to ultramafic rocks and the stability of amphibole and phlogopite at high temperatures and pressures in the upper mantle

High pressure and temperature experiments were performed by Esperanca et al., (1987) on minettes from Buell Park located in the Navajo volcanic field on the Colorado plateau. This area flanks the western edge of the Rio Grande rift. The potassic lamprophyres here are similar in composition, texture, and mineralogy to the relatively potassic samples of this study. The experiments show that clinopyroxene and phlogopite are the liquidous phases present at relatively low to medium temperatures (~1050 to ~1175^{o}C) and relatively high pressures (~17 to 20kbar). Additional experiments by Modreski et al., (1972) show that phlogopite is stable and in equilibrium with enstatite, olivine, and vapor up to

~35kbar at ~1190^{o}C. Wendlandt et al., (1980) yielded similar results showing a maximum stability of phlogopite at 30 kb and 1125^{o}C in a spinel lherzolite composition where phlogopite comprises 10% of the bulk composition. These experiments are consistent with phlogopite being a hydrous phase present at relatively high pressures (i.e. at depth) in the upper mantle.

High pressure and temperature experiments have been performed by Allen et al., (1975) on alkaline olivine basalts from Hualalai, Hawaii. The basalts are the anhydrous equivalent in chemical composition to the relatively sodic lamprophyres of this study. These alkaline olivine basalts were subjected to excess H_2O and relatively oxidizing conditions. Results show that amphibole is the dominant hydrous phase, stable at similar pressures and temperatures (~17 to 22kBar) compared to experiments conducted by Esperanca (1987). These observations (along with garnet peridotite xenoliths found in some Navajo minettes) imply that the parental sources of the lamprophyres are from altered upper mantle metasomatic veins rich in cpx and phlogopite and/or amphibole at depths where garnet is stable.

4.4.4. Petrogenesis of relatively sodic and relatively potassic lamprophyres at Spanish Peaks

As metasomatic fluid percolates through the mantle, elements can be leached from existing mineral phases. As mentioned earlier, potassium is an important element that plays a role in the metasomatic fluid that alters the mantle mineralogy. Edgar and Arima (1984) show that aqueous solutions with varying K levels under subsolidous conditions, produce phlogopite at 20 kbar (involving opx + garnet + olivine) and phlogopite at 30 kbar (involving spinel + amphibole + opx + cpx).

Sodium also is a significant element in metasomatic fluids infiltrating mantle material. At increasing depths and pressures, pyroxene incorporates Na into its mineral structure, and invading fluids passing through the mantle at this depth, will incorporate Na from these pyroxenes (Ryabchikov et al., 1980). As fluid ascends through the mantle, the fluid becomes increasingly rich in Na because of the leaching and relative depleted in K because of the phlogopite that forms. Consequently, with decreasing depths in the mantle, the K/Na ratio should decrease in the metasomatic fluid. Arai (1986) also suggests that Na-rich fluids dominate over K-rich fluids in the uppermost mantle. McNeil et al., (1987) conducted

experiments using pyrolite-Na_2O-rich or $Na_2O + K_20$ fluid (K/K + Na = 0.1) system at 950^oC and 20 kbars. The results show that when Na was dominant over K in the fluid at 950^oC and 20 kbar, amphibole was the hydrous phase present. These results are consistent with preliminary experiments by Edgar (1987) at 20kbar and 950^oC (involving aqueous solutions where Na and K were added in varying amounts to equal 3.8g per 10g of solution) which show that when Na was increased relative to K, amphibole stability increased relative to decreasing stability of phlogopite. Consequently, as K/Na decreases in the fluid, amphibole becomes the dominant hydrous phase. As a result, one could expect varying K/Na ratios from magmas generated by re-melting of these metasomatized veins in the mantle (Edgar, 1987).

Two competing models could explain the genesis of the two groups of alkaline rocks in this study. Model 1 could explain the differences in the relatively sodic and relatively potassic Spanish Peaks lamprophyres by melting of metasomatic veins at differing depths and phase assemblages in the mantle. One would expect that comparatively sodic metasomatized zones would be in shallower parts of the mantle and more potassic zones would occur at greater depths in the mantle. Relatively sodic lamprophyres could be derived from a primary melt of a metasomatic vein shallower in the mantle. This vein would be rich in amphibole (relative to phlogopite) and enriched in sodium relative to potassium. The relatively potassic lamprophyres then could be derived from a primary melt of a vein at greater depths, rich in phlogopite and enriched in potassium relative to sodium. In the deeper veins the amphibole, if present, would be K-richterite due to the instability and break down of pargasite at ~ 23 kbars (Edgar, 1987, Foley, 1992) and the relative increase in K/ (K + Na) with increasing pressures (Konzett, 1997). In this scenario, the formation of both types of veins must have occurred shortly before the petrogenesis of the lamprophyres due to the similarity in isotopic compositions of the two types of lamprophyres (Figure 4.10).

Alternatively, model 2 in Figure 4.11 shows the primary magma for the two types of lamprophyres could have been generated at more or less the same depth from a source that had little

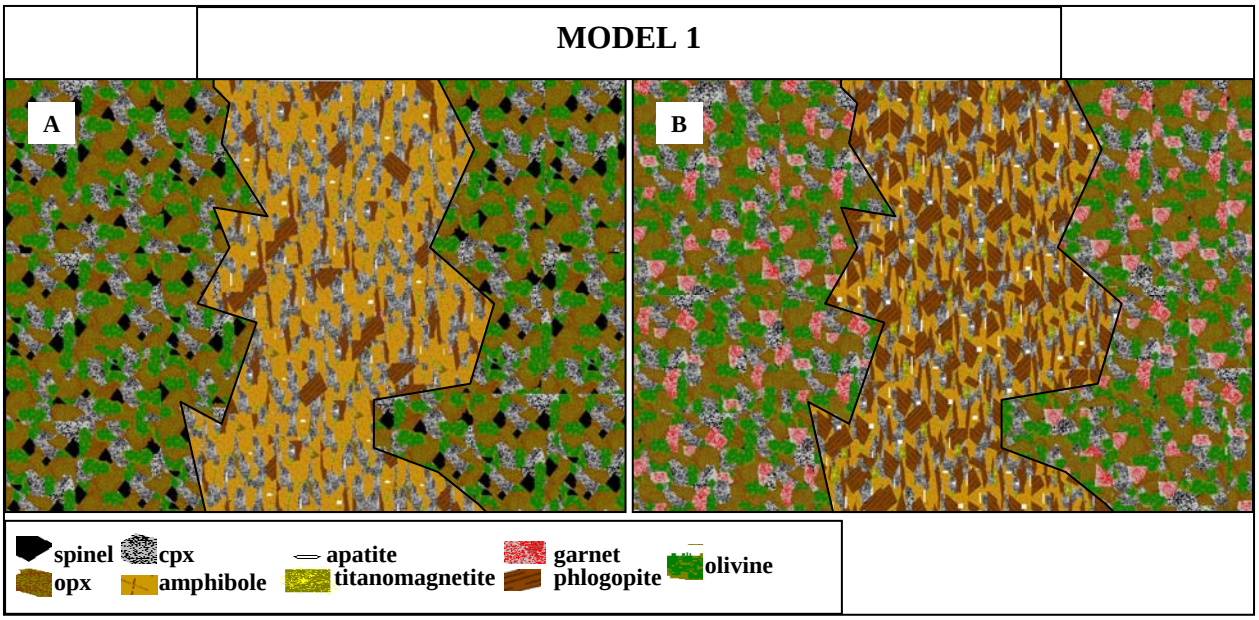

Figure 4.10. Model 1Illustration of metasomatic veins and surrounding mantle that could be possible sources of relatively potassic and relatively sodic lamprophyres. Panel A is a spinel-peridotite and Panel B is a garnet-peridotite. Note the modal change in mineralogy of the metasomatic veins. This reflects the change in K/Na ratio in the veins and hydrous mineral stability as pressure increases. See text for explanation.

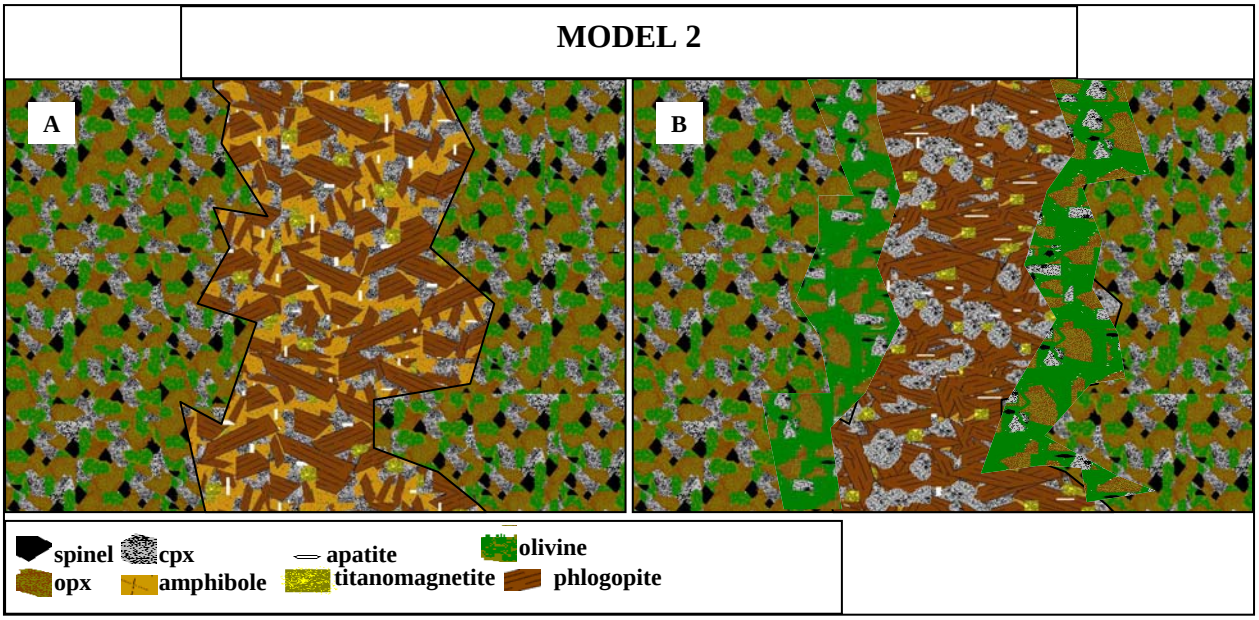

Figure 4.11 Model 2 Illustration depicting a metasomatic vein in spinel peridotite melting to generate two primary melts of differing compositions. Panel A is initial vein mineralogy with little to no melting. At this point amphibole is a contributor of Na_2O and Al_2O_3 to the melt. Later in the process, Panel B shows the same vein, but with amphibole exhausted and phlogopite as the only hydrous phase contributing to the melt. Modeled after Foley, (1992).

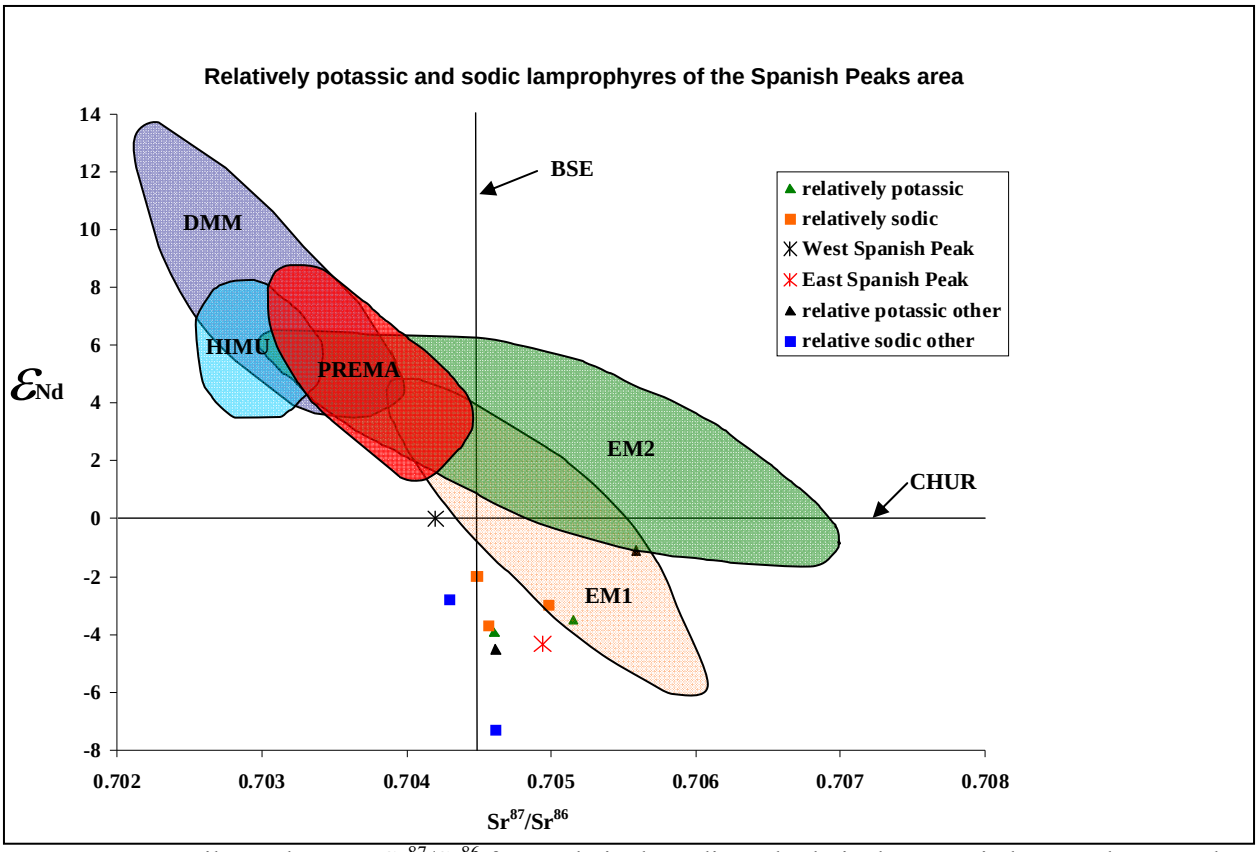

Figure 4.12 Epsilon Nd versus Sr^{87}/Sr^{86} from relatively sodic and relatively potassic lamprophyres and East and West Spanish Peaks. Epsilon Nd is equivalent to $(^{143/144}Nd_{sample}/^{143/144}Nd_{CHUR} -1)*10{,}000$. CHUR = Chondrite unfractionated reservoir, PREMA = primitive and enriched mantle averaged, HIMU = high mantle uranium, DMM = depleted mantle , EM1= enriched mantle 1, EM2= enriched mantle 2, BSE = bulk silicate earth (from Zindler et al., 1986). Green triangles and orange squares (relatively potassic and relatively sodic respectively) represent lamprophyres of this study. Blue squares and black triangles represent additional relatively sodic and relatively potassic lamprophyres of the Spanish Peaks area with different ages. Data compiled from Miggins, (2002), Penn, (1994), and Jahn (1979). Note close proximity of relatively sodic and relatively potassic lamprophyres from this study.

amphibole. The relatively sodic lamprophyres could represent earlier melts when amphibole was a main hydrous phase contributing to the Na_2O and Al_2O_3 wt% of the primary magma. The amphibole would be exhausted early in the melting process and as a result primary melts of phlogopite-rich vein material would begin to dominate (Figure 4.11). The green core xenocrysts could be cpx derived from wall rock when the increased melting of the veins occurred. Aliquots of melt extracted over time reflect the change in mineralogy of the source. Moreover this scenario accounts for the similarity in Sr, Nd isotopic compositions of the two types of lamprophyres in Figure 4.12. These two models may explain the range from sodic to potassic alkaline magmatism occurring between ~23 and 20Ma.

The trace element patterns (in particular the lack of an Nb negative anomaly) in Figure 3.40 preclude fluids derived from subduction processes as the only source of metasomatism of the upper mantle (Weaver et al, 1987). Prior subduction activity during accretion of Yavapai province, 1.76–1.72-Ga and the Mazatzal province, 1.7–1.6-Ga (Karlstrom et al., 1998), could account for incorporation of pelagic sediments in the uppermost mantle beneath the Rio Grande Rift and Spanish Peaks area. Pelagic sediments are enriched in Ti relative to primitive or depleted mantle (Prytulak et al., 2007). Pelagic sediments also are enriched in Ba and depleted in Rb relative to Sr, which would retard the growth of radiogenic Sr (Weaver, 1991). Elevated Ba, Nb, Ti, and low Rb/Sr indicate that ancient pelagic sediments could be part of the parent source of the primary magmas of the rocks from this study.

Gibson et al (1993) suggests that, during the Laramide orogeny the lithospheric upper mantle was shielded from the relatively hotter asthenospheric upper mantle by the subducting Farallon plate. At ~46 Ma, subduction ceased due to the East Pacific Rise impeding or "choking off" the trench. Subsequent roll back of the Farallon plate exposed relatively cool lithospheric upper mantle, to relatively hot asthenospheric upper mantle. Upwelling of the asthenosphere may have caused remelting of the metasomatic veins in the lithospheric upper mantle. Models of mantle conditions proposed by Gibson et al., (1993) and Kil et al., (2007), show the asthenosphere upwelling to ~70 to 100km on the flanks of the Rio Grande rift at ~23-20Ma. This range of 70 to 100km is consistent with the models in Figure 4.10 and Figure 4.11 where melting of metasomatic veins would produce sodic parent and potassic parent magmas.

5. CONCLUSIONS

The purpose of this study was to determine the relationship, if any, between the two types of alkaline lamprophyres (relatively potassic and relatively sodic) associated in space and time. My hypothesis that the relatively potassic and relatively sodic lamprophyres were related through fractional crystallization processes has been proven incorrect by the results yielded from this research.

Major elements (P_2O_5, TiO_2, Na_2O, and K_2O) plotted against Mg# of the most primitive and most evolved lamprophyres indicate the two types of rocks are not related through crystal fractionation processes. This is also evidenced by the relative enrichment of incompatible trace elements (Ba, Th, Rb, and Sr) in the most primitive potassic samples compared to the most primitive sodic samples.

The differences in element ratios Na_2O/TiO_2, Al_2O_3/TiO_2, and Na_2O/P_2O_5, which show little or no effect from crystal fractionation processes, indicate the two types of lamprophyres may have had two different parent sources. The idea of different parental sources is reinforced by a plot of MgO wt% against Al_2O_3 wt%, which indicates the primary melts of the relatively sodic lamprophyre lineage had higher abundances of aluminum compared to the primary melts of the relatively potassic lamprophyre lineage.

Trace element data and limited isotopic ratios indicate the two types of lamprophyres could have been generated from more or less the same type source. Elevated Ba, Ti, Nb and low Rb/Sr indicate that ancient pelagic sediments could be a component of the parental source.

Ti/Al ratios of pyroxenes indicate that the xenocrystic cores from the relatively potassic samples were formed at higher pressures compared to the xenocrystic cores of the relatively sodic samples. The Ti/Al ratios of pyroxenes without xenocrystic cores and the mantling rims of the green cores indicate that the relatively potassic lamprophyric magmas had less residence time in the lower crust/upper mantle at greater pressures and crystallized pyroxenes at relatively shallower depths in the crust compared to the relatively sodic lamprophyres. Amphibole and mica Ti/Al ratios from both types of lamprophyres reinforce this idea as well.

REFERENCES

Allégre, C., 1982, Chemical geodynamics, *Tectnophysics*, 81; 109-132.

Allen, J., Boettcher, A., Marland, G., 1975, Amphiboles in andesite and basalt: I, stability as function of P-T-fO_2, *American Mineralogist*, 60; 1069-1085.

Anders, E., Grevesse, N., 1989, Abundances of the elements, *Geochimica et Cosmochimica Acta*, 53; 197-214.

Anderson, D, 2007, *New theory of the Earth*, Cambridge University Press, New York, 384 p.

Arai, S., 1986, K/Na variations in phlogopite and amphibole of upper mantle peridotites due to fractionation of the metasomatizing fluids, *Journal of Geology*, 94; 436-444.

Bachinski, S., Simpson, E., 1984, Ti-phlogopites of the Shaw's Cove minette: a comparison with micas of other lamprophyres, potassic rocks, kimberlites, and mantle xenoliths, *American Mineralogist*, 69; 41-56.

Bachinski, S., Scott, R., 1979, Rare-earth and other trace element contents and the origins of minettes (mica-lamprophyres), *Geochimica et Cosmochimica Acta*, 43; 93-100.

Blatt, H., Tracy, R., Owens, B., 2006, *Petrology: Igneous, Sedimentary, and Metamorphic*, New York, W.H. Freeman and Company, 530 p.

Boettcher, A., O'neil, J., 1980, Stable isotope, chemical, and petrographic studies of high-pressure amphiboles and micas: evidence for metasomatism in the mantle source regions of alkali basalts and kimberlites, *American Journal of Science*, 280; 594-621.

Bor-ming, J., 1979, REE distribution and petrogenesis of the Spanish Peaks complex, Colorado, *Contributions to Mineralogy and Petrology*, 70; 281-298.

Brooks, K., 1976 The Fe_2O_3/FeO ratio of basalt analyses: an appeal for a standardized procedure, *Bulletin of the Geological Society of Denmark*, 25; 117-120.

Bussien, D., Bussy, F., Masson, H., Magna, T., Rodionov, N., 2008, Variscan lamprophyres in the Lower Penninic domain (Central Alps): age and tectonic significance, *Bulletin Society Geology of France*, 179; 361-381.

Carlier, G., Lorand, J., Liégeois, J., Fornari, M., Soler, P., Carlotto, V., Cárdenas, J., 2005, Potassic-ultrapotassic mafic rocks delineate two lithospheric mantle blocks beneath the southern Peruvian Altiplano, *Geology*, 33; 601-604.

Coombs, D., 1963, Trends and affinities of basaltic magmas and pyroxenes as illustrated on the diopside-olivine-silica diagram, *in* Special-Paper, *Mineralogical Society of America*, 1; 227-250.

Cox, K., Bell. J., Pankhurst, R., 1979, *The interpretation of igneous rocks*, George Allen & Unwin, London, 450 p.

Dacheng, J., Ruizhong, H., Yan, L., Guiquing, X., Xuelin, Q., 2004, Characteristics of the mantle source region of sodium lamprophyres and petrogenetic tectonic setting in northeastern Hunan, China, *Science in China Ser D Earth Sciences*, 47; 559-569.

Dawson, J., 1980, Kimberlites and their xenoliths, in *Minerals and Rocks*, Springer-Verlag, Berlin Heidelberg, New York, 15; 252 p.

Deer, W., Howie, R., Zussman, J., 1992, *An Introduction to the Rock-Forming Minerals*, Pearson/Prentice Hall Harlow, England, 696 p.

Dobosi, G., Fodor, R., 1992, Magma fractionation, replenishment, and mixing as inferred from green-core clinopyroxenes in Pliocene basanite, southern Slovakia, *Lithos*, 28; 133-150.

Droop, G., 1987, A general equation for estimating Fe^{3+} concentrations in ferromagnesian silicates and oxides from microprobe analyses, using stoichiometric criteria, *Mineralogical Magazine*, 51; 431-435.

Dyar, D., Burns, R., 1986, Mossbauer spectral study of ferruginous one-layer trioctahedral micas, *American Mineralogist*, 71; 955-965.

Edgar, A., 1987, The genesis of alkaline magmas with emphasis on their source regions: inferences from experimental studies, in Fitton, J., Upton, B., eds, *Alkaline Igneous Rocks*, Geological Society Special Publications No.30, 29-52.

Edgar, A,. Arima, M., 1984, Experimental studies on K-metasomatism of a model pyrolite mantle and their bearing on the genesis of ultrapotassic magmas, *Proc. 27th Intl. Geological Congress*, 9; 509-541.

Edgar, A., Vukadinovic, D., 1992, Implications of experimental petrology to the evolution of ultrapotassic rocks, *Lithos*, 28; 205-220.

Esperanca, S., Holloway, J., On the origin of some mica-lamprophyres: experimental evidence from a mafic minette, *Contributions to Mineralogy and Petrology*, 95; 207-216.

Fareeduddin, I., Kirmani, Basavalingu, B., 2001, Petrology of ocellar lamprophyres in South Delhi Fold Belt, Danva, Sirohi District, Rajasthan, India, *Gondwana Research*, 4; 497-508.

Foley, S., 1992, Petrological characterization of the source components of potassic magmas: geochemical and experimental constraints, *Lithos*, 28; 187-204.

Foley, S., 1992, Vein-plus-wall-rock melting mechanism in the lithosphere and the origin of potassic alkaline magmas, *Lithos*, 28; 435-453.

Frey, F., Prinz, M., 1978, Ultramafic inclusions from San Carlos, Arizona: petrologic and geochemical data bearing on their petrogenesis, *Earth and Planetary Science Letters*, 38; 129-176.

Gibson, S., Thompson, R., Leat, P., Morrison, M., Hendry, G., Dickin, A., Mitchell, J., 1993, Ultrapotassic magmas along the flanks of the Oligo-Miocene Rio Grande Rift, USA; monitors of the zone of lithospheric mantle extension and thinning beneath a continental rift, *Journal of Petrology*, 34; 187-228.

Haggerty, S., 1976, Opague mineral oxides in terrestrial igneous rocks, in Oxide Minerals, *Mineralogical Society of America Short Course Notes*, 3; Hg101-Hg300.

Irvine, T, Baragar, W., 1971, A Guide to the chemical classification of the common volcanic rocks, *Canadian Journal of Earth Sciences*, 8; 523-548.

Johnson, R., 1961, Patterns and origin of radial dike swarms associated with West Spanish Peak and Dike Mountain, south-central Colorado, *Geological Society of America Bulletin*, 72; 579-589.

Johnson, R., 1968, Geology of the igneous rocks of the Spanish Peaks region, *in* U.S. Geological Survey Professional Paper, Report, P 0594-G, 47.

Karlstrom, K., Humphreys, E., 1998, Persistent influence of Proterozoic accretionary boundaries in the tectonic evolution of southwestern North America:Interaction of cratonic grain and mantle modification events, *Rocky Mountain Geology*, 33; 161-179.

Kil, Y., Wendlandt, R., 2007, Depleted and enriched mantle processes under the Rio Grande rift: spinel peridotite xenoliths, *Contributions to Mineralogy and Petrology*, 154; 135-151.

Knopf, A., 1936, Igneous geology of the Spanish Peaks region, Colorado, *Geological Society of America Bulletin*, 47; 1727-1784.

Konzett, J., Sweeney, A., Thompson, Ulmer, P., 1997, Potassium amphibole stability in the upper mantle: an experimental study in a peralkaline KNCMASH system to 8.5 GPa, *Journal of Petrology*, 38; 537-568

Konzett, J., 1997, Phase relations and chemistry of Ti-rich K-richterite-bearing mantle assemblages: an experimental study to 8.0 GPa in a Ti-KNCMASH system, *Contributions to Mineralogy and Petrology*, 128; 385-404.

Le Bas, M., Le Maitre, R., Streckeisen, A., Zanettin, B., 1986, Chemical classification of volcanic rocks based on the total alkali-silica diagram, *Journal of Petrology*, 27; 745-750.

Leake, B., 1978, Nomenclature of amphiboles, *Canadian Mineralogist*, 16; 501-520.

Lipman, P., Prostka, H., Christiansen, R., 1972, Cenozoic volcanism and plate-tectonic evolution of the western United States, part 1 early and middle Cenozoic, in a discussion on volcanism and structure of the earth, *Royal Society of London Philosophical Transactions A*,, 271; 217-248.

Litasov, K., Foley, S., Litasov, Y., 2000, Magmatic modification and metasomatism of the subcontinental mantle beneath the Vitim volcanic field (East Siberia): evidence from trace element data on pyroxenite and peridotite xenoliths from Miocene picrobasalt, *Lithos*, 54; 84-114.

Lloyd, F., 1981, Upper-mantle metasomatism beneath a continental rift: clinopyroxenes in alkali mafic magmas and nodules from South West Uganda, *Mineralogical* Magazine, 44; 3l5-323.

Lofgren, G., Huss, G., Wasserburg, G., 2006, An experimental study of trace-element partitioning between Ti-Al-clinopyroxene and melt: equilibrium and kinetic effects including sector zoning, *American Mineralogist,* 91; 1596-1606.

McDonough, W., Sun, S., 1995, The composition of the earth, *Chemical Geology*, 120; 223-253.

McNeil, A., Edgar, A., 1987, Sodium-rich metasomatism in the upper mantle: Implications of experiments on the pyrolite-Na_2O-rich fluid system at 95O"C, 20 kbar, *Geochimica et Cosmochimica Acta*, 51; 2285-2294.

Menzies, M., Hawkesworth, C., 1987, *Mantle metasomatism*, Acad. Press, London, United Kingdom, 472 p.

Menzies, M., 1987, Alkaline rocks and their inclusions: a window on the Earth's interior, in Fitton, J., Upton, B., eds, *Alkaline Igneous Rocks*, Geological Society Special Publications No.30, 15-27.

Middlemost, E., 1975, The basalt clan, *Earth-Science Reviews*, 11; 337-364.

Miggins, D., 2002, Chronologic, geochemical, and isotopic framework of igneous rocks within the Raton Basin and adjacent Rio Grande Rift, south-central Colorado and northern New Mexico, unpublished thesis, University of Colorado at Boulder, 379 p.

Morimoto, N., 1989, Nomenclature of pyroxenes, *Canadian Mineralogist*, 27; 143-156.

Modreski, P., Boettcher, A., 1972, The stability of phlogopite + enstatite at high pressures: a model for micas in the interior of the earth, *American Journal of Science*, 272; 852-869.

Mullen, E., 1983, $MnO/TiO_2/P_20_5$ a minor element discriminant for basaltic rocks of oceanic environments and its implications for petrogenesis, *Earth and Planetary Science Letters*, 62; 53-62.

Muller, O., 1986, Changing stresses during emplacement of the radial dike swarm at Spanish Peaks, Colorado, *Geology*, 14; 157-159.

Nagasawa H., Schreiber, H., Morris, R., 1980, Experimental mineral/liquid partition coefficients of rare earth elements (REE), Sc and Sr for perovskite, spinel and melilite, *Earth and Planetary Science Letters*, 46; 431-437.

Nekvasil H., Dondolini A., Horn J., Filiberto J., Long H., Lindsley D., 2004, The origin and evolution of silica-saturated alkalic suites: an experimental study, *Journal of Petrology*, 45; 693–721.

Nenova, P., 1997, "Fe23": A computer program for calculating the number of Fe^{+2} and Fe^{+3} ions in minerals, *Computers & Geosciences*, 23; 215-219.

Odé, H., 1957, Mechanical analysis of the dike pattern of the Spanish Peaks area, Colorado, *Bulletin of the Geological Society of America*, 68; 567-576.

O'Reilly, W., 1984, *Rock Magmatism, Fundamentals and frontiers*, Blackie and Son Ltd, Bishopbriggs, Glasgow, 220 p.

Orejana, D., Villaseca, C., Paterson, B., 2006, Geochemistry of pyroxenitic and hornblenditic xenoliths in alkaline lamprophyres from the Spanish Central System, *Lithos*, 86; 167-196.

Patiño Douce, 1993, Titanium substitution in biotite: an empirical model with applications to thermometry, 0_2 and HeO barometries, and consequences for biotite stability, *Chemical Geology*, 108; 133-162.

Penn, B., 1994, An investigation of the temporal and geochemical characteristics and the petrogenetic origins of the Spanish Peaks intrusive rocks of south-central Colorado, unpublished Ph.D dissertation, University Colorado school of mines.

Penn, B., Lindsey, D, 1996, Tertiary igneous rocks and laramide structure and stratigraphy of the Spanish Peaks region, south –central Colorado, *in* Road Log and Descriptions from the Walsenburg to La Veta (first day) and La Veta to Aguilar (second day), Colorado Geological Survey Open-File Report, 96-4; 21.

Penn, B., Lindsey, D., 2009, $^{40}Ar/^{39}Ar$ dates for the Spanish Peaks intrusions in south-central Colorado, *Rocky Mountain Geology*, 44; 17-32.

Prytulak, J., Elliott, T., 2007, TiO_2 enrichment in ocean island basalts, *Earth and Planetary Science Letters,* 263; 388-403.

Rock, N., 1977, The nature and origin of lamprophyres: some definitions, distinctions, and derivations, *Earth-Science Reviews*, 13; 123-169.

Rock, N., 1987, The nature and origin of lamprophyres: an overview, from *Alkaline igneous rocks,* Geological Society Special Publications, 191-226.

Rock, N., 1990, *Lamprophyres*, Blackie and Son Ltd, Bishopbriggs, Glasgow, 285 p.

Roden, M., 1981, Origin of coexisting minette and ultramafic breccia, Navajo Volcanic Field, *Contributions to Mineralogy and Petrology*, 77; 195-206.

Roden, M., Shimizu, N., 1993, Ion microprobe analyses bearing on the composition of the upper mantle beneath the Basin and Range and Colorado Plateau provinces, *Journal of Geophysical Research*, 98; 14,091-14,108.

Roden, M., Shimizu, N., 2000, Trace element abundances in mantle-derived minerals which bear on compositional complexities in the lithosphere of the Colorado Plateau, *Chemical Geology*, 165; 283-305.

Ryabchikov, I., Boettcher, A., 1980, Experimental evidence at high pressure for potassic metasomatism in the mantle of the earth, *American Mineralogist*, 65; 915-919.

Shaw, C., Penczak, R., 1996, Barium- and titanium-rich biotite and phlogopite from the western and eastern gabbro, Coldwell alkaline complex, northwestern Ontario, *Canadian Mineralogist*, 34; 967-975.

Shaw, D., 1970, Trace element fractionation during anatexis, Geochimica et Cosmochimica Acta, 34; 237-243.

Shaw, D., Taylor, S., 2006, *Trace elements in magmas; a theoretical treatment*, Cambridge University Press, New York, New York, 243 p.

Shimizu, N., 1989, The oscillatory trace element zoning of augite phenocrysts, *Earth-Science Reviews*, 29; 27-37

Smith, R. 1975, Structure of the Spanish Peaks dikes, south-central Colorado, unpublished Ph.D dissertation, University of Colorado, 131 p.

Tronnes, R., Edgar, A., Arima, M., 1985, A high pressure-high temperature study of $Ti0_2$ solubility in Mg-rich phlogopite: implications to phlogopite chemistry, *Geochimica et Cosmochimica Acta*, 49; 2323-2329.

Wass, S., 1979, Multiple origins of clinopyroxenes in alkali basaltic rocks, *Lithos*, 12; 115-132.

Wass, S., Henderson, P., Elliott, C., 1980, Chemical heterogeneity and metasomatism in the upper mantle: evidence from rare earth and other elements in apatite-rich xenoliths in basaltic rocks from eastern Australia, *Philosophical Transactions of the Royal Society of London. Series A. Mathematical and Physical Sciences*, 297; 333-346.

Weaver, B., 1991, The origin of ocean island basalt end-member compositions trace element and isotopic constraints, *Earth and Planetary Science Letters*, 104; 381-397.

Weaver, B., Wood, D., Tarney, J., Joron, J., 1987, Geochemistry of ocean island basalts from the South Atlantic: Ascension, Bouvet, St. Helana, Gough and Tristan da Cunha, in Fitton, J., Upton, B., eds, *Alkaline Igneous Rocks*, Geological Society Special Publications No.30,

Wendlandt, R., Eggler, D., 1980, The origins of potassic magmas: 2. Stability of phlogopite in natural spinel lherzolite and in the system KAlSiO4-MgO-SiO2-H2O-CO2 at high temperatures, *American Journal of Science*, 280; 421-458.

White, W., 1985, Sources of oceanic basalts: radiogenic isotopic evidence, *Geology*, 13; 115-118.

Williams, H., Turner, F., Gilbert, C., 1982, Lamprophyres and ultrabasic rocks of extreme composition, in *Petrography An Introduction to the Study of Rocks in Thin Sections*, 227-259.

Wilkinson, J., Le Maitre, R., 1987, Upper mantle amphiboles and micas and TiO_2, K_2O, and P_2O_5 abundances and 100 $Mg/(Mg + Fe^{2+})$ ratios of common basalts and andesites: implications for modal mantle metasomatism and undepleted mantle compositions, *Journal of Petrology*, 28; 37-73.

Winter, J., 2001, *An introduction to igneous and metamorphic petrology*, Prentice Hall, Upper Saddle River, New Jersey, 697 p.

Vieten, K., Hamm, H., 1978, Additional notes "on the calculation of the crystal chemical formula of clinopyroxenes and their contents of Fe^{3+} from microprobe analyses, Neues Jahrbuch für Mineralogie – Monatshefte, 71-83.

Vinx, R., Jung, D., 1977, Pargasitic-kaersutitic amphibole from a basanitic diatreme at the Rosenberg, north of Kassel (North Germany), *Contributions to Mineralogy and Petrology*, 65; 135-142.

Yoder, H., Tilley, C., 1962, Origin of basalt magmas: an experimental study of natural and synthetic rock systems, *Journal of Petrology*, 3; 342-532.

Yoder, H., 1979, *The evolution of the igneous rocks; fiftieth anniversary perspectives*, Princeton University Press, Princeton, N.J., United States, 588 pp.

APPENDIX

The following appendix has detailed petrographic descriptions of thin section samples collected and used in determining modal mineralogy of rock samples. Modal % based on 200 point counts of phenocrysts only.

Sample: HM-2

Texture: This sample has a very fine-grained porphyritic texture. Moderate clinopyroxene, biotite/phlogopite, and olivine (~ 48%, 42%, and 10% respectively) are the framework of the large phenocrysts that range up to ~ 1.5mm in length. Most of the large phenocrysts (especially Fe, Mg silicates) show signs of alteration to some form of iron oxide. The surrounding groundmass consists of the above mentioned phenocrysts, abundant iron oxides, sparse apatite and slightly altered massive anhedral feldspar. Additionally there are ocelli (up to ~ 5mm) bound by prisms of clinopyroxene and are filled with an altered colorless mineral.

Phenocryst mineralogy:

Mineral: *Clinopyroxene*

Size: Seriate in size from groundmass to ~ 0.50mm, with a few ~1.25mm.

Habit: The majority of the grains are euhedral to subhedral and blocky with some forming clusters and having polysynthetic twinning seen under crossed polars. Most grains have inclusions of iron oxide with a few of the larger ones having inclusions of biotite.

Color: Clear to pale yellow-green with some having to clear centers and pale yellow-green rims

Zoning: normal concentric zoning

Modal %: ~48%

Mineral: *Biotite/phlogopite*

Size: Seriate from groundmass up to ~0.50mm in length

Habit: The majority of the grains are subhedral, blocky to elongate with inclusions iron oxide. There are sparse large phenocrysts up to 4.5mm in length, which have a rim of iron oxide.

Color: Brown to reddish brown pleochroism

Zoning: normal zoning even colored throughout

Modal %: ~ 42%

Mineral: *Olivine*

Size: Seriate from groundmass up to ~ 0.75mm in diameter

Habit: The majority of these grains are anhedral to subhedral in shape altered to some type of clay mineral and iron oxide.

Color: Greenish-brown

Zoning: darker colored to lighter colored from center to rim

Modal %: ~10%

Sample: HM-4

Texture: This sample has a fine-grained porphyritic texture. Abundant biotite and clinopyroxene (~80%, 20% respectively) comprise the majority of the large phenocrysts that range in size up to 3.00mm in length. The groundmass consists of smaller grains of biotite/phlogopite, cpx, apatite, and iron oxides all of which overprint a mass of anhedral, plated potassium feldspar.

Phenocryst mineralogy:

Mineral: *Biotite/phlogopite*

Size: Seriate from groundmass up to ~3mm in length

Habit: The majority of the grains are euhedral to subhedral, elongate to blocky with many inclusions of apatite, cpx, and iron oxide.

Color: Brown to reddish brown pleochroism

Zoning: normal zoning even colored throughout

Modal %: ~ 80%

Mineral: *Clinopyroxene*

Size: Seriate from groundmass up to ~ 0.75mm in length

Habit: The majority of the grains are euhedral to subhedral elongate, needle like with a few of the grains forming clusters.

Color: pale yellow-green

Zoning: normal concentric zoning

Modal %: ~20%

Sample: HM-3

Texture: This sample has a fine-grained porphyritic texture. Large fresh olivine with moderate biotite/phlogopite, clinopyroxene, and potassium feldspar (~30%, 30%, 25%, and 15% respectively) comprises the large phenocrysts that range in size up to 4.5mm in length. The groundmass consists of smaller grains of biotite, cpx, olivine, apatite, and iron oxides all of which overprint a mass of anhedral, enclosing, potassium feldspar. Additionally there are ocelli structures filled with prisms of clinopyroxene, quartz, and a slightly brownish to colorless mineral.

Phenocryst mineralogy:

Mineral: *Olivine*

Size: Seriate from groundmass to ~ 1.75mm in length

Habit: The majority of these grains are anhedral to subhedral in shape, blocky to elongate and ranging from fresh to complete alteration to some type of clay mineral.

Color: Colorless to Greenish-brown

Zoning: none seen

Modal %: 30%

Mineral: *Biotite/phlogopite*

Size: Seriate from groundmass up to ~1mm in length

Habit: The majority of the grains are subhedral, elongate to blocky with some inclusions of cpx, and iron oxide.

Color: Brown to reddish brown pleochroism

Zoning: normal zoning even colored throughout

Modal %: ~ 30%

Mineral: *Clinopyroxene*

Size: Seriate from groundmass up to ~ 1.5mm in diameter

Habit: The majority of the grains are euhedral to subhedral, elongate and blocky with some alteration to chlorite around the edges. A few of the grains have green cores and some have inclusions of biotite, apatite and iron oxides.

Color: Clear to pale yellow-green

Zoning: concentric zoning

Modal %: ~25%

Mineral: *Potassium feldspar*

Size: Bimodal with a few large phenocrysts up to ~4.5mm in size, but this mineral is mainly restricted to groundmass.

Habit: The majority of these grains is anhedral in shape and is completely restricted to the groundmass, but some are quite large. Some of the grains show signs of alteration to clay mineral.

Color: colorless

Zoning: none seen

Modal %: 15%

Sample: HM-5

Texture: This sample has a fine-grained porphyritic texture. Abundant biotite/phlogopite and clinopyroxene and minimal amounts of olivine (~48%, 42%, 10% respectively) comprise the large phenocrysts that range in size up to 2.5mm in length. The groundmass consists of smaller grains of biotite, cpx, altered olivine, apatite, sphene and iron oxides all of which overprint a mass of anhedral, enclosing, potassium feldspar. Additionally there are ocelli (up to ~ 6mm) bound by prisms of clinopyroxene and are filled with feldspar and a colorless mineral.

Phenocryst mineralogy:

Mineral: *Biotite*

Size: Seriate from groundmass up to ~1mm in length

Habit: The majority of the grains are subhedral to anhedral, elongate to blocky with some inclusions of cpx, and iron oxide.

Color: Brown to reddish brown pleochroism

Zoning: normal zoning even colored throughout

Modal %: ~ 45%

Mineral: *Clinopyroxene*

Size: Seriate from groundmass up to ~ 1mm in length

Habit: The majority of the grains are euhedral to subhedral, elongate and blocky with some altered to chlorite around the edges. A few of the larger blocky grains have green cores. Some have inclusions of biotite, apatite and iron oxides.

Color: Clear to pale yellow-green

Zoning: concentric zoning, with some hourglass zoning

Modal %: ~35%

Mineral: *Olivine*

Size: Seriate from groundmass to ~ 0.75mm in length

Habit: The majority of these grains are anhedral to subhedral in shape, blocky to elongate and range from fresh to complete alteration to some type of clay mineral.

Color: Colorless to Greenish-brown

Zoning: none seen

Modal %: 20%

Mineral: *Sphene*

Size: Generally one size ~ 0.20mm in diameter

Habit: The majority of these grains is euhedral to subhedral in shape and is restricted to the groundmass with a few larger ones that are distinct phenocrysts.

Color: pale yellow, slightly pleochroic

Zoning: concentric

Modal %: >>1%

Sample: HM-14

Texture: This sample has a fine-grained porphyritic texture. Biotite/phlogopite, olivine, clinopyroxene, and potassium feldspar (~35%, 35%, 20%, and 10% respectively) comprise the large phenocrysts that range in size up to 3mm in length. The groundmass consists of smaller grains of biotite, cpx, olivine, apatite, and iron oxides all of which overprint a mass of anhedral, enclosing, potassium feldspar.

Phenocryst mineralogy:

Mineral: *Biotite/phlogopite*

Size: Seriate from groundmass up to ~2.5mm in length

Habit: The majority of the grains are subhedral, elongate to blocky with some inclusions of cpx, iron oxide and some apatite.

Color: Brown to reddish brown pleochroism

Zoning: normal zoning even colored throughout

Modal %: ~ 35%

Mineral: *Olivine*

Size: ranging from ~0.20mm ~ 0.75mm in diameter

Habit: The majority of these grains are anhedral to subhedral in shape, blocky to elongate and range from fresh to complete alteration to some type of clay mineral.

Color: Colorless to Greenish-brown

Zoning: none seen

Modal %: ~35%

Mineral: *Clinopyroxene*

Size: Seriate from groundmass up to ~ 1.5mm in diameter

Habit: The majority of the grains are euhedral to subhedral, elongate and blocky with some altered to chlorite around the edges. A few of the grains have green cores and some have inclusions of biotite, apatite and iron oxides.

Color: Clear to pale yellow-green

Zoning: concentric zoning

Modal %: ~20%

Mineral: *Potassium feldspar*

Size: Bimodal with some large phenocrysts up to 3mm in size, but mainly restricted to groundmass

Habit: The majority of these grains is anhedral in shape and is completely restricted to the groundmass, but some are quite large. Some of the grains show signs of alteration to clay mineral.

Color: colorless

Zoning: none seen

Modal %: 10%

Mineral: *Apatite*

Size: ground mass restricted but a few up to 0.50mm

Habit: These grains are blocky, elongate, needle like and are restricted to the groundmass with one large one noted as a phenocryst.

Color: Colorless

Zoning: none seen

Modal %: >1%

Mineral: *Sphene*

Size: groundmass restricted but a few up to 0.50mm

Habit: The majority of these grains is euhedral to subhedral in shape and is restricted to the groundmass, with a few larger ones that are distinct phenocrysts.

Color: pale yellow, slightly pleochroic

Zoning: concentric

Modal %: >>1%

Sample: HM-28

Texture: This sample has a medium to coarse-grained porphyritic texture. The major phenocrysts present are clinopyroxene, biotite/phlogopite, and potassium feldspar (~40%, 40%, and 20% respectively). The groundmass consists of smaller grains of clinopyroxene, biotite, feldspar, calcite, iron oxides, apatite and sphene. Additionally there are ocelli type structures present filled with calcite and feldspar.

Phenocryst mineralogy:

Mineral: *Clinopyroxene*

Size: Seriate from groundmass up to ~ 3mm in diameter

Habit: The majority of the grains are euhedral to subhedral, elongate and blocky with some altered to biotite and or amphibole, and iron oxide around fractures and the edges. A few of the grains have relict cores of altered inclusions. Some have polysynthetic twinning.

Color: Clear to pale yellow-green

Zoning: concentric zoning

Modal %: ~40%

Mineral*: Biotite/phlogopite*

Size: Seriate from groundmass up to ~2.5mm in length

Habit: The majority of the grains are subhedral, elongate to blocky with some inclusions of cpx, iron oxide and some apatite.

Color: Brown to reddish brown pleochroism

Zoning: some have lighter colored cores surrounded by darker rims

Modal %: ~ 40%

Mineral: *Potassium feldspar*

Size: Bimodal with some large phenocrysts up to ~2.5mm in size, but mainly restricted to groundmass

Habit: The majority of these grains is anhedral in shape and is completely restricted to the groundmass and enclosing other minerals. Most of the grains show signs of alteration to fine grained carbonate.

Color: colorless

Zoning: none seen

Modal %: ~20%

Mineral: *Apatite*

Size: ground mass restricted but a few up to 0.50mm

Habit: These grains are blocky, elongate, needle like and are restricted to the ground mass with a few large ones noted as a phenocryst.

Color: Colorless

Zoning: none seen

Modal %: >1%

Mineral: *iron oxide*

Size: Generally one size ~ 0.07mm in diameter a few up to ~0.25mm

Habit: The majority of these grains is blocky to needle like, anhedral to subhedral in shape and is restricted to the groundmass or as inclusions and alteration of other phenocrysts.

Color: Black

Zoning: none seen

Modal %: >1%

Mineral: *Sphene*

Size: groundmass restricted but a few up to ~0.50mm

Habit: The majority of these grains is euhedral to subhedral in shape and is restricted to the groundmass, with a few larger ones that are distinct phenocrysts.

Color: pale yellow, slightly pleochroic

Zoning: none seen

Modal %: >>1%

Mineral: *Calcite*

Size: very fine-grained ranging from ground mass to large ~2.5mm clusters.

Habit: The majority of these grains is subhedral to anhedral in shape and is restricted to the groundmass, with a few larger ones that form distinct clusters and present as alterations of larger phenocrysts and ocelli structures.

Color: pale yellow, slightly pleochroic

Zoning: none seen

Modal %: >1%

Sample: HM-29

Texture: This sample has as very fine-grained porphyritic texture. Less than 2% of the sample consists of micro-xenocrysts, angular to rounded fragments from the surrounding sediments, which this magma intruded. A few of the larger groundmass amphibole exhibit alteration to iron oxides. Minerals present in the groundmass are bladed feldspar with a trachytic texture, blocky amphibole, and anhedral blocky shaped iron oxides. The xenocryst minerals are feldspar, quartz, clinopyroxene, sphene, and apatite. In this particular thin section iron oxides were the only grains to exceed 0.25mm

Phenocryst mineralogy:

Mineral: *iron oxide*

Size: Seriate from groundmass up ~0.50mm

Habit: The majority of these grains is blocky, anhedral to subhedral in shape and is restricted to the groundmass or as alterations of larger phenocryst.

Color: Black

Zoning: none seen

Sample HM-30

Texture: This sample has a fine to medium-grained porphyritic texture. The main phenocrysts are potassium feldspar, amphibole, iron oxide, clinopyroxene, (~ 40%, 24%, 19%, and 16% respectively) that range in size up to ~ 2.5mm in length. Lesser amounts of sphene and apatite are present ranging in size up to ~ 0.15mm. The groundmass consists of, clinopyroxene, amphibole, iron oxide, sphene and apatite. There is one large amygdule present (~3mm in diameter) that is filled with calcite.

Phenocryst mineralogy:

Mineral: *potassium feldspar*

Size: groundmass up to ~0.40mm

Habit: These grains are euhedral elongate and surround many of the larger phenocrysts of amphibole. Most shows signs of twining and alteration calcite and clay minerals.

Color: colorless

Zoning: none seen

Modal %: ~40%

Mineral: *Amphibole*

Size: Seriate ranging from groundmass to ~ 2.5mm in length

Habit: The majority of the grains are euhedral to subhedral, elongate to needle like with a few that are blocky. Some grains are twinned and have inclusions of apatite and sphene.

Color: Brown to clear pleochroism

Zoning: none seen

Modal %: ~24%

Mineral: *iron oxide*

Size: Groundmass up to ~ 0.25mm in diameter

Habit: The majority of these grains is blocky, anhedral to subhedral in shape and is associated with the amphibole phenocrysts in sample.

Color: Black

Zoning: none seen

Modal %: ~ 19%

Mineral: *Clinopyroxene*

Size: Seriate from groundmass up to ~ 0.20mm in length

Habit: The majority of the grains are euhedral to subhedral and elongate to blocky with a couple of large ~ 1mm euhedral grains clustered together.

Color: Clear to pale yellow-green

Zoning: some concentric zoning

Modal %: ~16%

Mineral: *Calcite*

Size: ~0.35mm Seriate from groundmass up to ~ 0.20mm in length

Habit: The majority of the grains is euhedral, blocky and appears in voids.

Color: colorless

Zoning: none seen

Modal %: >> 1%

Sample: HM-21

Texture: This sample has a fine to medium granular texture. The main mineral assemblage consists of feldspar, clinopyroxene, and iron oxide (~45%, ~45%, and ~10% respectively) and range up to ~ 1mm in size. This sample has significant alteration with much of the clinopyroxene altered to amphibole, biotite, or iron oxide, and much of the feldspar exhibits alteration to calcite and clays.

Phenocryst mineralogy:

Mineral: *feldspar*

Size: average size ~0.75mm ranging up to ~1mm

Habit: These grains are euhedral, elongate, and altered to calcite or some type of clay mineral. There is some twinning, but most of the original fabric is gone.

Color: colorless

Zoning: some oscillatory zoning seen

Modal %: ~45%

Mineral: *Clinopyroxene*

Size: average in size ~0.35mm with some ranging up to ~0.75mm

Habit: The majority of these grains are euhedral to subhedral and blocky with some of the grains showing alteration to a dark colored mineral and iron oxide.

Color: Light colored pink rims surrounding colorless centers.

Zoning: normal concentric, with some showing hourglass zoning

Modal %: ~45%

Mineral: *iron oxide*

Size: ~ 0.25mm or smaller in diameter

Habit: The majority of these grains are blocky, anhedral to subhedral in shape.

Color: Black

Zoning: none seen

Modal %: ~ 10%

Sample HM-8

Texture: This sample has a medium-grained porphyritic texture. The main phenocrysts consist of amphibole, feldspar, clinopyroxene, iron oxide, and biotite (~31%, ~25%, ~24%, 15% and ~5% respectively) and range up to ~ 4.5mm in size. Feldspar alteration to clays along with late stage biotite formation is associated with amphibole. The groundmass consists of feldspar, clinopyroxene, amphibole, biotite, iron oxide, sphene and apatite.

Phenocryst mineralogy:

Mineral: *Amphibole*

Size: Seriate ranging from groundmass to ~ 4.5mm in length

Habit: The majority of the grains are euhedral to subhedral, elongate to needle like with a few that are blocky and twinned. Some grains have inclusions of apatite, clinopyroxene, sphene and iron oxide with slight alteration of rims to some dark mineral.

Color: Brown to light brown pleochroism

Zoning: some color zoning with darker brown centers fading to lighter brown rims

Modal %: ~31%

Mineral: *feldspar*

Size: groundmass up to ~3mm

Habit: These grains are euhedral, elongate, with some twinning and showing signs of clay alteration.

Color: colorless

Zoning: none seen

Modal %: ~25%

Mineral: *Clinopyroxene*

Size: average in size ~0.75mm and ranging from groundmass up to ~1.5mm

Habit: The majority of these grains are euhedral to subhedral and blocky, with some of the grains clustered, exhibiting polysynthetic twinning, and showing alteration to amphibole.

Color: pale-yellow

Zoning: normal concentric

Modal %: ~24%

Mineral: *iron oxide*

Size: Groundmass up to ~ 0.25mm in diameter

Habit: The majority of these grains is blocky, anhedral to subhedral in shape and is associated with the amphibole phenocrysts in sample.

Color: Black

Zoning: none seen

Modal %: ~ 15%

Mineral*: Biotite/phlogopite*

Size: identified ~0.25mm with some probably in groundmass

Habit: The majority of the grains are anhedral to subhedral, elongate to blocky with most apparently to be secondary formation associated with amphibole in the sample.

Color: Brown to light brown pleochroism

Zoning: none seen

Modal %: ~ 5%

Sample: HM-20

Texture: This sample has a fine to medium granular texture. The main mineral assemblage consists of feldspar, amphibole, clinopyroxene and iron oxide (~40%, ~35%, and ~15%, and ~10% respectively) and range in size up to ~4.5mm. Much of the feldspar has secondary mineral alteration to some type of clay. Small amounts of late stage forming biotite are associated with amphibole.

Phenocryst mineralogy:

Mineral: *feldspar*

Size: seriate from ~0.25mm up to ~4.5mm

Habit: These grains are mostly euhedral to subhedral, elongate slightly blocky and encompassing clinopyroxene and amphibole. Most show some signs of alteration to clay minerals and with some Carlsbad twinning.

Color: colorless

Zoning: some concentric zoning seen

Modal %: ~40%

Mineral: *Amphibole*

Size: Seriate ranging from ~ 0.25mm up to ~4.5mm.

Habit: The majority of the grains are euhedral to subhedral, blocky, elongate to needle like. Some grains are twinned and have inclusions of apatite and alteration to iron oxide along with late forming biotite.

Color: dark reddish brown-to-brown pleochroism

Zoning: most have none visible but some larger ones exhibit compositional zoning, darker brown to a lighter brown rim.

Modal %: ~35%

Mineral: *Clinopyroxene*

Size: seriate from ~0.15mm up to ~1mm.

Habit: The majority of the grains are euhedral to subhedral and blocky.

Color: clear to pale yellow

Zoning: normal

Modal %: ~15%

Mineral: *iron oxide*

Size: ~ 0.25mm or smaller in diameter

Habit: The majority of these grains are blocky, anhedral to subhedral in shape and are an alteration mineral of the amphibole.

Color: Black

Modal %: ~10%

Sample: HM-26

Texture: This sample has a medium to large coarse-grained porphyritic texture. The phenocryst assemblage mainly consists of amphibole, iron oxide, feldspar, and altered clinopyroxene, (~42%, ~22, and ~21%, and ~15% respectively) and range in size up to 4.5mm. Many of the phenocrysts have inclusions and or alteration to a secondary mineral. The groundmass consists of amphibole, calcite, clays, iron oxide, and sparse amounts of apatite and late forming phlogopite.

Phenocryst mineralogy:

Mineral: *Amphibole*

Size: Seriate ranging from groundmass to ~ 4.5mm

Habit: The majority of the grains are euhedral to subhedral, blocky, elongate to needle like with some twinning and have inclusions of apatite and iron oxide.

Color: Brown to light brown pleochroism

Zoning: none seen

Modal %: ~42%

Mineral: *iron oxide*

Size: Groundmass up to ~ 0.25mm in diameter

Habit: The majority of these grains is blocky, anhedral to subhedral in shape and is associated with the amphibole phenocrysts in sample.

Color: Black

Zoning: none seen

Modal %: ~ 22%

Mineral: *feldspar*

Size: average size ~0.75mm ranging up to ~1.00mm

Habit: These grains are euhedral, elongate, and altered to calcite or some type of clay mineral. Some twinning, but most of the original fabric is gone.

Color: colorless

Zoning: some oscillatory zoning seen

Modal %: ~21%

Mineral: *Clinopyroxene*

Size: Seriate from groundmass up to ~1.5mm

Habit: The majority of these grains are euhedral to subhedral and blocky, with some of the grains clustered, exhibiting polysynthetic twinning, and showing alteration to amphibole or clay.

Color: pale-yellow

Zoning: normal concentric

Modal %: ~15%

Mineral*: Biotite*

Size: identified up to ~1.5mm, with most in groundmass

Habit: Most of these grains are anhedral to subhedral, blocky and associated with needle like amphibole in the sample.

Color: brown to light tan pleochroism

Zoning: none seen

Modal %: ~ >1%

Mineral: *Apatite*

Size: ground mass restricted but a few up to 0.25mm

Habit: The sporadic few large grains are blocky, elongate, and the rest are needle like and restricted to the ground mass.

Color: Colorless

Zoning: none seen

Modal %: ~>>1%

Sample: HM-25

Texture: This sample has a medium to large coarse-grained porphyritic texture. The phenocryst assemblage mainly consists of, feldspar, altered clinopyroxene, iron oxide, phlogopite, apatite and amphibole (~30%, ~20%, ~20%, ~19%, ~8%, and ~3% respectively) and range in size up to 4mm. Many of the phenocrysts have inclusions and alterations to a secondary mineral. The groundmass consists of clays, iron oxide, biotite and sparse amounts of apatite. There is one large amygdule present (~3mm in diameter) that is filled with quartz, altered cpx, and iron oxide.

Phenocryst mineralogy:

Mineral: *feldspar*

Size: average size ~0.75mm ranging up to ~1.5mm

Habit: These grains are euhedral, elongate, and altered to some type of clay mineral. Some twinning, but most of the original fabric is gone.

Color: colorless

Zoning: none seen

Modal %: ~30%

Mineral: *Clinopyroxene*

Size: Seriate from groundmass up to ~1.5mm

Habit: The majority of these grains are euhedral to subhedral, blocky, and showing alteration to some type of clay.

Color: pale-yellow

Zoning: none seen

Modal %: ~20%

Mineral: *iron oxide*

Size: Groundmass up to ~ 0.50mm in diameter

Habit: The majority of these grains is blocky, anhedral to subhedral in shape and is associated with the altered clinopyroxene and biotite phenocrysts in sample.

Color: Black

Zoning: none seen

Modal %: ~ 20%

Mineral*: Phlogopite*

Size: Seriate from groundmass to ~4mm

Habit: Most of these grains are anhedral to subhedral, blocky

Color: dark brown, reddish brown to light tan pleochroism

Zoning: none seen

Modal %: ~ >19%

Mineral: *Apatite*

Size: groundmass up to 0.25mm

Habit: The sporadic few large grains are blocky, elongate, and the rest are needle like

Color: Colorless

Zoning: none seen

Modal %: ~8%

Mineral: *Amphibole*

Size: ranging from groundmass to ~ 1mm

Habit: The majority of the grains are euhedral to subhedral, and are associated with the rims of the clinopyroxenes in the sample

Color: Brown to light brown pleochroism

Zoning: none seen

Modal %: ~3%

Sample: HM-24, HM-22, HM-19

Texture: These three samples come from one large sill (~ 3.5m) in the North Lake sill complex. The texture ranges from finer-grained porphyritic at the top (HM-22), to a larger-grained porphyritic at the base of the sill (HM-24, HM-19). The phenocryst assemblage consists of mica, clinopyroxene, feldspar, iron oxide and amphibole (~39%, ~24%, ~20%, ~17% and >1% respectively) and range in size up to `9mm. The groundmass consists of the aforementioned mineral phases in addition to apatite, calcite, and clays. In one sample there is a calcite filled segregation vein ~0.5mm in width that spans the length of the thin section.

Phenocryst mineralogy:

***Mineral**: Biotite/Phlogopite*

Size: most groundmass to ~1mm but some are up to ~5mm in size

Habit: Most of these grains are euhedral to subhedral, and equant to elongate in shape with inclusions of iron oxide and apatite.

Color: brown to dark brown pleochroism

Zoning: none seen

Modal %: ~ 39%

***Mineral:** Clinopyroxene*

Size: Seriate from groundmass up to ~4.00mm

Habit: The majority of these grains are euhedral to subhedral and blocky, with some of the grains clustered, exhibiting polysynthetic twinning, inclusions (iron oxide, biotite and apatite), and some showing alteration to amphibole or clay.

Color: pale-yellow light pink

Zoning: normal concentric, some compositional zoning

Modal %: ~24%

***Mineral:** feldspar*

Size: seriate from groundmass up to ~ 0.50mm but some are up to 4mm in size.

Habit: These grains are euhedral, elongate, seritized, and altered to calcite or some type of clay mineral.

Color: colorless

Zoning: none seen

Modal %: ~20%

Mineral: *iron oxide*

Size: Groundmass up to ~ 0.50mm in diameter

Habit: The majority of these grains is blocky, anhedral to subhedral in shape and appears as inclusions in other phenocrysts in the sample.

Color: Black

Zoning: none seen

Modal %: ~ 17%

Mineral: *Amphibole*

Size: one large one seen that is ~9mm

Habit: The majority of the grains are euhedral to subhedral, and are only seen in the samples from the base of the sill as large phenocrysts

Color: Brown to light brown pleochroism

Zoning: none seen

Modal %: ~>1%

Mineral: *Apatite*

Size: ground mass restricted but a few up to 0.50mm

Habit: The sporadic few large grains are blocky, elongate, and the rest are needle like and restricted to the ground mass.

Color: Colorless

Zoning: none seen

Modal %: ~>>1%